

UNIVERSITY *of*
TASMANIA

School of Physical Sciences

MALT-45: A 7 MM SURVEY OF THE SOUTHERN GALAXY

Christopher Harry Jordan

September 2015

Supervisors:

Dr. Andrew Walsh

Prof. Simon Ellingsen

Dr. Maxim Voronkov

Submitted in fulfilment of the requirements for the Degree of
Doctor of Philosophy

Declaration of Originality

This thesis contains no material which has been accepted for a degree or diploma by the University or any other institution, except by way of background information and duly acknowledged in the thesis, and to the best of my knowledge and belief no material previously published or written by another person except where due acknowledgement is made in the text of the thesis, nor does the thesis contain any material that infringes copyright.

Signed:  _____

Date: 17 / 09 / 15

Authority of Access

The publishers of the papers comprising Chapters 2 and 3 hold the copyright for that content, and access to the material should be sought from the respective journals. The remaining non published content of the thesis may be made available for loan and limited copying and communication in accordance with the Copyright Act 1968.

Signed:  _____

Date: 17 / 09 / 15

Statement of Co-Authorship

The following people contributed to the publication of work undertaken as part of this thesis:

Candidate	Jordan, C. H.	University of Tasmania, CSIRO Astronomy & Space Science
Co-Author 1	Walsh, A. J.	International Centre for Radio Astronomy Research, University of Tasmania
Co-Author 2	Ellingsen, S. P.	University of Tasmania
Co-Author 3	Voronkov, M. A.	CSIRO Astronomy & Space Science
Co-Author 4	Breen, S. L.	CSIRO Astronomy & Space Science

Chapter 2: *Pilot observations for MALT-45: a Galactic plane survey at 7mm*

Candidate (80%), Co-Author 1 (20%)

Candidate was the primary author and Co-Author 1 contributed to the idea, its formalisation, development and refinement. Writing was done primarily by the Candidate, with some paragraphs and feedback provided by Co-Author 1. Feedback and editing for the purposes of publication was provided by the remaining authors.

Chapter 3: *MALT-45: A 7mm survey of the southern Galaxy - I. Techniques and spectral line data*

Candidate (80%), Co-Author 1 (10%), Co-Author 2 (5%), remaining Co-Authors (5%)

Candidate was the primary author and Co-Author 1 contributed to the idea, its formalisation, development and refinement. Writing was done primarily by the Candidate. Feedback and editing for the purposes of publication was provided by the remaining authors.

Chapter 4: *MALT-45: A 7mm survey of the southern Galaxy - II. Follow-up observations of 44 GHz class I methanol masers*

Candidate (90%), Co-Authors 1, 2, 3 and 4 (10%)

Candidate was the primary author and Co-Authors 1, 2, 3 and 4 contributed to the idea, its formalisation, development and refinement. Writing was done primarily by the Candidate. Feedback and editing for the purposes of publication was provided by the Co-Authors 1, 2, 3 and 4.

Signed: _____ 

Date: _____ 17 / 09 / 15

Dr. Andrew Walsh, Primary Supervisor
International Centre for Radio Astronomy Research, Curtin University

Abstract

The last decade has seen vast improvement in the knowledge of star formation within our Galaxy, largely owing to improvements in instrumentation, allowing astronomers to compile more data. However, despite the advances of technology, the quest for understanding high-mass star formation (HMSF) continues. As we go on, breakthroughs have occurred; a prime example is the discovery of the class II methanol maser, which exclusively signposts on-going sites of HMSF, but still lacks the detail necessary to identify HMSF in all forms. Once we have understood where, why and how HMSF can occur, we will be able to diagnose Galactic structure and evolution.

Untargeted, large area surveys of molecular gas are ideal for identifying HMSF regions across a broad range of evolutionary phases. For example, the critical density of a molecular species can act as a probe for Galactic structure and star formation. Because HMSF occurs in regions of dense molecular gas, mapping high-density tracers serves well to identify target regions. The (1,1), (2,2) and (3,3) inversion transitions of ammonia (NH_3) have been successfully mapped by the H_2O Southern Galactic Plane Survey (HOPS), identifying previously unknown sites of star formation, as well as probing the structure of the Milky Way's spiral arms. Fortunately, HMSF can be identified by bright spectral lines in maser emission; HOPS also mapped the Galactic plane for water (H_2O) masers and, perhaps more importantly, the Methanol MultiBeam survey identifies class II methanol (CH_3OH) masers, which are exclusively associated with HMSF. While class II CH_3OH masers always signpost HMSF, they appear only in a specific evolutionary stage, and therefore other species (such as H_2O masers) are required to identify other stages.

Another, even higher density gas tracer useful for detecting HMSF and mapping the structure of our Galaxy is carbon monosulfide (CS). The ground state transition $J = 1 \rightarrow 0$ for CS lies within the 7 mm waveband, which also contains the poorly understood class I CH_3OH maser. Unlike the class II variant, class I masers are not exclusively associated with HMSF, but do appear in star-forming regions across a wide range of evolutionary stages. A large problem for class I CH_3OH maser studies is the bias in the targeted searches which have been used to find them; they have only been identified towards other masing regions (such as class II CH_3OH), and therefore the properties of these masers is somewhat unclear.

In this thesis, results focus on the MALT-45 survey using the Australia Telescope Compact Array (ATCA) in auto-correlation ('single-dish' mode). To date, MALT-45 has mapped the Galactic plane within $330^\circ < l < 335^\circ$, $|b| < 0.5^\circ$, which contains several known star-forming regions, including the G333 giant molecular cloud. MALT-45 surveys 12 spectral lines, but primarily CS, class I CH_3OH masers and SiO (1–0) $v = 0, 1, 2, 3$. Bright, extended CS emission is detected across the survey region, and highlight two distinct velocities, due to different spiral arms of the Galaxy. In addition to the previously known 19 class I CH_3OH masers, 58 new masers were detected. SiO masers were detected towards 47 regions, in various combinations of vibrational mode $v = 1, 2, 3$, all towards evolved infrared stars. Thermal SiO $v = 0$ emission is also detected across the survey region.

Major science results from MALT-45 include:

(i) A CS to NH₃ comparison, which highlights cold, dense clumps as well as hot, evolved regions. The cold and dense regions appear to have self-absorption of CS emission in their centres, due to a relative over-abundance of NH₃, while evolved regions appear to have very little NH₃ emission, despite being a dense gas tracer;

(ii) Almost all (94 per cent) of ATLASGAL 870 μ m dust emission point sources are associated with at least a 3σ peak of CS emission;

(iii) By comparing with peak CS velocities, class I CH₃OH masers are good indicators of the systemic velocities of clouds;

(iv) More than half (55 per cent) of the detected class I CH₃OH masers are not associated with any other kind of maser;

(v) Class II CH₃OH, H₂O and hydroxyl (OH) masers associate well with class I CH₃OH masers, confirming that class I CH₃OH masers occur towards a wide range of evolutionary stages in HMSF;

(vi) Class I CH₃OH masers appear to have no correlation in intensity or luminosity with other maser species;

(vii) Class I CH₃OH masers are have typical projected linear distances from other star-forming masers, peaks of CS and 870 μ oint sources within 0.5 pc;

(viii) Class I CH₃OH masers are spread over a larger area when also associated with OH masers, perhaps due to their more evolved state;

(ix) Almost all (95 per cent) of class I CH₃OH masers are associated with an ATLASGAL source;

(x) Using ATLASGAL source parameters, a clump mass is calculated. The population of class I CH₃OH masers has a broad range of associated masses ($10^{1.5}$ to $10^{4.5} M_{\odot}$), but peaks between $10^{3.0}$ and $10^{3.5} M_{\odot}$. Higher masses tend to be associated with evolved regions of star formation, while lower masses tend to be non-evolved regions;

(xi) SiO masers typically decrease in intensity with vibrational mode ($v = 1, 2, 3$), but eleven cases of stronger $v = 2$ than $v = 1$ emission were found, and two regions of only $v = 2$ emission were found;

(xii) The relatively rare $v = 3$ vibrational mode of SiO (1–0) was detected towards three evolved infrared stars.

Acknowledgements

This PhD project and thesis has really pushed me to the limit. As difficult as it has been, without the support offered by many people over the years, I would have crumbled under the pressure.

The work leading up to this thesis began at James Cook University, and due to unfortunate circumstances, could not continue there. Townsville was home for a long time, with many friends and family members helping my work to become a reality. I have been a university dweller for nearly 10 years, and it has taken me most of this time to realise how good my family has been to me. Without their unquestioning support, this thesis was surely doomed from the start. I also want to thank the ‘uni crew’, in no particular order: Bronson, Patty, Nick, Rhys, Clair, Liam, Nathan and Tim. Without your laughter and encouragement, nothing would have been possible.

I was incredibly fortunate to find a new home at the University of Tasmania. My new school, despite the cold climate (especially relative to Townsville!), was warm and friendly right from the start. That welcome was something I’ll never forget, and helped me through a very stressful time. I am indebted to all of the staff, but I particularly want to thank a few people. John Dickey had a knack for offering key advice at the right time. Jim Lovell was kind and considerate, supporting me during my UTAS years with many, many hours of paid observational work. Shari Breen, while not formally part of UTAS, always felt close by and has helped me at many points of my candidature. Simon Ellingsen deserves my biggest praise, for being a fantastic supervisor (especially in the circumstances). I don’t think I ever once heard him complain, even as I’ve received many comments on my poor attempt at writing. I am proud and grateful to have conducted my work through UTAS.

Thanks must also go to CSIRO Astronomy and Space Science. The opportunities granted to me through many duty astronomer shifts, schools and discussions with staff proved invaluable, and I hope future students are as lucky as I was. Maxim Voronkov co-supervised me with methanol maser expertise; always friendly and helpful, it was great to have someone so passionate on board.

My time in Tasmania was supported by many other wonderful people, possibly too many to name. Jay and Anita were always nearby, and helped me fit right in. Vasaant was always up for an interesting chat, especially concerning emacs. Courtney shared many laughs with me, especially towards the end, sharing an office where we were both finishing our theses. A few friendly Europeans - Lucia, Liza, Alvaro, Sara (and Jamie, the native Tasmanian) - were great company with garlic prawn pizzas at the nearby pub. Finally, I had amazing housemates in Dave and Tim; between many curry nights, there are way too many laughs to remember. One final mention to Christian (Kevin), who could always crack me up. Thank you all so much.

Special mention goes to my Rebecca, who has participated in many fantastic holidays, shares my dreams and has particularly given a lot of support at the end of this thesis. I hope that this thesis acts as a foundation to build our successes upon.

Finally, last but certainly not least, I give my biggest thanks to Andrew Walsh. He has been with me from the start, and I could not have asked for a better supervisor. But more

than a supervisor, he was a mentor and a great friend. Always generously facilitating his love of beer, many good times have passed over the years. I can never repay the effort lent to me, but I hope that I can at least pass on the kindness to others in the future. Cheers!

Contents

1	Introduction	1
1.1	Motivation	2
1.2	A general timeline of HMSF	4
1.2.1	Molecular clouds and Infrared dark clouds	4
1.2.2	Hot molecular core	6
1.2.3	H II region	7
1.2.4	Summary	8
1.3	Astrophysical diagnostics	9
1.3.1	Spectral lines	9
1.3.2	Continuum	11
1.4	Star-forming tracers	13
1.4.1	Hydrogen	13
1.4.2	Carbon monoxide (CO)	13
1.4.3	Ammonia (NH ₃)	14
1.4.4	Carbon monosulfide (CS)	15
1.4.5	Silicon monoxide (SiO)	16
1.5	Star-forming masers	17
1.5.1	Theory	17
1.5.2	Class II methanol (CH ₃ OH)	18
1.5.3	Hydroxyl (OH)	19
1.5.4	Water (H ₂ O)	21
1.5.5	Class I methanol (CH ₃ OH)	22
1.5.6	Silicon monoxide (SiO)	23
1.5.7	An evolutionary timeline of HMSF with masers	24
1.6	Motivation of this thesis	25
1.6.1	Thesis overview	25
2	Pilot observations for MALT-45	27
2.1	Introduction	27
2.2	MALT-45 Design	28
2.2.1	The G333 GMC	29
2.3	Observations	29
2.4	Auto-correlation	31
2.4.1	Procedure	31
2.4.2	Software	32

2.5	Results	33
2.5.1	CS (1–0) at 48.990 GHz	34
2.5.2	Class I CH ₃ OH 7(0,7)–6(1,6) A ⁺ masers at 44.069 GHz	35
2.5.3	SiO (1–0) $v = 1, 2$ masers at 43.122 and 42.820 GHz	36
2.5.4	Other detected lines	38
2.6	Discussion	43
2.6.1	Weather Effects	43
2.6.2	Telescope Performance	43
2.6.3	Comparison with other observations	43
2.6.3.1	G333.227–0.057	44
2.6.3.2	G333.726+0.366	45
2.6.3.3	G333.314+0.109	45
2.7	Future work and refinement of the MALT-45 survey	45
3	MALT-45 techniques and spectral line data	47
3.1	Introduction	48
3.2	Survey Design	49
3.2.1	Australia Telescope Compact Array characterisation	49
3.2.1.1	CABB zoom modes	51
3.2.2	MALT-45 observations	51
3.2.3	Data reduction	52
3.3	Results	54
3.3.1	CS (1–0) at 48.990 GHz	54
3.3.2	Class I CH ₃ OH 7(0,7)–6(1,6) A ⁺ masers at 44.069 GHz	54
3.3.3	SiO (1–0) $v = 0$ thermal emission at 43.424 GHz	62
3.3.4	SiO (1–0) $v = 1, 2, 3$ masers at 43.122, 42.820 and 42.519 GHz	62
3.3.5	Survey completeness	63
3.4	Discussion	64
3.4.1	Comparing CS (1–0) with HOPS NH ₃ (1,1)	64
3.4.1.1	G330.95–0.19	65
3.4.1.2	G332.10–0.42	67
3.4.1.3	G333.60–0.20	67
3.4.1.4	Summary	68
3.4.2	Comparing CS (1–0) with class I CH ₃ OH maser regions	68
3.4.3	Comparing class I CH ₃ OH maser regions with SiO (1–0)	70
3.4.4	Class I CH ₃ OH maser comparison with GLIMPSE	71
3.4.5	95 GHz class I CH ₃ OH masers	72
3.4.6	Class I CH ₃ OH maser associations	73
3.4.6.1	Class II masers from the MMB	73
3.4.6.2	H ₂ O masers from HOPS	75
3.4.6.3	OH masers from Sevenster et al. (1997) and Caswell (1998)	76
3.4.6.4	Summary of star-formation maser associations	78
3.4.7	SiO $v = 1, 2, 3$ maser associations	78

3.5	Summary	79
4	Follow-up observations of class I methanol masers	81
4.1	Introduction	81
4.2	Observations	82
4.2.1	Data reduction	83
4.2.1.1	Cross-correlation	83
4.2.1.2	Auto-correlation	84
4.3	Results	85
4.4	Discussion	91
4.4.1	Properties of detected class I CH ₃ OH masers	91
4.4.2	Comparing class I CH ₃ OH masers with other masers and thermal lines	93
4.4.2.1	Separation from star-forming maser species	93
4.4.2.2	Velocities	95
4.4.2.3	Brightness	97
4.4.3	Class I CH ₃ OH masers on a HMSF evolutionary timeline	99
4.4.4	Comparing class I CH ₃ OH masers with ATLASGAL	102
4.4.4.1	Class I CH ₃ OH masers without an ATLASGAL source	105
4.4.5	Comparing class I CH ₃ OH masers in cross- and auto-correlation	106
4.5	Summary and Conclusions	110
5	Additional analyses with CS (1–0)	111
5.1	Temperature	111
5.1.1	Methodology	111
5.1.2	Relation with CS (1–0)	113
5.1.3	Individual source descriptions	115
5.1.3.1	Regions near G331.03–0.32	117
5.1.3.2	Regions near G331.48–0.23	121
5.1.3.3	G332.24–0.04	121
5.1.3.4	G333	121
5.1.3.5	Regions near G333.60–0.20	122
5.1.3.6	G333.72+0.37	123
5.1.3.7	Summary	123
5.2	Offsets between CS (1–0) peaks and class I CH ₃ OH masers	123
5.2.1	Methodology	124
5.2.2	Results and discussion	124
5.3	CS (1–0) and ATLASGAL 870 μ m dust emission	125
6	Summary and conclusion	129
6.1	Future work	130
6.1.1	Short-term projects	130
	Appendices	141
A	Supplementary material from the MALT-45 survey	143

A.1	RMS noise maps	143
A.2	Class I CH ₃ OH maser spectra	145
A.3	Auto-correlated maps	151
A.4	SiO maser spectra	152
B	Supplementary material from follow-up obs.	159
B.1	Gaussian fits to class I CH ₃ OH masers	159
B.2	Gaussian fits to thermal lines	167
B.3	GLIMPSE images	170

List of Figures

1.1	The R136 star cluster within the Tarantula nebula	1
1.2	Schematic of low-mass star formation	3
1.3	The ‘Nessie’ infrared dark cloud	5
1.4	Velocity gradient of G31.41+0.31	6
1.5	Schematic of accretion and outflows	7
1.6	NGC 604: A giant H II region	8
1.7	Schematic of H I hyperfine line emission	9
1.8	Isotopologues of CO emission	11
1.9	Infrared imagery featuring an ‘Extended Green Object’	12
1.10	Sample figure from Lu et al. (2014)	15
1.11	Schematic of stimulated emission	18
1.12	VLBI image of class II CH ₃ OH masers in a ring	20
1.13	18 cm energy levels of OH hyperfine lines	21
1.14	SiO and H ₂ O maser emission toward Orion-KL	24
1.15	An evolutionary timeline of HMSF through maser emission	25
2.1	An example of ATCA baselines	31
2.2	The auto-correlation baselining procedure	32
2.3	A diagram outlining the auto-correlation pipeline used for MALT-45.	33
2.4	MALT-45 CS overlaid with HOPS NH ₃ (1,1)	34
2.5	Class I CH ₃ OH emission mapped by MALT-45	35
2.6	Auto-correlated spectra from MALT-45	36
2.7	SiO $v = 2$ maser emission mapped by MALT-45	37
2.8	Follow-up class I CH ₃ OH maser spectra from Mopra.	38
2.9	Follow-up SiO maser spectra from Mopra.	39
2.10	GLIMPSE 8.0 μm emission overlaid with MALT-45 CS	40
2.11	GLIMPSE images of MALT-45 maser regions	41
2.11	GLIMPSE images of MALT-45 maser regions, continued	42
3.1	GLIMPSE 8.0 μm emission overlaid with part of a MALT-45 mosaic	51
3.2	CS (1–0) emission map overlaid with class I CH ₃ OH masers	53
3.3	CS (1–0) in longitude-velocity, overlaid with CO and class I CH ₃ OH masers	53
3.4	CS (1–0) overlaid with HOPS NH ₃ (1,1)	53
3.5	Histogram of new and previously known class I CH ₃ OH masers	55
3.6	GLIMPSE 3-colour image with detected class I CH ₃ OH masers	61
3.7	SiO $v = 0$ thermal emission overlaid with CS (1–0)	61

3.8	GLIMPSE 3-colour image with detected SiO masers	61
3.9	Examples of SiO maser associations	63
3.10	A ratio image of MALT-45 CS (1–0) to HOPS NH ₃ (1,1)	64
3.11	Examples of significant C ³⁴ S/CS ratios within CS/NH ₃ clumps	66
3.12	Scatter plot of class I CH ₃ OH and CS integrated intensities	68
3.13	Velocity offsets between the peak velocity of class I CH ₃ OH and CS (1–0)	69
3.14	An example of a class I CH ₃ OH maser with associated ‘green’ emission	71
3.15	Scatter plot of 95- vs 44-GHz class I CH ₃ OH masers	72
3.16	Luminosity-luminosity plot of class I against class II CH ₃ OH masers	73
3.17	Histogram of class I CH ₃ OH masers with and without class II CH ₃ OH masers	74
3.18	Histogram of class I CH ₃ OH masers with and without H ₂ O masers	75
3.19	Histogram of class I CH ₃ OH masers with and without OH masers	76
3.20	Four-set Venn diagram of star-forming maser associations	77
4.1	Auto-correlation reduction procedure used by the follow-up observations	87
4.2	Luminosities, linear sizes and velocity spreads of class I CH ₃ OH masers	92
4.3	Histogram of distances between class I CH ₃ OH masers and other masers	94
4.4	Velocity differences between class I CH ₃ OH masers and other species	96
4.5	Comparing the brightness of class I CH ₃ OH masers against thermal lines	98
4.6	Relative populations of evolved and non-evolved class I CH ₃ OH masers	100
4.7	Class I CH ₃ OH maser spot counts with and without OH associations	101
4.8	Offsets between ATLASGAL sources and associated class I CH ₃ OH masers	103
4.9	Clump masses with class I CH ₃ OH masers	103
4.10	Brightness scatter plot of ATLASGAL dust and class I CH ₃ OH masers	104
4.11	Brightness scatter plot of ATLASGAL dust and CS	105
4.12	Examples of class I CH ₃ OH maser cross- and auto-correlation spectra	107
4.13	Histogram of brightness ratios between cross- and auto-correlation spectra	108
4.14	Scatter plots of maser-ness ratios against the brightness of thermal lines	109
5.1	Gas temperatures calculated via NH ₃ (1,1) and (2,2)	114
5.2	Scatter plot of temperature vs. peak CS (1–0) luminosity	117
5.3	Gas temperatures overlaid with MALT-45 CS (1–0)	118
5.4	Distances between CS (1–0) and class I CH ₃ OH masers	125
5.5	MALT-45 CS (1–0) emission with ATLASGAL point sources	126
5.6	Projected distances between ATLASGAL sources and associated CS peaks	127
5.7	Brightnesses of ATLASGAL sources with associated CS peaks	128

List of Tables

1.1	Properties of various HMSF-associated stages.	4
1.2	Properties of various molecular cloud types.	5
2.1	Spectral lines mapped by the MALT-45 pilot survey	30
2.2	Properties of detected MALT-45 maser emission as determined by Mopra. . .	39
2.3	MALT-45 parameters from the pilot survey and full survey.	46
3.1	Spectral lines mapped by the MALT-45 survey	50
3.2	Properties of detected MALT-45 class I CH ₃ OH maser emission	56
3.3	Properties of detected MALT-45 SiO (1–0) maser emission	59
4.1	Spectral lines mapped by follow-up observations	83
4.2	List of class I CH ₃ OH masers targeted for follow-up observations	88
4.3	Associations with each of the targeted class I CH ₃ OH masers	89
5.1	Regions with temperature information	116

List of Equations

1.1	The ground-state transition of CO	10
1.2	The critical density of $j \rightarrow k$	10
1.3	Optical depth using NH_3	14
1.4	Rotational temperature using NH_3 (1,1) and (2,2)	14
1.5	Total column density using NH_3 (1,1)	15
1.6	Optical depth using CS and C^{34}S	16
2.1	Calibration of auto-correlated data	32
4.1	Clump mass from optically thin dust emission	102
5.1	Optical depth of NH_3 (1,1) gas	111
5.2	Optical depth of NH_3 (2,2) gas	112
5.3	Rotational temperature from $\tau_{(1,1)}$ and $\tau_{(2,2)}$	112
5.4	Kinetic temperature from rotational temperature	112
5.5	Characterisation of NH_3 (1,1) satellite lines	112
5.6	General form of a Gaussian	113
5.7	Rotational temperature from $T_B(1,1)$ and $T_B(2,2)$	113
5.8	Relation between temperatures derived from Lowe et al. (2014) and HOPS data	115
5.9	Function employed to modulate CS pixel values by distance	124

Chapter 1

Introduction

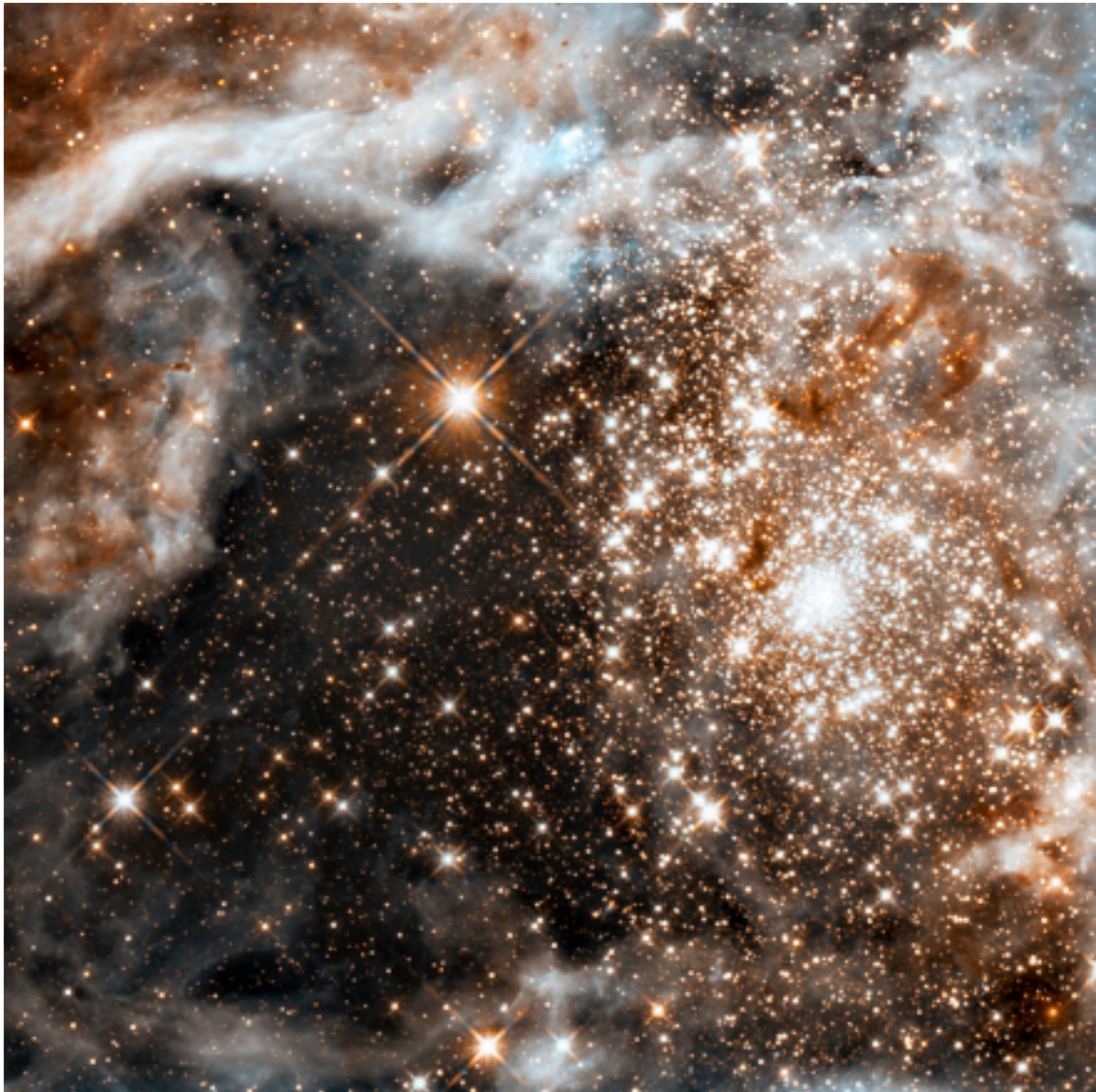


Figure 1.1: R136, a star cluster within the Tarantula nebula, contains hundreds of high-mass stars. This image was taken in infrared from the Hubble space telescope.

1.1 Motivation

How are stars created? Until the realisation of gravity, this was perhaps too difficult a question to broach throughout human history. Newton was indeed a talented individual: along with his theory of Gravity, he was the first to speculate on gravitational collapse being a chief component. This provided the catalyst for research, and after many centuries, we have a good understanding for the overall process of star formation.

However, nature is not without complication. Star formation is not a readily explained simple procedure, applicable everywhere; it can be divided into sub-categories of low- and high-mass star formation (LMSF, HMSF). LMSF is better understood and characterised, and often occurs in isolation with minimal requirements. HMSF, however, is vastly more complicated. Perhaps the most striking difference is that low-mass stars are simultaneously created alongside the high-mass stars, yielding an entire star cluster, such as that seen in Fig. 1.1. Formally, high-mass stars are categorised by possessing eight or more solar masses ($>8 M_{\odot}$, also known as O- or B-type stars), as such stars die via supernovae. HMSF is defined as the formation of such stars. High-mass stars are important, as only they provide the means for producing heavy elements (such as iron), and scatter these throughout the interstellar medium (ISM). High-mass stars are also incredibly energetic; the amount of energy they produce over their lifetime rivals that of their supernova deaths. By understanding how high-mass stars are created, we are able to determine galaxy evolution and structure, through the evolution of molecular clouds and spiral arms. Before further discussing HMSF, a simplified, generalised timeline of LMSF is given:

- i) A core of gas and dust within a molecular cloud is unable to support its internal pressure against gravitational self-collapse, also known as the Jeans instability (Jeans 1902);
- ii) Matter within the core falls into a focus, via a procedure termed ‘inside-out collapse’. The most central part of the core collapses inwards fastest, followed by the surrounding shell, and so on, until the material is exhausted (Shu 1977);
- iii) The focus of the core becomes a young stellar object (YSO), which is fed by an accretion disk and exhibits perpendicular outflows. These features are necessary to remove the excess angular momentum of in-falling material;
- iv) Through a combination of the disk being exhausted and blown away by the outflows, accretion halts. Eventually, the internal temperature of the YSO rises to begin hydrogen fusion, at which point the star joins the main sequence. The remaining accretion disk may become a protoplanetary disk.

These stages can be seen in Fig. 1.2. HMSF complicates the LMSF scenario: it is not a ‘scaled-up’ version of LMSF. Unlike LMSF, accretion continues once a high-mass YSO has joined the main sequence (Kahn 1974), and the turbulence of HMSF greatly slows the in-falling rate of the gas (Caselli & Myers 1995). Additionally, bigger and hotter stars may restrict further accretion with significant blackbody radiation, yielding an outward pressure. Once complete, HMSF does not yield one or a few high-mass objects; rather, a whole cluster of low-mass stars is born surrounding the high-mass ones. Despite decades of research, HMSF is still poorly understood. Observationally, there are a few factors which slow progress:

- i) HMSF requires high-mass molecular clouds, and the nearest to Earth is Orion at

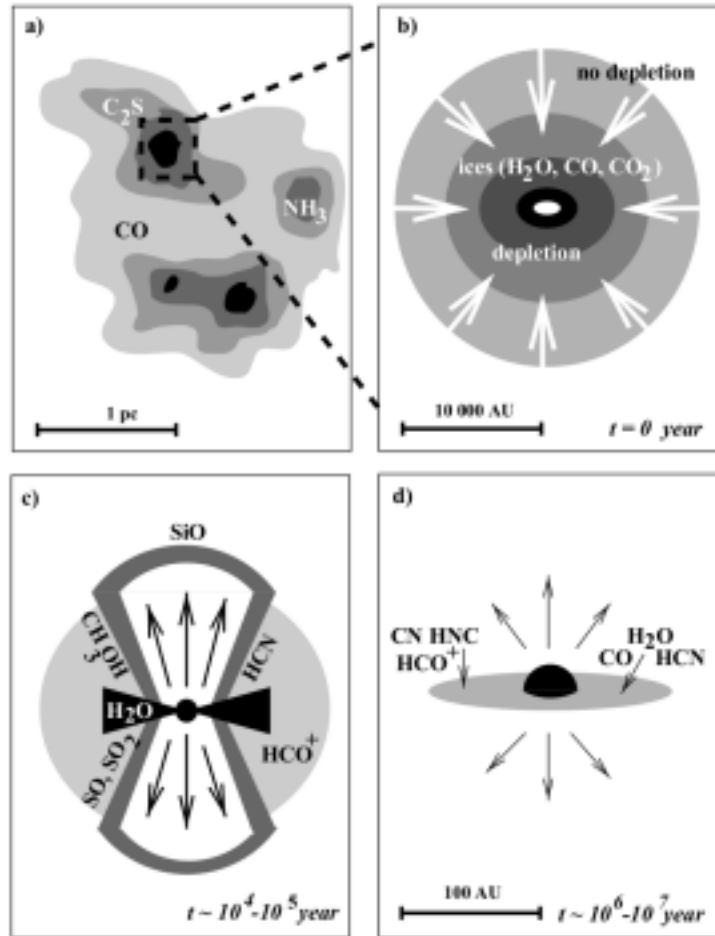


Figure 1.2: Evolutionary stages of LMSF, taken from van Dishoeck & Blake (1998).

~ 450 pc, while LMSF has been observed even closer (e.g. Taurus-Auriga, 150 pc). High resolution instruments are needed to discern the finer details at great distances;

ii) HMSF occurs in the most dense regions of molecular clouds, effectively requiring the use of radio and infrared astronomy. Shorter-wavelength emission from YSOs is re-processed into long-wavelengths by the natal environment. Ground-based observations are susceptible to radio frequency interference as well as atmospheric effects, increasing the difficulty of observations;

iii) Rather than forming isolated stars, HMSF tends to form clusters of stars, also called OB associations. Isolating the conditions feeding a high-mass YSO are difficult when the whole region is star-forming;

iv) High-mass stars are created and evolve over much shorter timescales than low-mass stars. Additionally, they are rare, typically being restricted to giant molecular clouds (which are also rare). Therefore, witnessing HMSF ‘in the act’ is difficult, in addition to all the above.

Parallels do exist between LMSF and HMSF. Molecular clouds fragment to form clumps and cores, and there is overwhelming evidence of outflows occurring in HMSF (Moscadelli & Goddi 2014; Yu & Wang 2014; Navarete et al. 2015). The presence of outflows also hints at the existence of accretion disks. However, the traditional inside-out collapse model (*core accretion*) may not be the solution to accretion within HMSF; an alternate theory of

competitive accretion asserts that gas is drawn over larger spatial scales within molecular clouds, because the surrounding low-mass YSOs are formed simultaneously, and are also able to accrete gas. Additionally, if the density of YSOs is high enough, high-mass YSOs may be formed by mergers (Bonnell et al. 1998). Mergers are proposed due to the difficulty of accretion being efficient enough to yield high-mass YSOs. While mergers remain a possibility for generating high-mass stars, it is unlikely to affect typical HMSF; modelling shows that mergers are efficient mechanisms in high-population star clusters, and that one or two extreme objects result (Moeckel & Clarke 2011).

Currently, HMSF studies have allowed us to understand how to generate stars up to $20 M_{\odot}$, yet we see stars in excess of $100 M_{\odot}$ in nature. How are these stars created? There are many directions of study to help answer this question. In the following sections, evolutionary stages of HMSF and tools used to identify them are discussed.

1.2 A general timeline of HMSF

All star formation occurs within molecular clouds (MCs), but HMSF typically occurs within giant molecular clouds (GMCs), with masses exceeding $10^4 M_{\odot}$. In an attempt to understand HMSF, we must categorise the various evolutionary stages. Table 1.1 lists some properties of these stages, although these should be treated with care. The remainder of this section describes each evolutionary stage in further detail.

1.2.1 Molecular clouds and Infrared dark clouds

MCs are regions of the ISM both sufficiently cold and dense for molecules to survive. The neutral H I population is allowed to form covalent bonds with one another, yielding the primary component H₂. However, MCs also contain heavier molecules; because H₂ is difficult to detect, the amount of H₂ present is usually estimated in terms of the heavier molecules using so-called ‘ \mathcal{X} -factors’. The archetypal example is carbon monoxide (CO); it is easily excited and very abundant, making it useful for probing the edges of MCs. Table 1.2 gives some typical properties of MCs. As the ISM contains energetic photons (ultraviolet or shorter wavelength) which are able to dissociate H₂, a molecular cloud might not survive long enough to allow star formation to occur. Clouds with sufficient mass are resistant to destruction via a process called self-shielding; simply put, H₂ on the exterior of a MC is dissociated,

Table 1.1: Properties of various HMSF-associated stages. These values serve as ‘rules of thumb’ for classification. Temperatures of H II regions refer to molecular gas, rather than the ionised regions.

	Size (pc)	Density ($n_{H_2} \text{ cm}^{-3}$)	Temperature (K)	Reference
Clump	~ 10	$\sim 10^2$	10	Kim & Koo (2001)
Core	~ 1	$\sim 10^5$	10^5	Kim & Koo (2001)
Hot core	< 0.1	$> 10^7$	> 100	de Villiers et al. (2015)
HC H II region	< 0.1	$> 10^6$	> 200	Lizano (2008)
UC H II region	< 0.5	$> 10^5$	100-200	Churchwell (2002)

Table 1.2: Properties of various molecular cloud types, taken from Stahler & Palla (2005).

Cloud type	A_V (mag)	n_{tot} (cm^{-3})	Diameter (pc)	Temp. (K)	Mass (M_\odot)	Examples
Diffuse	1	500	3	50	50	
GMCs	2	100	50	15	10^5	Orion
Dark clouds						
Complexes	5	500	10	10	10^4	Taurus-Auriga
Individual	10	10^3	2	10	30	B1
Dense cores/Bok globules	10	10^4	0.1	10	10	TMC-1/B335

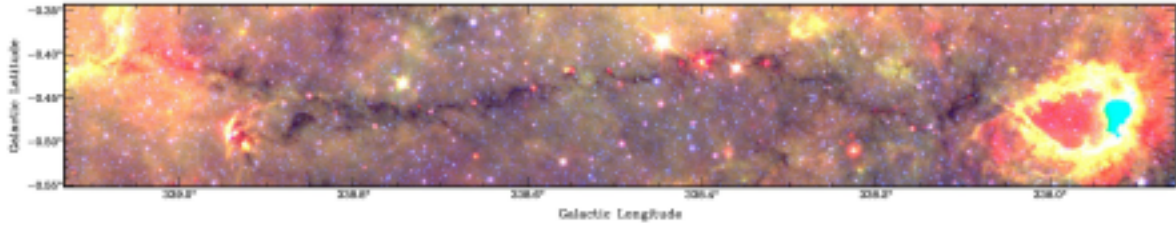


Figure 1.3: An exceptional example of an infrared dark cloud, Fig. 1a of Jackson et al. (2010): A false three-colour image of the Nessie Nebula. The $3.6\ \mu\text{m}$ (blue) and $8.0\ \mu\text{m}$ (green) emission is from GLIMPSE, and the $24\ \mu\text{m}$ (red) emission is from MIPSGAL.

leaving the internal H_2 intact.

Dust grains also contribute to shielding of molecules by absorbing some of the ultraviolet radiation. By mass, grains are mostly made up of silicon (Draine 2003), and are important for the chemistry within MCs. In addition to gas-phase chemistry, sufficiently dense regions allow the various molecules present to react with one another by using electrostatic forces on dust grain surfaces, which yield more complicated molecular species. This is especially useful for the study of HMSF, as the signatures of these molecules allow us to diagnose the conditions within MCs. In young regions of star formation, certain species experience ‘freeze-out’ on to the dust grains; as the density increases and temperature remains low, the observed molecular emission decreases, as molecules freeze onto dust grains. Other species are resistant to depletion, which allow diagnosis of evolutionary state. Depleted species may be released later by shocks or radiation from newly formed stars, which further detail the evolutionary state. Eventually, dust grains may be destroyed by shocks, providing further useful species for study, such as silicon monoxide (SiO).

What is the analogue of LMSF core collapse in HMSF? Relatively new objects of study, infrared dark clouds (IRDCs), may be the solution. Discovered by Egan et al. (1998) and Carey et al. (1998), IRDCs have the highest densities within GMCs, and are characterised by a bright infrared background being obscured by foreground filaments; a beautiful example can be seen in Fig. 1.3. Space-based observations have provided relevant infrared imagery in various wavelengths, including the Galactic Legacy Infrared Mid-Plane Survey Extraordinaire (GLIMPSE). Using this imagery, large catalogues of IRDC candidates have been formed (Simon et al. 2006; Peretto & Fuller 2009). However, the lack of clear criteria may lead to false-positives; there are large differences between the catalogues presented by Simon et al.

(2006) and Peretto & Fuller (2009). Nonetheless, exciting results have come from the study of these objects, including an extremely dense cloud that may form a stellar cluster similar to Orion (SDC335.579–0.272; Peretto et al. 2013). Improvements in isolating IRDCs are on-going, utilising the Herschel space telescope (Battersby et al. 2011; Wang et al. 2015).

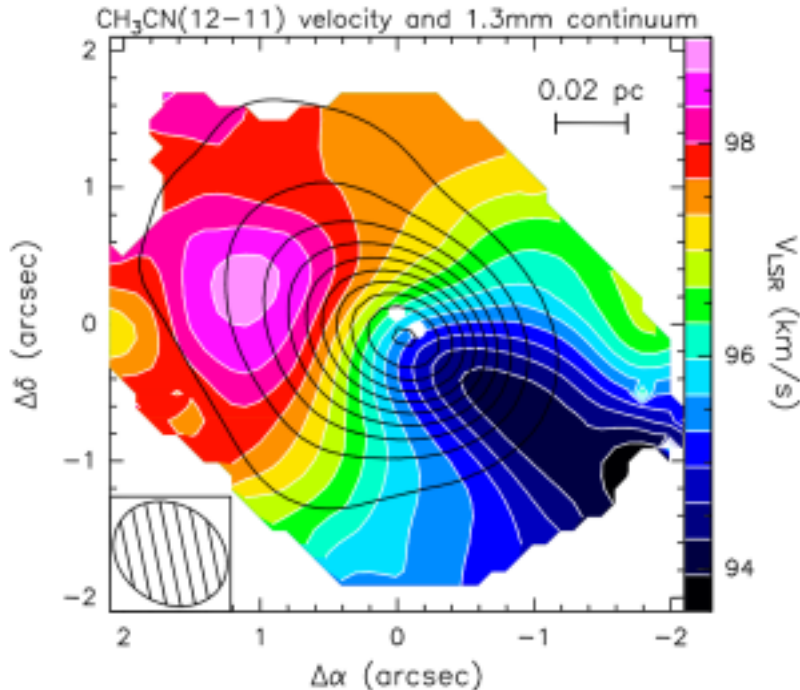


Figure 1.4: Fig. 5 of Cesaroni et al. (2011) shows evidence of a circumstellar disk: *Overlay of the map of the 1.3 mm continuum emission (contours) on that of the CH_3CN (12–11) line velocity (colour scale). Contour levels range from 0.1 to 2 in steps of 0.2 Jy/beam. Offsets are measured with respect to the phase centre. The two white dots denote the free-free continuum sources detected by Cesaroni et al. (2010). The synthesized beam is shown in the bottom left.*

1.2.2 Hot molecular core

As accretion is on-going, the high-mass YSO becomes hot, irradiating its environment with thermal energy. Additionally, the outflows from an accretion disk shock and further inject thermal energy into the medium. These conditions allow unique chemistry to occur, signposting this hot molecular core phase. Evidence does exist for accretion disks in HMSF, but it still remains somewhat of a ‘Holy grail’ to observe. An effective technique of inferring the presence of a disk is using high-level molecular transitions, which are rare and powered by high temperatures. One successful case of detection is via methyl cyanide (CH_3CN): it traces extremely dense gas $n_c > 10^5 \text{ cm}^{-3}$ and is excited in relatively warm regions $> 100 \text{ K}$ (Purcell et al. 2006). Using emission from this molecule, Cesaroni et al. (2011) were able to map a velocity gradient across a well-studied hot molecular core; see Fig. 1.4.

Recently, a H_2O maser line with high excitation temperature ($> 3000 \text{ K}$) was used to identify a circumstellar disk in Orion Source I. This complements other studies done in this region, including SiO maser emission highlighting the interface between disk and outflow (Niederhofer et al. 2012). These results required very-high frequency interferometry observations with ALMA, which is not yet fully operational; the future is certainly an exciting place for

star-formation studies.

Outflows are relatively obvious, typical signatures of star formation. As mass collapses on to a YSO via an accretion disk, the built-up angular momentum is shed as perpendicular outflows. Interaction between the core medium, accretion disk and outflow is difficult to model; an example schematic attempting to quantify all mass flows can be seen in Fig. 1.5. One study finds that outflowing mass is a useful indicator of core mass, with a first-order linear relation (Beuther et al. 2002). The same study also finds that the physical processes are largely the same as in LMSF. While outflows are commonly seen in LMSF and HMSF, evidence for extremely low mass examples exist, such as toward brown dwarfs (Whelan et al. 2012). However, outflows from HMSF are empirically not as neatly collimated as in LMSF. Identification of outflows is commonly done by observing H_2 and SiO , as well as high-level transitions of CO , although heavier molecules such as HCO^+ and CS help to discriminate regions of HMSF (Gibb et al. 2003; Garay et al. 2007; López-Sepulcre et al. 2009).

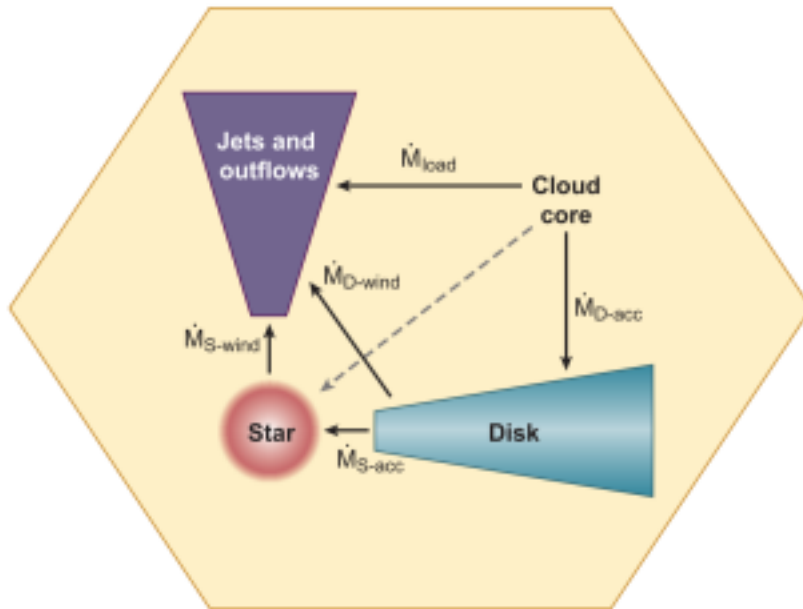


Figure 1.5: Fig. 1 of Zinnecker & Yorke (2007): *Accretion and mass loss as exchange between components: the accretion disk is the reservoir and interface between the molecular cloud core and the forming star.*

1.2.3 H II region

Eventually, a high-mass YSO is hot and luminous enough to ionise the surrounding natal gas. As well as converting molecular hydrogen to H II , the ultraviolet radiation effectively destroys many of the complex molecules in the vicinity, such as CH_3OH , by disassociation. The brightest of these can appear spectacular and even to the naked eye; see Fig. 1.6. Young H II regions are of particular interest to star formation astronomers, as they still signpost a late stage of HMSF. They can be detected in a few ways, but primarily through radio continuum observations as well as the presence of radio recombination lines. UCH II regions are best detected at frequencies ≥ 5 GHz, where free-free continuum emission is optically thin (Purcell et al. 2013). Even higher frequencies are required to observe hyper-compact H II



Figure 1.6: NGC 604 as viewed from the Hubble space telescope. Contained in the nearby galaxy M33, it is a giant H II complex, containing several OB and WR stars (Eldridge & Relaño 2011).

(HCH II) regions.

H II regions evolve over time, and can be roughly classified by their size. Empirically, UCH II regions have sizes ≤ 0.1 pc and densities $\geq 10^4$ cm^{-3} (Hoare et al. 2007). Around the mid-2000s, properties of HCH II regions were beginning to become clear; with sizes ≤ 0.01 pc and densities $\geq 10^6$ cm^{-3} , these are clearly much more extreme than their UCH II relatives (Beuther et al. 2007). The Coordinated Radio and Infrared Survey for High-Mass Star Formation (CORNISH) complements the plethora of Galactic plane surveys with arcsecond resolution at 5 GHz, in a direct effort to detect H II regions, especially UCH II regions (Hoare et al. 2012). However, CORNISH is insensitive to HCH II regions, due to their tiny spatial sizes and optical thickness at 5 GHz (Purcell et al. 2013).

HCH II regions are younger, more extreme objects that will evolve into UCH II regions. One useful probe for identifying these are radio recombination lines, as these have been demonstrated to have linewidths in excess of 40 km s^{-1} ; UCH II regions typically have linewidths upto 30 km s^{-1} (Lizano 2008). Another useful tool for identification could be bright H_2O masers, which are powered in strongly shocked regions.

1.2.4 Summary

The different stages of HMSF have quite different properties. To understand the whole picture, it is important to discriminate and identify each evolutionary stage. The following section describes commonly used probes and techniques to do so.

1.3 Astrophysical diagnostics

1.3.1 Spectral lines

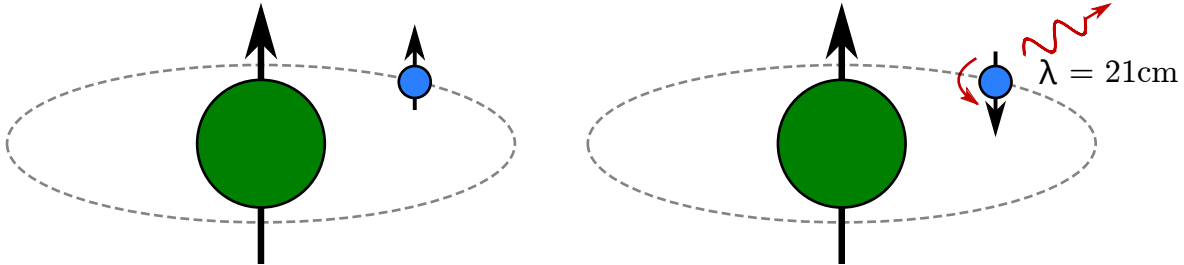


Figure 1.7: A schematic of the hyperfine HI transition. The arrow of the proton (green) and electron (blue) indicates the direction of quantum mechanical spin. If the spins are aligned, the energy configuration of the system is slightly higher than a mis-aligned pair; when the transition to this lower state occurs, a weak photon is produced at 21 cm.

Hydrogen is the most abundant element in the universe, mostly existing in the atomic form, designated HI. The ‘HI line’ serves as a useful introduction to spectral lines, and is perhaps the most important astronomical spectral line; in practice, HI emission is easily detected, because it is ubiquitous in our Galaxy as well as others. HI is primarily useful for galactic structure and ISM studies. HI is produced by the quantum mechanical interaction between proton and electron, and because energy shift is so small in magnitude, is termed hyperfine; see Fig. 1.7 for a schematic. Such low-energy photons lie within the radio regime ($\lambda \approx 21$ cm, $f \approx 1420$ MHz). Additionally, this transition is highly forbidden, given the Einstein A coefficient:

$$A_{10} \simeq 2.85 \times 10^{-15} \text{ s}^{-1}$$

and the half-life time:

$$\begin{aligned} \tau_{\frac{1}{2}} &= A_{10}^{-1} \\ &\simeq 11 \text{ million years} \end{aligned}$$

These types of emission are termed *spontaneous emission*, and are characterised by their Einstein A coefficients. Despite the large half-life time of HI, this hyperfine line is easily detected due to the extremely high abundance of hydrogen. Indeed, it is readily detectable in other galaxies at high redshifts, and instruments are currently searching for this spectral signature during the epoch of reionization.

To study star formation, it is important to identify dense regions of gas in space. Similar to HI, all atoms and molecules exhibit spectral lines by quantum mechanical transitions. These transitions have various methods of being triggered, such as total angular momentum loss, or inversion (tunnelling), but the technical components are largely unimportant in this thesis. What matters are the conditions to cause the emission (or absorption); for example, the ground-state transition of carbon monoxide (CO $J = 1 \rightarrow 0$, shorthand (1–0)) is easily excited by low temperatures:

$$\begin{aligned}
\Delta E (J = 1 \rightarrow 0) &\equiv E(J = 1) - E(J = 0) = \frac{h^2}{4\pi^2 \mathcal{I}_{\text{CO}}} \\
&\simeq 7.6 \times 10^{-23} \text{ J} \\
&\simeq k [5.5 \text{ K}] \\
&\simeq h [115 \text{ GHz}] \\
&\simeq hc [2.6 \text{ mm}]^{-1}
\end{aligned} \tag{1.1}$$

where $\mathcal{I}_{\text{CO}} \simeq 1.5 \times 10^{-46} \text{ kg m}^2$ (Ward-Thompson & Whitworth 2011). This means that, with sufficient amounts of CO present, this transition is excited in cold regions of the ISM. Higher transitions refer to further excited states, such as (2–1), and can discriminate hotter, denser regions; however, practical limitations exist, such as the resilience of a molecule in hot or photon-dominated regions. CO, as well as other diatomic star-forming molecules (H_2 , OH, CS), have such spectral lines due to the permanent electric dipole moment between both atoms. Unfortunately, despite being the most abundant molecule in the universe, H_2 is almost invisible to observers due to its small dipole moment. H_2 has a few ground-state transitions, but most require temperatures exceeding 100 K, which likely destroys H_2 before the line can be exhibited (Bolatto et al. 2013). As star formation occurs in dense gas, we must infer the presence of dense gas through other means.

As seen above, the ground-state transition of CO emits at radio frequencies. This is fortunate, given that longer wavelengths suffer less extinction in dense regions of space, allowing detection of these molecules within MCs. To relate various molecules back to H_2 , and thus total mass, astrophysicists use conversion factors to estimate the amount of H_2 . However, these \mathcal{X} -factors are difficult to determine and vary depending on optical depth or abundance. A similar, but perhaps more convenient metric is critical density:

$$n_c(jk) = \frac{A_{jk}}{\gamma_{jk}} \tag{1.2}$$

where A_{jk} is the Einstein A coefficient and γ_{jk} is the collisional de-excitation rate per molecule in level j . Evans (1999) lists common star-forming spectral lines along with critical densities at 10 and 100 K; for example, the detection of CS (1–0) implies a gas density of at least $4.6 \times 10^4 \text{ H}_2$ molecules per cm^{-3} at 10 K. Critical density is useful as a qualitative estimate of density, but better analysis is necessary for true density determination.

Molecules, despite their rarity compared to H_2 , can become so abundant in regions of HMSF that the emission saturates, which is referred to as optically thick emission. CO is quite illustrative of this, as it is so easily excited and abundant. Optically thick emission is usually identified by a ‘flat-top’ in the spectrum; see Fig. 1.8. Heavier molecules and rarer isotopes are useful for circumventing optically thick emission, to better diagnose properties such as mass, column density and temperature. Other molecules can highlight specific mechanisms within star-forming regions, which is useful for determining evolutionary sequences. Common star-forming molecules and their diagnostics, especially applicable to this thesis, are discussed in §1.4.

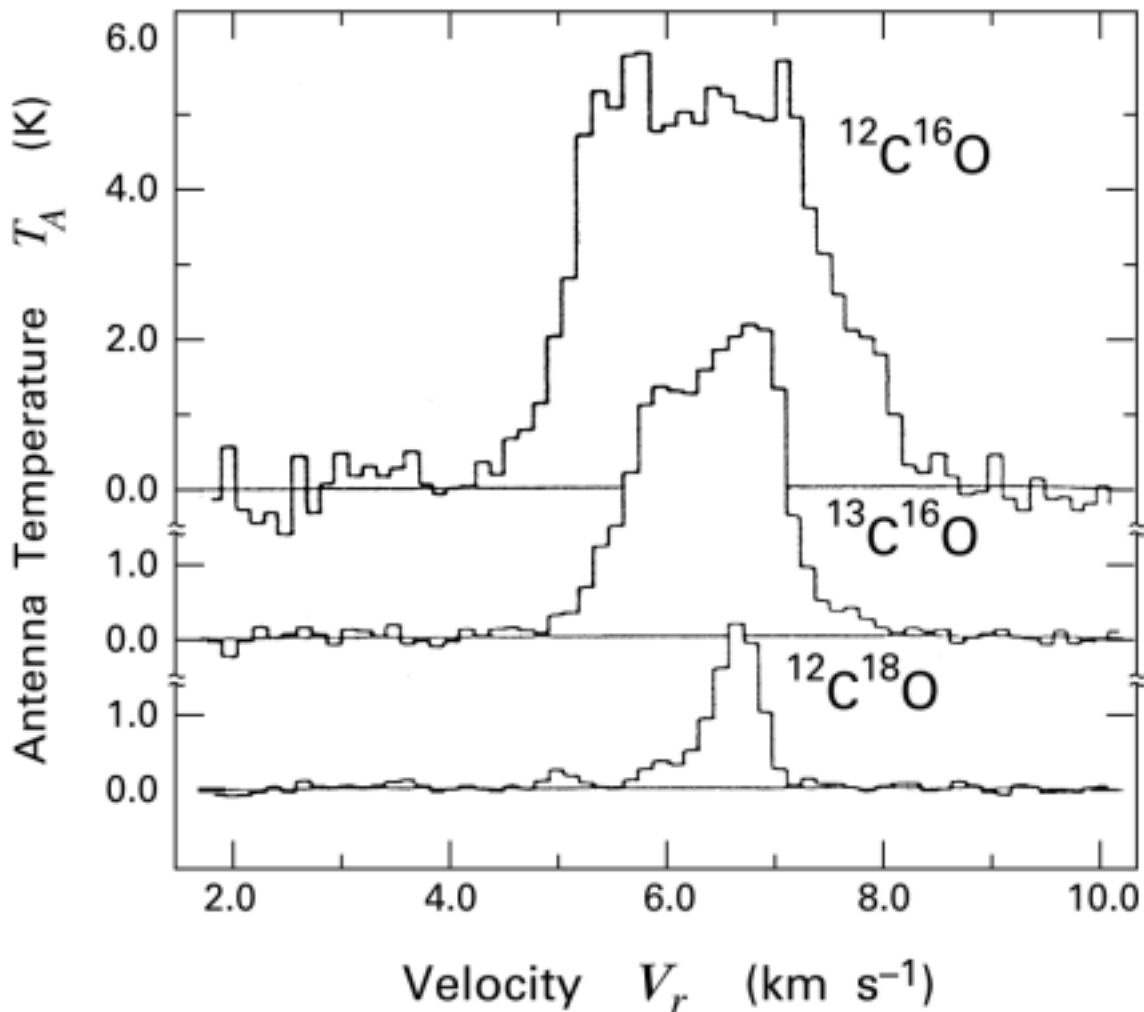


Figure 1.8: Rare molecules and isotopologues help to isolate the most dense regions of gas, Fig. 6.1 of Stahler & Palla (2005): *Intensity profiles of the $J = 1 \rightarrow 0$ line in three CO isotopologues, observed toward Taurus-Auriga.*

1.3.2 Continuum

Brightness temperature acts as a classic probe of continuum radiation; given an observed intensity I_ν at frequency ν , the temperature of a blackbody may be inferred. In the same way, continuum measurements can be used to determine the age of a star-forming region, based on its spectral energy distribution, which are not purely blackbody spectra. Protoclusters have strong sub-millimetre continuum emission, while older regions have brighter mid-infrared emission.

This thesis is primarily concerned with spectral line emission rather than continuum properties. However, there are a few continuum properties of particular interest. The GLIMPSE survey maps the Galactic plane in 3.6, 4.5, 5.4 and 8.0 μm continuum bands, which reveal intriguing properties. The 8.0 μm band primarily traces the 7.7 μm feature of polycyclic aromatic hydrocarbon (PAH) molecules, which have some similarity with dust grains contained in star-forming regions. An extensive review of PAH molecules is given in Tielens (2008). The 4.5 μm is usually attributed to strongly shocked gas, such as H_2 and CO in outflows (Cyganowski et al. 2008); however, this may not be true in all regions (De Buizer & Vacca

2010). Star-formation study often combines these *Spitzer* bands into three-colour images composed of $rgb \rightarrow 8.0, 4.5$ and $3.6 \mu\text{m}$. Most notably, an excess of $4.5 \mu\text{m}$ emission relative to the others manifests as bright green objects, which have successfully identified HMSF; see Fig. 1.9. Infrared imagery from GLIMPSE is often used to compare against the results presented in this thesis.

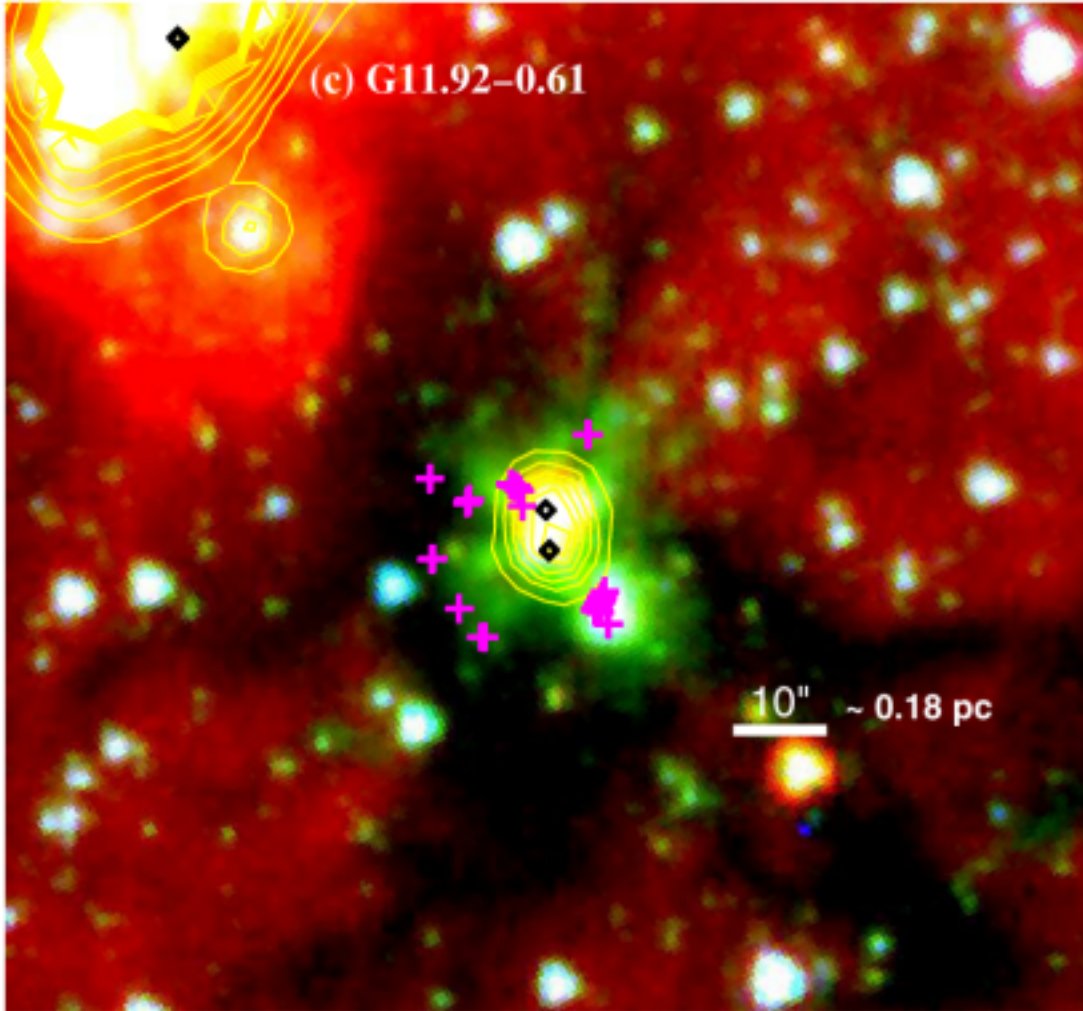


Figure 1.9: Sample of Fig. 1 of Cyganowski et al. (2009). The image is constructed from three infrared GLIMPSE bands, $rgb \rightarrow 8.0, 4.5$ and $3.6 \mu\text{m}$. The study of Extended Green Objects, highlighting an excess of $4.5 \mu\text{m}$ emission, have been successful in identifying HMSF through maser emission. 6.7 GHz class II CH_3OH masers are marked with diamonds, and 44 GHz class I CH_3OH masers are marked with magenta crosses. Yellow contours show $24 \mu\text{m}$ MIPS GAL emission.

Millimetre and sub-millimetre continuum has also received a lot of attention in recent years. Sub-millimetre continuum highlights thermal dust emission from a wide range of temperatures, including very cold dust. Additionally, this kind of emission is optically thin, which helps to calculate column densities, and is associated with all stages of HMSF. To this end, the APEX Telescope Large Area Survey of the GALaxy (ATLASGAL) maps a large area of the Galactic plane in $870 \mu\text{m}$ emission (Contreras et al. 2013). Similarly, the Bolocam Galactic Plane Survey (BGPS) maps a large fraction of the Galactic plane at 1.1 mm (Aguirre et al. 2011). Finally, the Herschel space observatory provides the means to image other

wavebands, such as $70\ \mu\text{m}$. Results from this next-generation instrument are still forthcoming, but recent observations used Herschel $70\ \mu\text{m}$ emission to map high-mass YSOs (Olguin et al. 2015).

1.4 Star-forming tracers

In this section, spectral lines and their relation to HMSF are discussed. Spectral lines are powerful tools for diagnosing the ISM, due to the relative ease of detection, and the information gleaned by their presence. One advantage over continuum observations is the observed Doppler shift, which reveals kinematics and perhaps structure of the gas.

1.4.1 Hydrogen

Despite being the most abundant molecule in MCs, H_2 is mostly undetectable due to its lack of dipole moment. However, interstellar H_2 has been detected, and is useful for star-formation study. It was first detected through Lyman-alpha ($\text{Ly}\alpha$) absorption toward the star ξ Persei, and acted as a probe for optical depth (Carruthers 1970). Much more recently, H_2 has been useful in tracing very hot, shocked gas, including SNRs, expanding H II regions and outflows (Habart et al. 2005). Especially interesting is the $4.5\ \mu\text{m}$ infrared band, which can highlight shocked H_2 and CO has revealed evolved regions of HMSF (Cyganowski et al. 2008, 2009); see Fig. 1.9.

As discussed, the final evolutionary state of HMSF is a H II region. These arise when a YSO is hot enough to produce ultraviolet radiation, which requires a high-mass YSO. As the H II region expands by radiative and outflow processes, the neutral H I is constantly being ionised and pairing with electrons. This procedure produces recombination lines, often referred to as radio recombination lines (RRLs), as they are brightest around 8 GHz. The detection of RRLs is a bona-fide method of inferring the presence of a H II region; because HMSF occurs in high-density gas, likely associated with Galactic spiral arms, surveys for RRLs have been productive in identifying structure (Bania et al. 2010, Brown et al. *in prep.*).

1.4.2 Carbon monoxide (CO)

As discussed in §1.3.1, CO is an easily excited molecule in cold, dense regions of the ISM. It is so abundant, that it becomes optically thick with density, owing to its low critical density ($\sim 10^2\ \text{cm}^{-3}$). Therefore, CO is important for both star formation and Galactic structure studies, as it easily highlights MCs. The CO survey of Dame et al. (2001) is one of the largest-scale surveys to date, and reveals spiral-arm structure of our Galaxy. Such an investment was huge, due to the beam size of a radio-telescope at relevant frequencies, but helps to understand the global properties of MCs both in our Galaxy and others.

The CO molecule depletes within star-forming core collapse. However, because the surrounding exterior of the core suffers no depletion of CO, the core is not obvious. To become more sensitive to the interior of MCs and avoid the optical thickness of the $^{12}\text{C}^{16}\text{O}$ isotopologue, observations seek less abundant species such as ^{13}CO and C^{18}O . Indeed, the

characterising fractionation of isotopologues is also useful for other molecules to determine the properties of gas. Fractionation is particularly important, given that observations of other J -transitions may not be possible on the same instrument, owing to the large differences in rest frequency. For example, CO (1–0) has a rest frequency of 115 GHz, while (2–1) is at 231 GHz. An instrument such as Mopra cannot observe the (2–1) line, but has many significant CO results published from the (1–0) transition (Braiding et al. 2015; Barnes et al. 2015).

1.4.3 Ammonia (NH₃)

The first polyatomic molecule detected in interstellar space, NH₃ provides incredibly important information for HMSF. Discovered by Cheung et al. (1968) toward Sgr A, the authors were able to calculate the kinetic temperature of optical depth of the gas.

The (1,1) inversion line of NH₃ is easily detected in star-forming regions, and has a critical density of $\sim 10^3 \text{ cm}^{-3}$ (Evans 1999), which is useful for probing dense gas. This formed part of the motivation of the H₂O Galactic Plane Survey (HOPS; Walsh et al. 2011), which used the Mopra radio-telescope* to search for many star-forming spectral lines, including NH₃ (1,1), (2,2) and (3,3). Higher inversion transitions are more forbidden than the (1,1) line, which indicate additional properties of the host region. Such NH₃ observations from HOPS helped isolate one of the most extreme examples of a proto-cluster, G0.253+0.016, with a high mass ($\sim 10^5 M_{\odot}$) and low temperature ($\sim 20 \text{ K}$) (Longmore et al. 2012). The new and upcoming instrument ALMA† has revealed unprecedented detail of this molecular cloud, which is thought to be on the verge of star formation (Rathborne et al. 2015).

While the critical density of NH₃ is clearly useful, other gaseous properties may be obtained from the same data. The optical depth of NH₃ can be calculated using relation of intensities between hyperfine transitions (Ho & Townes 1983). For the (J, K) inversion line:

$$\frac{\Delta T_a^*(J, K, m)}{\Delta T_a^*(J, K, s)} = \frac{1 - e^{-\tau(J, K, m)}}{1 - e^{-a\tau(J, K, m)}} \quad (1.3)$$

where ΔT_a^* is the observed brightness temperature, m and s refer to the main and satellite hyperfine components, $\tau(J, K, m)$ is the optical depth of the main component, and a is the ratio of the intensity for the satellite compared with the main component. This equation assumes equal beam-filling factors and excitation temperatures for the different hyperfine components, but this is not problematic due to the small frequency differences between hyperfine components and the likelihood of excitation mechanisms being different. Additionally, the temperature of gas may be estimated via:

$$T_{rot} = -41 \text{ K} / \ln \left(\frac{9}{20} \frac{\tau_{2,2}}{\tau_{1,1}} \right) \quad (1.4)$$

where T_{rot} is the rotational temperature (Purcell 2006), which provides a good indicator of the kinetic temperature (Ho & Townes 1983). Note that this equation assumes $\Delta\nu_{2,2}/\Delta\nu_{1,1} \approx 1$. Finally, the column density may be estimated via:

* A 22 m antenna near Coonabarabran, New South Wales, Australia.

† The Atacama Large Millimeter/submillimeter Array, a 66-element interferometer located on the Chajnantor plateau, Chile.

$$N \approx N_{(1,1)} \left[\frac{1}{3} e^{23.26/T_{rot}} + 1 + \frac{5}{3} e^{41.18/T_{rot}} + \frac{14}{3} e^{-100.25/T_{rot}} + \frac{9}{3} e^{-177.21/T_{rot}} + \frac{11}{3} e^{-272.02/T_{rot}} + \frac{26}{3} e^{-284.67/T_{rot}} + \dots \right] \quad (1.5)$$

where N is the total column density, and $N_{(1,1)}$ is the column density of the NH_3 (1,1) line (Purcell 2006). With yet more diagnostics revealed by this molecule, it is not difficult to imagine why astrophysicists refer to NH_3 as the ‘molecular thermometer’.

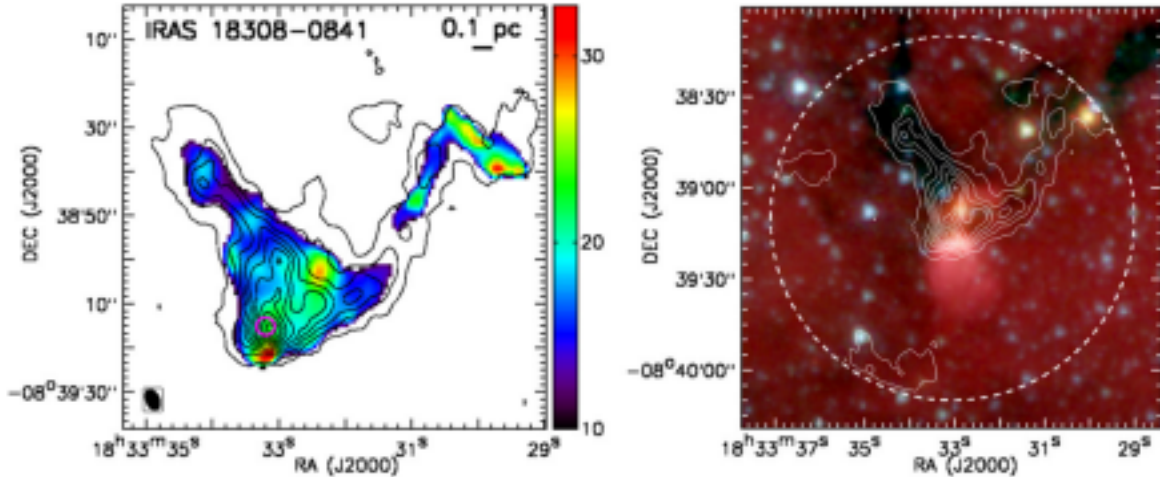


Figure 1.10: A sample figure from Lu et al. (2014): *Rotational temperature and IRAC three-colour images of IRAS 18308–0841*. Left: Rotational temperatures are presented in colour scales. The black contours are the integrated intensities of NH_3 (1,1) main hyperfine line, from 5 to 95 per cent of the peak intensity in steps of 10 per cent. Maser detections with interferometers are marked with either circles (water maser), crosses (class II methanol maser), or triangles (hydroxyl maser). The synthesized beam of the integrated intensities is shown in the lower-left corner, while the beam of the rotational temperatures should be slightly larger given that the temperatures are derived from the smoothed data. Right: The Spitzer IRAC composite image, with $8\ \mu\text{m}$ (red), $4.5\ \mu\text{m}$ (green) and $3.6\ \mu\text{m}$ (blue) emission. The NH_3 (1,1) integrated intensity contours are identical to those in the left panels. The dashed circle shows the $2''$ FWHM primary beam of the VLA.

Astrophysicists typically use the ‘thermometer’ properties of NH_3 by observing it towards hot molecular cores. A recent interferometric survey of bright ($L_{bol} > 10^3 L_{\odot}$) high-mass star-forming regions exploits the properties of NH_3 , and generally reveals a kinematic flow toward the focus of star formation; see Fig. 1.10 (Lu et al. 2014). Another survey toward the Galactic centre finds that dust is necessary to form detectable NH_3 , among other results (Ott et al. 2014).

1.4.4 Carbon monosulfide (CS)

As discussed earlier, CS traces dense gas, with a critical density $n_c = 4.6 \times 10^4\ \text{cm}^{-3}$ at 10 K (Evans 1999). Overall, CS is not as useful for diagnostics as NH_3 , but does allow for optical depth probing when combined with rarer isotopes (e.g. C^{34}S). One such equation is:

$$\frac{T(\text{C}^{34}\text{S})}{T(\text{CS})} = \frac{1 - e^{-\tau}}{1 - e^{-a\tau}} \quad (1.6)$$

where $T(x)$ is the brightness temperature of x , τ is the C^{34}S optical depth and a is the abundance ratio of $^{32}\text{S}/^{34}\text{S}$ (Bergin et al. 2001). The relative abundance of CS to C^{34}S is somewhat uncertain; Chin et al. (1996) quote the solar system value of 22.5 ± 5.5 as well as 24.4 ± 5.0 from their own observations, but Pratap et al. (1997) claims a ratio between 12 and 14 provided better statistical fits for their work. Care must be taken when assuming relative abundance values.

Wu et al. (2010) performed CS observations towards dense clumps associated with H_2O masers. The authors note that most clumps are associated with compact or UC H II regions, highlighting relatively evolved star formation. Given the late evolutionary status of these objects, and the presence of H_2O masers, outflow activity is expected (see §1.5.4). Unsurprisingly, observations find that the (2–1) transition of CS traces a larger area than (7–6); however, the linewidths of (7–6) is greater than that of (2–1). As (7–6) is closely associated with the most compact gas, the increased linewidth compared to (2–1) is attributed to outflow activity (and/or expanding H II regions). Subsequent modelling of hot cores shows CS to be one of the best tracers of very dense gas (Bayet et al. 2011).

Especially interesting are differences between the distribution of CS and NH_3 . Despite having a higher critical density than NH_3 , CS has been observed to be more extended in emission; specifically, observations performed by Lopez et al. (1994) identify extended CS emission over star-forming regions where NH_3 emission is typically confined to an outflow. Taylor et al. (1998) attempt to resolve this phenomenon with a model, classifying CS (and other carbon-bearing species) as ‘early-type’ molecules and NH_3 (and other nitrogen-bearing species) as ‘late-type’. Observations by Tafalla et al. (2004) strengthen this argument; N_2H^+ , another molecule resilient against depletion similar to NH_3 , was observed at constant abundance in each targeted core, while CS and CO depleted as a function of density. Tafalla et al. (2004) also observed an increased abundance of NH_3 in the centre of these cores, and conclude them to be starless. The Taylor et al. (1998) categories of early- and late-type star formation appear to be separated by molecular cloud fragmentation, before core collapse occurs. Additionally, Lee et al. (2013) targeted starless cores in Orion, and did not detect N_2D^+ (2–1) alongside detections of CS (2–1) and (3–2); they assume that the target cores are chemically young.

Given that high transitions of CS have large linewidths compared to lower transitions within hot cores, CS molecules are apparently sublimating from dust grains. Therefore, regions of star formation with an over-abundance of nitrogen-bearing molecules compared to carbon-bearing species (Taylor et al. (1998) ‘late-type’) should only be considered until the hot core phase, upon when carbon-bearing species are comparably abundant. Such considerations allow some probing of evolutionary stage merely through detection of each type of molecule, e.g. CS and NH_3 .

1.4.5 Silicon monoxide (SiO)

Thermal emission from SiO is well understood to trace shocked regions, especially outflows (Martin-Pintado et al. 1992; Leurini et al. 2014). It is greatly enhanced in hot core chemistry, signposting a specific evolutionary stage. Dust grains within dense cores, being primarily composed of silicates, are destroyed by collisions and liberate Si into the gas phase. SiO can

then be produced by oxidation (Schilke et al. 1997):



Traditional views on SiO a strongly-shocked gas tracer have remained in place for years. Interestingly, a recent investigation discusses the possibility of SiO emission being triggered by weaker shocks (Nguyen-Lu'o'ng et al. 2013). As the SiO (2–1) emission has the same velocity as N_2H^+ and CO, as well as the lack of an outflow profile, the authors speculate that the SiO emission is driven by low-velocity shocks.

SiO masers can also be found in the ISM, but these usually trace very different conditions to the thermal emission discussed above, and are usually found toward evolved stars with vibrational mode $v = 1, 2, 3$. However, Orion-KL provides one of the very few star-forming SiO masers, even in the $v = 0$ mode (Cho et al. 2005). Further discussion of SiO masers is contained in §1.5.6.

1.5 Star-forming masers

Masers were first described in 1952 and created in the laboratory in 1953. However, the astrophysical community appeared to have no notion to believe that masers could (or would) naturally exist outside of laboratories. This is evident after their discovery and subsequent disbelief of the strong spectral lines observed. Powered by a chain-reaction to amplify emission, these spectral lines can be detected across vast distances, from the other side of our Galaxy, to mega-masers in other galaxies. This makes masers invaluable tools for observations, particularly surveys, given their great intensities.

Weaver et al. (1965) are credited with the discovery of the first interstellar masers. This publication reported unusual results from a search for hydroxyl (OH) within the Galaxy. The authors discuss the presence of ‘strong, unidentified emission lines’ towards the Orion nebula and radio continuum sources W3, W49, W51 and W75. Dubbed ‘Mysterium’, the authors note that it is found towards some strong H II regions, but not all. Very quickly, further observations were done towards Mysterium. A problem existed in the temperature; linewidths implied a temperature of 10^2 K, but the brightness temperature was at least 10^3 K. Eventually, Mysterium was confirmed as masing OH in the ISM.

Masers are commonly seen in regions of star formation, due to the special conditions and high energies required. In this review, an overview of maser theory is given, as well as a discussion on typical HMSF masers and their currently understood characteristics.

1.5.1 Theory

Most of the thermal line emission discussed in §1.4 is generated through spontaneous emission. The mechanism governing maser emission is *stimulated emission*. A simple scenario for stimulated emission is as follows:

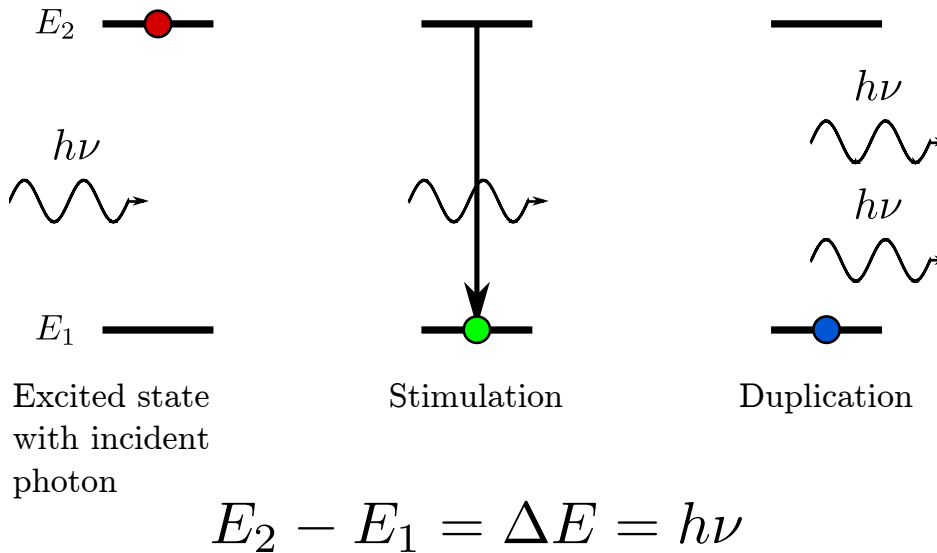


Figure 1.11: A typical schematic of stimulated emission. An inverted population exists with energy E_2 (panel 1), is stimulated by a photon of characteristic energy $E_2 - E_1 = h\nu$ (panel 2), leaving an identical photon and a depressed state (panel 3).

- i) The species in question (atom or molecule) has two energy states, E_1 and E_2 , with the majority being in the elevated state. This is referred to as an inverted population;
- ii) A photon with an energy of (or close to) $E_2 - E_1 = h\nu$ interacts with a member of the elevated species. This photon induces stimulated emission;
- iii) The species decays to the lower energy state E_1 , releasing another photon of energy $h\nu$.

This procedure is described in Fig. 1.11. The regions providing the population inversion are just right for maser conditions, and are of special interest to astronomers. One can think of the ‘stimulation’ step as negative absorption; rather than absorbing the incident photon, another is emitted. The optical depth τ normally measures attenuation by photon absorption, but when the stimulation is combined with the population inversion, an exponential increase in emission is observed along the path of inverted species. This explains the extreme brightness temperatures that are calculated by observing masers. Masers are well characterised by their compact, unresolved spatial structure as well as very small linewidths.

1.5.2 Class II methanol (CH_3OH)

Interstellar CH_3OH masers were discovered by Barrett et al. (1971) towards Orion-KL in 25 GHz lines ($J = \{4,5,6,7,8\}$, $\Delta J = 0$, $K = 2 \rightarrow 1$). Quickly, many more CH_3OH maser lines were discovered, but the next important discovery was by Wilson et al. (1984), who detected CH_3OH masers in the 9_2-10_1 A^+ transition. Their results note unusual absorption of CH_3OH toward W31, but are otherwise unaware of the importance of this transition; being the first to find CH_3OH emission beyond Orion-KL, these observations demonstrated how bright CH_3OH masers could be (9.5 Jy). The publication by Batrla et al. (1987) made an important distinction by classifying CH_3OH masers into two groups: class I and class II. Most observations at that point had unwittingly focused on class I, which is collisionally excited, but could occur at large offsets from H_2O and OH masers. Quickly, more observations were

conducted toward the 2_0-3_{-1} E line, revealing a tight correlation with H II regions and OH masers (Norris et al. 1987). At this point, depending on the class, it was evident that class I and class II CH₃OH masers traced very different things.

The discovery of the 6.7 GHz 5_1-6_0 A⁺ line has proven to be one of the most important for star formation tracers (Menten 1991). Since its discovery, this line (as well as all class II CH₃OH species) have been determined to occur exclusively towards regions of HMSF (Breen et al. 2013). This was established by the absence of CH₃OH masers toward low-mass YSOs (Minier et al. 2003). We now understand class II CH₃OH masers are powered by mid-infrared radiation from YSOs, seemingly only powerful enough in HMSF. A very recent investigation finds that 6.7 GHz CH₃OH masers must appear after outflows are generated (de Villiers et al. 2015).

In the 1990s, UCH II regions were rich objects for star formation study. Naturally, the connection with class II CH₃OH masers was investigated, which revealed a surprisingly small overlap of ~ 20 per cent (Walsh et al. 1998). An explanation is obtained through the diagnosis of evolutionary phase; the age of YSOs and brightness of associated class II CH₃OH masers is thought to be correlated (Breen et al. 2011; Bartkiewicz et al. 2014; de Villiers et al. 2015). Notably, the presence of the 37.7 GHz $7_{-2}-8_{-1}$ E class II CH₃OH maser line was found toward brighter 6.7 GHz lines; if brighter 6.7 GHz masers occur in older regions, the presence of 37.7 GHz masers is thought to indicate the ‘apocalypse’ of all class II CH₃OH maser activity (Ellingsen et al. 2011). Clearly, constraints exist for when class II CH₃OH maser emission could occur, but when do class II CH₃OH masers turn on?

It is currently well understood that class II CH₃OH masers occur very near to a YSO. The morphology of these masers appears to be contentious in literature; profoundly, there are many examples of rings surrounding YSOs (see Fig. 1.12). Very-long-baseline interferometry (VLBI) observations of such rings reveals radii of order a few hundred to ~ 1000 AU (Bartkiewicz et al. 2009). Bartkiewicz et al. (2009) also suggest that these maser morphologies occur at the interface of the ring and outflow, highlighting a relatively evolved class II CH₃OH stage of HMSF. However, not all class II CH₃OH morphologies are rings; further observations by Bartkiewicz et al. (2014) observe linear, ring-like and ‘complex’ morphologies within their sample. Linear morphologies were speculated as edge-on ring features, although this idea has been largely rejected. Through infrared emission analysis, an investigation of ring morphologies argues that the masers do not behave as if they lie within a circumstellar disk (De Buizer et al. 2012). This is consistent with investigations of outflow tracers H₂ and SiO not being perpendicular to class II CH₃OH masers (De Buizer 2003; De Buizer et al. 2009).

1.5.3 Hydroxyl (OH)

The commonly detected hydroxyl spectral lines are at 18 cm (1612, 1665, 1667 and 1720 MHz) and can be seen in Fig. 1.13. The presence of this molecule in the ISM was confirmed by Weinreb et al. (1963); detected in absorption, the 1665 and 1667 MHz lines were found toward the SNR Cassiopeia A. Since the discovery, OH has also been seen in emission and absorption for all 18 cm lines, and can have been characterised in relative intensity as 1:5:9:1, in order of increasing frequency (Townes & Schawlow 1955). By observing the relative strengths of

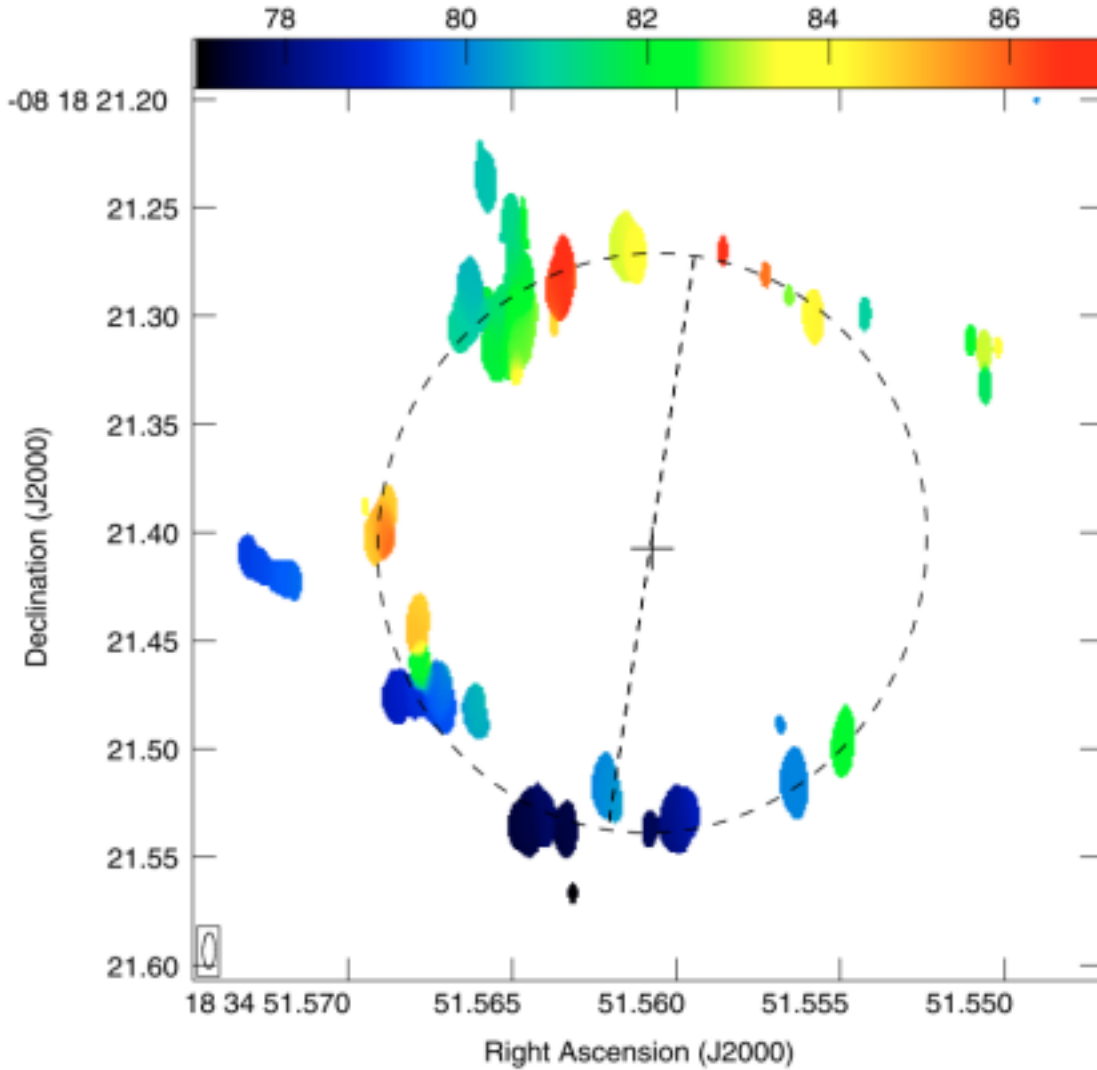


Figure 1.12: Class II CH_3OH masers in a ring morphology, Fig. 1 from Bartkiewicz et al. (2005): *Velocity field of maser components (first moment map). The colour scale varies linearly from 77.0 to 87.0 km s^{-1} . The beam is indicated by the ellipse in the bottom left-hand corner of the image. The cross indicates the inferred position of a central object.*

each hyperfine line, one can determine optical depth and excitation temperatures of the gas (Guibert et al. 1978). Similar to CO, OH traces low-density gas, but is susceptible to Zeeman splitting, allowing diagnosis of local magnetic fields. Clearly, OH is a versatile molecule, not just for probing star-forming regions.

OH masers are of particular interest to the research within this thesis. Surveys in the 1990s for OH masers revealed that, in almost all cases, their positions coincided with class II CH_3OH masers within errors, clearly signposting star formation (Caswell 1997). At the same time, Caswell (1997) noted the preference for OH masers to be associated with UCH II regions, especially compared to class II CH_3OH masers. This study was one of the first to isolate HMSF sequencing through only maser emission, which began a new avenue to pursue the ‘Holy grail’ - can we identify and diagnose a HMSF timeline purely through maser emission? The motivation of this thesis is influenced by this thought, and overall maser association is discussed further in §1.5.7.

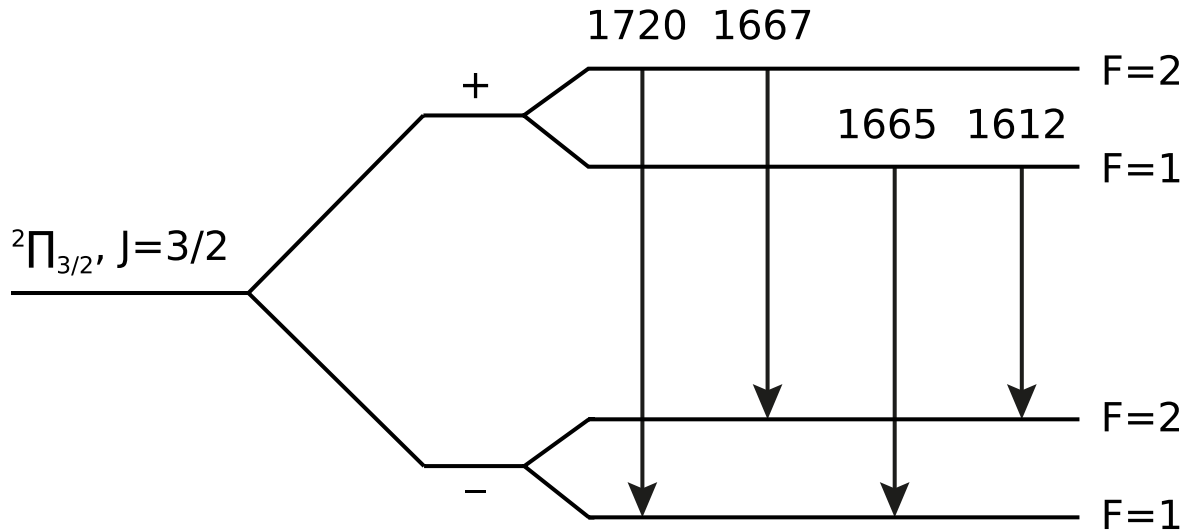


Figure 1.13: Fig. 1 from Dawson et al. (2014): *Energy level diagram of the ground-state hyperfine structure transitions of OH. Here F is the total angular momentum quantum number, including the nuclear spin. Frequencies are in MHz.*

The 18 cm OH maser lines can be produced through non-star-forming mechanisms. In particular, 1612 MHz masers primarily occur from so-called OH/IR stars, shedding mass during their transition along the asymptotic giant branch Sevenster et al. (1997). The outflowing mass powers the maser via radiation, which in turn is powered by the stellar radiation. This proved useful for a large survey of 1612 MHz masers, conducted by (Sevenster et al. 1997) to investigate Galactic kinematics and the evolution of stellar populations. Other maser lines, such as 1665 and 1667 MHz, have been used to diagnose polarisation (Gonidakis et al. 2014) toward AGB and post-AGB stars. The rare 1720 MHz maser, unlike the others, is collisionally excited; although it commonly occurs toward star-forming regions, it has been detected towards SNRs (Green et al. 1997) and planetary nebulae (Gómez 2007, Qiao et al. *in preparation*). More recently, 1720 MHz OH masers are claimed as signposts of SNR and molecular cloud interactions (Brogan et al. 2013). Results of the Southern Parkes Large Area Survey in Hydroxyl (SPLASH) project, surveying a large portion of the Galactic plane for OH, will reveal more detail in all 18 cm maser lines, using Parkes* as the survey instrument and ATCA† for high-resolution follow-up observations (Dawson et al. 2014).

1.5.4 Water (H₂O)

Frozen H₂O forms a major component of dust grains within star-forming regions (di Francesco et al. 2007). Once sublimated, thermal emission from this line can be observed, although almost all interest of interstellar H₂O lies with its maser activity. H₂O masers are classic tracers of outflows; they are created and pumped by a mass outflow from a central star or YSO with clumps or inhomogeneities in the surrounding cloud (Elitzur 1992). There are endless examples of H₂O masers tracing outflows, in both LMSF and HMSF (Moscadelli et al. 2005, 2006; Goddi & Moscadelli 2006; Felli et al. 1992). Extreme examples exist,

* A 64 m antenna near Parkes, New South Wales, Australia.

† Australia Telescope Compact Array, a six-element interferometer located near Narrabri, New South Wales, Australia.

with velocity spans of nearly 300 km s^{-1} (Titmarsh et al. 2013). Accretion disks were once proposed to explain VLA observations of H_2O masers; however, follow up VLBI observations revealed that water masers close to YSOs are arranged in circular, expanding arcs (Goddi et al. 2005). This suggests that water masers found very near (within hundreds of AU) YSOs are associated with their outward winds, rather than a rotating mechanism.

As for when H_2O masers appear in an evolutionary timeline, a survey towards high-mass YSOs and UCH II regions shows that H_2O masers are equally likely to be detected in either state; the ‘high-mass YSO state’ is taken to mean a class II CH_3OH maser phase, before a UCH II is apparent (Urquhart et al. 2009). Recent evidence affirms the overlap between a class II CH_3OH maser dominated phase and H II region phase (Titmarsh et al. 2014).

Similar to CO and NH_3 , H_2O is formed through gas-phase reactions. Within shocked cloud regions, the major sequence for production is:



This also helps to explain why OH can be detected through collisions. One might expect the occurrence of H_2O masers to overlap with 1720 MHz OH masers. However, at least in the case of SNRs, 1720 MHz OH masers are found without H_2O maser counterparts. This imposes constraints upon the gas densities that allow for both species to pump masers; the authors state that the density of the post-shock region is 10^5 cm^{-3} , and that densities of four orders of magnitude higher are required for H_2O maser detection (Claussen et al. 1999).

1.5.5 Class I methanol (CH_3OH)

Practically, for the period between the discovery of the 6.7 GHz class II CH_3OH maser and a decade ago, class I CH_3OH masers had not been well-studied. There are a few reasons for this, but perhaps primarily for its relative tenuous association with star formation compared to class II masers. Another was that finding new class I masers was difficult; the 44 GHz line is the brightest, and without targeting known regions of star formation, the feasibility of conducting a survey of these masers is too inefficient. Our understanding of these masers is therefore limited to those already found, typically toward other star-forming masers.

Unlike class II masers, class I masers can occur in LMSF, albeit rarely. Kalenskii et al. (2010) targeted LMSF outflows for 44 and 36 GHz class I masers, finding a weak association. Gan et al. (2013) confirms this by observing outflows from both LMSF and HMSF, finding a 9 and 38 per cent association rate, respectively. Clearly, there is a good relation with outflows, but the certainty of finding class I masers is not strong. The EGOs discussed earlier have a stronger connection with class I masers; Cyganowski et al. (2009) and Chen et al. (2011) report a 90 and 55 per cent detection rate toward EGOs, respectively. The large difference between these rates might be explained by the lines targeted; Cyganowski et al. (2009) observed 44 GHz lines, whereas Chen et al. (2011) used 95 GHz lines. Val’ts et al. (2000) find the ratio between peak flux densities, i.e. $P(44 \text{ GHz})/P(95 \text{ GHz})$ is approximately 3. The relatively weak line used by Chen et al. (2011) may help to explain the low detection rate. Gan et al. (2013) also used the 95 GHz line, which may mean their statistics are under-

represented.

The publication by Voronkov et al. (2014) acts as one of the most comprehensive reviews of class I CH₃OH masers. The authors observed 71 known maser sources and find a few important results:

- i) The number of class I maser spots falls exponentially with distance from a class II maser;
- ii) Class I CH₃OH masers are more spread out when associated with an OH maser;
- iii) Class I masers are good tracers of cloud systemic velocities.

Point i) suggests that the shocked gas from a high-mass YSO originates near the class II maser, and class I masers are more likely to be excited at shorter distances. Point ii) agrees, as OH masers turn on after class II CH₃OH masers, suggesting an even more evolved phase; this makes conditions more ideal for a large spatial spread of class I maser emission. Point iii) may suggest that class I masers are powered by weak shocks, as it is not too perturbed from the systemic velocity. Another result by Voronkov et al. (2010a) finds a high-velocity class I maser, potentially contradicting this assertion. However, this high-velocity feature is speculated as being due to an outflow permeating molecular gas, which can still agree with weak shocks as being the powering mechanism.

Through modelling, Cragg et al. (1992) predict the collisionally-excited nature of class I masers. Given their strong association with outflows discussed above, this seems clear. Non-star-forming observations further affirm collisional excitation, by its presence in SNRs (Pihlström et al. 2014), and an extra-galactic merger (Chen et al. 2015). However, very little is known about when class I masers turn on. Without an untargeted survey for these masers, identifying them in their earliest stages will be difficult.

1.5.6 Silicon monoxide (SiO)

Typically, SiO masers are not related to the star-forming thermal line, and are found towards asymptotic giant branch (AGB) and red super-giant (RSG) stars (Elitzur 1992; Gonidakis et al. 2013). As these stars shed large amounts of mass (10^{-7} to $10^{-4} M_{\odot}$), there exists a so-called circumstellar envelope. SiO masers can be powered in the densities and temperatures just beyond these envelopes, within the ‘extended atmosphere’. The morphology of these masers can appear as a shell, presumably centred on a star, and experience in-falling as well outflowing motions (Assaf et al. 2011).

Concerning star formation, the SiO maser appears to be extremely rare. Zapata et al. (2009) conducted sensitive interferometric observations towards 60 high- or intermediate-mass star-forming regions for SiO maser emission. Despite this extensive search, only three regions, all previously known, had detectable SiO masers (Orion-KL, W51 North and Sgr B2). Observations of Orion-KL are particularly exciting, revealing a bi-polar wind, likely driven by an accretion disk (Goddi et al. 2009). The SiO results are augmented with observations of high-frequency H₂O masers, which appear to trace a disk (Hirota et al. 2014); see Fig. 1.14. Hence, the value of detecting star-forming interstellar SiO masers cannot be understated.

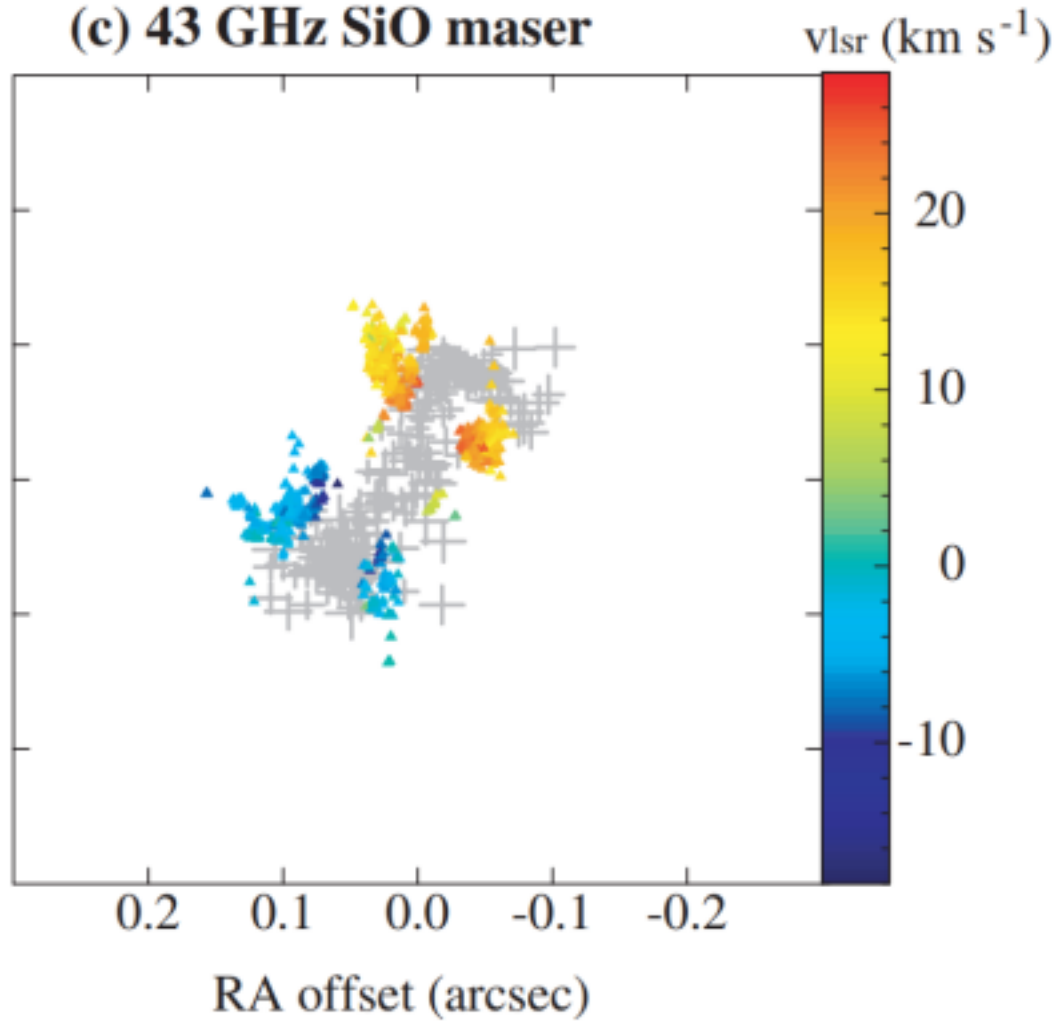


Figure 1.14: Fig. 3c from Hirota et al. (2014), showing maser emission toward Orion-KL. The SiO maser emission from Kim et al. (2008) is given in colour, with 336 GHz H₂O maser emission in grey. These results are some of the best evidence for accretion disk HMSF.

1.5.7 An evolutionary timeline of HMSF with masers

Given the range of evolutionary phases that star-forming masers can trace, research has invested in large-scale surveys to identify HMSF purely through maser emission. Three prominent surveys include HOPS, for H₂O masers; the Methanol MultiBeam (MMB), for class II CH₃OH masers; and SPLASH, for OH masers. The wealth of data available led to comparisons between these three types of maser, and found strong associations (Breen et al. 2010a). Another publication by Breen et al. (2010b) attempts to quantify HMSF through maser emission with a graphical figure; see Fig. 1.15.

Since this timeline has been published, it has been refined; class I CH₃OH masers are not unusual toward OH masers, for example. One useful way to improve this timeline is through a large-scale survey for class I CH₃OH maser emission. Such a survey could determine if these masers occur earlier than other masers in a HMSF timeline, and how they relate to other masers. With this knowledge, detection of class I CH₃OH masers can then reveal basic properties of the host region, without the need for long observations or rigorous analysis.

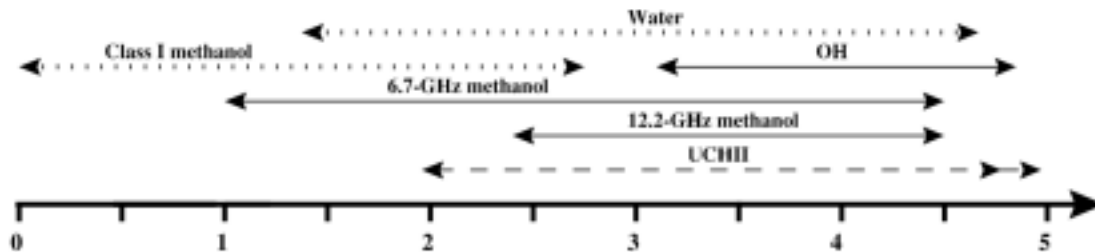


Figure 1.15: Fig. 6 of Breen et al. (2010b): *Evolutionary sequence for masers associated with high-mass star formation. Lifetimes represented by dotted lines indicate that they have been estimated from the literature along with unpublished data. The lifetime of the UCHII region is represented by a dashed line as the onset of radio continuum emission is particularly dependent on the mass of the associated star. The double arrow head on the far end of the UCHII region lifetime is to show that it will persist past the end of the range of the plot.*

1.6 Motivation of this thesis

There are many intermediate stages to HMSF, each with unique ways of being identified. Due to improvements in technology, large-scale astronomical surveys have become much more feasible. The last decade has been extremely productive in mapping evolutionary stages of HMSF, but detail could be improved in some areas.

The HOPS and MMB surveys are prominent examples of star formation surveys with Australian radio telescopes. Another project, MALT90, is similar to HOPS and complements these surveys with observations of 3 mm star-forming tracers. In a similar fashion, MALT-45 aims to map the Galactic plane at ~ 45 GHz (7 mm) in an untargeted way. This waveband contains the CS (1–0) line, which has not been surveyed thoroughly, as well as 44 GHz class I CH₃OH masers, which are biased toward known regions of star formation. The SiO (1–0) family of spectral lines also exist in this waveband, presenting the opportunity to detect shocked gas from the thermal line and exotic locations through masers. As discussed, these spectral lines contain valuable association with HMSF, and can help identify new star-forming locations. For the first time, with a statistically complete sample, such a survey will help to isolate the conditions necessary to produce class I CH₃OH maser emission.

An initial attempt to conduct this survey à la HOPS with Mopra proved inefficient; the primary beam was too small to map a large area in a short time, with appreciable sensitivity. Additionally, this waveband is more susceptible to poor weather than HOPS, making the project quite difficult. Unless MALT-45 could become a targeted survey, like MALT90, another solution was necessary.

1.6.1 Thesis overview

Each antenna (dish) of the ATCA is similar to Mopra; by combining the antennas in auto-correlation, MALT-45 can be feasibly conducted, owing to the improved sensitivity. This thesis has two associated publications which are modified into chapters, described below.

Chapter 2 details the pilot observations conducted for MALT-45, to determine the feasibility of the survey. The auto-correlation pipeline is also detailed, as non-standard techniques are required. The data is of poor quality, because:

i) Inclement weather was present over a large portion of the observations; ii) The desired correlator configuration was unavailable, as well as a lack of on-the-fly mapping; iii) The survey technique and pipeline was unrefined.

Despite the poor conditions of the pilot survey, emission in CS is detected, as well as class I CH₃OH and SiO masers, vindicating the auto-correlation data reduction. The CS emission matches HOPS NH₃ over the region, although with poorer sensitivity, and highlights an IRDC. Seven class I CH₃OH masers were identified along with three SiO $v = 1$ masers toward evolved stars. Refinement of the survey technique is suggested.

Chapter 3 details the MALT-45 survey conducted within $330^\circ \leq l \leq 335^\circ$, $b = \pm 0.5^\circ$. The improved mapping procedure since the pilot observations greatly enhances the sensitivity to emission, revealing extended CS emission across the entire survey region, as well as detecting 77 class I CH₃OH masers and 47 SiO maser regions. A comparison between CS from MALT-45 and NH₃ from HOPS shows that CS experiences a combination of being depleted and becoming optically thick in the centres of gas clumps, while NH₃ is enhanced. Class I CH₃OH masers are found to possess similar peak velocities to that of CS, highlighting their value as systemic velocity tracers. Furthermore, class I CH₃OH masers are found toward most of the other known star-forming masers in the survey region, yet a large population of class I CH₃OH masers have no other maser association. Finally, all SiO masers appear to be associated with evolved stars, and a few regions curiously have stronger emission in their $v = 2$ lines compared to $v = 1$.

Chapter 4 details interferometric follow-up observations toward each of the class I CH₃OH masers detected by MALT-45, in Chapter 3. Within the maser regions observed, a total of 238 maser spots are found, and compared to other star-forming tracers. In particular, the typical distances between class I CH₃OH masers and other masers does not exceed 0.5 pc. More evolved regions of star formation tend to have more class I CH₃OH maser spots, larger velocity spreads and larger spatial distributions. The brightness of class I CH₃OH masers do not have strong correlations in any comparison, although the CS (1–0) emission detected in each maser region has a strong correlation with 870 μm dust emission.

Chapter 5 gives additional investigations with CS emission detected by MALT-45, detailed in Chapter 3. A weak correlation between the CS luminosity and kinetic temperature is observed. Projected linear distances from CS peaks to class I CH₃OH masers and 870 μm dust emission point sources are found to be within 0.5 pc.

Chapter 6 summarises and concludes the thesis, with a scope for long- and short-term projects derived from this work.

Chapter 2

Pilot observations for MALT-45

This chapter includes a co-authored publication. The bibliographic details of the paper are: Jordan, C. H., Walsh, A. J., Lowe, V., Lo, N., Purcell, C. R., Voronkov, M. A. and Longmore, S. N., *Monthly Notices of the Royal Astronomical Society*, 429, 469. doi: 10.1093/mnras/sts350. The published paper is referenced by this thesis as Jordan et al. (2013).

The auto-correlation methodology is expanded, to further detail this procedure. The introduction and discussion sections have been modified to streamline the discussed literature, to avoid unnecessary overlap with Chapter 1.

Abstract

We introduce the MALT-45 (Millimetre Astronomer’s Legacy Team - 45 GHz) Galactic plane survey and describe pilot survey results with the Australia Telescope Compact Array (ATCA). The pilot survey was conducted to test the instrumentation and observational technique of MALT-45, before commencing the full survey. We mapped two half-square degree regions within the southern Galactic plane around the G333 giant molecular cloud, using fast mosaic mapping. Using the new Compact Array Broadband Backend (CABB) on the ATCA, we were able to observe two 2048 MHz spectral windows, centred on frequencies 43.2 and 48.2 GHz. Although only a coarse spectral resolution of around 7 km s^{-1} was available to us, we detect widespread, extended emission in the CS (1–0) ground state transition. We also detect eight class I CH₃OH masers at 44 GHz and three SiO masers in vibrationally excited (1–0) transitions. We also detect the H53 α radio recombination line, non-vibrationally excited SiO (1–0) and emission in the CH₃OH 1_0-0_0 A⁺ line.

2.1 Introduction

High mass star formation (HMSF) is a poorly understood process due to the rapid evolution of high mass stars, the rarity of high mass stars, and high levels of dust extinction (Zinnecker & Yorke 2007). HMSF does not occur in isolation, thus making it difficult to disentangle mechanisms involved with HMSF from other sites of star formation in the vicinity. HMSF is

known to occur within dense regions of giant molecular clouds (GMCs; e.g. Lo et al. 2011). In order to comprehend the earliest stages of HMSF, a catalogue of their regions must be identified and mapped through high density tracers.

Previous surveys have been productive in identifying many sites of HMSF, but emphasise signposts that pick out only a subsection of the various stages, are typically targeted toward known regions. For example, methanol maser surveys (e.g. Walsh et al. 1998; Green et al. 2009) pick out hot cores and young ultra-compact H II regions; infrared dark clouds (IRDCs; e.g. Rathborne et al. 2006) are only seen when they are close to us, and projected against a bright infrared background from the Galaxy and may not always identify sites of high mass star formation (Kauffmann & Pillai 2010); radio continuum sources are only found once a high mass star has had time to reach the main sequence and push its ionising wind through the surrounding material (e.g. Purcell & Hoare 2010).

Untargeted Galactic plane surveys not only give us an opportunity to address these concerns, but they also allow us to study aspects of HMSF on a Galaxy-wide scale, with higher resolution and sensitivity than is achievable in external galaxies. For example, we can study the structure of the Galaxy through CO surveys (e.g. Dame & Thaddeus 2008) and HI surveys (e.g. McClure-Griffiths et al. 2005). The nature of CO and HI mean that these tracers typically pick out low density gas (critical density $\approx 10^1$ - 10^2 cm $^{-3}$) that is not directly related to HMSF. These tracers are also sensitive to inter-spiral arm gas, making it difficult to identify spiral structure in the Galaxy. Higher density gas tracers, such as NH $_3$ and HC $_3$ N, observed as part of the H $_2$ O southern Galactic Plane Survey (HOPS; Walsh et al. 2008, 2011), do trace gas directly associated with HMSF and may more clearly trace spiral structure. However, HOPS is a shallow survey, sensitive to typical HMSF regions within a few kpc. In order to study the spiral structure of the Galaxy, as well as the gas associated with HMSF, we have devised the MALT-45 survey. This paper introduces the MALT-45 survey design and outlines the auto-correlation results of pilot survey. MALT is the Millimetre Astronomer's Legacy Team - the result of a successful meeting of star formation astronomers to collaborate on major southern hemisphere millimetre surveys. MALT currently consists of the MALT-90 (Foster et al. 2011) and MALT-45 surveys.

2.2 MALT-45 Design

MALT-45 aims to provide a comprehensive survey of star formation tracers at 7 mm (~ 45 GHz) in the southern Galactic plane. MALT-45 is to be conducted on the Australia Telescope Compact Array (ATCA), exploiting the newly available technologies made by the Compact Array Broadband Backend (CABB; Wilson et al. 2011). In particular, MALT-45 seeks to employ the CABB provided auto-correlations. Using these data, the CABB can be used to image extended emission with a collecting area similar to $6 \times$ Mopra (a single 22 m dish radio-telescope similar to a single ATCA antenna). Hence, MALT-45 achieves the advantages of using an interferometer to accurately position interstellar masers associated with HMSF, while simultaneously mapping the Galaxy for extended emission.

MALT-45 is an untargeted Galactic plane survey, with a Galactic latitude width of $\pm 0.5^\circ$ (the longitude range is yet to be determined). The survey will focus on the dense gas tracer

CS (1–0), and identify previously unknown sources of both class I CH₃OH and SiO (1–0) masers, which occur towards sites of star formation and evolved stars, respectively. The survey region of MALT-45 will be a subsection of HOPS (which covers a range $l = 290^\circ$ through $l = 0^\circ$ to $l = 30^\circ$, $b = \pm 0.5^\circ$), allowing comparison with 12 mm star-forming tracers, particularly NH₃ (1,1) and H₂O masers. Other lines of possible interest are outlined in Table 2.1. The CABB allows a 64M-32k zoom mode configuration (see §2.3), which yields fine velocity resolution while also providing large velocity coverage.

2.2.1 The G333 GMC

The MALT-45 pilot survey was conducted partially over the GMC associated with the H II region RCW 106. RCW106 has a centre located roughly at $l = 333^\circ$, $b = -0.5^\circ$. We are particularly interested in this GMC, commonly referred to as the G333 complex, located at a distance of 3.6 kpc (Lockman 1979). The G333 GMC has been thoroughly investigated for molecular spectral lines relevant to star formation (Bains et al. 2006; Wong et al. 2008; Lo et al. 2009), and has shown evidence of HMSF (Lo et al. 2011). See Bains et al. (2006), Wong et al. (2008) and Lo et al. (2009) for a detailed description of the G333 complex. G333 is an ideal location to test MALT-45 before commencing the full survey, as we can expect extended CS thermal emission and Class I CH₃OH masers to be detected (Slysh et al. 1994).

2.3 Observations

The first observations for MALT-45 were conducted on the ATCA over 36 hours from the 18th to 20th of March 2010, using the H168 array configuration. Additional MALT-45 observations were conducted on the 7th and 8th of June 2010, using the 6C array configuration. These observations were necessary to test the feasibility of MALT-45, as conducting an untargeted survey at this frequency will be demanding on time, and may yield poor data if not allowed to observe optimally.

A mosaic of source pointings was constructed to observe over one square-degree, with interleaved points spaced on a square grid of 42 arcsec, which is slightly larger than Nyquist sampled at the highest frequency (29 arcsec, assuming a beam of 57 arcsec). The mosaic contained roughly 12,000 points, and thus required short exposure times for each point to be completed within the allocated observation time, hence only 6 seconds of observation was allowed for each pointing. Prior testing to the pilot survey revealed that the ATCA required nominally 1.5 seconds settling time between adjacent points, thus leaving at most 4.5 seconds per pointing. This pilot survey was also necessary to test the 6 second cycle time used instead of the ATCA default 10 seconds.

Due to software limitations, a single mosaic of 12,000 discrete pointings was not possible on the ATCA. Instead, it was split into two half-mosaics, observed one after the other. However, an unfortunate miscalculation on the position of each half-mosaic caused an approximate half-degree gap between each mosaic. Nevertheless, an entire square-degree was mapped as planned. The centres of each half-mosaic are approximately 333.4° and 334.1° in Galactic longitude. This region was selected for its known rich star-forming regions, including the

Table 2.1: Bright spectral lines in the 42.2 to 49.2 GHz range. Radio recombination lines (RRL) are taken from Lilley & Palmer (1968). All other rest frequencies are taken from the Cologne Database for Molecular Spectroscopy (CDMS; Müller et al. 2005).

Spectral line	Frequency (GHz)	Pilot survey detection	Maser or thermal?	Beam size (arcsec)
SiO (1-0) $v = 3$	42.51934	N	Maser	66
SiO (1-0) $v = 2$	42.82048	Y	Maser	66
H53 α (RRL)	42.95197	Y	Thermal	65
SiO (1-0) $v = 1$	43.12203	Y	Maser	65
SiO (1-0) $v = 0$	43.42376	Y	Thermal	65
CH ₃ OH 7(0,7)-6(1,6) A ⁺	44.06941	Y	Maser (Class I)	64
H51 α (RRL)	48.15360	N	Thermal	58
C ³⁴ S (1-0)	48.20694	Y	Thermal	58
CH ₃ OH 1 ₀ -0 ₀ A ⁺	48.37246	Y	Thermal	58
CH ₃ OH 1 ₀ -0 ₀ E	48.37689	N	Thermal	58
OCS (4-3)	48.65160	N	Thermal	58
CS (1-0)	48.99095	Y	Thermal	57

G333 GMC. The reference position used for auto-correlation processing was G334.0-1.0, and was observed for 5 cycles (30 seconds) approximately every 34 minutes.

At the time of observation, the CABB was unable to provide the 64M-32k zoom mode, providing only broadband mode windows. The 64M-32k zoom windows, when completed and ready for use on the CABB, provide 16 simultaneous observing windows per 2048 MHz broadband window, each with 2048 channels over 64 MHz, yielding a 32 kHz fine resolution. At the rest frequency of a class I CH₃OH maser, each channel of a zoom window provides a resolution of approximately 0.22 km s⁻¹. Without the zoom modes, the ATCA provides two broadband windows simultaneously, each with 2048 MHz of bandwidth, and 2048 channels. These windows were centred on frequencies of 43.2 and 48.2 GHz, and were placed to observe SiO (1-0) masers, class I CH₃OH masers and CS (1-0) thermal emission. These spectral lines and hence the 2 GHz band placements have been selected as being easiest to detect without sacrificing too many other lines of interest, and therefore some lines are neglected (e.g. HC₃N (5-4) at 45.49031 GHz). As each channel corresponds to 1 MHz in the spectrum, the approximate resolution at these frequencies is a coarse 6.8 km s⁻¹. Future MALT-45 observations using the 64M-32k zoom windows on each of the 12 spectral lines listed in Table 2.1 will provide much higher channel resolution, resulting in more detailed velocity information.

It was found that data from antenna 6 of the ATCA (CA06) had increased noise levels by a factor of 3.5. The removal of CA06 data from the other antenna data improved the quality of images substantially, and therefore no data with CA06 is presented here. The poorer performance of CA06 is due to its different dish surface, yielding poor sensitivity to 7 mm emission. Furthermore, at the time of observation, the CABB also had bad channel issues with the broadband windows, specifically, on the channel range 250-500, and all multiples of 512.

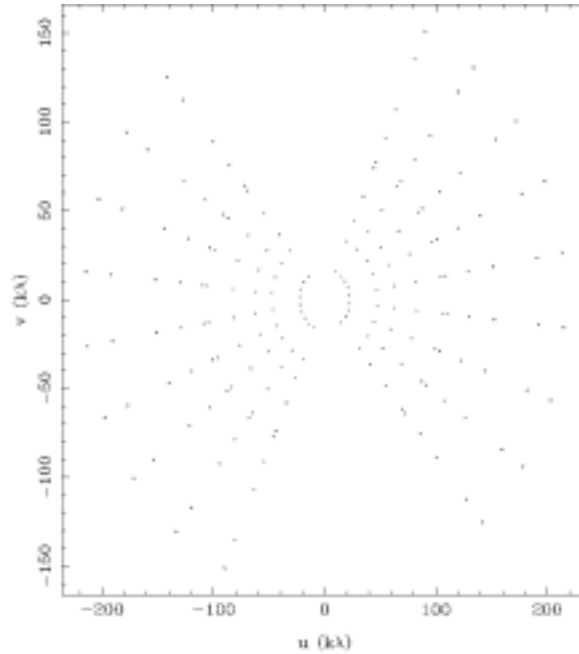


Figure 2.1: An example of ATCA baselines in the 1.5A array configuration. Note the lack of data in the centre of the plot, typical of an interferometer.

2.4 Auto-correlation

Interferometers, such as the ATCA, are popular in radio astronomy for their increased spatial resolution over a single dish. The quality of the images produced by an interferometer is determined by the uv -coverage over the observations, as interferometers observe in the uv -plane. uv -coverage is determined by the baselines used in an observations, referring to the distance between any two antennas; see Fig. 2.1 for an example of uv -coverage. One problem that will always occur in interferometry is the lack of spatial coverage at low uv -distances; the distance between two antennas is limited by their physical size. For example, observations with the ATCA cannot have a pair of antennas closer than 22 m to each other, as each antenna is 22 m in diameter. This is known as the ‘short-spacing problem’.

Low uv -distances are important, because they contain the total-power properties, where the higher frequencies are better at resolving fine structure. When imaging emission (or absorption) without fine structure, ignoring low uv -distances may cause all emission to appear absent; such extended emission is ‘resolved out’. Although short-baseline configurations of interferometers can observe extended emission, single dish observations observe all low uv -distances, having no gaps in the uv -plane, making them more ideal for detection.

Cross-correlation refers to the detection of emission in an interferometer. Auto-correlation is similar, but refers to single dish data processing, and not necessarily from the same dish; here, we discuss auto-correlation processing of spectral lines using multiple antennas of the ATCA.

2.4.1 Procedure

Data reduction with Mopra, another radio-telescope which similar to each of the six antennas comprising the ATCA, acts as the reference for the auto-correlation procedure described

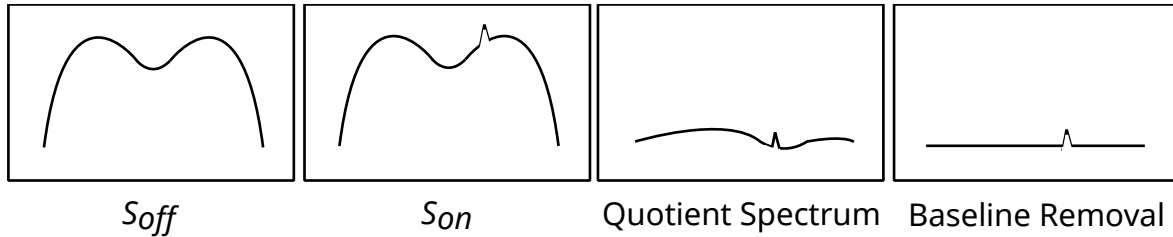


Figure 2.2: An example of the baselining procedure used to identify spectral lines.

here. Observations with a single dish are typically divided between sources and reference calibrators. When reducing data to identify spectral lines, a quotient spectrum is formed from the source (on) and reference (off) spectra:

$$T_{Source} = \left(\frac{S_{on} - S_{off}}{S_{off}} \right) T_{ref} \quad (2.1)$$

where T is an antenna temperature, and S is a spectrum. T_{ref} refers to the system temperature of the reference source; this is used to calibrate antenna temperatures and flux densities. This procedure is referred to as baselining; a graphical representation can be seen in Fig. 2.2. Baselining relies on the system response between a source and reference being very similar, such that what remains after performing the subtraction and quotient is only source emission or absorption. Because the system response varies with pointing position, and the atmosphere intervening, resulting spectra may have significant variation in intensity with frequency, rather than being flat. Post-baselining solutions typically help this problem with the removal of a polynomial fit to the whole spectrum. Note that depending on the capabilities of the receiver system, observed continuum spectra may have a significant slope, which is hard to distinguish from instrumental effects; extra care must be taken when subtracting polynomials in these cases.

2.4.2 Software

CSIRO Astronomy and Space Science (CASS), in addition to running and maintaining the ATCA, Mopra and Parkes radio-telescopes, provides various software packages to process raw data. Mopra raw data files are formatted and immediately ready to be processed by LIVEDATA, which performs the baseline procedure outlined above. It also removes a polynomial of user specified order. If imaging is desired, LIVEDATA products may be processed by GRIDZILLA, which regrids the spectra to form a data cube.

ATCA raw data files are not ready to be processed in such a fashion. Our pipeline strategy of auto-correlation with the ATCA was as follows:

- (i) MIRIAD, another software package provided by CASS, is used to interpret ATCA raw data, using tasks ATLOD and UVAVR to isolate auto-correlations for every antenna, and select specific channel ranges of the data applicable to emission;
- (ii) A specifically-designed program, developed by Maxim Voronkov, is used to convert products into a LIVEDATA readable format. This involves correctly designating a reference scan and performing rest frequency frame conversions;
- (iii) LIVEDATA performs the baselining routine for each antenna product, followed with a linear subtraction to the spectra;

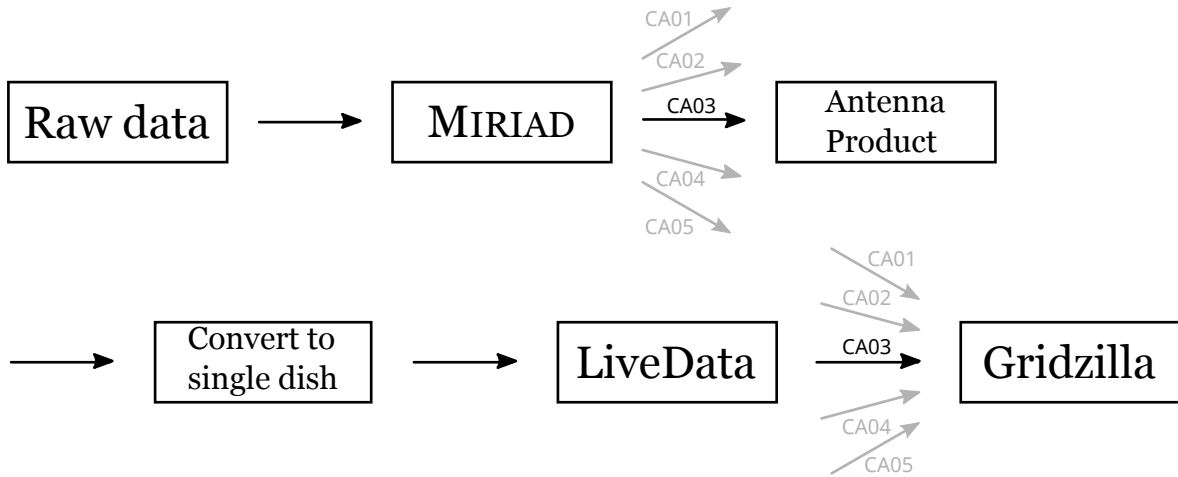


Figure 2.3: A diagram outlining the auto-correlation pipeline used for MALT-45.

- (iv) GRIDZILLA takes all antenna products, and produces a data cube.

The procedure is outlined graphically in Fig. 2.3. LIVEDATA parameters used include a referenced method with a mean estimator, a robust linear fit for post-baselining subtraction, and a Doppler frame of LSRK. GRIDZILLA parameters include a beam FWHM of 1 arcmin, a kernel FWHM of 1.5 arcmin, a cutoff radius of 0.8 arcmin and a mean gridding statistic.

2.5 Results

Auto-correlated data cubes were produced for each of the lines listed in Table 2.1 from the ATCA broadband data. We detected emission in CS (1–0) (Fig. 2.4), class I CH₃OH masers at 44 GHz (Figs 2.5 and 2.6), vibrationally excited SiO masers (Figs 2.6 and 2.7), as well as occasional detections of H53 α , SiO (1–0) $v = 0$ and CH₃OH 1₀–0₀ A⁺. Radio recombination lines H53 α and H51 α were anticipated detections, as the brightest H69 α detection in the Galactic plane found by HOPS is located at G333.609–0.211. The survey region of this pilot survey did not cover the known regions of emission, but some H53 α recombination line emission was found cospatial with the class I CH₃OH maser G333.281–0.382.

As only the broadband modes were available at the time of observation, the results provide a coarse spectral resolution of about 6.8 km s⁻¹. Fortunately, some observing time was permitted on the Mopra radio-telescope to briefly follow-up some of the detected class I CH₃OH and SiO masers. Observations on Mopra were carried out using a standard position-switch mode, where each on-source position was observed for 5 minutes, resulting in a higher sensitivity than the ATCA observations. Maser emission characteristics are detailed in Table 2.2 and Figs 2.8 and 2.9.

The sensitivity of auto-correlated data varies greatly with the different days of observation. The MIRIAD task IMSTAT calculates a mean RMS of 15 mK per channel in antenna temperature, although this seems vastly too small. The authors feel that the true sensitivity of these data is approximately 40 mK per channel, although with good weather, this may improve.

By comparing the positions of the same maser feature in G333.227–0.057, the estimated

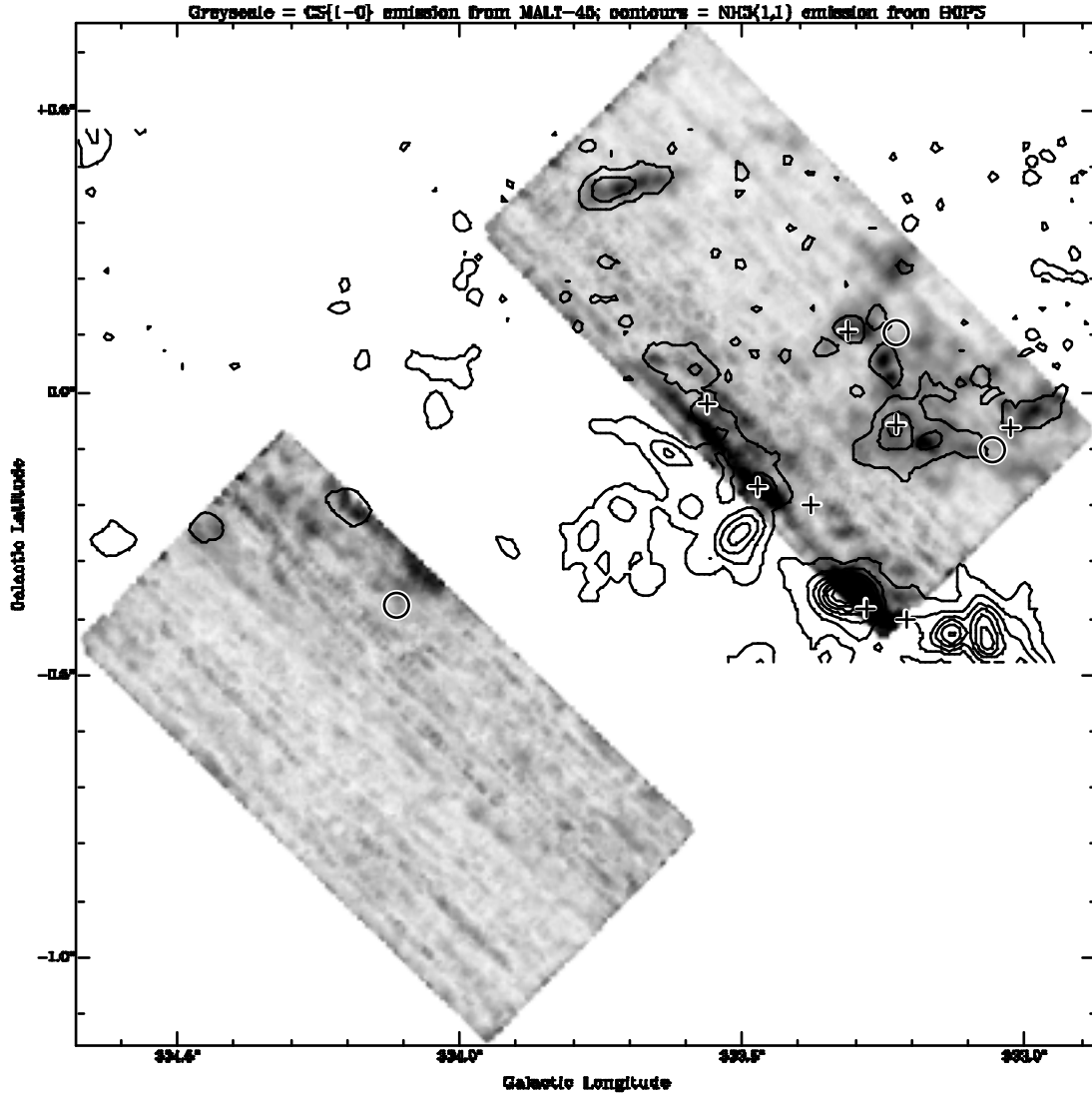


Figure 2.4: Auto-correlated CS peak-intensity map, overlaid with HOPS thermal NH₃ (1,1) contours. Contour levels are 10, 20, ..., 90 per cent of 1.09 K in units of antenna temperature. Circle symbols represent SiO $v = 2$ maser positions, while plus symbols designate class I CH₃OH maser positions.

astrometric errors are derived from new ATCA data from Voronkov et al. (2012). We find an offset of 9 arcsec and so ascribe the estimated astrometric error of the pilot survey work to be 10 arcsec.

2.5.1 CS (1–0) at 48.990 GHz

The main isotopologue of CS was detected in extended emission across a large portion of the survey region (Fig. 2.4). Also shown in Fig. 2.4 is NH₃ (1,1) emission, as detected in HOPS (Purcell et al. 2012). The CS emission appears to closely follow the NH₃ emission, as might be expected from the two quiescent dense gas tracers (e.g. Purcell et al. 2009). The strongest CS emission occurs cospatial with the G333 GMC, which is close to the edge of the surveyed area around G333.3–0.4.

Extended CS emission is seen between Galactic longitudes of 329.9° and 333.3° and Galactic latitudes -0.2° and $+0.3^\circ$. NH₃ emission is detected within this region, but covers a much

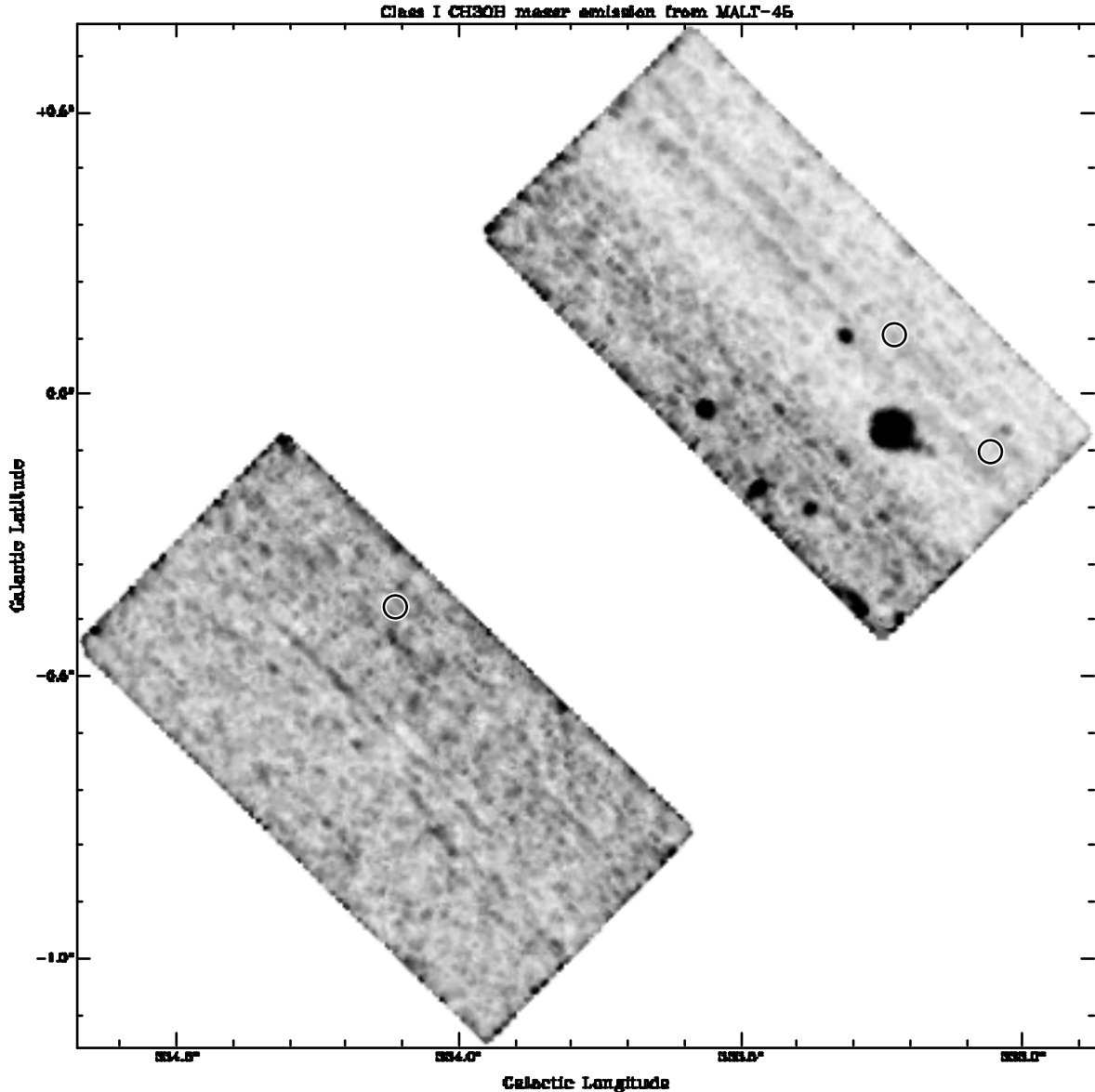


Figure 2.5: Auto-correlated class I CH₃OH maser peak-intensity map. Circles represent SiO $v = 2$ maser positions.

smaller area than the CS emission, possibly highlighting differences in the distribution of each dense gas tracer.

At G333.70+0.35, we see a filamentary CS structure that is oriented close to the Galactic plane. This structure is also seen in NH₃ emission (Fig. 2.4), as well as an infrared dark cloud (Fig. 2.10). See §2.6.3 for more details.

2.5.2 Class I CH₃OH 7(0,7)–6(1,6) A⁺ masers at 44.069 GHz

In the survey region, we found eight possible class I CH₃OH masers, whose properties are listed in Table 2.2 and shown as greyscale emission in Fig. 2.5, and positions are shown in Figs 2.4, 2.7, 2.10 and 2.11 as plus symbols. Most of the masers (5 of 8) are cospatial with the G333 GMC and have line of sight velocities within 10 km s⁻¹ of the GMC systemic velocity. They are thus likely to be associated with the star formation occurring in and around the

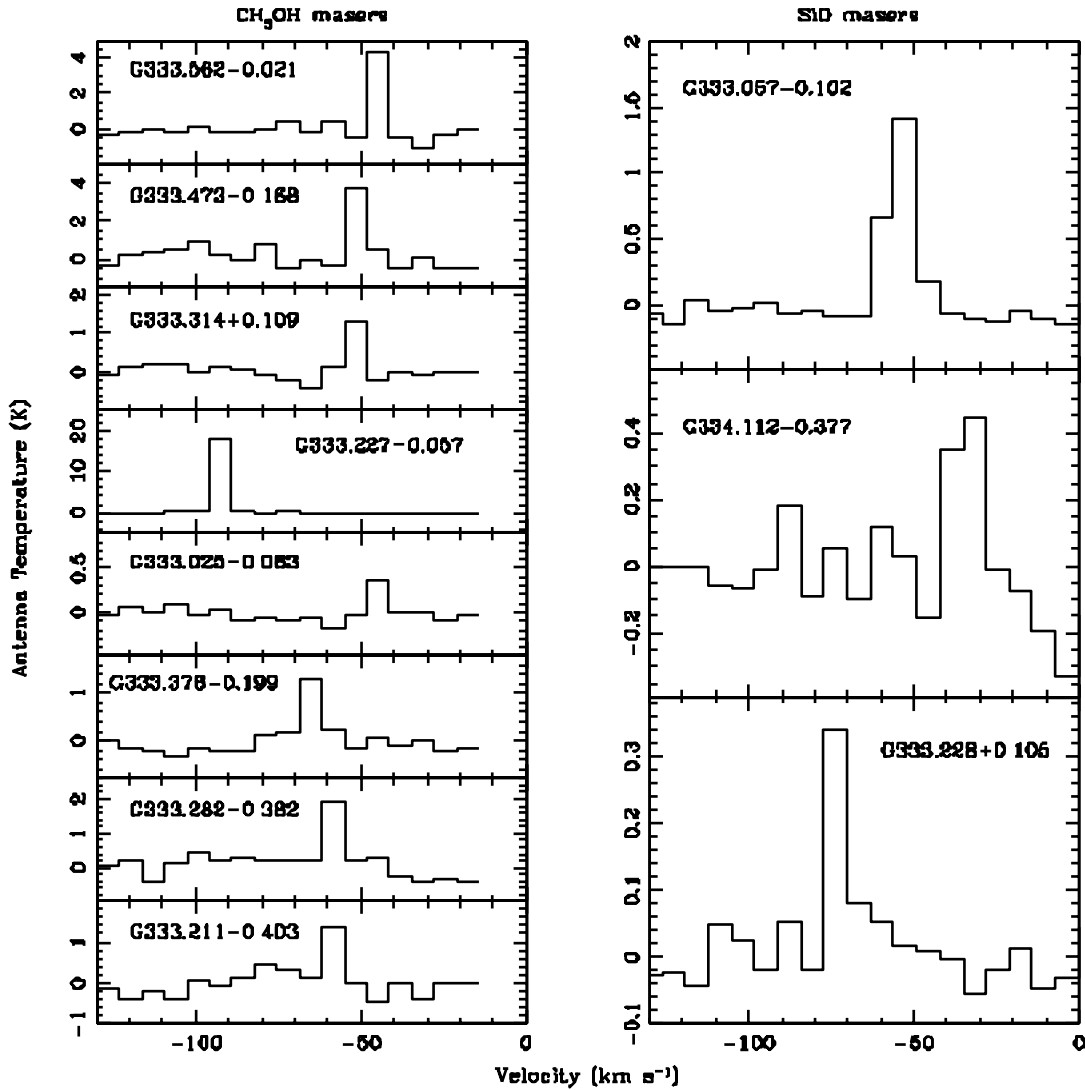


Figure 2.6: Auto-correlated spectra for each class I CH_3OH (left) and $\text{SiO } v = 2$ maser (right) detected. The deviations in the baselines are a result of poor weather. The channel width is approximately 6.8 km s^{-1} .

GMC. The other three appear cospatial with extended CS emission. The CABB broadband spectra for each maser are provided in Fig. 2.6. For each of these detections, we managed to acquire time on the Mopra radio-telescope to re-observe the CH_3OH spectra, as shown in Fig. 2.8. With the superior spectral resolution of Mopra, more convincing detections are made and finer velocity detail becomes apparent. Of all the CH_3OH detections, G333.227–0.057 has been previously reported as a detection at 44 GHz by Slysh et al. (1994) and G333.473–0.168 by Voronkov et al. (2012).

2.5.3 $\text{SiO } (1-0) v = 1, 2$ masers at 43.122 and 42.820 GHz

SiO emission in the vibrationally excited transitions, which are known to show maser activity, was tentatively detected towards three positions, shown as circles in Figs 2.4, 2.5, 2.10, and 2.11, and as greyscale in Fig. 2.7. All three positions appear to exhibit emission in the $v = 2$

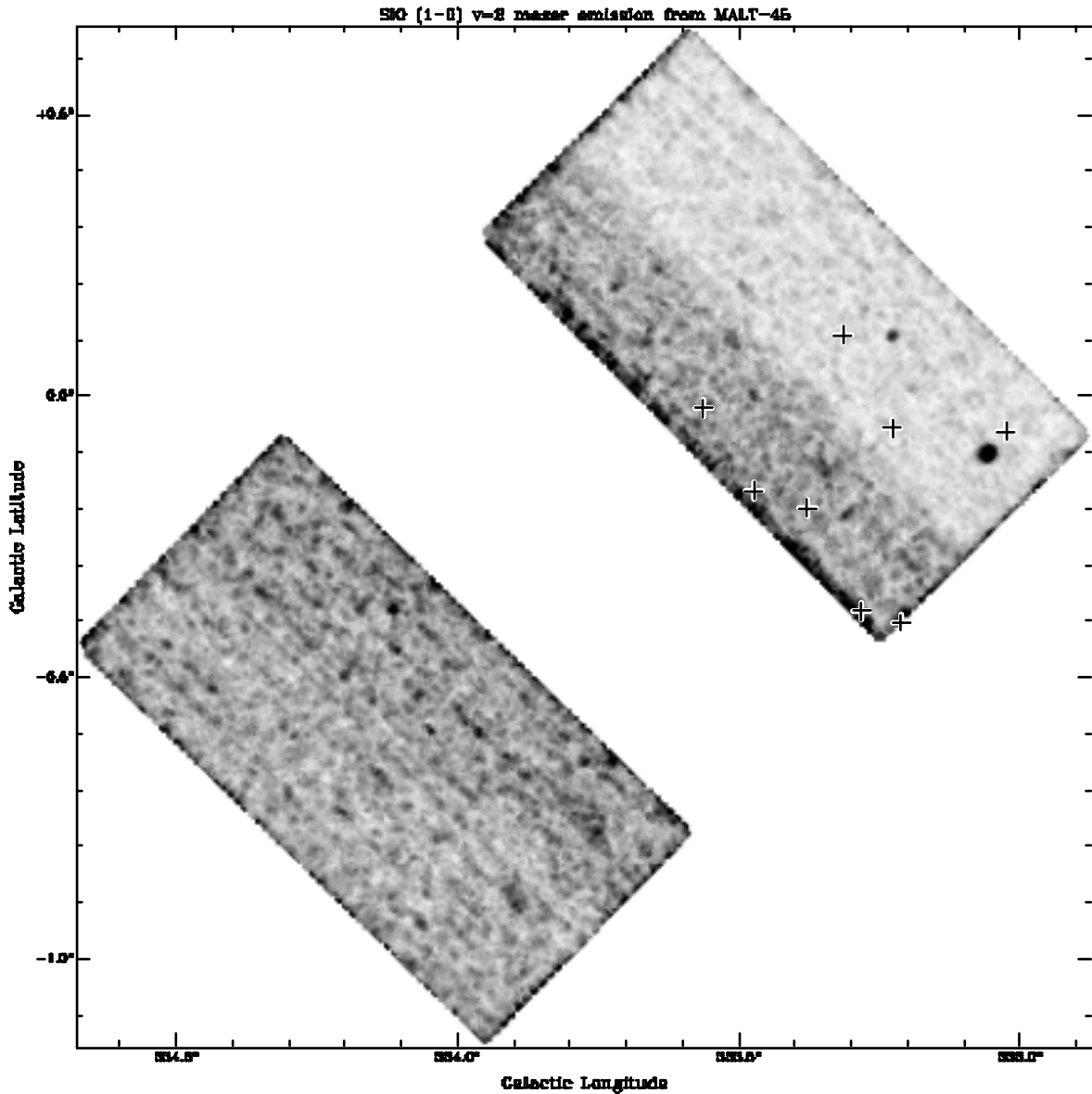


Figure 2.7: Auto-correlated SiO (1-0) $v = 2$ maser peak-intensity map. Class I CH₃OH maser positions are designated by plus symbols.

transition and two of the three in the $v = 1$ transition (the exception being G333.228+0.105). Spectra for the $v = 2$ transition are shown in Fig. 2.6. Again, emission is restricted to a small number of channels, using the CABB broadband mode. Each of the three tentative masers were re-observed with Mopra and high-resolution spectra are provided for two in Fig. 2.9, where more detail of the spectra can be seen. The maser at G333.228+0.105 was not detected by Mopra, leaving its detection status by the CABB as tentative. Figs 2.10 and 2.11 show the locations of the SiO masers with respect to infrared emission from GLIMPSE. Each SiO maser is cospatial with a bright infrared star which is likely to be an evolved star in each case.

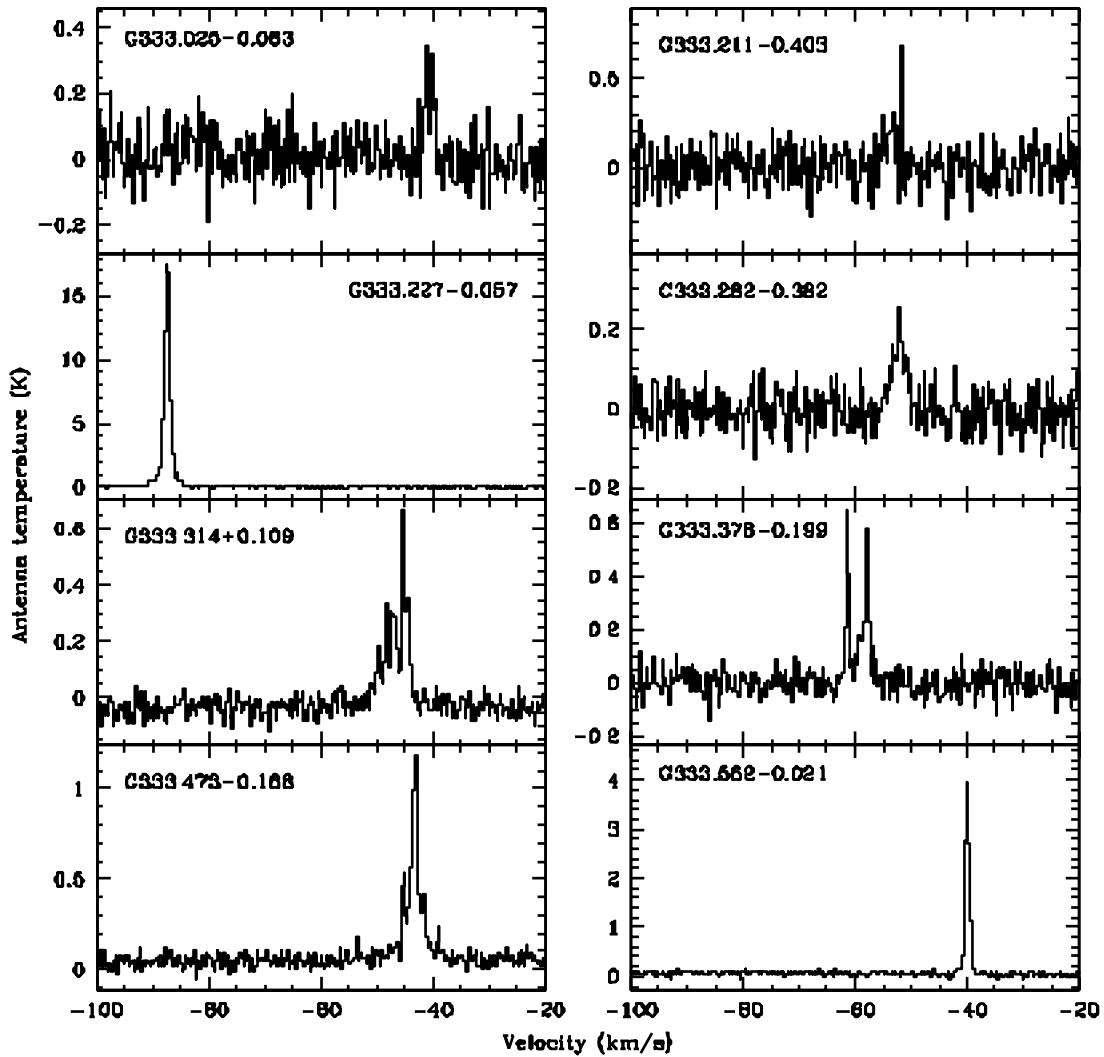


Figure 2.8: Follow-up class I CH_3OH maser spectra from Mopra.

2.5.4 Other detected lines

In addition to the main lines mentioned above, we made tentative detections in the SiO ($1-0$) $v = 0$ and CH_3OH 1_0-0_0 A^+ lines. The SiO was detected towards G333.227-0.057, which is cospatial with a class I CH_3OH maser. The CH_3OH 1_0-0_0 A^+ and E lines are thermally emitting lines that are close in frequency (equivalent to 27.5 km s^{-1}). We detect thermal emission at G333.227-0.057 and G333.314+0.109 in the A^+ transition, but not the E transition. Kalenskii & Sobolev (1994) indicate that the E- CH_3OH transition may require higher densities to produce line strengths comparable to A^+ - CH_3OH . The emission at G333.227-0.057 is cospatial with the thermal SiO source above and thermal methanol at G333.314+0.109 is cospatial with another class I CH_3OH maser, leading to a likely star formation origin for both thermal CH_3OH sources.

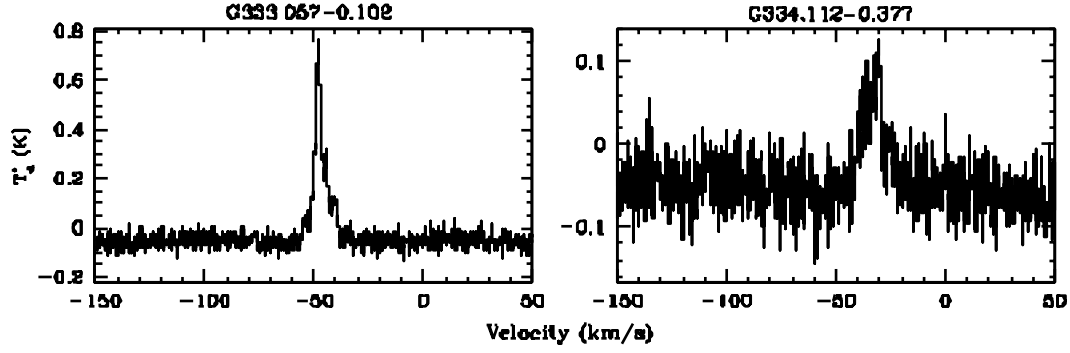


Figure 2.9: Follow-up SiO maser spectra from Mopra.

Table 2.2: Properties of detected MALT-45 maser emission as determined by Mopra.

Source Name	RA	Dec	Peak antenna temperature (K)	Peak velocity (km s^{-1})	Velocity range		Maser detected
	(J2000) (h m s)	(J2000) ($^{\circ}$ ' ")			Min.	Max.	
G333.025-0.063	16 18 55.6	-50 24 03.6	0.34	-41	-42	-39	Class I CH_3OH
G333.057-0.102	16 19 15.0	-50 24 12.1	0.84	-48	-45	-50	SiO $v = 1, 2$
G333.211-0.403	16 21 15.6	-50 30 45.1	0.69	-52	-54	-51	Class I CH_3OH
G333.227-0.057	16 19 48.6	-50 15 17.2	18	-87	-86	-88	Class I CH_3OH
G333.282-0.382	16 21 29.0	-50 26 52.0	0.25	-52	-55	-50	Class I CH_3OH
G333.314+0.109	16 19 28.8	-50 04 45.0	0.70	-45	-45	-48	Class I CH_3OH
G333.378-0.199	16 21 05.8	-50 15 00.9	0.65	-61	-62	-56	Class I CH_3OH
G333.473-0.168	16 21 22.7	-50 09 42.6	1.1	-43	-42	-44	Class I CH_3OH
G333.562-0.021	16 21 08.1	-49 59 47.8	3.8	-40	-39	-41	Class I CH_3OH
G334.112-0.377	16 25 06.7	-49 51 28.5	0.14	-30	-29	-34	SiO $v = 1, 2$

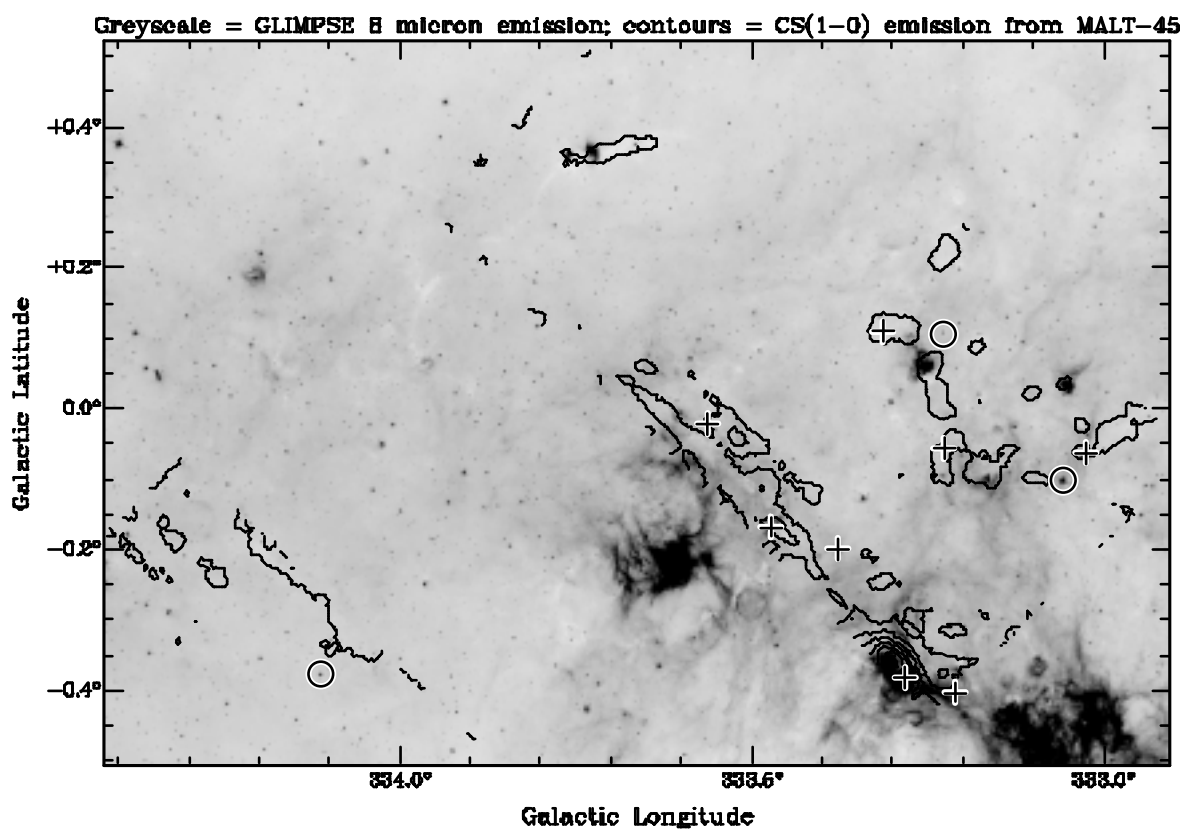


Figure 2.10: *Spitzer* GLIMPSE 8.0 μm greyscale image with MALT-45 pilot survey CS (1-0) thermal emission in black contours, with the positions of detected CH_3OH and SiO masers designated by plus symbols and circles, respectively. Contour levels are 7, 17, ..., 87 per cent of 0.72 K, in units of antenna temperature.

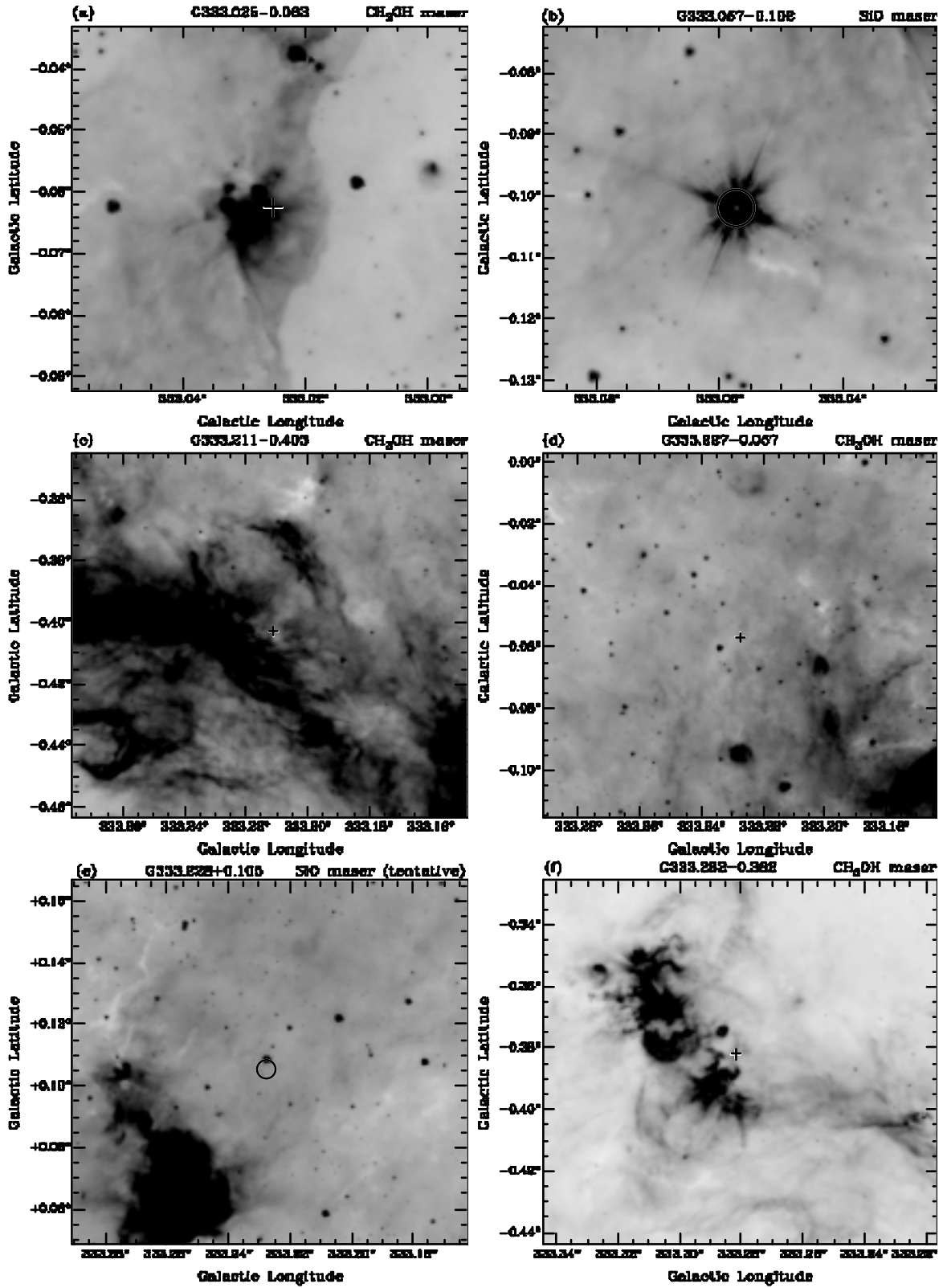
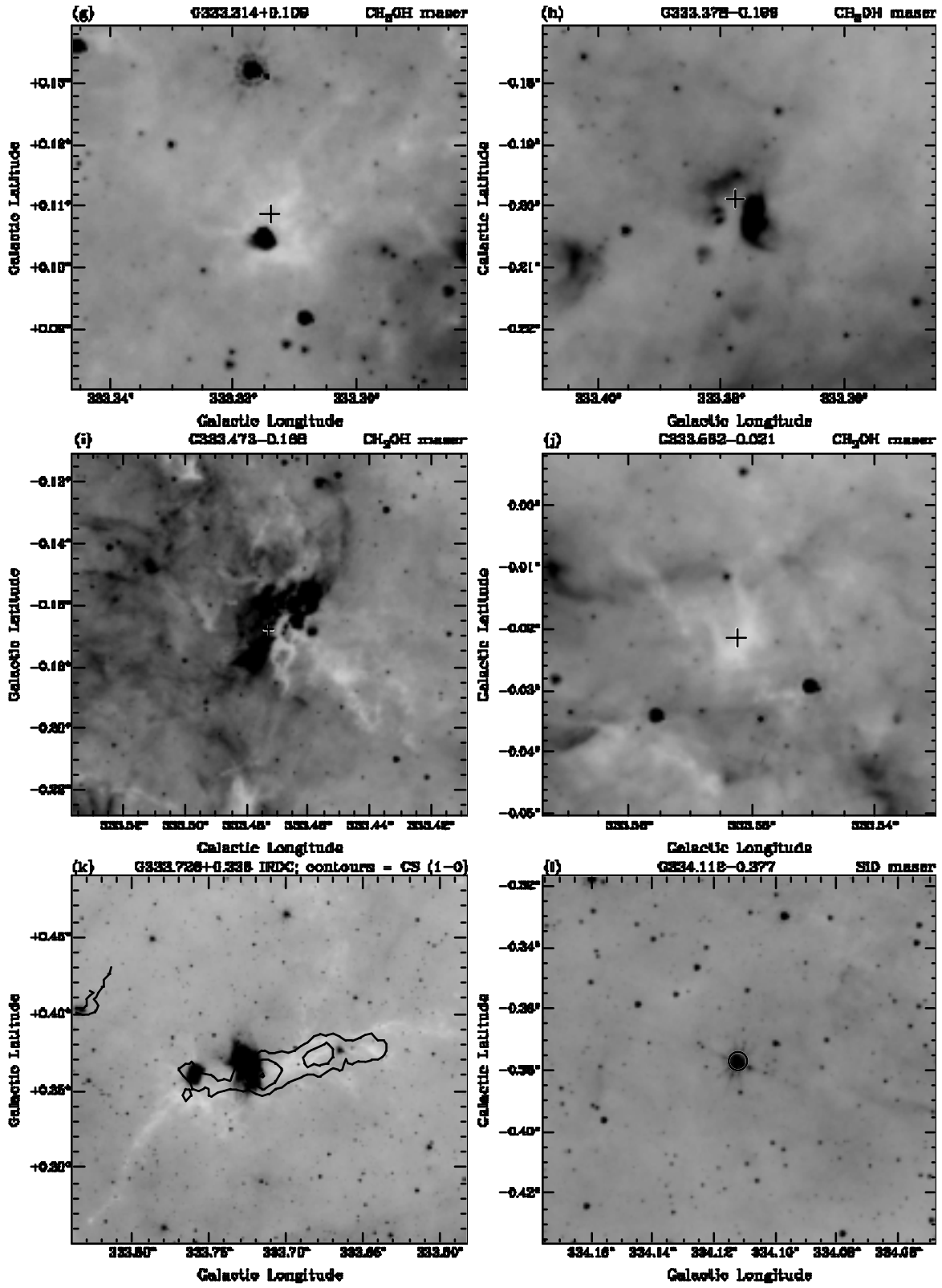


Figure 2.11: GLIMPSE 8 μm images of maser detection regions. Plus symbols designate positions of class I CH_3OH masers, and circles represent SiO maser positions. (k) contours are CS (1-0) emission at 7, 9 and 11 per cent of 0.72 K, in units of antenna temperature.

Figure 2.11: *continued*

2.6 Discussion

2.6.1 Weather Effects

As can be seen in Fig. 2.4, significant ‘striping’ artifacts exist in the data. The stripes coincide with the scanning direction of the observations. One contributing factor to the poor data is the fast-mosaic method; due to the fast transition times between pointings, antennas were occasionally unable to keep up and did not contribute data. However, the main factor in poor data is the inclement weather experienced during observations. The most prominent stripes seen in Fig. 2.4 coincide with periods of light rain. Lagging antennas serve to decrease our sensitivity to emission, but the weather hampers our ability at determining real astrophysical emission from noise. This weather introduced noise into both broadband spectral windows, but has affected some frequencies more than others. See Fig. 2.6 for CH₃OH and SiO spectra. Examples of species with poor spectra include CH₃OH 1₀-0₀ A⁺ (and its E species), H53 α and H51 α . The noise is apparent on all relevant frequencies of emission, but fortunately has permitted reasonable detections for the primary lines of interest (CS, class I CH₃OH and SiO masers).

It must be mentioned that the problems experienced in the pilot will not plague the overall MALT-45 survey, as the pilot survey merely seeks to provide a proof-of-concept on the techniques used and reveal potential problems before committing to the full observation.

2.6.2 Telescope Performance

Given the demands of our observational setup, we found some limitations to the ATCA that have affected the outcome of our pilot observations. Initially we found software limitations that meant changes to the intended survey design. These included: mosaic scans in Right Ascension and Declination coordinates only, rather than Galactic coordinates; no more than 999 pointings per mosaic file; no more than 2000 individual commands in a schedule file. These limitations resulted in a survey region that is at an angle to the Galactic plane, as can be seen in Fig. 2.4, and a complicated mosaicing system.

During the observations, zoom modes with the CABB were not available, so we used the broadband mode. This had the unfortunate effect of greatly limiting the amount of spectral detail seen, as described in §2.3. We also expect that the broadband mode is less sensitive to narrow-line emission (e.g. masers) by a factor of up to three. Also as mentioned previously, we found that some of the antennas had difficulty in keeping up with the demanding 6-second pointing regime. Indeed we found that RMS errors on the position of antenna 3 were typically 20 arcsec, which has reduced the sensitivity of the resulting data. We believe these excessive pointing errors can be eliminated with on-the-fly (OTF) mapping, where the antennas are driven smoothly and subsequent testing of this method suggests OTF mapping will resolve this issue for the full survey.

2.6.3 Comparison with other observations

In this subsection, we compare selected sources within the MALT-45 pilot survey region to observations from previous surveys. In particular, we compare our results with the mid-

infrared *Spitzer* Galactic Legacy Infrared Mid-Plane Survey Extraordinaire (GLIMPSE; Benjamin et al. 2003), for a visual correlation with infrared structures and objects. Mid-infrared extended emission is typically seen towards regions of active star formation, where the interstellar dust has been heated by newly formed stars. In addition to infrared emission, GLIMPSE also reveals prominent regions of infrared absorption, projected against the bright infrared background emission from the Galaxy (IRDCs; Rathborne et al. 2006).

Infrared emission can also arise from a variety of other astrophysical objects. One such example is emission from evolved stars, that may also give rise to SiO masers, which appear as bright infrared stars in the GLIMPSE images (Robitaille et al. 2008). The evolved stars appear unresolved in the GLIMPSE images, which may occasionally be confused with confined sites of star formation. A useful, but not entirely robust, method to distinguish between evolved and young stars is that an infrared star is likely to be evolved if it is not associated with extended infrared emission or an IRDC and has a $4.5\ \mu\text{m}$ magnitude brighter than 7.8 (Robitaille et al. 2008). Young stars are more likely to be fainter and associated with either extended emission or IRDCs.

A comparison of MALT-45 CS to HOPS NH_3 would be a valuable scientific addition to this paper, providing insight into star formation within these clouds. However, the data being presented is not of a sufficient quality to merit an accurate analysis. A variation in the CS/ NH_3 ratio may be apparent in a region such as G333.24+0.21, where there appears to be an over-abundance of CS, relative to NH_3 , as can be seen in Fig. 2.4. A thorough analysis will instead be performed with data from the full MALT-45 survey.

2.6.3.1 G333.227–0.057

GLIMPSE images in Figs 2.10 and 2.11 reveal that the region at G333.227–0.057 is on the edge of extended emission, but does not appear to be closely associated with a prominent infrared feature. We note there is an infrared source located approximately 15 arcsec to the lower left of the maser position in Fig. 2.11(d), which could be the powering source for an outflow that creates the maser. The class I CH_3OH maser spectrum (Fig. 2.8) is dominated by a single peak at around $-87\ \text{km s}^{-1}$. This region has been studied previously, and contains OH maser emission (Sevenster et al. 1997), class II CH_3OH maser emission (Ellingsen et al. 1996) and water maser emission (Kaufmann et al. 1976; Breen et al. 2010a). The spectra of all maser species are remarkably similar, with a peak close to $-87\ \text{km s}^{-1}$, indicating a likely common origin for all masers. This velocity is significantly different from velocities of gas found associated with the G333 GMC, which are more typically around $-45\ \text{km s}^{-1}$. Lockman (1979) calculate a distance of 3.6 kpc to G333. Based on a kinematic model of Galactic rotation, we estimate the distance to G333.227–0.057 is 5.1 kpc, putting it at a significant distance behind G333.

The class I CH_3OH maser associated with G333.227–0.057 was first detected by Slysh et al. (1994), with a peak flux density over 300 Jy. Using the high velocity resolution Mopra observations (Fig. 2.8), we see that the spectrum shows weaker emission, with a peak flux density 250 Jy, assuming a Jy/K conversion factor of 14.1 (Urquhart et al. 2010). This difference may be partially due to intrinsic variability of the maser, but can likely be attributed

to calibration uncertainties which are at the 20 per cent level.

We have detected unresolved SiO (1–0) $v = 0$ emission coincident with G333.227–0.057. This emission is seen in a single channel in the CABB data, but also as a well-defined single peak in the Mopra follow up data. Based on the Mopra spectrum at this position, the SiO emission has an integrated intensity of 2.2 K km s^{-1} , a peak velocity of -88.6 km s^{-1} and line full-width at half-maximum (FWHM) of 12.7 km s^{-1} . The velocity of the SiO emission is within 2 km s^{-1} of the peak of the class I CH₃OH maser, suggesting that the two are associated. As previously discussed, this ground state thermal transition is known to trace outflows associated with star formation. Using the CABB data, we also tentatively detect thermal CH₃OH emission in the 1_0-0_0 A^+ transition. Since this transition was not covered by the Mopra follow up observations, we cannot be certain that this is a real detection. If this is a real detection, then we can expect occasional detection of these thermal lines throughout the main MALT-45 survey, which will be useful to compare the thermal and masing properties of CH₃OH in such regions.

2.6.3.2 G333.726+0.366

The CS image shows a clear elongated structure at this position. Comparison with the GLIMPSE $8 \mu\text{m}$ image indicates that there is an IRDC, whose morphology closely follows that of the CS emission (Fig. 2.11). HOPS NH₃ emission also closely follows the CS emission and IRDC. The NH₃ emission is strongest at -34.9 km s^{-1} and the CS emission appears to peak close to this, although the velocity of the peak is not known accurately due to the broadband channels of the CABB. The close velocity and shape suggests both CS and NH₃ arise from the IRDC. The IRDC is cospatial with bright, extended emission at $8 \mu\text{m}$ which lies at the peak of both CS and NH₃ emission. The extent of the CS and NH₃ emission is almost 0.2° , which, assuming a distance of 3.6 kpc (Lockman 1979), is equivalent to a projected distance of 10 pc. The GLIMPSE image indicates that the IRDC may extend significantly beyond this.

2.6.3.3 G333.314+0.109

We detect both CS and a class I CH₃OH maser emission at this position. The GLIMPSE image of this region shows a faint IRDC, with an extended and reddened emission feature within the IRDC. The peak of weak NH₃ emission appears at this position, as well as a water maser, detected in HOPS. All spectral features appear to peak around -45 km s^{-1} , which is similar to the velocity of the G333 GMC. It is likely that this cloud and the G333 GMC are located a similar distance from us.

2.7 Future work and refinement of the MALT-45 survey

The pilot survey has been successful in many ways, perhaps most notably with the successful auto-correlation data reduction for each of the spectral lines relevant to MALT-45. The pilot has detected extended CS emission, as well as eight class I CH₃OH masers, two SiO masers in

Table 2.3: MALT-45 parameters from the pilot survey and full survey.

MALT-45	Correlator configuration	Channel resolution (km s^{-1})	Cycle time (seconds)	Targeted spectral lines	On-the-fly mapping	Orthogonal scans / Nyquist sampling
Pilot survey	2×2048 MHz broadband windows	~ 7	6	12	No	No
Full survey	32×64 MHz zoom windows	~ 0.2	6	12	Yes	Yes

the $v = 1$ and 2 transitions, and another tentative detection in the $v = 2$ transition. We have also detected thermal emission in CS, SiO $v = 0$ and CH₃OH 1_0-0_0 A⁺ detections, with CS emission being extended across a large fraction of the surveyed area. However, we anticipate great improvements for the main survey, based on the results of this work, and the expected completion of the CABB upgrade on the ATCA.

With CABB 64M-32k zoom modes available, we expect to achieve spectral channel resolution of $\sim 0.2 \text{ km s}^{-1}$, which will not only allow us to identify more spectral features, but will also effectively increase our sensitivity to narrow-lined emission, such as from masers. For a maser of line 1 km s^{-1} FWHM, we expect to gain a factor of ~ 2.5 in sensitivity.

We expect to employ an OTF mapping technique, which will eliminate problems with the antenna drive systems not being able to keep up with the rigorous 6 second pointing we have used in this work. Early tests using OTF have indeed proven this to be the case. Overall, this could increase sensitivity by a factor of about 2, as some mapped regions had only three antennas sufficiently close to the desired pointing position to have usable data.

Early problems with the CABB blocks that cause noisy channels to be flagged out (as mentioned in §2.6.2) should be greatly reduced, as the cause of such problems become identified. We are currently aware that the problems with some blocks have already been addressed.

The ATCA scheduler now allows us to write schedule files in Galactic coordinates, as well as allowing many more pointings per mosaic and commands per schedule file. This will allow for a much smoother running schedule, as well as a smoother final mapped region, without jagged edges that would be a result of RA/Dec scans.

We will employ a method of scanning in two orthogonal directions (Galactic longitude and latitude). We expect that this will greatly reduce stripe features that are evident in the current data. Such stripes are mainly caused by varying weather conditions, but can also be affected by the changing elevation of the observations. Our experience in the pilot work is that observations should not be undertaken under heavy cloud, light rain or worse weather conditions. Scanning in two directions has proven very successful for OTF mapping with the Mopra radio-telescope, such as those used in HOPS. Scanning in two directions will also increase the sensitivity. Furthermore, the combination of both OTF mapping and orthogonal scans will produce data that is effectively Nyquist sampled with closest spacing between adjacent observations of 30 arcsec. The differences between both surveys are highlighted in Table 2.3.

Chapter 3

MALT-45 - I. Techniques and spectral line data

This chapter includes a co-authored publication. The bibliographic details of the paper are: Jordan, C. H., Walsh, A. J., Lowe, V., Voronkov, M. A., Ellingsen, S. P., Breen, S. L., Purcell, C. R., Barnes, P. J., Burton, M. G., Cunningham, M. R., Hill, T., Jackson, J. M., Longmore, S. N., Peretto, N. and Urquhart, J. S., *Monthly Notices of the Royal Astronomical Society*, 448, 2344. doi: 10.1093/mnras/stv178. The published paper is referenced by this thesis as Paper I.

The introduction section has been modified to streamline the discussed literature, to avoid unnecessary overlap with Chapter 1.

Abstract

We present the first results from the MALT-45 (Millimetre Astronomer’s Legacy Team - 45 GHz) Galactic Plane survey. We have observed 5 square-degrees ($330^\circ \leq l \leq 335^\circ$, $b = \pm 0.5^\circ$) for spectral lines in the 7 mm band (42–44 and 48–49 GHz), including CS (1–0), class I CH₃OH masers in the 7(0,7)–6(1,6) A⁺ transition and SiO (1–0) $v = 0, 1, 2, 3$. MALT-45 is the first unbiased, large-scale, sensitive spectral line survey in this frequency range. In this paper, we present data from the survey as well as a few intriguing results; rigorous analyses of these science cases are reserved for future publications. Across the survey region, we detected 77 class I CH₃OH masers, of which 58 are new detections, along with many sites of thermal and maser SiO emission and thermal CS. We found that 35 class I CH₃OH masers were associated with the published locations of class II CH₃OH, H₂O and OH masers but 42 have no known masers within 60 arcsec. We compared the MALT-45 CS with NH₃ (1,1) to reveal regions of CS depletion and high opacity, as well as evolved star-forming regions with a high ratio of CS to NH₃. All SiO masers are new detections, and appear to be associated with evolved stars from the *Spitzer* Galactic Legacy Infrared Mid-Plane Survey Extraordinaire (GLIMPSE). Generally, within SiO regions of multiple vibrational modes, the intensity decreases as $v = 1, 2, 3$, but there are a few exceptions where $v = 2$ is stronger than $v = 1$.

3.1 Introduction

The mechanism of high-mass star formation (HMSF) remains an important unsolved problem in astrophysics. Understanding HMSF is difficult for a number of reasons: the rarity of HMSF regions, high dust extinction within molecular clouds, rapid evolution, and large distances from our Solar System (Zinnecker & Yorke 2007) all combine to hinder our understanding. HMSF is known to begin within Giant Molecular Clouds (GMCs) and eventually end with star clusters or associations (Lada & Lada 2003). To understand the various stages of HMSF, an inventory of regions must be compiled in a range of known tracers.

Large area surveys of molecular gas are ideal for identifying HMSF regions across a broad range of evolutionary phases. In particular, the critical density of a gas tracer can act as a probe for Galactic structure and star formation. Critical density (n_c) is a measure of the density required to produce detectable emission (Evans 1999). Previous surveys for star formation in external galaxies, typically for low-density gas tracers ($n_c < 10^3 \text{ cm}^{-3}$), suffer from poor resolution (on the order of kpc) and sensitivity. Untargeted Galactic plane surveys avoid these issues, while simultaneously offering the ability to detect new, less obvious regions of star formation within our Galaxy. Other untargeted surveys have been productive in identifying extended emission, such as in CO (Dame et al. 2001; Jackson et al. 2006; Burton et al. 2013), OH (Dawson et al. 2014) and HI (McClure-Griffiths et al. 2005). However, HMSF occurs in regions of dense molecular gas, and so mapping higher density tracers serves well to identify target regions. Examples include NH_3 (1,1) ($n_c \approx 10^3 \text{ cm}^{-3}$; Evans 1999) and HC_3N (4–3) ($n_c \approx 10^4 \text{ cm}^{-3}$; Fuller & Myers 1993), which have been mapped by the H_2O Galactic Plane survey (HOPS; Walsh et al. 2011). HOPS has been successful in identifying previously unknown sites of star formation, as well as probing the structure of the Milky Way’s spiral arms.

Another, even higher density gas tracer useful for detecting HMSF and mapping the structure of our Galaxy is CS. The ground state transition $J = 1 \rightarrow 0$ for CS lies within the 7 mm waveband, and has an effective critical density $n_c = 4.6 \times 10^4 \text{ cm}^{-3}$ at 10 K (Evans 1999). Previous large scale observations towards specific regions, such as RCW 106 (Rodgers et al. 1960) for CS and other high-critical-density molecules have been productive in HMSF research (Lo et al. 2009). Untargeted observations of CS over bright infrared regions such as RCW 106 and regions without infrared emission reveal the full population of star-forming candidates to a small sensitivity limit.

The 7 mm waveband also contains the 44 GHz 7(0,7)–6(1,6) A^+ class I methanol maser line, which is the brightest of the class I species. Previous observations of the class I maser have almost always been targeted (e.g. Slysh et al. 1994; Voronkov et al. 2014), which limits and biases our understanding of this astrophysical phenomenon. The 7 mm waveband includes other spectral lines detailed in Table 3.1. To help develop our understanding of HMSF using the diagnostics in the 7 mm waveband, we have devised the MALT-45 untargeted Galactic plane survey.

In this paper, we focus on detailing the survey from $330^\circ \leq l \leq 335^\circ$, $b = \pm 0.5^\circ$ and present results of the global properties of CS (1–0), class I CH_3OH masers and SiO (1–0) thermal and maser emission. This paper is one of a series; another paper will be dedicated to

maser follow-up observations, and another for clump analysis with CS data. In this paper, we focus on comparing: CS emission to NH_3 and class I CH_3OH masers; class I CH_3OH masers to class II CH_3OH , H_2O and OH masers, thermal SiO and infrared emission, and 95 GHz class I CH_3OH masers; and SiO masers to infrared emission. We emphasise that the science cases presented in this paper are used primarily to highlight a few intriguing results and discuss some qualitatively plausible explanations. Full analyses for these cases will appear in future publications.

3.2 Survey Design

MALT-45 is an untargeted Galactic plane survey for spectral lines which are commonly bright in star-forming regions at 45 GHz (7 mm waveband). We have so far observed 5 square-degrees within the region bounded by $330^\circ \leq l \leq 335^\circ$, $b = \pm 0.5^\circ$. MALT-45 observations were conducted on the Australia Telescope Compact Array (ATCA), which provides 2×2048 MHz broadband continuum windows for observing. The rest frequencies of surveyed spectral lines dictate the positions of the broadband windows for MALT-45. Within the frequency ranges of the broadband windows, we survey for 12 spectral lines; see Table 3.1.

3.2.1 Australia Telescope Compact Array characterisation

The ATCA is an interferometer composed of six 22 m antennas, CA01 through CA06. In recent years, the ATCA correlator has been upgraded to the Compact Array Broadband Backend (CABB; Wilson et al. 2011), which now provides auto-correlation spectra. In addition to this upgrade, the ATCA obtained on-the-fly (OTF) mosaicing capabilities. We are particularly interested in the auto-correlations, as combining the six antennas in this way is similar to observing six times longer with an individual 22 m antenna such as Mopra. By using the ATCA auto-correlations for 7 mm surveying, we obtain an excellent metric on sensitivity versus survey speed. See Jordan et al. (2013) for pilot observations with MALT-45.

For the results presented here, only data from antennas CA01 through CA05 are presented. CA06 has a higher surface root-mean-square (RMS) and poorer sensitivity in the 7 mm wavelength range. In future observations, it may be possible to include CA06 data by weighting its contribution accordingly, but it is ignored at present.

Table 3.1: Bright spectral lines mapped by MALT-45 between 42.2 and 49.2 GHz. Column 1 lists the spectral line. Column 2 lists the rest frequency of the line. Column 3 lists the uncertainty of the rest frequency. Column 4 classifies the line as either a maser or thermal line. Column 5 gives the ATCA pointing beam size at this frequency. Column 6 indicates whether this line is discussed in this paper ('Y') or not ('N'). Columns 7 and 8 detail the local standard of rest velocity range covered by the CABB zoom band for this spectral line. Column 9 lists the median RMS noise level per spectral channel, with errors representing the standard deviation. The RMS noise is given to two significant figures. Radio recombination line (RRL) frequencies are taken from Lilley & Palmer (1968). All other rest frequencies are taken from the Cologne Database for Molecular Spectroscopy (CDMS; Müller et al. 2005). The velocity resolution ranges from 0.225 km s^{-1} (lowest rest frequency) to 0.195 km s^{-1} (highest rest frequency) per channel.

Spectral line	Frequency (GHz)	Uncertainty (kHz)	Maser or thermal?	Beam size (arcsec)	Detailed in this paper?	Velocity range		Median RMS noise level
						Min.	Max. (km s^{-1})	
SiO (1-0) $v = 3$	42.51934	1	Maser	66	Y	-287	167	$0.85 \pm 0.07 \text{ Jy}$
SiO (1-0) $v = 2$	42.82048	1	Maser	66	Y	-194	257	$0.82 \pm 0.06 \text{ Jy}$
H53 α (RRL)	42.95197		Thermal	65	N			
SiO (1-0) $v = 1$	43.12203	2	Maser	65	Y	-321	127	$0.83 \pm 0.06 \text{ Jy}$
SiO (1-0) $v = 0$	43.42376	2	Thermal	65	Y	-224	221	$27 \pm 1.7 \text{ mK}$
CH ₃ OH 7(0,7)-6(1,6) A ⁺	44.06941	10	Maser (Class I)	64	Y	-183	256	$0.90 \pm 0.09 \text{ Jy}$
H51 α (RRL)	48.15360		Thermal	58	N			
C ³⁴ S (1-0)	48.20694	2	Thermal	58	N			
CH ₃ OH 1 ₀₋₀ A ⁺	48.37246	0.7	Thermal	58	N			
CH ₃ OH 1 ₀₋₀ E	48.37689	10	Thermal	58	N			
OCS (4-3)	48.65160	1	Thermal	58	N			
CS (1-0)	48.99095	2	Thermal	57	Y	-157	237	$34 \pm 6.8 \text{ mK}$

3.2.1.1 CABB zoom modes

Chapter 2 discussed the CABB 64M-32k zoom mode configuration. These observations made use of this configuration, and each spectral line listed in Table 3.1 was observed with a 64M-32k zoom window (with the exception of the thermal $\text{CH}_3\text{OH } 1_0-0_0$ A⁺ and E lines, which are separated by 4 MHz and were simultaneously observed within one zoom), using a total of 11 zooms. The channel resolution at observed frequencies is approximately 0.2 km s^{-1} per channel. Each zoom window is ideally placed upon the spectral line centre frequency, although the exact placement depends on the way the correlator distributes the zooms. Every zoom provides approximately 400 km s^{-1} of velocity coverage, and is detailed in Table 3.1.

3.2.2 MALT-45 observations

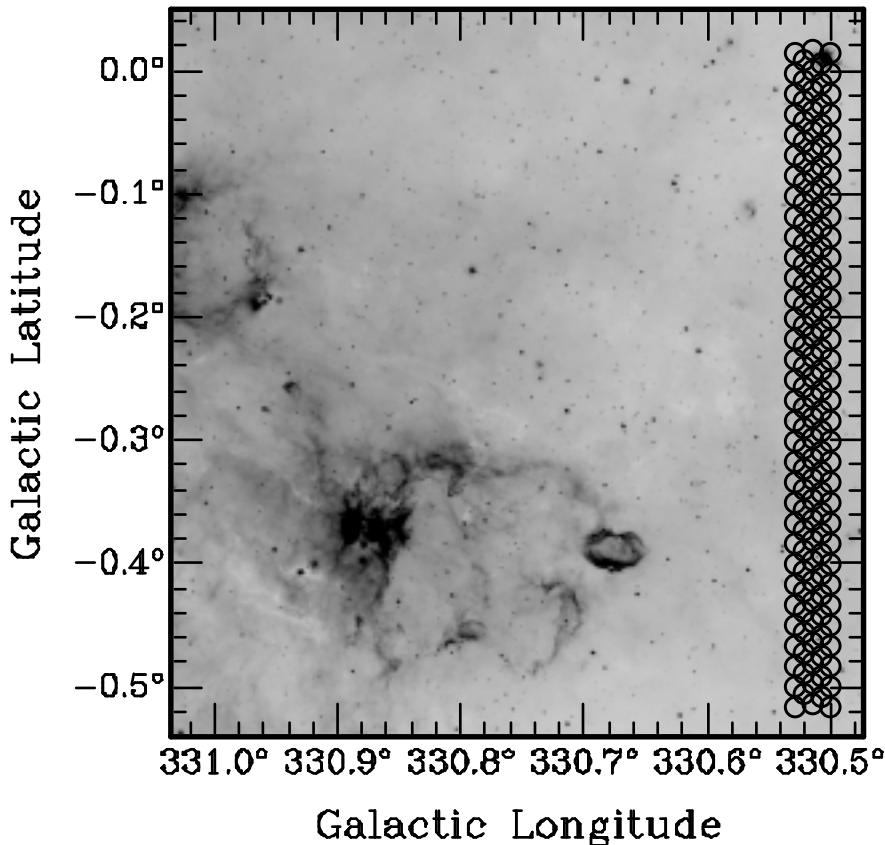


Figure 3.1: GLIMPSE $8.0 \mu\text{m}$ emission overlaid with part of a MALT-45 mosaic. Each circle represents the primary beam of the ATCA at 49.2 GHz, and is a pointing of the mosaic. Every quarter-square-degree region mapped by MALT-45 is built up of pointing ‘rows’ seen here. These five rows represent the start of the Galactic latitude scans for the G330.5–0.5 region. A similar mosaic is made for each region in Galactic longitude. When both Galactic latitude and longitude mosaics are combined, a fully Nyquist sampled map is obtained. Rows are classified as either ‘long’ or ‘short’; in this figure, the three long rows have two short rows interleaved.

The MALT-45 results presented here were observed over eight months on the ATCA. The first set of observations were conducted on 2012 September 21-23, 28 and 30, and October 1-13. The second set of observations were conducted from 2013 April 10-19. All observations

were conducted in the H214 array configuration. The region $330^\circ \leq l \leq 333^\circ$, $b = \pm 0.5^\circ$, and part of $333.0^\circ \leq l \leq 333.5^\circ$, $0^\circ \leq b \leq 0.5^\circ$ were surveyed in the first observing run. The remainder ($333^\circ \leq l \leq 335^\circ$, $b = \pm 0.5^\circ$) was completed during the second observing run. Weather conditions across all observations were generally good, with typical path noises below $300 \mu\text{m}$. Path noise is a measure of the weather quality, based on the phase delay between successive measurements of a geosynchronous satellite. Values above $500 \mu\text{m}$ are considered poor, but conditions only affect interferometric data.

All observations were conducted with the same surveying technique. Scans were observed in quarter-square-degree regions in Galactic coordinates, in both latitude and longitude directions. For both latitude and longitude scans, the mosaics are represented by ‘long’ and ‘short’ interleaved pointings. See Fig. 3.1 for an illustrative example. Within a mosaic row, consecutive pointing centres are separated by 1.045 beams, and centres of each mosaic row are separated by 0.45 beams. Each beam (pointing) is observed for 6 seconds in OTF mode observing. The frequency used to calculate the size of the primary beam is 49.2 GHz (the highest observed frequency), thus the beam used was 57.13 arcsec, and separation parameters are 59.7 and 25.7 arcsec, respectively. When combined, the scans provide a fully Nyquist sampled spatial map.

Each quarter square-degree region required approximately 14 hours observation time, including the typical setup and calibration. Pointing corrections were determined using PMN J1646–5044 and applied approximately every 70 minutes. The reference position G334.0–1.0 was observed every 45 minutes for calibration of the auto-correlation data. In addition, to allow interferometric calibration, bandpass calibration was derived from PKS B1253–055, phase calibration from PMN J1646–5044 and flux density from PKS 1934–63.

3.2.3 Data reduction

Data reduction was undertaken in a similar manner to that of the MALT-45 pilot survey (Jordan et al. 2013). Unlike the pilot survey data reduction, the LIVEDATA products were processed by more robust baselining using the ATNF Spectral line Analysis Package (ASAP). ASAP averages each of the antenna auto-correlations together before performing further baseline smoothing. ASAP then provides both XX and YY polarisation products, which are used by GRIDZILLA to create data cubes.

Flux density calibration was achieved with antenna efficiencies and T_B -to-Jy conversion factors taken from Urquhart et al. (2010). Using these values assumes that the 7 mm antenna and receiver response from Mopra is similar to the ATCA. Once the data cubes were gridded, the factors were applied to provide appropriate flux density scaling.

The average RMS noise levels were calculated for each data cube. The median values and their errors are listed in Table 3.1. Values are calculated by using the MIRIAD task IMSTAT, which determines RMS values for each channel in a cube. Error values represent the standard deviation of all RMS values. RMS noise maps may be seen in Appendix A.1, Figs 1 through 6.

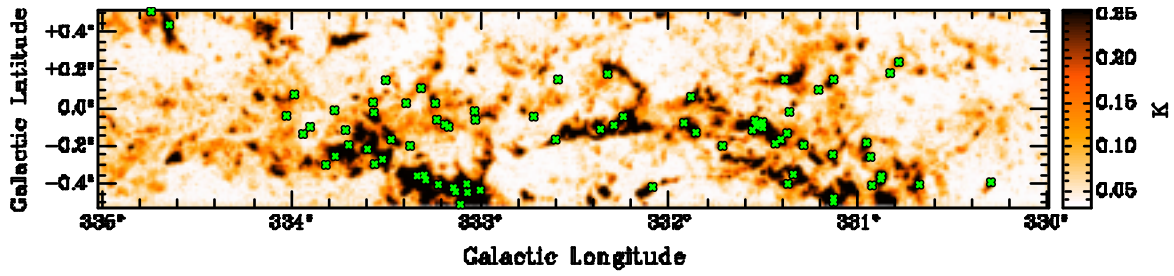


Figure 3.2: Auto-correlated CS (1–0) peak-intensity map overlaid with positions of detected class I CH₃OH masers (green cross symbols). A main-beam temperature of 0.1 K represents a 5σ peak of emission; note that the RMS of this image is less than that stated in Table 3.1 (20 mK vs. 34 mK), because this image has been produced by binning channels into groups of 10.

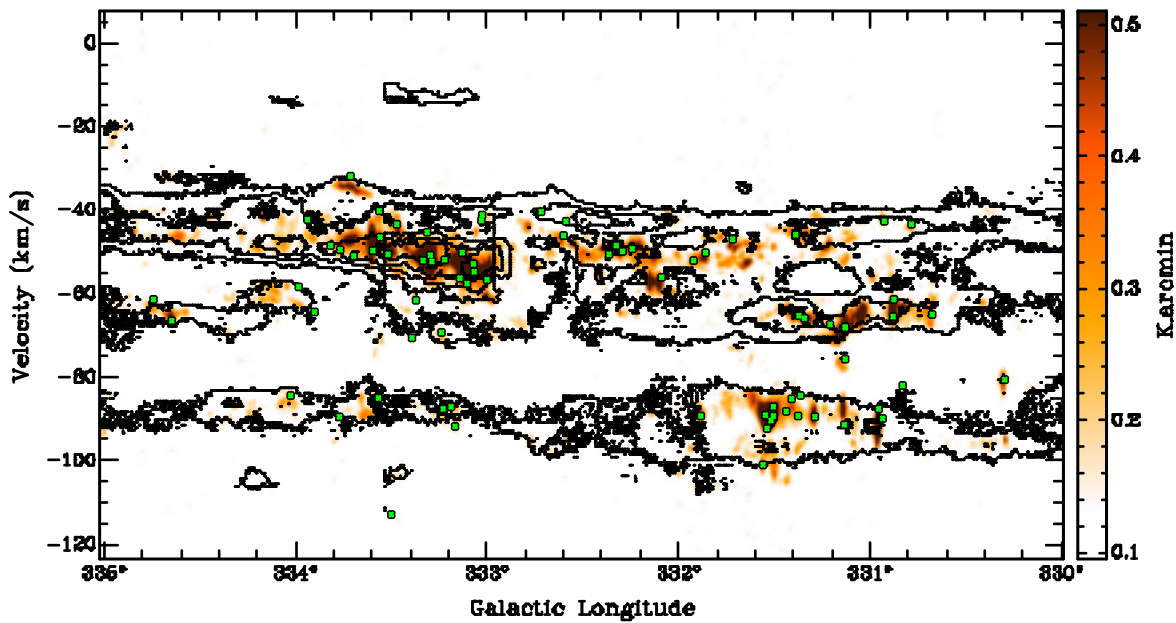


Figure 3.3: CS (1–0) from MALT-45 overlaid with CO contours from Barnes et al. (2015). Contour levels are 90, 180, ..., 450 K arcmin in units of main-beam temperature, integrated over Galactic latitude. There is excellent agreement in regions of concentrated CO with CS emission. Green cross symbols represent MALT-45 class I CH₃OH masers, which generally occur in bright regions of CS; only 4 of the CH₃OHno masers (5 per cent) have a CS peak intensity less than 0.11 K ($\sim 3\sigma$) at their peak position.

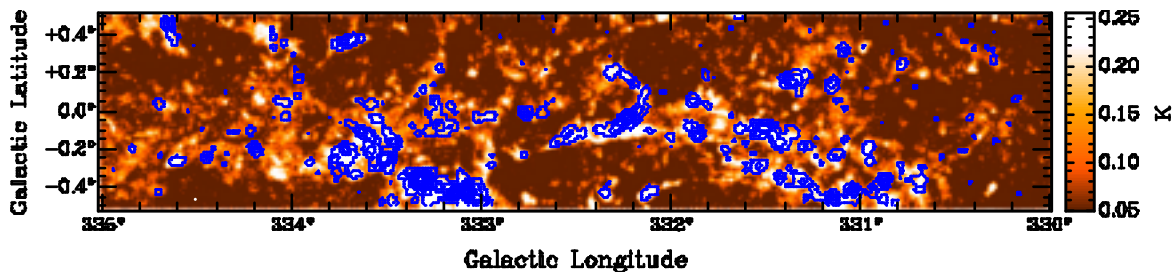


Figure 3.4: Auto-correlated CS (1–0) peak-intensity map overlaid with HOPS NH₃ (1,1) peak-signal-to-noise contours. Contour levels are 8, 18, ..., 88 per cent of 11.13 K in units of main-beam temperature. The white circle seen at G334.5–0.45 is the size of the beam.

3.3 Results

For this paper, auto-correlated data cubes were produced for CS (1–0), class I CH₃OH masers, each of the SiO (1–0) $v = 1, 2, 3$ maser lines and SiO (1–0) $v = 0$ thermal emission. Emission was detected in each data cube. The absolute scale of intensity calibration is not well established, and can be affected by systematic effects such as the bandpass subtraction. However, comparing the peak flux densities of MALT-45 class I methanol masers with Voronkov et al. (2014), we ascribe 20 per cent as the uncertainty of the intensities in MALT-45 data.

The positions of class I methanol masers from MALT-45 and Voronkov et al. (2014) were compared to derive a survey astrometric error. The median RMS offset was determined by deriving the offset for each maser site in Voronkov et al. (2014) and the MALT-45 position. This median is 15 arcsec, and so we ascribe a 15 arcsec astrometric error to MALT-45.

3.3.1 CS (1–0) at 48.990 GHz

The most abundant isotopologue of CS (¹²C³²S) was detected in extended emission across the entire survey region, as shown in Figs 3.2, 3.3 and 3.4. Also shown in Fig. 3.4 is NH₃ (1,1) emission, as detected in HOPS (Purcell et al. 2012). Bright CS emission is largely coincident with HOPS NH₃ (1,1) emission, but despite having a higher critical density, the CS appears to be more extended than the NH₃; this is discussed further in §3.4.1. A longitude-velocity-latitude plot reveals a few velocity components to the CS data, which trace the spiral arms of the Galaxy over the survey region; see Fig. 3.3.

C³⁴S (1–0) at 48.20694 GHz is also detected across the survey region, but is not detailed in this paper due to an incomplete data reduction. However, a preliminary reduction has been conducted for analysis in §3.4.1. C³⁴S data will be presented in future publications.

3.3.2 Class I CH₃OH 7(0,7)–6(1,6) A⁺ masers at 44.069 GHz

Within the survey region, 77 class I CH₃OH masers were detected. Class I CH₃OH maser catalogues from Slysh et al. (1994); Val'tts et al. (2000); Ellingsen (2005) and Chen et al. (2011) were used to determine previously known masers. All 19 previously known masers were detected by MALT-45. Note that these articles report findings of 95 GHz class I CH₃OH masers, rather than 44 GHz masers (except Slysh et al. 1994); if a 44 GHz maser has not been reported in a position where a 95 GHz maser has been detected, we still deem this class I maser as a previously known detection. Therefore, 58 of the 77 detections are previously unknown (hereinafter new masers). A histogram of these populations can be seen in Fig. 3.5, revealing the number of new masers for various peak flux densities. Images showing the locations of class I CH₃OH masers with respect to thermal molecular gas are shown in Figs 3.2, 3.3 and 3.6. The properties of each class I maser spectrum is classified in Table 3.2. Each un-smoothed maser spectrum can be seen in Appendix A.2, and a peak signal-to-noise map is presented in Appendix A.3.

Masers were identified by visual inspection of the data by analysing various binned versions of the cube, such as 0.4, 0.6, 0.8, 1.0 and 2.0 km s⁻¹ bins. This is effective at highlighting weak but broad maser emission; see for example G330.83+0.18 in Appendix A.2. Any peak of emission exceeding 3σ in the various binned cubes with at least two adjacent channels

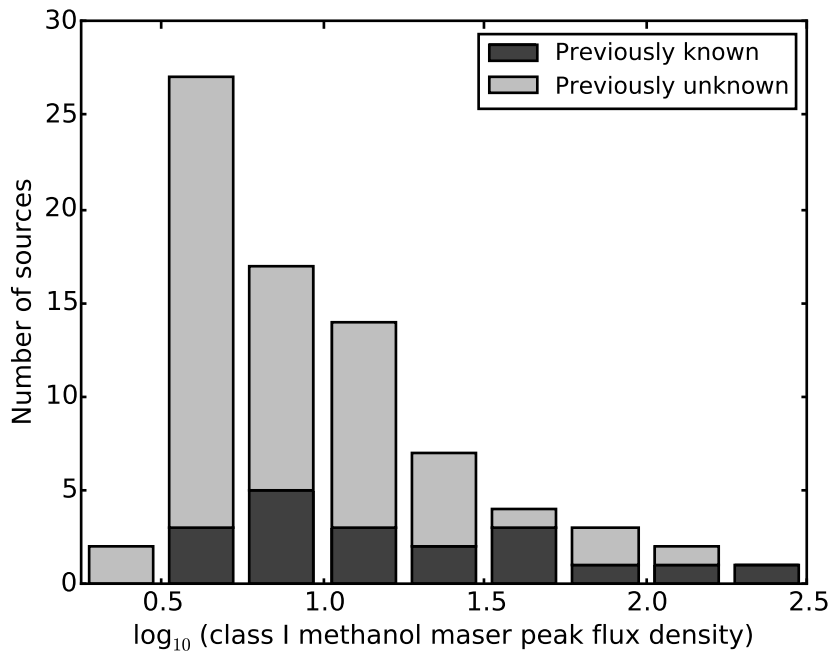


Figure 3.5: A stacked histogram of known and new class I CH₃OH maser peak flux densities. Previously known masers have a near even spread of flux densities, but the new MALT-45 population favours the weaker bins.

of 2σ was considered for candidacy. The position of each maser reflects the brightest pixel within the neighbourhood of bright maser pixels. We compared the velocity of weaker maser candidates with CS and SiO $v = 0$ emission at the same location to strengthen their candidacy. In future work, we will re-observe each maser candidate to greater sensitivity and spatial resolution to confirm (or otherwise) its existence. The velocity range of each maser is determined by a 1.5σ cutoff in intensity from the peak velocity. As the channel resolution is approximately 0.2 km s^{-1} , velocities are specified to 0.1 km s^{-1} . All flux densities are specified with two significant figures. Intrinsic variation of masers along with calibration uncertainties place peak flux density errors within 20 per cent.

Using the program supplied by Reid et al. (2009), kinematic distances have been calculated and are included for each maser in Table 3.2. Parameters used for determining revised velocities and kinematic distances were taken from Green & McClure-Griffiths (2011), and the V_{LSR} uncertainty from Voronkov et al. (2014): $\Theta_0 = 246 \text{ km s}^{-1}$, $R_\odot = 8.4 \text{ kpc}$, $U_\odot = 11.1 \text{ km s}^{-1}$, $V_\odot = 12.2 \text{ km s}^{-1}$, $W_\odot = 7.25 \text{ km s}^{-1}$, $U_s = 0 \text{ km s}^{-1}$, $V_s = -15.0 \text{ km s}^{-1}$, $W_s = 0 \text{ km s}^{-1}$, $\sigma(V_{LSR}) = 3.32 \text{ km s}^{-1}$. All distances are assumed to be kinematically ‘near’, unless the distance prescribed by Green & McClure-Griffiths (2011) is ‘far’.

Table 3.2: Properties of detected MALT-45 class I CH₃OH maser emission. Each maser was detected within a 64 MHz zoom window. Column 1 lists the source name, derived from Galactic coordinates of the brightest peak. Columns 2 and 3 give the coordinates of the maser. Column 4 lists the source peak flux density. Column 5 lists the RMS noise level of the peak. Columns 6 and 7 list the velocity range of maser emission, within a 1.5 σ cutoff. Column 8 lists the velocity at the peak. Column 9 lists kinematic distance calculated, based on position and peak velocity. Columns 10 and 11 list the errors for the kinematic distance. Columns 12 and 13 list the integrated intensity of CS (1–0) and SiO (1–0) $v = 0$ at the brightest peak. Column 14 gives additional remarks, mentioned in the footnotes^a. Column 15 lists associations with other masers and EGOs, and is detailed in the footnotes^b. Association is credited for any presence within 60 arcsec of the class I CH₃OH maser peak position. All velocities are specified to 0.1 km s⁻¹, and all flux densities are specified to two significant figures. Kinematic distances are derived using the kinematic distance model of Reid et al. (2009). All distances are assumed to be kinematically ‘near’, unless labelled otherwise.

Source name	RA (J2000) (h m s)	Dec. (J2000) ($^{\circ}$ $'$ $''$)	Peak flux density (Jy)	RMS noise level	Velocity (km s ⁻¹)		Kinematic distance (kpc)	Distance error (kpc)	Integrated intensity (K km s ⁻¹)		Remarks ^a	Other masers and EGOs ^b
					Min.	Max.			CS	SiO		
G330.30–0.39	16 07 37.8	-52 30 52.1	4.4	4.9	-80.8	-79.5	4.90	0.16	-0.16	3.1		W
G330.67–0.40	16 09 31.2	-52 16 03.9	5.3	5.6	-65.9	-64.6	4.16	0.15	-0.15	2.5		
G330.78+0.24	16 07 12.8	-51 43 03.4	3.7	4.3	-43.8	-43.1	3.12	0.17	-0.17	1.2		
G330.83+0.18	16 07 41.1	-51 43 48.0	3.1	3.8	-82.3	-79.7	4.95	0.16	-0.16			
G330.87–0.36	16 10 16.6	-52 05 54.3	10	15	-67.0	-58.0	4.00	0.15	-0.16	8.0	0.42	C
G330.88–0.38	16 10 22.3	-52 06 28.1	7.8	10	-67.4	-58.0	4.19	0.15	-0.15	8.6	0.56	C
G330.92–0.41	16 10 44.3	-52 06 04.0	28	33	-44.0	-41.0	3.09	0.17	-0.17	1.4		MWSCG
G330.93–0.26	16 10 06.9	-51 59 07.3	5.0	5.9	-91.4	-89.3	5.33	0.17	-0.16	1.4		
G330.95–0.18	16 09 53.1	-51 54 57.9	4.0	4.7	-94.8	-86.7	5.21	0.16	-0.16	9.6	1.4	MWCG
G331.13–0.48	16 12 00.3	-52 00 38.5	5.6	7.5	-69.1	-66.7	4.30	0.15	-0.15	5.3	0.15	
G331.13–0.50	16 12 05.9	-52 01 33.3	8.6	11	-68.7	-67.8	4.31	0.15	-0.15	4.5		
G331.13–0.25	16 11 00.7	-51 50 24.8	71	88	-92.9	-82.5	5.39	0.17	-0.16	4.4	0.49	SVE
G331.13+0.15	16 09 15.5	-51 33 08.1	68	60	-79.1	-74.6	4.65	0.15	-0.15	1.2		MWCG MW
G331.21+0.10	16 09 52.2	-51 32 18.6	3.5	3.3	-67.8	-67.0	4.27	0.15	-0.15			
G331.29–0.20	16 11 31.3	-51 41 54.8	15	20	-95.7	-85.0	5.29	0.16	-0.16	3.7	0.17	MWC
G331.34–0.35	16 12 27.4	-51 46 26.9	32	37	-67.2	-65.0	4.21	0.15	-0.15	2.1		MWCG
G331.36–0.02	16 11 06.4	-51 31 09.7	4.7	5.8	-84.6	-84.2	5.05	0.16	-0.15			
G331.37–0.40	16 12 48.9	-51 47 26.2	5.9	7.3	-65.9	-65.0	4.18	0.15	-0.15	1.6		G
G331.37–0.13	16 11 39.5	-51 35 35.3	3.7	4.5	-89.5	-88.8	5.28	0.16	-0.16	1.6		
G331.39+0.15	16 10 28.7	-51 22 37.6	6.5	5.8	-46.5	-45.5	3.26	0.16	-0.17	2.5	0.19	
G331.41–0.17	16 11 57.8	-51 35 40.6	4.9	6.6	-86.3	-84.8	5.08	0.16	-0.15	2.7		
G331.44–0.19	16 12 11.4	-51 35 24.1	14	18	-92.5	-86.3	9.53	0.16	-0.16	2.3	0.25	VF
G331.50–0.08	16 12 00.6	-51 27 44.3	38	49	-92.7	-86.7	5.27	0.16	-0.16	4.1	0.14	P3
G331.50–0.10	16 12 08.2	-51 29 01.0	11	14	-101.8	-86.1	5.17	0.16	-0.15	6.5	0.31	WSC
G331.52–0.08	16 12 06.3	-51 27 35.5	20	18	-94.0	-88.0	5.33	0.16	-0.16	5.8	0.13	P1
G331.54–0.10	16 12 15.4	-51 27 17.1	77	77	-94.2	-89.1	5.42	0.17	-0.16	7.4	0.29	P2
G331.55–0.07	16 12 10.1	-51 25 39.9	4.9	5.3	-92.9	-86.3	5.26	0.16	-0.16	4.9	0.15	MC

Table 3.2: *continued*

Source name	RA (J2000) (h m s)	Dec. (J2000) ($^{\circ}$ $'$ $''$)	Peak flux density (Jy)	RMS noise level	Velocity (km s $^{-1}$)		Kinematic distance (kpc)	Distance error (kpc)	Integrated intensity (K km s $^{-1}$)		Remarks ^a	Other masers and EGOs ^b
					Min.	Max.			CS	SiO		
G331.56-0.12	16 12 26.8	-51 27 20.4	14	16	-104.8	-98.2	5.87	0.19	2.9	0.18		MWC
G331.72-0.20	16 13 33.1	-51 24 28.0	4.1	3.8	-47.2	-46.8	3.32	0.16	-0.17	2.0		
G331.86-0.13	16 13 54.0	-51 15 32.1	5.6	6.5	-51.4	-49.5	3.48	0.16	-0.16	2.6	0.44	
G331.88+0.06	16 13 11.6	-51 06 19.8	10	13	-90.1	-85.9	5.26	0.16	-0.15	2.4	0.45	
G331.92-0.08	16 13 58.2	-51 10 46.7	5.8	6.4	-52.7	-51.6	3.57	0.16	-0.16	1.5		MW
G332.09-0.42	16 16 13.7	-51 18 30.7	17	21	-59.5	-55.5	3.76	0.15	-0.16	3.6		
G332.24-0.05	16 15 18.1	-50 56 03.2	140	180	-51.2	-45.9	3.44	0.16	-0.16	3.4	0.32	
G332.30-0.09	16 15 43.9	-50 55 57.8	41	37	-52.5	-49.9	3.47	0.16	-0.16	3.0		VE
G332.32+0.18	16 14 42.0	-50 42 50.2	9.3	11	-51.0	-48.0	3.40	0.16	-0.16	1.2		W
G332.36-0.11	16 16 08.8	-50 53 55.2	9.8	12	-51.2	-49.9	3.51	0.16	-0.16	1.7		MWCG
G332.59+0.15	16 16 01.3	-50 33 12.6	3.4	4.0	-43.6	-42.5	11.79	0.17	-0.17			MG
G332.60-0.17	16 17 28.1	-50 46 21.2	15	18	-47.6	-45.5	3.29	0.16	-0.17	2.2		MWCG
G332.72-0.05	16 17 27.9	-50 36 16.5	6.4	7.3	-41.0	-39.1	3.01	0.17	-0.17			
G333.00-0.43	16 20 27.1	-50 40 58.3	6.6	9.8	-57.2	-56.1	3.80	0.15	-0.15	4.8		W
G333.02-0.06	16 18 55.5	-50 24 04.3	6.8	7.9	-41.7	-39.7	3.06	0.17	-0.17	1.2		MW
G333.03-0.02	16 18 44.6	-50 21 56.0	5.6	7.0	-42.9	-42.1	3.12	0.17	-0.17			M
G333.07-0.44	16 20 48.4	-50 38 41.3	2.7	3.2	-55.3	-54.8	3.72	0.15	-0.16	6.5	0.20	MW
G333.07-0.40	16 20 37.3	-50 36 33.5	4.1	4.6	-54.4	-52.7	3.63	0.15	-0.16	4.2	0.21	
G333.10-0.51	16 21 15.1	-50 39 45.6	14	8.1	-58.9	-57.0	3.85	0.15	-0.15	4.2		M
G333.13-0.44	16 21 04.0	-50 35 52.0	120	150	-57.2	-45.5	3.50	0.16	-0.16	11	0.64	MWC
G333.14-0.42	16 21 01.8	-50 34 27.1	16	18	-56.7	-45.9	3.79	0.15	-0.15	10	0.51	W
G333.16-0.10	16 19 43.4	-50 19 43.0	5.6	7.7	-92.9	-91.2	5.33	0.15	-0.14	1.3		M
G333.18-0.09	16 19 45.7	-50 18 18.3	5.6	7.1	-88.4	-85.7	5.13	0.14	-0.14	1.7		MG
G333.22-0.40	16 21 18.6	-50 30 23.5	17	19	-55.3	-51.0	3.59	0.15	-0.16	2.7		MWSC
G333.23-0.06	16 19 50.3	-50 15 28.9	250	310	-92.3	-84.4	5.15	0.14	-0.14	1.0	0.25	
G333.24+0.02	16 19 29.5	-50 11 23.5	3.9	5.4	-69.5	-67.8	4.37	0.14	-0.14	1.4		
G333.29-0.38	16 21 29.7	-50 26 30.3	5.4	6.3	-53.6	-50.6	3.61	0.15	-0.16	11	0.27	
G333.30-0.35	16 21 25.3	-50 25 05.4	3.5	3.6	-53.1	-49.5	3.54	0.16	-0.16	9.8	0.18	
G333.31+0.10	16 19 28.7	-50 04 50.9	7.7	13	-50.6	-43.8	11.74	0.17	-0.16	2.1	0.12	MWG
G333.33-0.36	16 21 36.4	-50 23 40.6	22	22	-53.8	-49.5	3.60	0.15	-0.16	6.0	0.27	
G333.37-0.20	16 21 04.4	-50 15 21.6	13	16	-62.3	-57.6	4.03	0.15	-0.15			W
G333.39+0.02	16 20 10.6	-50 04 53.7	4.1	6.5	-72.9	-69.7	10.60	0.14	-0.14			W
G333.47-0.16	16 21 22.1	-50 09 42.5	21	23	-46.1	-41.4	3.18	0.16	-0.17	3.6		MWC
G333.50+0.15	16 20 07.6	-49 55 10.1	3.5	5.9	-114.4	-112.0	6.35	0.21	-0.19			MWCG
G333.52-0.27	16 22 01.9	-50 12 11.2	6.4	8.7	-51.2	-50.2	3.53	0.16	-0.16	3.5		
G333.56-0.30	16 22 19.6	-50 11 28.6	7.8	11	-48.0	-45.9	3.33	0.16	-0.17	2.4		
G333.56-0.02	16 21 09.0	-49 59 48.3	54	63	-41.7	-39.1	12.02	0.17	-0.17	1.8		M

Table 3.2: *continued*

Source name	RA (J2000) (h m s)	Dec. (J2000) ($^{\circ}$ ' '')	Peak flux density (Jy)	RMS noise level	Velocity (km s $^{-1}$)		Kinematic distance (kpc)	Distance error (kpc)	Integrated intensity (K kms $^{-1}$)		Remarks ^a	Other masers and EGOs ^b	
					Min.	Max.			CS	SiO			
G333.57+0.03	16 20 55.9	-49 57 19.4	6.2	6.4	-85.7	-84.8	5.04	0.14	0.14	0.95			
G333.59-0.21	16 22 08.5	-50 06 31.7	26	34	-51.2	-47.6	3.49	0.16	-0.16	11	0.31	SV	WSC
G333.70-0.20	16 22 29.4	-50 01 23.8	4.4	6.1	-51.2	-50.8	3.55	0.16	-0.16	2.4			
G333.71-0.12	16 22 12.8	-49 57 20.1	6.6	6.9	-32.3	-31.2	2.58	0.18	-0.19				
G333.77-0.01	16 22 00.7	-49 50 26.5	16	20	-90.5	-88.8	5.22	0.14	-0.14	2.3			
G333.77-0.25	16 23 03.5	-50 00 51.0	6.4	8.0	-50.2	-49.3	3.49	0.16	-0.16	2.4	0.12		
G333.82-0.30	16 23 28.8	-50 00 39.2	19	24	-49.5	-47.8	3.44	0.16	-0.16	1.3			
G333.90-0.10	16 22 57.7	-49 48 39.2	3.4	4.1	-65.3	-62.9	10.92	0.15	-0.14			F	M
G333.94-0.14	16 23 17.4	-49 48 38.4	4.6	4.9	-43.1	-42.3	3.14	0.17	-0.17				MW
G333.98+0.07	16 22 34.6	-49 37 52.8	4.5	5.7	-60.8	-58.0	3.90	0.15	-0.15				
G334.03-0.04	16 23 15.0	-49 40 51.7	11	14	-84.8	-84.0	5.01	0.14	-0.14	2.0			
G334.64+0.44	16 23 50.4	-48 54 08.7	5.7	6.4	-67.2	-66.5	4.27	0.14	-0.14	2.2			
G334.74+0.51	16 23 56.6	-48 47 03.7	18	6.7	-65.5	-61.4	4.05	0.14	-0.15	1.1	0.17		

^aS - 44 GHz detection from Slysh et al. (1994); V - 95 GHz detection from Val'tts et al. (2000); E - 95 GHz detection from Ellingsen (2005); C - 95 GHz detection from Chen et al. (2011); P - indicates a blended spectrum of emission. P1 contains a strong peak of emission at a spatially distinct position, with a different velocity to nearby strong masers (but not as strong as the neighbour), P2 is the strong neighbour, and P3 is the next strongest neighbour; F - this maser has been labelled as being kinematically 'far', due to a class II CH₃OH maser being labeled as such by Green & McClure-Griffiths (2011). Note that a source without a S, V, E or C remark is a new detection.

^bM - presence of a 6.7 GHz class II methanol maser (Caswell et al. 2011); W - presence of a 22 GHz H₂O maser (Walsh et al. 2011, 2014; Breen et al. 2010a); G - presence of an EGO classified by Cyganowski et al. (2008); S - presence of a 1612 OH maser (Sevenster et al. 1997); C - presence of a 1665 or 1667 MHz OH maser (Caswell 1998).

Table 3.3: Properties of detected MALT-45 SiO (1–0) maser emission. Each maser was detected within a 64 MHz zoom window. Column 1 lists the source name, derived from Galactic coordinates of the brightest peak. Columns 2 and 3 give the coordinates of the maser. Columns 4 through 15 are categorised into $v = 1$, $v = 2$ and $v = 3$. For each category, there are four columns, listing the peak flux density within this vibrational mode (if detected), and the minimum, maximum and peak velocities. Column 16 lists the RMS noise level, which indicates the most statistically significant maser peak detected among the three modes. Column 17 lists the kinematic distance calculated, based on position and peak velocity. Columns 18 and 19 list the errors for the kinematic distance. Column 20 gives additional remarks, clarified in the footnotes^a. If data are not available in one of the lines for a source, it was not detected by MALT-45. Velocity ranges (between minimum and maximum) are determined by a 1.5σ cutoff. All velocities are specified to 0.1 km s^{-1} , and all flux densities are specified to two significant figures. Association is credited if the source position is within 30 arcsec of the peak SiO maser position. Kinematic distances are derived using the kinematic distance model of Reid et al. (2009). All distances are assumed to be kinematically ‘near’, except for G330.14–0.39, G331.08+0.17, G332.40–0.33 and G334.20+0.22; when assumed to be near, unphysical distances and errors are generated.

Source name	RA (J2000) (h m s)	Dec. (J2000) ($^{\circ}$ ' ")	SiO $v = 1$ properties				SiO $v = 2$ properties				SiO $v = 3$ properties				RMS noise level	Kinematic distance (kpc)	Distance error (kpc)	Remarks ^a	
			Peak flux density (Jy)	Min. (km s ⁻¹)	Max. (km s ⁻¹)	Peak velocity (km s ⁻¹)	Peak flux density (Jy)	Min. (km s ⁻¹)	Max. (km s ⁻¹)	Peak velocity (km s ⁻¹)	Peak flux density (Jy)	Min. (km s ⁻¹)	Max. (km s ⁻¹)	Peak velocity (km s ⁻¹)					
G330.12–0.31	16 06 24.3	-52 34 33.5	6.3	-2.6	4.5	-53.7	7.5	-65.8	-61.2	-61.4	3.5	-59.7	-51.6	5.5	3.6	3.46	0.23	-0.23	
G330.14+0.39	16 06 52.6	-52 37 04.9	23	-59.5	-48.3	-53.7	13	-3.0	5.5	3.6	5.5	-59.7	-51.6	-54.4	2.5	5.05	0.45	-0.41	W
G330.47+0.03	16 06 36.7	-52 05 15.6	11	-13.7	-9.8	-12.2	19	-15.5	-10.2	-12.8	19	-15.5	-10.2	-17.8	26	3.12	0.24	-0.24	W
G330.51+0.01	16 06 53.2	-52 04 19.6	4.0	-68.7	-67.8	-68.0	2.7	-69.7	-68	-69.3	4.9	-69.7	-68	-69.3	3.80	0.76	0.34	-0.36	
G330.55+0.15	16 06 28.1	-51 56 41.6	2.9	-66.1	-65.2	-65.8	2.7	-69.7	-67.1	-69.3	2.7	-69.7	-68	-69.3	3.8	3.80	0.22	-0.23	
G330.75+0.20	16 07 15.2	-51 46 25.6	4.9	-32.0	-30.7	-31.7	3.4	-32.0	-30.7	-31.7	3.4	-32.0	-30.7	-31.7	3.8	3.63	0.22	-0.23	
G330.85+0.44	16 10 29.3	-52 10 34.9	3.4	-6.1	-3.9	-5.2	4.9	-6.1	-3.9	-5.2	3.8	-6.9	-3.7	-5.8	4.3	1.98	0.28	-0.29	W
G331.08+0.17	16 08 55.8	-51 34 14.6	4.6	-31.5	-30.0	-30.7	4.7	-32.1	-30.3	-31.0	3.0	-32.1	-30.3	-31.0	7.7	4.45	0.40	-0.37	
G331.13–0.27	16 11 06.2	-51 51 19.7	2.9	-36.7	-34.6	-36.1	3.0	-37.1	-36.0	-36.3	5.7	-69.7	-62.9	-68.4	4.4	1.94	0.28	-0.29	
G331.21+0.25	16 09 10.8	-51 25 19.1	2.7	-90.0	-89.1	-89.1	2.9	-90.0	-89.1	-89.1	3.0	-37.1	-36.0	-36.3	4.4	2.24	0.27	-0.28	
G331.24–0.02	16 10 32.2	-51 36 05.6	7.0	-69.5	-66.3	-68.0	2.7	-69.7	-68.0	-68.4	5.7	-69.7	-62.9	-68.4	3.2	4.69	0.22	-0.21	
G331.48–0.03	16 11 43.7	-51 26 46.0	2.8	-33.7	-32.4	-32.8	2.7	-33.7	-32.4	-32.8	7.8	-97.3	-94.0	-96.0	9.1	3.80	0.22	-0.22	
G331.58+0.07	16 11 44.5	-51 18 06.2	2.7	-96.5	-93.9	-95.6	2.8	-96.5	-93.9	-95.6	7.8	-97.3	-94.0	-96.0	3.4	2.06	0.28	-0.29	
G331.60–0.14	16 12 42.8	-51 26 42.7	4.4	-38.3	-34.8	-36.5	3.5	-39.1	-35.4	-36.5	3.5	-39.1	-35.4	-36.5	5.7	2.27	0.27	-0.28	CS
G331.65–0.25	16 13 28.8	-51 29 34.6	4.4	-26.1	-25.2	-25.4	3.1	-26.1	-25.2	-25.4	1.7	-25.5	-24.7	-25.3	3.6	1.63	0.30	-0.31	S
G331.70–0.03	16 12 43.5	-51 17 20.4	4.2	-18.9	21.1	-20.0	4.2	-18.9	21.1	-20.0	2.4	-34.1	-24.2	-29.7	4.9	6.97	0.62	-0.57	S
G331.72+0.45	16 10 43.2	-50 55 38.7	2.8	-36.1	-23.9	-29.1	2.4	-34.1	-24.2	-29.7	2.5	-99.7	-102.5	-99.7	4.0	1.79	0.29	-0.30	W
G331.76–0.33	16 14 19.0	-51 28 22.3	2.8	-102.8	-98.4	-101.9	2.5	-99.7	-102.5	-99.7	2.5	-99.7	-102.5	-99.7	3.6	3.6	0.22	-0.21	W
G331.95+0.08	16 13 23.5	-51 02 50.8	2.8	-81.5	-80.2	-80.8	3.0	-81.5	-80.2	-80.8	2.8	-98.2	-98.6	-98.2	3.9	5.19	0.22	-0.21	W
G331.96–0.24	16 14 52.6	-51 16 07.2	2.9	-99.1	-97.1	-98.0	2.8	-98.2	-98.6	-98.2	2.8	-98.2	-98.6	-98.2	3.9	4.35	0.21	-0.21	
G331.99–0.04	16 14 05.7	-51 06 12.7	2.9	-36.7	-35.2	-36.5	5.1	-36.7	-35.2	-36.5	2.8	-98.2	-98.6	-98.2	3.9	5.07	0.21	-0.21	
G332.14–0.51	16 16 52.0	-50 20 23.1	3.4	-121.2	-120.6	-121.0	3.4	-121.2	-120.6	-121.0	2.8	-98.2	-98.6	-98.2	4.5	2.28	0.27	-0.28	
G332.22+0.36	16 13 25.5	-50 39 30.7	6.2	-56.3	-54.1	-55.4	6.2	-56.3	-54.1	-55.4	2.1	-122.2	-122.7	-122.2	4.4	6.17	0.32	-0.27	
G332.30+0.44	16 13 27.9	-50 32 16.3	4.1	-145.1	-144.7	-144.9	4.1	-145.1	-144.7	-144.9	3.6	-56.4	-54.4	-55.3	8.4	3.24	0.23	-0.24	
G332.40–0.33	16 17 16.5	-51 01 21.2	4.8	-34.3	-31.7	-33.7	4.8	-34.3	-31.7	-33.7	2.7	-7.4	-5.0	-5.6	3.8	4.61	0.41	-0.38	
G332.83+0.19	16 16 57.1	-50 21 10.2	2.2	-102.1	-99.7	-101.0	2.2	-102.1	-99.7	-101.0	3.4	-101.7	-102.5	-101.7	5.1	2.15	0.27	-0.29	
G332.90–0.37	16 19 14.3	-50 42 31.2	4.4	-48.9	-43.3	-45.4	4.4	-48.9	-43.3	-45.4	3.4	-101.7	-102.5	-101.7	4.9	5.20	0.21	-0.20	
G333.06–0.10	16 19 14.4	-50 24 16.6	4.3	-96.9	-95.4	-96.3	4.3	-96.9	-95.4	-96.3	6.8	-48.5	-43.7	-45.7	9.5	2.79	0.25	-0.26	W
G333.44–0.07	16 20 49.1	-50 06 52.0	3.3	-63.0	-61.5	-63.0	3.3	-63.0	-61.5	-63.0	2.7	-97.1	-98.6	-97.1	4.2	5.00	0.20	-0.20	
G333.46–0.34	16 22 06.3	-50 17 29.4	4.3	-145.1	-144.7	-144.9	4.3	-145.1	-144.7	-144.9	4.3	-64.7	-58.6	-64.3	5.4	3.55	0.22	-0.23	
G333.53+0.41	16 19 06.9	-49 42 21.9	3.3	-16.1	-15.0	-15.7	3.3	-16.1	-15.0	-15.7	3.0	-16.3	-15.7	-15.9	4.0	7.52	0.77	-0.77	
G333.60–0.49	16 23 21.6	-50 18 09.7	4.1	-70.6	-67.8	-69.5	4.1	-70.6	-67.8	-69.5	3.0	-16.3	-15.7	-15.9	4.8	1.06	0.34	-0.36	W
G333.64–0.37	16 22 59.3	-50 11 06.3	4.1	-70.6	-67.8	-69.5	4.1	-70.6	-67.8	-69.5	4.5	-70.8	-69.1	-70.2	6.3	3.93	0.21	-0.21	

Table 3.3: *continued*

Source name	RA (J2000) (h m s)	Dec. (J2000) ($^{\circ}$ ' ")	SIO $v = 1$ properties			SIO $v = 2$ properties			SIO $v = 3$ properties			RMS noise level	Kinematic distance (kpc)	Distance error (kpc)	Remarks ^a
			Peak flux density (Jy)	Min. (km s ⁻¹)	Max. (km s ⁻¹)	Peak flux density (Jy)	Min. (km s ⁻¹)	Max. (km s ⁻¹)	Peak flux density (Jy)	Min. (km s ⁻¹)	Max. (km s ⁻¹)				
G333.72-0.39	16 23 25.8	-50 08 36.6	5.2	-44.3	-40.4	-43.3	5.0	-45.7	-41.5	-43.5	7.1	2.71	0.25	-0.26	
G333.78-0.36	16 23 35.6	-50 04 53.2	2.1	-93.4	-92.1	-92.4	1.6	-93.1	-92.7	-92.9	3.1	4.85	0.20	-0.20	
G333.90-0.09	16 22 56.6	-49 48 07.4	3.8	-126.0	-123.2	-123.9	4.0	-123.8	-122.9	-123.1	4.5	6.12	0.26	-0.23	S
G334.01-0.02	16 23 06.3	-49 40 30.9	3.3	-94.3	-93.0	-93.4	3.3	-95.5	-93.6	-93.8	3.9	4.89	0.19	-0.19	
G334.11-0.37	16 25 05.0	-49 50 58.6	3.9	-32.8	-30.9	-31.5					4.7	2.08	0.28	-0.30	
G334.20+0.22	16 22 49.6	-49 22 18.8	2.7	-7.4	-7.0	-7.2	2.8	-5.2	-7.4	-5.2	4.4	4.78	0.42	-0.39	
G334.35-0.36	16 26 03.3	-49 40 15.0	3.2	-22.8	-21.5	-22.6					4.1	1.54	0.31	-0.33	
G334.35+0.06	16 24 13.2	-49 22 24.8	3.8	-82.6	-81.9	-82.1					3.8	4.44	0.20	-0.20	
G334.41+0.22	16 23 44.6	-49 13 15.1	3.9	-32.8	-31.7	-32.2					4.7	2.13	0.28	-0.30	
G334.49-0.37	16 26 41.1	-49 34 40.5	3.8	-9.8	-8.5	-9.1					4.7	0.62	0.38	-0.41	
G334.61-0.43	16 27 29.9	-49 32 14.1	5.0	-139.5	-138.2	-138.8					5.7	6.97	0.36	-0.36	
G334.68+0.44	16 23 57.9	-48 52 53.8	3.6	-96.9	-95.2	-95.2					3.8	4.96	0.19	-0.19	
G334.68+0.35	16 24 22.8	-48 56 34.8	4.0	-55.6	-55.2	-55.2					4.4	3.34	0.23	-0.23	
G334.68+0.13	16 25 20.5	-49 05 30.2	5.1	-94.5	-89.1	-91.1					6.1	4.83	0.19	-0.19	W

^aC - presence of a 1665 MHz OH maser from Caswell (1998); S - presence of a 1612 MHz OH maser from Sevenster et al. (1997); W - presence of a H₂O maser from Walsh et al. (2011, 2014).

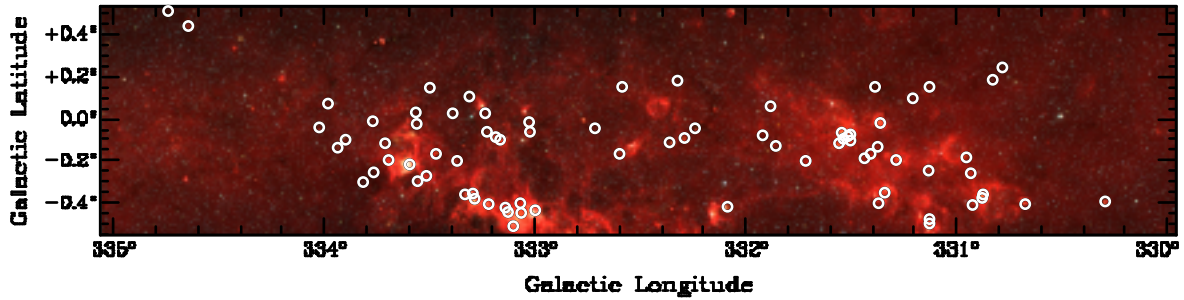


Figure 3.6: *Spitzer* GLIMPSE 3-colour (RGB = 3.6, 4.5 and 8.0 μm) image with MALT-45 positions of class I CH_3OH masers (circle symbols).

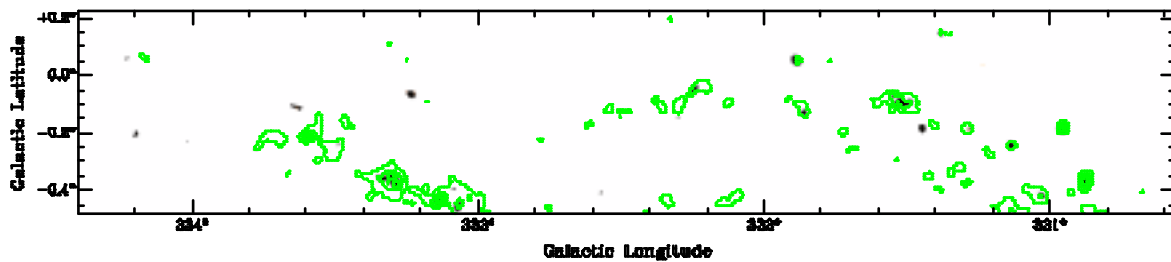


Figure 3.7: Auto-correlated map of SiO (1-0) $v = 0$, overlaid with CS (1-0) thermal emission contours. This image shows SiO emission at and above 0.04 K ($\sim 1.5\sigma$). Contour levels are 14, 34, ..., 74 per cent of 2.62 K.

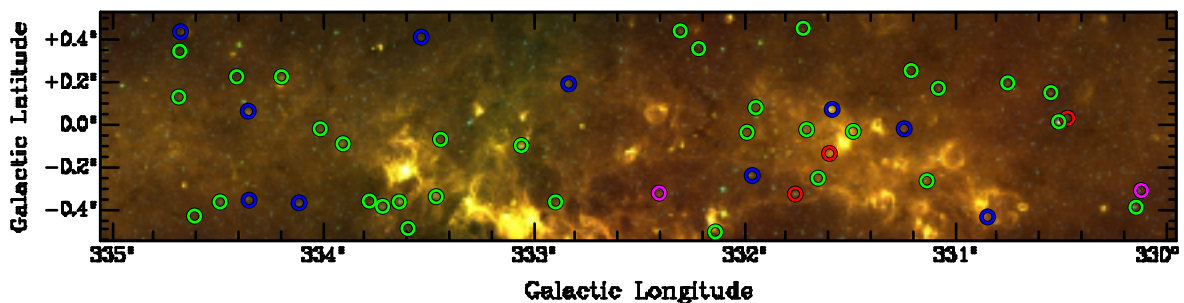


Figure 3.8: *Spitzer* GLIMPSE 3-colour (RGB = 3.6, 5.8 and 8.0 μm) image with MALT-45 positions of detected SiO (1-0) $v = 1, 2, 3$ masers (circle symbols). The circles have been colour-coded by the vibrational modes within each region. Red: region containing $v = 1, 2, 3$ maser emission; green: $v = 1, 2$; blue: $v = 1$; magenta: $v = 2$.

The positions of class I CH_3OH masers have been compared with the published positions of class II CH_3OH , H_2O and OH masers to establish associations. When considering the maximum distance between masers that still constitute an association, we use 60 arcsec from the class I position as suitable for defining associations. Csengeri et al. (2014) analysed a large distribution of clumps associated with HMSF in their source sample, and find that all clumps have effective radii within 55 arcsec. Additionally, we note that increasing the maximum offset beyond 60 arcsec does not increase the number of unique associations. These findings suggest for our purposes that 60 arcsec is sufficient to group masers within a single star-forming region. We have chosen not to define an association based on source distance or size, as it is difficult to implement across a wide range of objects, kinematic distances may be erroneous, and maser geometry may be wide-spread. An angle of 60 arcsec on the sky

corresponds to approximately 1.5 pc at a distance of 5 kpc.

There are two targets where the spread of class I CH₃OH maser emission is large and these have been considered as two separate maser regions. The weaker masers (G331.52–0.08 and G333.14–0.42) near to each of these bright masers (G331.50–0.08 and G333.13–0.44) possess a distinct spectral velocity component and are sufficiently spatially offset to be considered a different site (54 and 87 arcsec, respectively). See the spectra in Appendix A.2. These sources are marked with a ‘P’ in Table 3.2.

Integrated intensity values for CS and SiO $v = 0$ have been included for each maser, where possible, in Table 3.2. Emission was integrated $\pm 10 \text{ km s}^{-1}$ from the peak velocity of the maser. Values were not included if the emission was not significant ($< 3\sigma$).

3.3.3 SiO (1–0) $v = 0$ thermal emission at 43.424 GHz

Extended SiO $v = 0$ emission is detected in some regions, as shown in Fig. 3.7, which shows that SiO $v = 0$ emission tends to be associated with bright peaks of CS emission. Note that emission from the SiO $v = 0$ is typically weaker than for CS, hence the signal-to-noise is lower for this transition; Fig. 3.7 shows all emission above 1.5σ . Discussion on the relation between class I CH₃OH masers and SiO $v = 0$ emission is contained in §3.4.3.

3.3.4 SiO (1–0) $v = 1, 2, 3$ masers at 43.122, 42.820 and 42.519 GHz

The vibrationally excited SiO (1–0) lines were detected towards 47 regions, as shown in Fig. 3.8. The properties of each maser region are classified in Table 3.3. The search procedure for SiO masers was the same as with CH₃OH masers; they were identified by visual inspection of the data, and had velocities categorised by a 1.5σ cutoff from the peak velocity. Velocities are specified to 0.1 km s^{-1} , and flux densities to two significant figures. Many masers have low signal-to-noise values, but are considered real detections based on their association in GLIMPSE, and simultaneous detection of emission in another SiO maser transition. The positions of SiO masers have been compared with OH and H₂O masers; see Table 3.3 and §3.4.7. CH₃OH maser species were searched at these positions, but none were found, implying that any class I CH₃OH maser emission associated with the SiO masers has a peak flux density $< 4.5 \text{ Jy}$. Peak intensity maps are presented in Appendix A.3, and each un-smoothed maser spectrum can be seen in Appendix A.4.

Fig. 3.8 shows the locations of SiO masers detected by MALT-45 with respect to infrared emission from GLIMPSE. All SiO masers are detected towards point-like, isolated sources that appear to be evolved stars, based on their infrared colours and lack of obvious associations with star formation, such as IRDCs or extended infrared emission. Fig. 3.9 shows the relative locations of three SiO masers compared to infrared stars; these masers were chosen as they show various colours of infrared stars towards all SiO masers. It can be seen that the maser locations are not identical to the stars, but are within one beam. Therefore, we cannot conclusively argue that each SiO maser site is coincident with an evolved star, although the evidence we have suggests this is the case. Further higher spatial resolution observations of the maser sites will be able to demonstrate conclusively whether or not each SiO maser is associated with an evolved star.

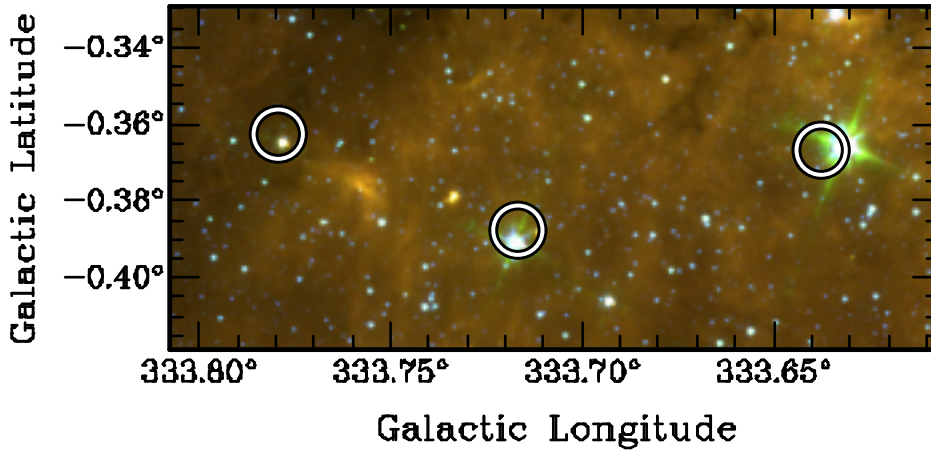


Figure 3.9: *Spitzer* GLIMPSE 3-colour (RGB = 3.6, 5.8 and 8.0 μm) image with examples of detected SiO masers towards infrared stars. Circles are centred on the peak position of maser emission, and are beam sized (≈ 1 arcmin). All three of these SiO maser regions contain the $v = 1$ and $v = 2$ lines, but all other maser region variants have similar infrared colours.

Of the 47 SiO maser regions, 45 contain $v = 1$ emission, 37 contain $v = 2$, and only 3 have $v = 3$ emission. We have found no previously published data for any of these SiO masers and consider them all to be new detections. Some SiO maser regions have greater $v = 2$ emission than $v = 1$, and two have no detected emission $v = 1$; this is discussed further in §3.4.7. There are also 12 SiO maser regions with an associated OH or H₂O maser; see §3.4.7.

Parameters used in determining kinematic distances are the same as those found in §3.3.2, except for a more generous velocity uncertainty $\sigma(V_{LSR}) = 5.0 \text{ km s}^{-1}$, and $V_s = 0 \text{ km s}^{-1}$. Four masers are labelled at the far kinematic distance, because the position and errors for a near distance are unrealistic; see Table 3.3.

3.3.5 Survey completeness

By analysing the RMS noise values per pixel distributed across the MALT-45 region, we find that the noise levels may vary by up to a factor of three due to some data being flagged or insufficient time on the telescope to complete the observations. However, we determine that approximately 95 per cent are consistent with the values listed in Table 3.1, and only 5 per cent show RMS levels worse than these values. Thus, we assess that to first order the survey has uniform sensitivity and only a small fraction of the area has sensitivity poorer than nominal.

Tables 3.2 and 3.3 include the RMS value for each detected maser peak, which help to identify the completeness of the MALT-45 survey. We detect many masers at less than 5σ significance. However, we consider the survey complete at the 5σ level for 95 per cent of the survey area. This completeness limit is equivalent to 4.5 Jy for class I CH₃OH masers, and approximately 4.3 Jy for each SiO maser line.

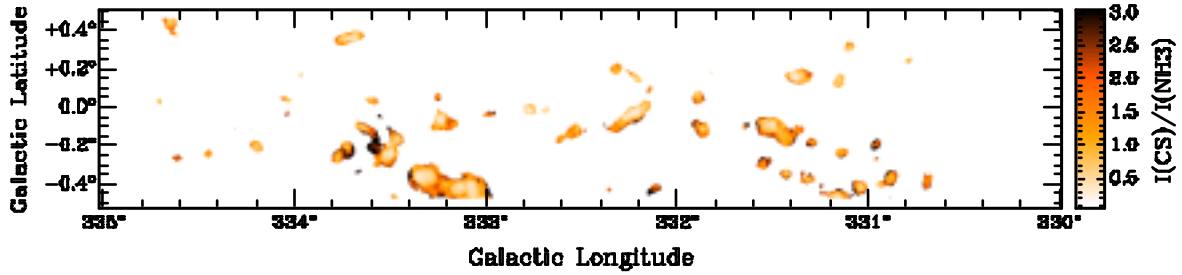


Figure 3.10: A ratio image of integrated MALT-45 CS (1–0) to HOPS NH₃ (1,1). The clumps visible here contain at least 0.5 K km s⁻¹ of integrated NH₃ (1,1) emission. Most clumps have edge values around 2, and centres of clumps can have values as low as 0.4.

3.4 Discussion

3.4.1 Comparing CS (1–0) with HOPS NH₃ (1,1)

Fig. 3.4 shows that NH₃ (1,1) from HOPS is closely correlated with bright CS (1–0) emission, but with prominent exceptions; examples include G330.30–0.40, G332.17–0.10 and G334.17+0.06. We calculate that MALT-45 is more sensitive to CS (1–0) emission than HOPS is to NH₃ (1,1) by a factor approximately 9, therefore CS without NH₃ in Fig. 3.4 may be due to the superior sensitivity of MALT-45 over HOPS. However, it is also likely attributable to the phenomena described by Taylor et al. (1998), who reason that CS is an ‘early-type’ star-forming molecule, tracing quiescent gas, while NH₃ is ‘late-type’, associated with dense cores. For this reason, despite having a higher effective critical density, CS without NH₃ may be tracing molecular clouds before cold, dense cores have formed. Additionally, Bergin et al. (2001) and Tafalla et al. (2002) indicate that CS tends to deplete in core collapse. This means a relatively high abundance of NH₃ to CS should reflect a cold, dense core, which is a Taylor et al. (1998) ‘late-type’ scenario. As results indicate later in this section, NH₃ is not persistent in even further developed stages of HMSF, as it is not detected or very faint. We distinguish ‘late-type’ sources from these evolved sources through bolometric luminosities and the presences of infrared features, such as stars or H II regions.

We produced a map of the ratio between the integrated intensities of CS and NH₃ in order to highlight the differences between their distributions. Before performing the quotient of integrated intensity, the CS data were smoothed to the HOPS NH₃ resolution (~ 2 arcmin). We used a cutoff at 0.5 K km s⁻¹ (3σ) of the less sensitive NH₃ data; CS data is $>3\sigma$ everywhere NH₃ is $>3\sigma$. Integration of emission was taken between -100 and -40 km s⁻¹, to eliminate subtle baseline effects which decrease the robustness of analysis; this velocity range is where most of the emission in this part of the Galaxy lies (see Fig. 3.3 for the longitude-velocity plot). Quotients use units of main-beam temperature for both CS and NH₃. See Fig. 3.10 for the full ratio map.

Moving inward from the clump edges, the CS/NH₃ ratio quickly changes. We observe the amount of both CS and NH₃ to increase, with the NH₃ intensity increasing more ‘quickly’. Edge values are mostly about 2, while clump centres are usually between 1 and 0.5, but can be as low as 0.4.

We now discuss the ratio map qualitatively, reserving radiative transfer modelling for

future work. In almost every clump, the centre is dominated by NH_3 over CS. This could be due to any or a combination of enhanced NH_3 , depleted CS, or both species being enhanced but CS becoming optically thick. The hyperfine line structure of NH_3 means that it remains optically thin at higher column densities than CS. To test for optically thick CS, we compared CS with MALT-45 C^{34}S .

We conducted the analysis of CS against C^{34}S in a similar manner to that of CS against NH_3 . Both integrated maps were smoothed to the same resolution, the velocity range of integration was -100 to -40 km s^{-1} , and emission was limited to detectable C^{34}S (0.15 K km s^{-1}). A preliminary analysis of the C^{34}S data was undertaken only to investigate the CS optical depth within these clumps.

Fig. 3.11 shows contours of the ratio of $\text{C}^{34}\text{S}/\text{CS}$ against GLIMPSE, with contours of CS/NH_3 . Progressively higher levels of $\text{C}^{34}\text{S}/\text{CS}$ indicate CS self-absorption, but appear to be slightly offset from the lowest CS/NH_3 ratios. This implies that the relatively fainter CS emission in the presence of an abundance of NH_3 is due to both depletion and optical thickness. Additionally, the higher ratios of $\text{C}^{34}\text{S}/\text{CS}$ appear to be associated with bright infrared emission, and correlate well thermal SiO emission. We speculate that high $\text{C}^{34}\text{S}/\text{CS}$ ratios may be due to high CS optical depth as a result of high CS relative abundance in the presence of an outflow or shocked gas. C^{34}S is not detected in other regions of these clumps; aside from having poor signal-to-noise, this is likely due to the isotopologue depleting similar to CS, and emission is only apparent in hotter, shocked regions where these molecules have been released into the gas phase.

A similar analysis to the one we have conducted was performed in Tafalla et al. (2004) towards two cold, dense cores. Their results indicate significant depletion of CS and C^{34}S towards the core centres, while NH_3 peaks in abundance. We have not undertaken a detailed analysis of the temperature or mass of the MALT-45 molecular gas clumps in this paper; this will be investigated in a future publication focusing on the CS emission. In future work, we will present radiative transfer modelling (including depletion, time-dependant chemistry and the relative sensitivity limits of the various surveys) of the dust, CS and NH_3 emission to quantitatively understand the physical reason for these effects.

The following subsections briefly discuss three unusual clumps, which have the largest CS/NH_3 ratios.

3.4.1.1 G330.95–0.19

This source is one of the brightest in CS across the MALT-45 survey region (peak of 1.5 K), and is the brightest in thermal SiO emission (peak of 0.17 K). The source also contains all the common star formation region masers: class I and II CH_3OH , H_2O and OH . The CS spectrum has a broad profile of $\sim 10 \text{ km s}^{-1}$ FWHM, possibly due to a powerful molecular outflow. A strong outflow would not be surprising given the strength of the thermal SiO detected, relative to all other SiO sources in MALT-45.

Garay et al. (2010) have targeted this source which has a high IRAS far-infrared luminosity, as well as detection of CS (2–1) by Bronfman et al. (1996). Garay et al. (2010) present data for SiO (2–1) and note that of the four sources they discuss, this source is brightest in SiO, and conclude that an outflow is present due to the spectral profiles of CS and SiO.

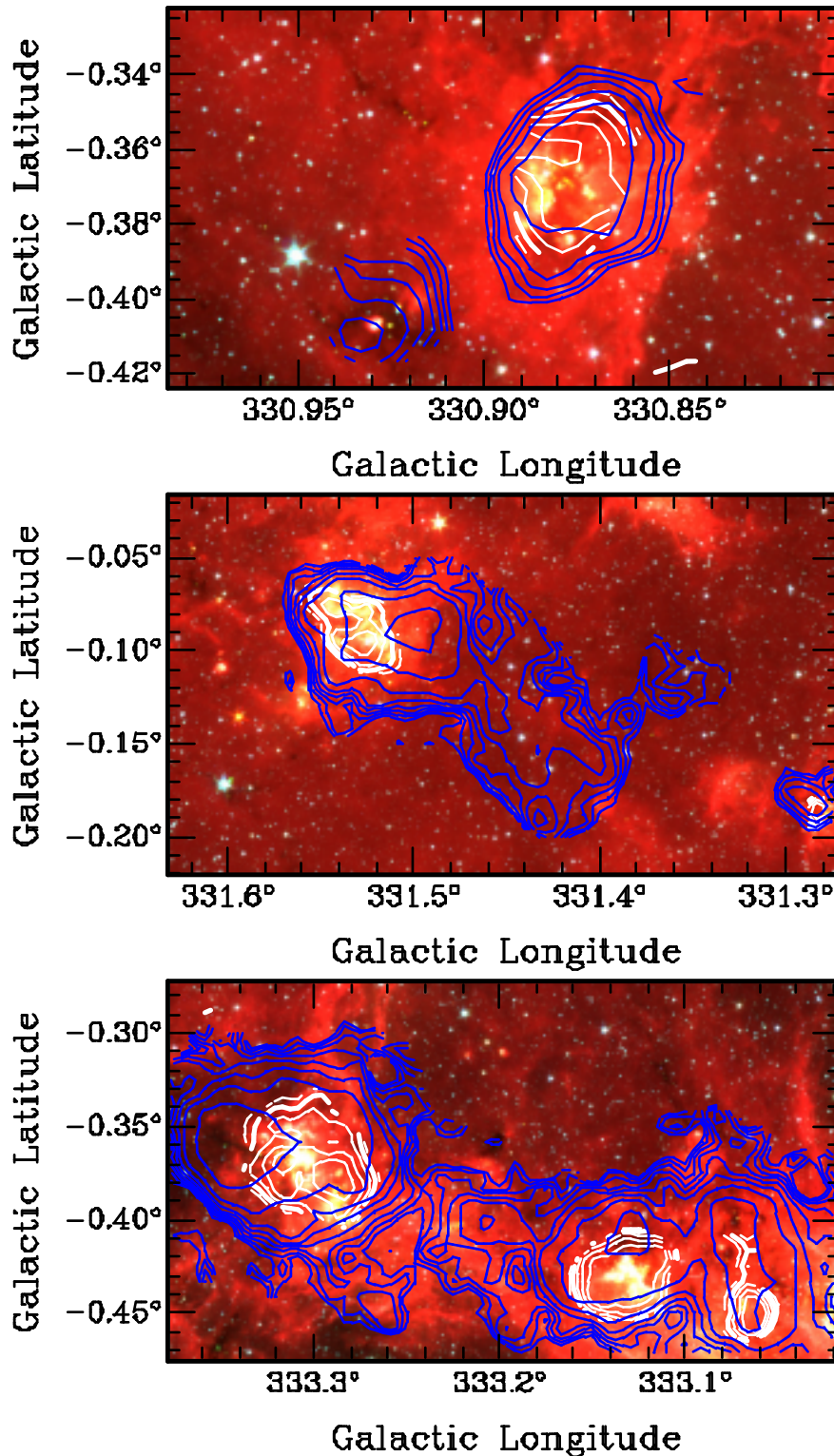


Figure 3.11: Examples of significant $\text{C}^{34}\text{S}/\text{CS}$ ratios within CS/NH_3 clumps. *Spitzer* GLIMPSE 3-colour (RGB = 3.6, 4.5 and $8.0\ \mu\text{m}$) image with contours of $I(\text{C}^{34}\text{S})/I(\text{CS})$ (white) and contours of $I(\text{CS})/I(\text{NH}_3)$ (blue). $I(\text{C}^{34}\text{S})/I(\text{CS})$ contour levels are 0.08, 0.10, ..., 0.16, and $I(\text{CS})/I(\text{NH}_3)$ contour levels are 0.3, 0.5, ..., 1.9. Note that contour levels for $I(\text{CS})/I(\text{NH}_3)$ move from large to small, outside-in. The lowest CS/NH_3 and highest $\text{C}^{34}\text{S}/\text{CS}$ ratios appear to be slightly offset. High $\text{C}^{34}\text{S}/\text{CS}$ ratios appear to occur with bright infrared emission; this is likely due to C^{34}S is only detectable where the overall CS abundance is enhanced in hotter, shocked regions where these molecules have been released into the gas phase.

Garay et al. (2010) also discuss the requirement of OB stars to produce the ionised gas seen in other observations. The evolved nature of the source is the likely reason for the faint NH_3 , because it is being destroyed or dispersed by outflows or young stellar objects.

3.4.1.2 G332.10–0.42

The CS/ NH_3 ratio of this source is approximately 3. Of the three unusual sources discussed in this section, this is the only one without detected thermal SiO emission. A small region (~ 30 arcsec) of the clump has a constant $\text{C}^{34}\text{S}/\text{CS}$ ratio of 0.08, and is coincident with a H_2O and class II CH_3OH maser, as well as what appears to be a star in GLIMPSE. A new class I CH_3OH maser is detected by MALT-45, but is slightly offset from this position (~ 30 arcsec).

This source has been targeted by Ilee et al. (2013) to determine disc properties through CO observations, and is listed with a very high bolometric luminosity ($1.8 \times 10^5 L_\odot$). The Red MSX Source (RMS; Lumsden et al. 2013) survey also lists a K -band magnitude of 5.9. These values suggest that the source is not embedded. As a star is visible in GLIMPSE and the source is not embedded, it may be assumed that the star (and the region) are post star-forming. However, we are confident that the associated star is not evolved (beyond the main-sequence), as a near-infrared (NIR) spectrum of the source contains $\text{Br}\gamma$, indicating the presence of an H II region. The spectrum is taken from the RMS survey, although the data remain unpublished; Cooper et al. (2013) present detailed analysis of the NIR spectroscopy, but note that it does not cover this specific source. We conclude that this source is somewhat evolved because of its exposure from natal clouds, but is pre-main-sequence because of the class II CH_3OH maser emission. Again, the evolved nature of this region is the likely reason for the relatively faint NH_3 .

3.4.1.3 G333.60–0.20

This region is the brightest H II region within the MALT-45 survey, and appears to harbour evolved sources. C^{34}S emission is detected within this source, and the $\text{C}^{34}\text{S}/\text{CS}$ ratio varies from 0.09 to 0.14. Thermal SiO emission is also detected towards the source. As well as a previously known class I CH_3OH maser, this region is associated with 1612-, 1665- and 1667-MHz OH masers (Sevenster et al. 1997; Caswell 1998), and many H_2O masers from HOPS (Walsh et al. 2014). The peak velocity of the class I CH_3OH maser is -49.7 km s^{-1} , -51 km s^{-1} for OH, and -75.5 to -43.1 km s^{-1} for the H_2O masers. MALT-45 CS also has a double-peak profile in this region; a strong, broad peak is associated with -48.1 km s^{-1} and a weaker one at -89.8 km s^{-1} , both at the same position ($16^h 22^m 06^s$, $-50^\circ 06' 17''$ J2000).

Fujiyoshi et al. (2006) conducted observations of $\text{H}90\alpha$ towards this source, which also reveal two peaks of emission, and reason that it contains many O-type stars. The peak velocity of each $\text{H}90\alpha$ component varies greatly over the region, from -78.5 to -52.9 km s^{-1} and -42.8 to -22.8 km s^{-1} , where the second peak is weaker and not present across the observed area. Note that the position of peak MALT-45 CS is outside of the data presented in Fujiyoshi et al. (2006); it is possible that the spatial resolution of our CS data is limiting our ability to interpret the physics of this region. However, it is interesting that the peak

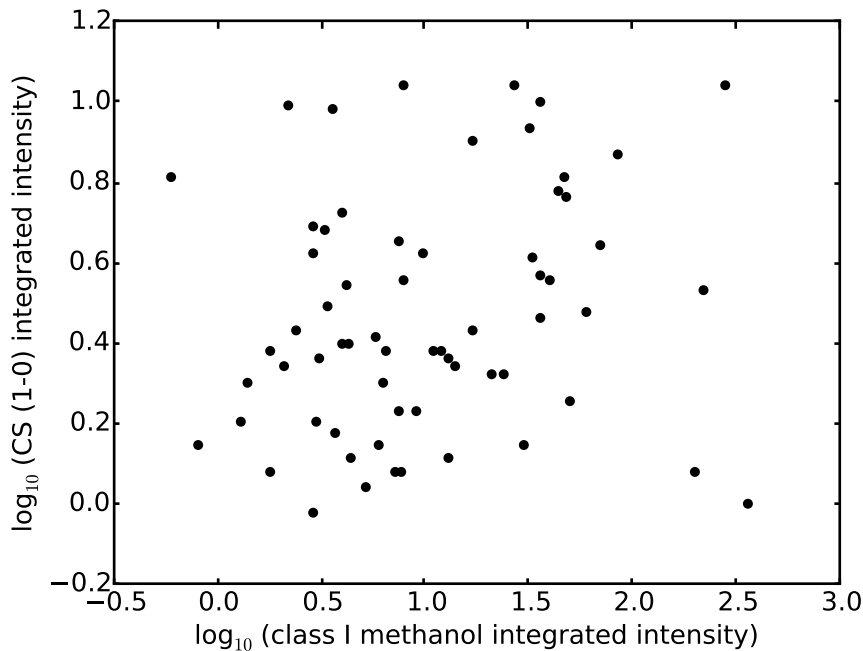


Figure 3.12: A log-log scatter plot of class I CH_3OH and CS integrated intensities. Units of integrated intensity are Jy km s^{-1} for class I CH_3OH , and K km s^{-1} for CS. There is no significant correlation observed.

velocities of CS are quite different to H90 α ; this may indicate complex structure of the source, and indeed this is discussed in Fujiyoshi et al. (2006).

The weak presence of NH_3 (1,1) emission is mysterious. The high CS/ NH_3 ratio may be attributable to the region being at a higher temperature, preventing CS depletion. Lowe et al. (2014) attempted a NH_3 (1,1) and (2,2) analysis of this clump, but were unable to detect significant emission. They suggested that the relatively faint NH_3 emission could be due to extreme self-absorption. Lo et al. (2009) comment that in general, CS (2–1) and HCO^+ (1–0) have similar velocity structure, except at this location; the HCO^+ has a strong self-absorption feature. However, given that the source is clearly evolved, it is consistent with the other sources discussed in having little NH_3 emission.

3.4.1.4 Summary

The cause for the high ratios ($\text{CS}/\text{NH}_3 > 3$) in our analysis appears to stem from evolved regions of HMSF. The other clumps are more difficult to classify - are they less evolved? Do they have significantly different temperatures or column densities? More analysis is needed, and will be presented in a future MALT-45 paper with CS clump analysis.

3.4.2 Comparing CS (1–0) with class I CH_3OH maser regions

Table 3.2 includes the integrated flux density of CS (1–0) in each maser region. The kinematic distance calculated for each source is used to determine the luminosities. Fig. 3.12 compares the integrated CS intensity with the integrated class I CH_3OH maser intensity.

Fig. 3.2 shows that most class I CH_3OH masers appear to be associated with a bright

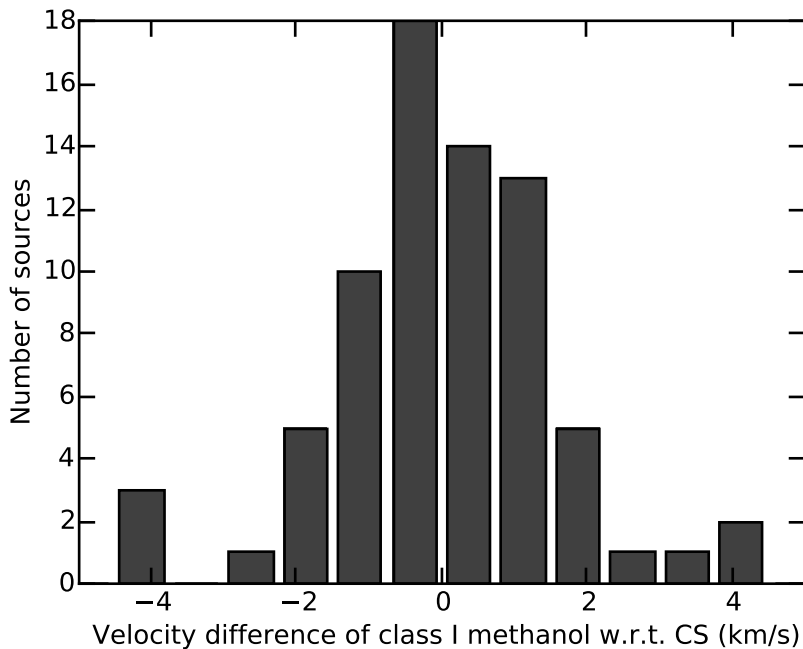


Figure 3.13: The distribution of velocity offsets between the peak velocity of class I CH_3OH and CS (1–0). The bin size was chosen to be 0.75 km s^{-1} . The histogram is approximated by a Gaussian with a mean velocity $0.0 \pm 0.2 \text{ km s}^{-1}$ and standard deviation $1.5 \pm 0.1 \text{ km s}^{-1}$.

peak of CS emission (73/77 masers with $>0.11 \text{ K}$ of peak intensity CS). This is quantified (using integrated intensity) in Fig. 3.12. However, there is no correlation observed between the relative intensity of a class I CH_3OH maser and its associated CS.

A class I CH_3OH maser with CS emission suggests association with a star-forming region, because sufficient gas and shocks exist to power their emission. However, without being able to associate these lines with other diagnostics of star formation, it is not certain that the masers are stimulated by star formation; cloud-cloud collisions have been found to stimulate class I CH_3OH emission (Sjouwerman et al. 2010). While the possibility of being a non-star-forming maser extends to all candidates without additional tracers (such as class II CH_3OH masers), we expect that these are exceptional cases, and that the majority if not all class I CH_3OH masers in the MALT-45 sample are associated with star formation.

A comparison of class I and class II CH_3OH masers was undertaken by Voronkov et al. (2014), and found a broad Gaussian distribution of velocity differences. We have performed a similar analysis with the peak velocities of both CS and class I CH_3OH masers from the MALT-45 data. The resulting histogram of the velocity difference of CH_3OH with respect to CS is found in Fig. 3.13. The distribution is approximated by a Gaussian with a mean velocity difference $0 \pm 0.2 \text{ km s}^{-1}$ and standard deviation $1.5 \pm 0.1 \text{ km s}^{-1}$. The median velocity difference is -0.1 km s^{-1} .

The FWHM of the population presented by Voronkov et al. (2014) is approximately 7.8 km s^{-1} , while ours is approximately 3.5 km s^{-1} . Because CS is a dense gas tracer, it will occur in cloud cores and thus trace systemic motions accurately. Given the resulting Gaussian of velocity differences, this means that class I CH_3OH masers are also good indicators of systemic velocities. Voronkov et al. (2010b) discuss class I CH_3OH masers having similar

velocities to the quiescent gas, due to a small amount of gas actually being shocked in these regions. As is noted in Voronkov et al. (2014), Garay et al. (2002) indicate that CH₃OH emission arising without thermal SiO emission is due to mild shocks, destroying dust grain mantles but not dust grain cores. Hence the dispersion in class I CH₃OH maser velocities is thought to be small, and is reflected here. This also indicates that the large dispersion seen by Voronkov et al. (2014) is likely due to the large class II CH₃OH maser velocity spread. This is readily explained by class II CH₃OH maser emission radiating from close to a high-mass young stellar object, and therefore having a higher dispersion.

The histogram in Fig. 3.13 appears to have a slight blueshifted component. This is also discussed in Voronkov et al. (2014) as perhaps due to maser emission being easier to detect on the near-side of a cloud to the observer. While the median velocity offset is negative, it is statistically insignificant. A larger data set is required to determine if the blueshift phenomena is real or not.

3.4.3 Comparing class I CH₃OH maser regions with SiO (1–0)

As discussed in Chapter 1, SiO $v = 0$ is a good tracer of shocked gas and outflows. Regions of thermal SiO and positions of class I CH₃OH masers correlate weakly; 23 of 77 masers (30 per cent) have at least a 2σ peak of SiO emission. As class I masers are collisionally excited, it is perhaps not surprising to find some association with thermal SiO. However, the majority of masers are detected without SiO $v = 0$ emission. This could be due to: insufficient sensitivity to extended SiO emission; class I CH₃OH masers having stronger intensity than thermal SiO; or not all class I CH₃OH masers being associated with SiO $v = 0$ emission. Garay et al. (2002) found that thermal CH₃OH emission may be triggered by less energetic shocks, which destroy dust grain mantles but not their cores, which explains a lack of SiO emission. In more energetically shocked regions (such as a jet or molecular outflow), CH₃OH may not survive, which may explain SiO emission without CH₃OH.

Three regions with strong SiO emission (0.04 K) are not associated with any maser species: G331.02–0.42, G333.63–0.11 and G334.20–0.20. Each of these regions has a CS peak of at least 0.4 K ($>10\sigma$), but no obvious infrared emission. Table 3.2 lists 28 class I CH₃OH masers with detected SiO emission, implying that these three regions without masers are in the minority. This could be due to the variability of any masers making them undetectable during observations, or that conditions in these regions are unfavourable for masers to exist.

It is clear that sensitivity to CH₃OH and/or SiO will play a part in the detectability of each. However, the fact that we see regions with both CH₃OH and SiO, regions with only CH₃OH masers and regions with only SiO emission suggests that there are multiple conditions under which each of these will exist. If we assume that all class I CH₃OH masers are associated with star formation, then given that the majority of masers are not associated with thermal SiO emission, these masers may be tracing weaker shocks that do not produce detectable SiO emission. 30 per cent of CH₃OH masers also show thermal SiO emission. It is not clear whether the masers and SiO are physically connected, although a reasonable interpretation is that the SiO originates in a jet, whereas the masers are associated with the surrounding outflow. In a subsequent paper for MALT-45, maser follow-up observations will be conducted at high spatial resolution. We will simultaneously observe SiO with greater

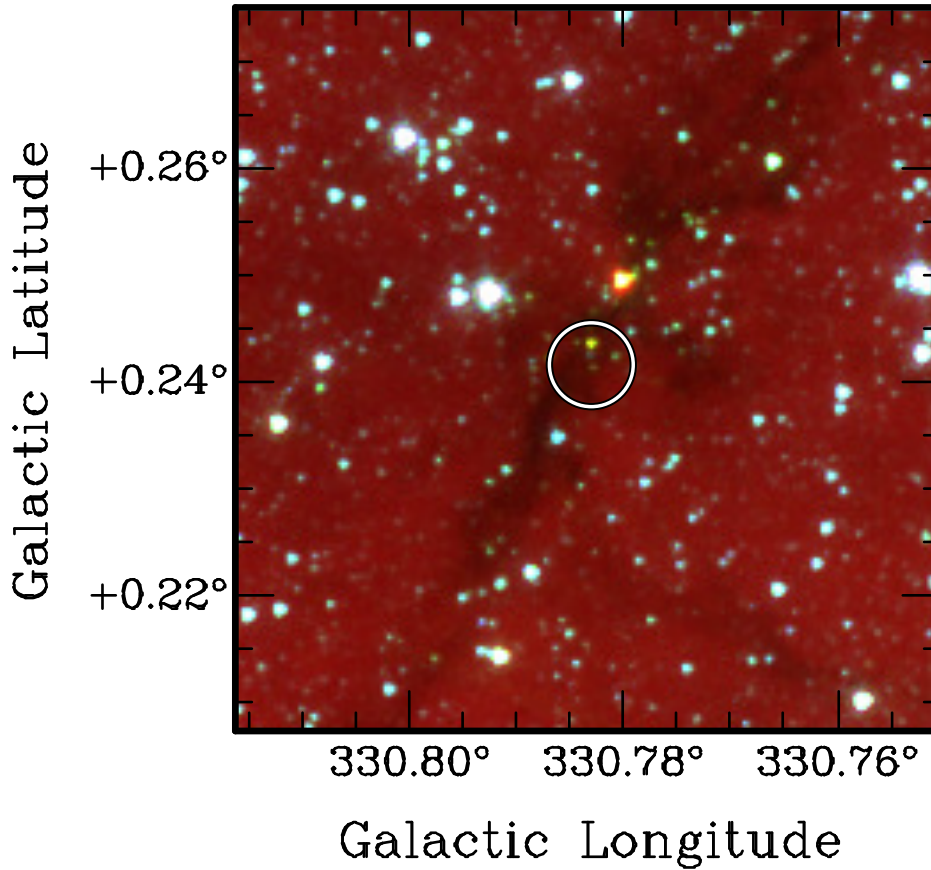


Figure 3.14: An example of a class I CH_3OH maser with associated ‘green’ emission. This region is not classified as an EGO by Cyganowski et al. (2008), but may have similar properties. The circle represents 15 arcsec centred on the peak of the class I CH_3OH maser emission, which is the expected positional error.

sensitivity, and using this data we will more thoroughly investigate the association of class I CH_3OH masers and thermal SiO emission.

3.4.4 Class I CH_3OH maser comparison with GLIMPSE

GLIMPSE mapped the Galactic plane in four infrared bands (3.6, 4.5, 5.8 and $8.0\ \mu\text{m}$). These images are useful for investigating potential relationships between infrared emission and MALT-45 detections. A common example of how GLIMPSE data is used in star formation research is by combining the 3.6, 4.5 and $8.0\ \mu\text{m}$ bands in a three-colour image (blue, green and red, respectively) to reveal EGOs (extended green objects). As discussed in Cyganowski et al. (2008), EGOs have a strong correlation with class I CH_3OH maser regions.

The catalogue provided by Cyganowski et al. (2008) was used to investigate the presence of EGOs over the survey region. The catalogue covers $10^\circ \leq l \leq 65^\circ$ and $295^\circ \leq l \leq 350^\circ$, $b = \pm 1.0^\circ$, and lists 22 candidate EGOs within the MALT-45 survey region. Of the 77 class I masers found by MALT-45, 12 are associated with an EGO. Association is credited for any spatial overlap within 60 arcsec. Of the 12 EGO-associated class I CH_3OH masers, 11 were previously known (G330.95–0.18 is new). EGOs are classified by visual inspection and as such are intrinsically subjective. However, it is clear that many of the new class I CH_3OH maser detections are associated with GLIMPSE sources with ‘green’ (i.e. $4.5\ \mu\text{m}$ excess)

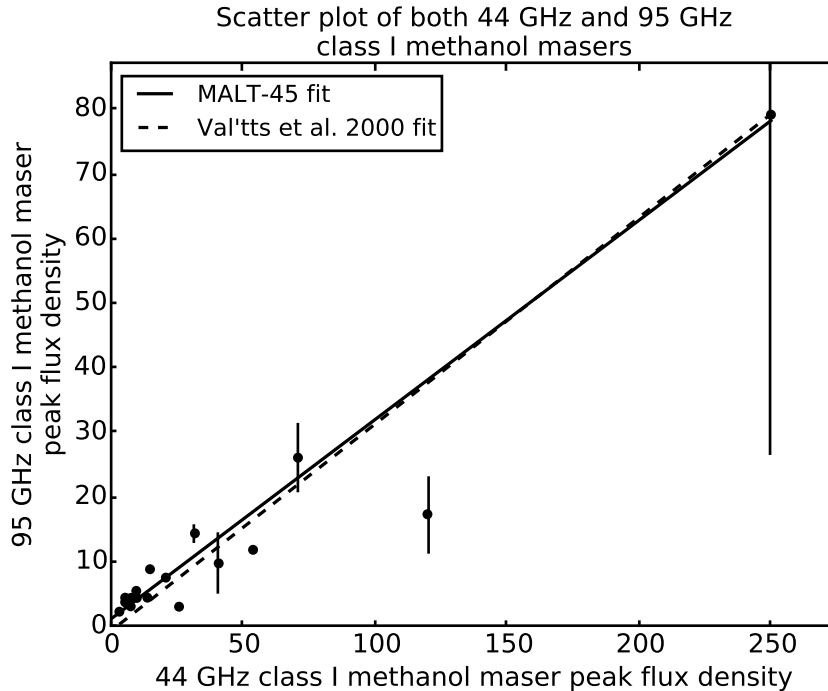


Figure 3.15: A scatter plot of 44 GHz class I CH_3OH masers from MALT-45 with known 95 GHz class I CH_3OH maser emission. There are 19 masers with both 44 and 95 GHz emission. The line of best fit for these data is plotted alongside the line of best fit presented by Val'tts et al. (2000). Vertical lines indicate the minimum and maximum recorded values for 95 GHz masers, if available, on top of the plotted average. Units of peak flux density are in Jy.

emission; see Fig. 3.14 for an example source. Cyganowski et al. (2009) explains that the green emission band of GLIMPSE contains both H_2 and CO (1–0) lines, which are excited by shocks. Indeed, some of the new masers detected by MALT-45 have similar ‘green’ emission as with EGOs, although less prominently so. This shows a close association between shocks traced by EGOs and class I CH_3OH masers.

3.4.5 95 GHz class I CH_3OH masers

Val'tts et al. (2000) found a relationship between the peak flux density of the 95 and 44 GHz class I methanol masers (which come from the same transition family). They found that the peak flux density of 44 GHz masers is approximately three times greater than the 95 GHz masers.

Information for 95 GHz class I CH_3OH masers towards MALT-45 44 GHz masers are obtained from Val'tts et al. (2000); Ellingsen (2005) and Chen et al. (2011). In total, we have 19 class I maser sources with both 44 and 95 GHz peak flux densities. When faced with more than one peak flux density over various epochs, we use the average of all values. Analysing the distribution in Fig. 3.15, we find that our results agree with those of Val'tts et al. (2000). Our line of best fit is $P_{95} = 0.31 \times P_{44} + 1.0$, with an r^2 -value of 0.98, while the Val'tts et al. (2000) fit is $P_{95} = 0.32 \times P_{44} - 8.1$, with an r^2 -value of 0.53. The uncertainty of our fitted slope is ± 0.01 . Note that our fit does not use the 44 GHz maser with 120 Jy; if we do include it, our fit becomes $P_{95} = 0.28 \times P_{44} + 1.0$, with an r^2 -value of 0.91 and uncertainty ± 0.02 .

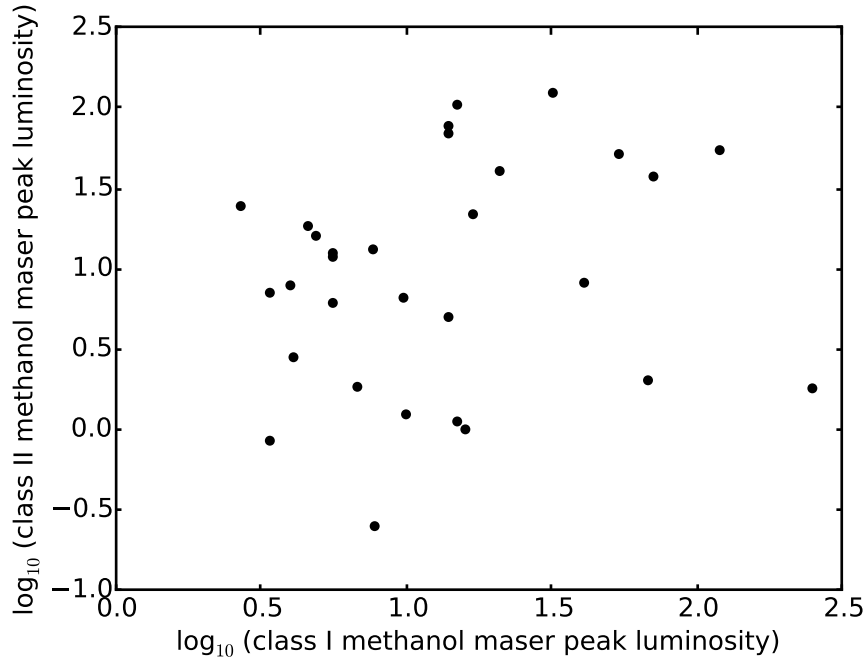


Figure 3.16: The luminosities of associated class I and class II CH_3OH masers plotted against each other. No significant correlation is observed. Units of luminosity for the masers are Jy kpc^2 , using peak flux densities.

This is not significantly different, but our slope closely agrees with Val'tts et al. (2000) when the outlier is omitted.

3.4.6 Class I CH_3OH maser associations

In this section, we discuss other maser species and transitions and their association with the class I CH_3OH masers detected in MALT-45. Association with each maser is credited if the emission in question is within 60 arcsec of the class I maser position.

3.4.6.1 Class II masers from the MMB

In the past, class I methanol masers have been identified from targeted searches towards class II maser sites (Ellingsen 2005). For the first time, we are able to make an unbiased comparison of the rate at which each class of methanol maser occurs and their degree of overlap.

Within the MALT-45 survey region, 54 6.7 GHz class II methanol masers have been detected by the MMB (Caswell et al. 2011). To compare against MALT-45 class I maser regions, 7 class II masers have been grouped together into ‘clusters’, as they are close together (within 60 arcsec). The clusters containing grouped masers are G330.88–0.37, G331.54–0.07, G332.30–0.09, G333.13–0.44 and G333.23–0.06. While the velocities of each maser site grouped together may be different, there is significant overlap in the range of emission (not greater than 9 km s^{-1} apart). Without high-resolution positions, inferring which class II maser is associated with the class I emission is difficult, and it is more practical to only compare their clustered position, especially as a class I CH_3OH maser is almost certainly associated with

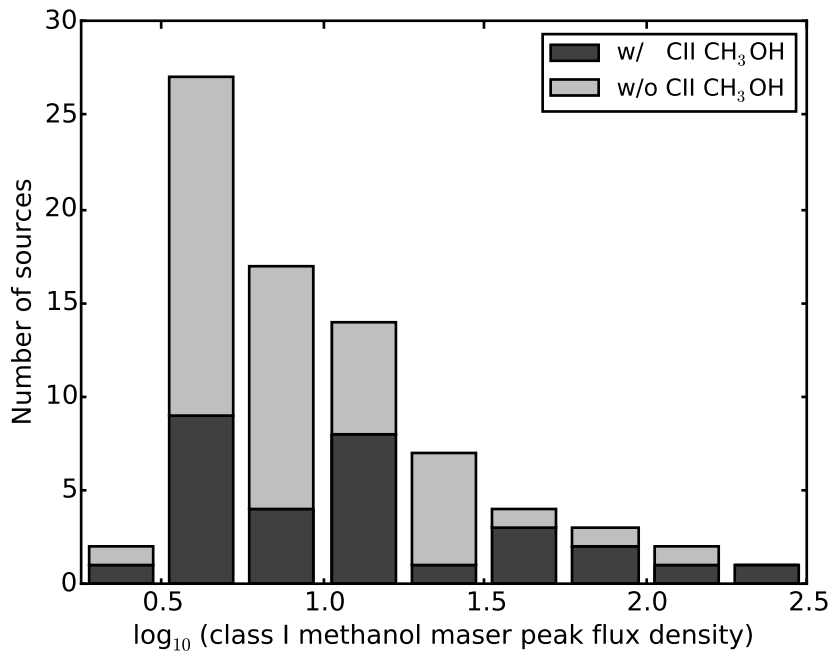


Figure 3.17: A stacked histogram of class I CH₃OH masers with and without class II methanol masers. This plot shows that class II masers can be associated with a wide range of class I intensities.

the class II source. Therefore, we compare 47 class II methanol masers positions against the 77 class I sources detected in MALT-45. There are 28 class I CH₃OH masers associated with the clusters, and 16 of these class I masers are new; see Table 3.2. An association exception is made for G331.13–0.25, where the class II CH₃OH maser is slightly further offset than 60 arcsec from the MALT-45 class I CH₃OH maser position, but is well studied and known to be related (Ellingsen 2005; Voronkov et al. 2014). Additionally, the next closest class I and class II CH₃OH maser pair is approximately 100 arcsec, which aids to rule out mis-association. Thus, 60 per cent of class II masers have a class I counterpart (28/47), while approximately 36 per cent of class I masers have a class II counterpart (28/77).

Ellingsen (2005) reports a 38 per cent association of class II sources with a 95 GHz class I maser counterpart. Given that the 44 GHz species is typically stronger than the 95 GHz transition, and that the MALT-45 sensitivity is better, we perhaps expect our reported class II-to-class I association to be greater. As discussed in §3.4.5, Val’tts et al. (2000) finds the relative peak flux density of 95 GHz class I CH₃OH masers to 44 GHz class I CH₃OH masers to be approximately one-third. Assuming Ellingsen (2005) had a sensitivity cutoff for 95 GHz masers at 3 Jy, we can limit the results of the 44 GHz population by a 9 Jy cutoff. There are 17 44 GHz masers with a peak flux density greater than 9 Jy associated with a class II CH₃OH maser (36 per cent), which is only slightly lower than the proportion of associations found by Ellingsen (2005). Therefore, our results are reasonably consistent. Considering that the MALT-45 sensitivity to class I CH₃OH masers is better than that of Ellingsen (2005) by approximately a factor of 2, and that we search for 44 GHz masers instead of 95 GHz masers, we are assured that there is a higher association rate than previously reported.

The luminosities of class I and class II CH₃OH masers were compared, but no correlation

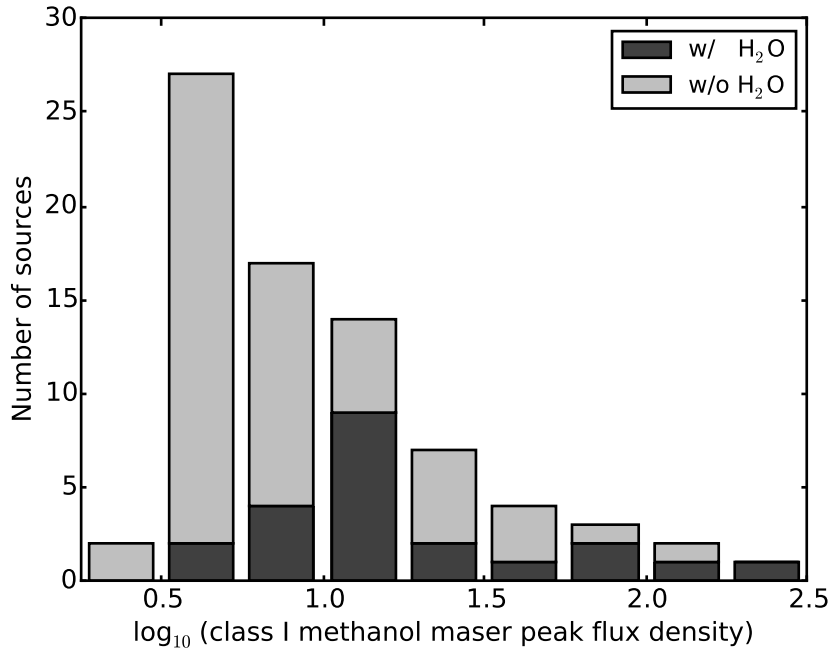


Figure 3.18: A stacked histogram of class I CH₃OH masers with and without H₂O masers. This plot shows that H₂O masers tend to be associated with brighter class I methanol masers.

was found (r^2 -value of 0.03); see Fig. 3.16. The relative populations for class I masers with and without a class II source are compared in Fig. 3.17; the histogram reveals that class II sources are associated with a wide range of class I brightnesses, which reaffirms the lack of correlation. With sensitive, targeted 44 GHz observations of class II masers, more data can be collected for a better analysis. Note that the search radius should be at least an arcmin to cover the range of separations between class I and class II masers; see §4.2 of Voronkov et al. (2014).

3.4.6.2 H₂O masers from HOPS

Water masers are another maser species that are collisionally excited. Therefore, we might expect a close association between class I methanol and water masers. HOPS has found H₂O masers in an untargeted way, and catalogues their findings into three association groups: star-forming, evolved star, and ‘unknown’ (Walsh et al. 2014). Breen et al. (2010a) also presents a catalogue of H₂O masers, typically associated with class II CH₃OH masers and/or OH masers.

HOPS has detected a total of 48 H₂O masers within the MALT-45 survey region (Walsh et al. 2011, 2014). Of these, HOPS has classified 10 as being associated with an evolved star, leaving 38 as star-forming or ‘unknown’. Including the Breen et al. (2010a) detections brings the total to 71, but there is a large overlap with the HOPS catalogue, as well as many H₂O masers near to others (within 60 arcsec). Similar to the MMB class II CH₃OH masers, after grouping masers into clusters, we compare MALT-45 class I CH₃OH masers against a total of 43 H₂O maser clusters.

Of these 43 H₂O maser clusters, 27 are associated with a class I CH₃OH maser (63 per

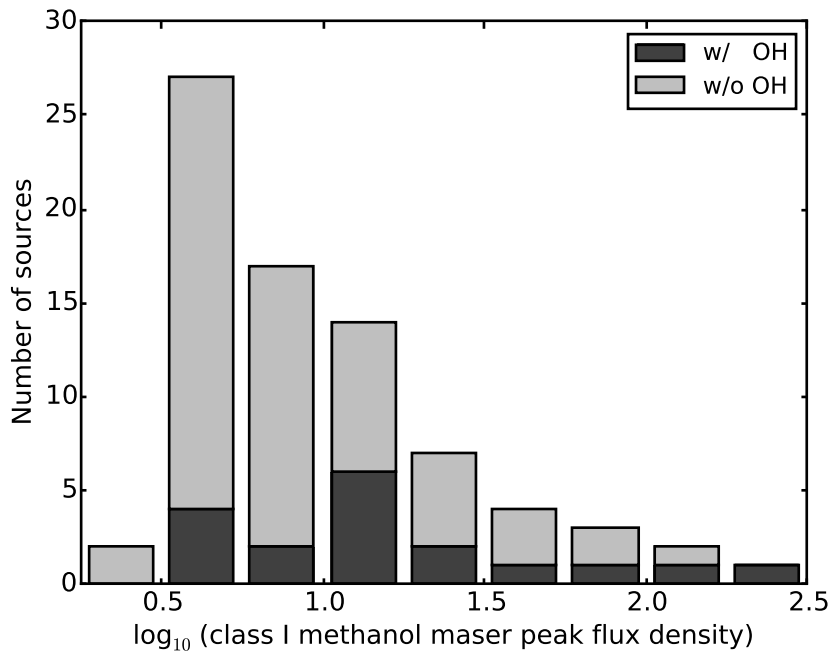


Figure 3.19: A stacked histogram of class I CH₃OH masers with and without OH (1612, 1665, or 1667 MHz) masers. OH masers appear to be associated with a wide range of class I methanol masers.

cent). It is possible that the class I CH₃OH population have more H₂O maser associations, but have not been found yet. Breen et al. (2010a) targeted observations towards known sources, and HOPS has a lower-bound sensitivity between 5 and 10 Jy. Follow-up observations for H₂O masers towards new class I CH₃OH masers may be productive in identifying new H₂O masers.

In the HOPS catalogue recently published (Walsh et al. 2014), the water masers G331.86+0.06 and G333.46−0.16 were not redetected in the high-resolution follow-up survey. The G333.46−0.16 water maser is associated with a MALT-45 class I CH₃OH maser, but this was a known class I CH₃OH maser region (along with other maser species). The G331.86+0.06 water maser, however, is slightly offset from a new class I CH₃OH maser. The offset is enough to not be included as an association, but it lends credence that this variable water maser is likely highlighting star-forming activity.

3.4.6.3 OH masers from Sevenster et al. (1997) and Caswell (1998)

Voronkov et al. (2010b) discuss the positioning of class I methanol maser emission on a HMSF evolutionary timeline, especially compared to other masers. Class II methanol masers have been characterised well in terms of their position in a HMSF timeline, associated with millimetre sources, but typically not H II regions. Unlike class II masers, class I masers are currently thought to be associated with both early- and late-type HMSF. This stems from finding class I masers associated with outflows, but also with OH masers.

To date, no unbiased comparison between OH and class I methanol masers has been performed. With the first unbiased sample of class I masers, we are able to analyse the

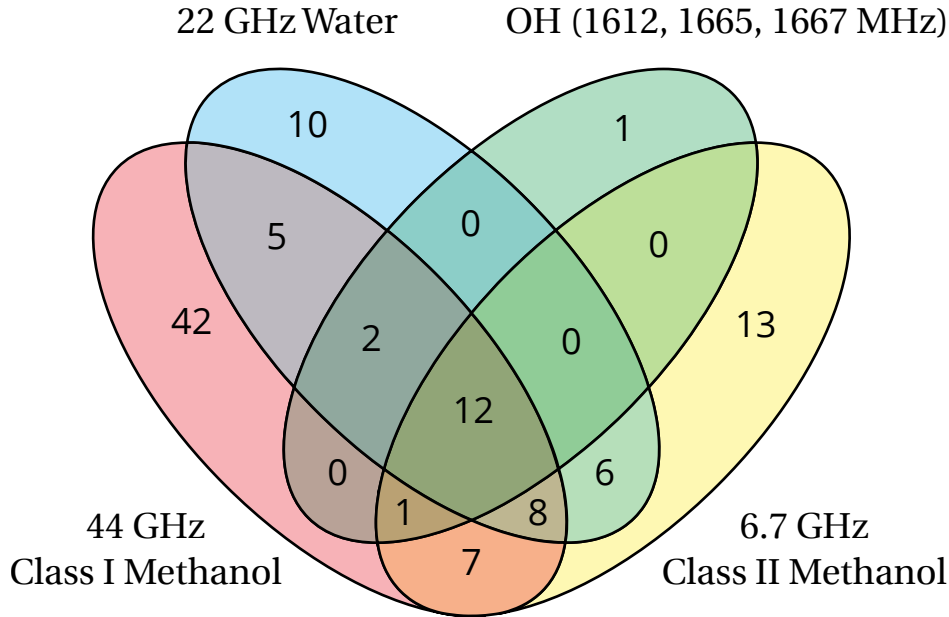


Figure 3.20: Venn diagram of all discussed maser region associations. The majority of maser regions have a class I CH_3OH component, particularly with class II CH_3OH as well, but there is a large population of class I masers without any associations.

relative populations and perhaps refine class I masers on an evolutionary timeline. Voronkov et al. (2010b) mentions that class I masers associated with OH masers are known primarily due to the class II methanol maser emission present, as most class I sources have been found toward class II sources. Caswell (1997) discuss how OH favoured maser regions have a greater number of associated H II regions than class II masers, indicating that OH masers typically signpost later stages of an evolutionary timeline than class II masers. Combining the OH masers found by Sevenster et al. (1997) and Caswell (1998), there are 16 star-forming OH masers within the MALT-45 survey region. The other OH masers in Sevenster et al. (1997) and Caswell (1998) are associated with evolved OH/IR stars, determined from SIMBAD and individual source descriptions within Caswell (1998). 94 per cent (15/16) of star-forming OH masers are associated with a class I CH_3OH maser. Of these 15, only 2 masers are without a 6.7 GHz class II methanol maser (13 per cent; G331.50–0.10 and G333.59–0.21). It is difficult to contrast maser regions containing OH but not class II methanol, as almost every OH maser in the survey region is associated with a class II CH_3OH maser. If a population of OH masers without class II CH_3OH was isolated, a better comparison with class I CH_3OH could be established. The MALT-45 survey results merely indicate that class I CH_3OH is associated with all maser species found.

There are 30 class I CH_3OH maser regions with associated class II CH_3OH or OH maser emission, indicating late stages of star formation. The remaining 47 masers are unaccounted for; if these are all associated with early-type star-formation, then class I CH_3OH masers appear to be more closely associated with earlier stages in an evolutionary timeline.

3.4.6.4 Summary of star-formation maser associations

A Venn diagram of the maser associations can be seen in Fig. 3.20. There appears to be a strong overlap between class I and class II CH₃OH masers, with and without the presence of H₂O and/or OH masers. This may suggest that the majority of class II CH₃OH masers are associated with class I CH₃OH masers because of an abundance of CH₃OH. The smaller population of class II CH₃OH masers without class I CH₃OH emission (40 per cent; 19/47) may indeed have no association, or even weaker class I CH₃OH emission than is detected by MALT-45.

There is a large population of class I CH₃OH masers without any other maser counterpart. As discussed, these may highlight non-star-forming phenomena, young regions of HMSF, or low mass star-forming regions. However, given the strong association with CS seen in Fig. 3.3 and with other HMSF masers seen in Fig. 3.20, the majority of class I CH₃OH masers are likely associated with HMSF.

Figs 3.17, 3.18 and 3.19 show the luminosity population of class I CH₃OH masers as stacked histograms. Generally, the presence or absence of other maser transitions does not appear to correlate with the class I CH₃OH maser luminosity.

Titmarsh et al. (2014) discuss the placement of H₂O masers within an evolutionary timeline for HMSF, and concluded that they are not likely to be associated with any specific phase of a timeline, but rather dependant on the environment. As H₂O masers are collisionally excited like class I CH₃OH masers, and class I masers are associated with a wide range of other species (with and without class II CH₃OH, OH), we tend to agree that the environment plays perhaps the predominant role in determining the likelihood of a region having an associated class I CH₃OH maser rather than the evolutionary phase.

Investigation of the peak flux densities and luminosities of class I CH₃OH masers versus class II CH₃OH, H₂O and OH masers does not reveal any relation. Investigation will be performed again in a subsequent MALT-45 maser follow-up paper, where maser regions can be better associated and flux density calibration is able to be more accurately determined.

3.4.7 SiO $v = 1, 2, 3$ maser associations

MALT-45 has detected 47 regions with at least one of the vibrationally excited lines $v = 1, 2, 3$ of SiO (1–0) maser emission. Of these, 4 are associated with a OH maser (all 1612 MHz, G331.60–0.14 has an additional 1665 MHz), and 8 are associated with a H₂O maser. OH and H₂O masers are common companions with evolved infrared stars (Caswell 1998; Walsh et al. 2014), and indeed GLIMPSE reveals that all SiO maser regions have an infrared star associated within 30 arcsec of the peak maser position. There is no overlap of SiO masers associated with both an OH and H₂O maser. The population presented in this paper associated with OH and H₂O masers is insufficient to perform correlation tests upon. None of the SiO masers detected have been reported previously; thus, MALT-45 is a productive survey for identifying evolved stars not found in other searches.

The SiO $v = 1$ line generally appears to be the strongest of the three maser lines, and is the most common detection. There are eleven cases where the $v = 2$ line is stronger than $v = 1$, and two regions contain only $v = 2$ emission. This result is somewhat unexpected, as

generally the lower v transitions should be brighter than the higher v transitions. Gray et al. (2009) predict that SiO masers should have brightness decreasing with $v = 1, 2, 3$, and the $v = 2$ is often weaker due to overlap with a water line. Neither of the two regions with only SiO $v = 2$ emission have other masers associated, but the sub-population of SiO regions with brighter $v = 2$ than $v = 1$ have three H₂O masers and two OH masers associated. This is almost half of all masers associated with SiO regions. However, we currently cannot explain why some $v = 2$ masers are stronger than their $v = 1$ counterparts. Only three $v = 3$ lines are detected, and these are all quite weak, especially compared to the $v = 1, 2$ lines within the same region; it appears that this line is difficult to detect without sensitive observations.

The only SiO maser with nearby CH₃OH masers is G333.90–0.09, but is separated by 33 arcsec. The same SiO maser is 13 arcsec from a Sevenster 1612 MHz OH maser, which is cospatial with a star in GLIMPSE. As the nearby class I and class II CH₃OH masers are only 4 arcsec apart but separated from the star, we consider both pairs of masers to not be associated.

3.5 Summary

MALT-45 has successfully probed the Galactic plane for CS (1–0), 44 GHz class I methanol masers, and the SiO (1–0) family of $v = 0, 1, 2, 3$ lines. This is the first survey to produce a large scale unbiased map of CS, and is the first untargeted search of class I CH₃OH masers and SiO emission. Further publications will reveal the full 7 mm star-forming environment, through the remaining lines mapped by this survey. With time, MALT-45 could be extended to map more of the Galactic plane, revealing more about the nature of star formation within our Galaxy. With the current survey, we have determined:

(i) Across the survey region, the CS/NH₃ ratio is low in the centres of many clumps, but higher at the edges. This is likely due to a combination of increased NH₃ abundance and CS being depleted and/or becoming optically thick in the centres of clumps;

(ii) A large population of class I methanol masers are not associated with other masers (55 per cent);

(iii) Class I methanol masers are good indicators of systemic velocities;

(iv) Class I methanol masers are found towards most known class II methanol, water and hydroxyl masers within the survey region. Thus, positioning class I methanol on a maser timeline of HMSF is difficult, and the occurrence of class I methanol masers is perhaps more likely due to environmental factors;

(v) Silicon monoxide masers associated with evolved stars are most commonly detected in their $v = 1$ vibrational mode. When a region contains more than one vibrational mode, the intensity typically descends with vibrational mode ($v = 1, 2, 3$). However, we find two cases where we only detect $v = 2$ and eleven cases where both $v = 1$ and $v = 2$ are detected, but the $v = 2$ is stronger.

Chapter 4

MALT-45 - II. Follow-up observations of 44 GHz class I methanol masers

This chapter details an in-progress, co-authored publication. The authors of this paper are: Jordan, C. H., Walsh, A. J., Ellingsen, S. P., Voronkov, M. A., Breen, S. L. When complete, this work will be submitted to the Monthly Notices of the Royal Astronomical Society.

The introduction section has been modified to streamline the discussed literature, to avoid unnecessary overlap with Chapter 1.

Abstract

We detail interferometric observations of 44 GHz class I methanol masers detected by MALT-45. We detect 238 maser spots across 77 maser regions. Using high-resolution positions, we compare the detected masers to other star-forming maser species, and use single-dish data provided by these observations for brightness comparisons. We find that the majority of class I methanol masers have small spatial and velocity spreads, and closely trace the systemic velocities of associated clouds. Using ATLASGAL sources, we determine clump masses associated with class I masers, and find they are generally associated with clumps between 1000 and 3000 M_{\odot} . We use the presence of class II CH₃OH masers, OH masers or radio recombination lines to distinguish younger and older regions of high-mass star formation, and find that young regions have lower luminosities and appear toward dark infrared regions.

4.1 Introduction

Methanol masers are one of the best high-mass star-forming tracers available to astronomers. Empirically, they are divided into two groups: class I and class II. Class II CH₃OH masers are exclusively associated with high-mass star formation (HMSF) and signpost a distinct evolutionary stage (Minier et al. 2003; Green et al. 2012; Breen et al. 2013). The connection

between HMSF and class I CH₃OH masers is less certain; observations have shown that these masers can be found towards many star-forming regions and evolutionary stages, but not consistently, and not necessarily with or without the presence of class II masers (Ellingsen 2006; Voronkov et al. 2010b; Breen et al. 2010a; Ellingsen et al. 2013). Additionally, class I maser emission has been found towards low-mass star formation (Kalenskii et al. 2010), supernova remnants (Pihlström et al. 2014; McEwen et al. 2014) and the centres of galaxies (Yusef-Zadeh et al. 2013; Ellingsen et al. 2014).

The MALT-45 survey paper (Jordan et al. 2015; hereafter Paper I) discussed the mapped region $330^\circ \leq l \leq 335^\circ$, $b = \pm 0.5^\circ$, and found 77 class I CH₃OH masers, 58 of which were new detections. For the first time, with a flux-density limited sample of class I sources, we are able to test the bulk-properties of these masers. Paper I in this series of MALT-45 publications briefly investigated the association of methanol masers with other detected spectral lines, but was ultimately limited by the spatial resolution of the auto-correlation survey (~ 1 arcmin). In this chapter, we detail the results of interferometric follow-up observations towards each of the class I CH₃OH masers observed in Paper I, in order to derive accurate positions.

4.2 Observations

Observations were conducted on 2013 September 7 and 8 using the Australia Telescope Compact Array. The array configuration was 1.5A, which has 5 antennas distributed in the East-West direction with baselines ranging from 153 m to 1.5 km; the maximum baseline is 4.5 km including antenna 6 (CA06), however, CA06 has a different surface to the others, and suffers poor sensitivity at 7 mm. Consequently, data from CA06 is not included in this chapter.

The correlator was programmed in the 64M-32k mode, which provides a 32 kHz channel resolution over 64 MHz. However, unlike Paper I, each spectral line used ‘stitched zooms’, which increases the frequency coverage to 96 MHz (except for the zoom containing H51 α and C³⁴S (1–0), which covers 224 MHz). For observations in this waveband, the 32 kHz channel resolution results in a spectral resolution of approximately 0.2 km s^{–1} per channel. The spectral lines observed are identical to that of Paper I. The list of observed lines and velocity coverage information is contained in Table 4.1. Since Paper I, the rest frequencies of the SiO (1–0) molecular lines have been updated (Müller et al. 2013).

Targets were chosen from Paper I for their class I CH₃OH emission; see Table 4.2. Note that the targets for these observations are not identical to those listed in Paper I; these observations used a source list extracted from preliminary MALT-45 data reduction. Consequently, not all masers listed in Paper I are discussed in this chapter. The additional sources detailed in this chapter but not Paper I are G331.44–0.14, G331.44–0.16, G333.01–0.46, G333.12–0.43. The sources not detailed in this chapter but listed in Paper I are G331.36–0.02 and G334.64+0.44. For more details, refer to §4.3. Hence, a total of 79 targets were observed over the two days of observations. Each target was observed in a series of one minute cuts spread out over a single observing day. Each target has at least seven cuts, but some have up to ten; the noise levels for each target are also listed in Table 4.2.

Bandpass calibration was derived from PKS B1253–055, phase calibration from PMN

Table 4.1: Bright spectral lines between 42.2 to 49.2 GHz, targeted by MALT-45 and these observations. Column 1 lists the spectral line. Column 2 lists the rest frequency of the line. Column 3 classifies the line as either a maser or thermal line. Column 4 gives the ATCA pointing beam size at this frequency. Column 5 indicates whether this line is detailed in this chapter (‘Y’) or not (‘N’); this refers to the inclusion of Gaussian fits to the emission from these lines. Column 6 lists the median RMS noise level per spectral channel, with errors representing the standard deviation. The RMS noise is given to two significant figures. Radio recombination line (RRL) frequencies are taken from Lilley & Palmer (1968). All other rest frequencies are taken from the Cologne Database for Molecular Spectroscopy (CDMS; Müller et al. 2005). Note that RMS noise levels are specified for auto-correlation data; cross-correlation noise levels are given in Table 4.2.

Spectral line	Frequency (GHz)	Maser or thermal?	Beam size (arcsec)	Detailed in this chapter?	Median RMS noise level
SiO (1-0) $v = 3$	42.51938	Maser	66	N	
SiO (1-0) $v = 2$	42.82059	Maser	66	N	
H53 α (RRL)	42.95197	Thermal	65	N	8.7 \pm 1.5 mK
SiO (1-0) $v = 1$	43.12207	Maser	65	N	
SiO (1-0) $v = 0$	43.42385	Thermal	65	Y	5.9 \pm 0.67 mK
CH ₃ OH 7(0,7)–6(1,6) A ⁺	44.06941	Maser (Class I)	64	Y	170 \pm 62 mJy
H51 α (RRL)	48.15360	Thermal	58	N	
C ³⁴ S (1-0)	48.20694	Thermal	58	N	8.1 \pm 0.85 mK
CH ₃ OH 1 ₀ –0 ₀ A ⁺	48.37246	Thermal	58	Y	7.7 \pm 1.8 mK
CH ₃ OH 1 ₀ –0 ₀ E	48.37689	Thermal	58	N	
OCS (4–3)	48.65160	Thermal	58	N	
CS (1–0)	48.99095	Thermal	57	Y	8.9 \pm 1.3 mK

J1646–5044 and flux-density calibration from PKS 1934–638. The assumed flux-density of PKS 1934–638 was 0.39 Jy for both days of observation at the rest frequency of the 44 GHz class I CH₃OH maser line.

4.2.1 Data reduction

4.2.1.1 Cross-correlation

Class I CH₃OH maser data were reduced using standard interferometric techniques with MIRIAD. For all data cubes reduced, the synthesised beam is approximately 0.5 \times 1 arcsec in right ascension and declination, respectively. Voronkov et al. (2014) observed many 44 GHz class I CH₃OH masers with the ATCA; similar to that publication, the results presented in this chapter make use of self-calibrated data cubes. Self-calibration arbitrarily affects the absolute positional accuracy of data; to remove this effect, a reference maser feature was used. The position of this reference feature was determined before and after self-calibration and the measured difference was used to determine the absolute positions for all spectral features in the self-calibrated data cube. Ideally, the reference position before and after self-calibration has not shifted significantly (>0.5 arcsec), but some significant offsets were unavoidable in these data ($\gg 10$ arcsec). Prior experience with the ATCA in this waveband suggests that the absolute positional accuracy is around 0.5 arcsec (Voronkov et al. 2014). However, given that we experience non-ideal self-calibration offsets and the synthesised beam for each region is approximately 0.5 \times 1 arcsec, the absolute positional error for any maser

spot should be considered as being no better than 1 arcsec.

Data cubes were produced for each of the target regions, then maser spots were identified by inspection. In this chapter, a maser spot refers to a spatial and spectral peak of emission. Spots were classified if the spectrum contained at least three consecutive channels of 3σ emission, with a peak of at least 5σ . We employ this conservative approach of maser identification so the reader can be confident that all identified maser spots are real. A small number of weaker, narrow features may have been missed using these criteria; however, from past experience and comparison of our cubes with previous observations (where available), we suggest that this is not common. The requirement of three consecutive channels has the effect of limiting our maser detections to a velocity width of at least 0.65 km s^{-1} . Similar to Voronkov et al. (2014), dynamic range limitations exist for channels containing extremely bright maser emission. This reduces the ability to identify real maser emission at a similar velocity to the bright feature; maser spots were not classified if they were believed to be the product of such dynamic range artefacts.

Once each maser spot was identified, positions were fitted with the MIRIAD task IMFIT for each channel of emission ($>3\sigma$). IMFIT used a 3×3 arcsec box around each maser spot to generate a position, except for those with nearby bright masers. To accurately position weaker masers close to bright ones, either the velocity range of emission was altered for position fitting, or the size of the box for fitting was decreased. Decreasing the size of the box for IMFIT was found to not significantly affect resultant positions, so we do not specifically identify the maser spots using these modified procedures. Each channel-fitted position is then flux-weighted and is listed in Appendix B.1. The uncertainty reflects the 1σ of each channel-fitted position. In some cases, the maser spot positions have uncertainties of a few tens of milliarcsec. We caution that we are unlikely to determine relative positions to this accuracy for these observations, as dynamic range and calibration uncertainties become a limiting factor. Additionally, we remind the reader that the absolute positional accuracy of the observations is around 1 arcsec. In general, we found the class I maser spots were spatially distinguished by our observations, with separations of 1 arcsec or greater, but occasionally spots were very near to a bright neighbour. In these cases, positions were manually assigned by using the brightest pixel, with a more generous position uncertainty of 100 milliarcsec in Right Ascension and 200 milliarcsec in Declination. Such maser spots are designated with an asterisk (*) in Appendix B.1.

Spectral information for each maser spot were derived from image cubes, which were then characterised with Gaussian fits. Each Gaussian was fitted to minimise residuals, but in many cases it was not possible to match the root-mean-square (RMS) noise of the spectrum. This is partially due to the channel resolution being broad for maser parameterisation ($\sim 0.2 \text{ km s}^{-1}$). However, all Gaussian residuals are within 10 per cent of the fitted peak intensity. Coupled with uncertainties in calibration, we ascribe a 20 per cent uncertainty to all quoted flux-density values.

4.2.1.2 Auto-correlation

Each targeted maser region simultaneously observed for CS (1–0), SiO (1–0) $v = 0$ and $\text{CH}_3\text{OH } 1_0\text{--}0_0 \text{ A}^+$. However, due to their thermal nature and the uv -coverage of the obser-

vations, these thermal emission lines were not detectable in the cross-correlation data. To report on these properties, a RUBY script was written to assist with the analysis of the auto-correlated data. Unlike Paper I, no dedicated reference position was observed. Instead, data collected at the location where the emission is known to be weak and have a simple spectral profile was used as the reference location for auto-correlations. The script routine pipeline was as follows:

- (i) For each source, a raw auto-correlation spectrum was produced for each antenna and each cut;
- (ii) For each antenna source cut, a quotient spectrum was formed from the source and reference cut data;
- (iii) A first-order polynomial was fitted to and removed from the spectra. The velocity range of the fit was restricted to -160 and 20 km s^{-1} , as this contains all of the emission in this section of the Galaxy, and constraining the fit improves the quality of the resulting spectra;
- (iv) All quotient spectra from an antenna are averaged together, before averaging all antennas together;
- (v) The flux-density calibration is achieved by using values from Paper I.

This procedure is graphically demonstrated to the CS emission of G330.95–0.18 in Fig. 4.1. Existing software solutions for auto-correlation processing were inadequate for the data collected, however, this auto-correlation script is robust at producing publication quality results.

For each of the auto-correlated CS, SiO and CH₃OH thermal lines, spectra are smoothed with a Hanning window of 9 spectral channels, and up to two Gaussians were fitted to characterise the data. This smoothing results in a velocity resolution of $\sim 0.39 \text{ km s}^{-1}$ for CS, $\sim 0.44 \text{ km s}^{-1}$ for SiO $v = 0$ and $\sim 0.40 \text{ km s}^{-1}$ for CH₃OH 1_0-0_0 A^+ . As with the cross-correlation data, Gaussians are fitted to minimise residuals; however, occasionally 10 per cent residuals are unavoidable. With additional flux-density calibration uncertainty applied to auto-correlation data, we place a 20 per cent uncertainty on all intensity values derived.

This auto-correlation procedure was also used for class I CH₃OH masers, which is used for integrated intensities, luminosities, and comparison with the cross-correlation data in §4.4.5.

4.3 Results

The basic properties of each observed target are listed in Table 4.2. Note that five sources were not detected in cross-correlation by these observations, but three of these five were detected in auto-correlation (G331.44–0.14, G331.72–0.20 and G333.24+0.02). Their non-detection in cross-correlation is likely caused by the emission being too extended, and hence are resolved out by interferometric observations. Poor phases may also affect the lack of maser spots detected. Extended CH₃OH emission at 44 GHz could be caused by quasi-thermal rather than masing mechanisms, or even broad but weak maser components. Further discussion of cross-correlation spectra compared to the auto-correlation data for the same source is contained in §4.4.5. The remaining two sources (G330.83+0.18 and G331.21+0.10) may have varied in their intensity, resulting in them not being detected by these observations in cross- and auto-correlation. However, false-positives listed by Paper I are more probable; the

auto-correlation sensitivity of the observations reported in this chapter is ~ 170 mJy, and the Paper I peak flux densities are 3.1 and 3.5 Jy, observed at October 2013. Our non-detection therefore requires a flux-density variation in these masers of a factor of 20. Additionally, each of these masers only appear to have a single feature. Given that class I CH₃OH maser variability is not well characterised, and that the flux-densities of other masers detected in Paper I and these observations are largely consistent, we deem these two regions as false-positives of Paper I. For the remainder of this chapter, we discuss the 77 regions containing 44 GHz class I CH₃OH emission.

Associations with other maser transitions and selected HMSF tracers are detailed in Table 4.3. Each region is compared with published positions of class II CH₃OH (Caswell et al. 2011), water (H₂O) (Breen et al. 2010a; Walsh et al. 2014) and hydroxyl (OH) masers (Sevenster et al. 1997; Caswell 1998), as well as ATLASGAL sources (Contreras et al. 2013). The presence of each thermal line is determined by the method described in §4.2.1.2, using data from these observations. CS is detected towards every source, and because of this is not listed in Table 4.3. The Gaussian parameters determined for each of the thermal lines are listed in Appendix B.2. Uncertainties for each of the fitted parameters are quoted, however, we remind the reader to consider the 20 per cent uncertainty placed upon all intensity values.

Kinematic distances are also contained in Table 4.3. Like Paper I, distances were calculated using the program supplied by Reid et al. (2009); however, all distances in this chapter have been calculated using a ‘near’ kinematic distance, whereas Paper I used a ‘far’ distance when prescribed by Green & McClure-Griffiths (2011). Given the similar velocities to other nearby masers and how well the class I CH₃OH masers trace the dense gas, we abandon the far distance prescription; see Fig. 3.3 of Paper I. The affected masers are G332.583+0.147, G333.313+0.106, G333.387+0.031, G333.562–0.025 and G333.900–0.098. The need for accurate near/far selection arises in analysis conducted later in this chapter, particularly with mass calculation in §4.4.4. All distances presented in this chapter use the same parameters as Paper I, specifically: $\Theta_0 = 246 \text{ km s}^{-1}$, $R_\odot = 8.4 \text{ kpc}$, $U_\odot = 11.1 \text{ km s}^{-1}$, $V_\odot = 12.2 \text{ km s}^{-1}$, $W_\odot = 7.25 \text{ km s}^{-1}$, $U_s = 0 \text{ km s}^{-1}$, $V_s = -15.0 \text{ km s}^{-1}$, $W_s = 0 \text{ km s}^{-1}$, $\sigma(V_{LSR}) = 3.32 \text{ km s}^{-1}$.

The complete collection of Gaussian fits to class I CH₃OH spots are included in Appendix B.1, and Gaussian fits to thermal emission are included in Appendix B.2. Maser positions overlaid on infrared images from the *Spitzer* Galactic Legacy Infrared Mid-Plane Survey Extraordinaire (GLIMPSE; Benjamin et al. 2003) can be seen in Appendix B.3.

The auto-correlation sensitivity of these observations is approximately a factor of 5 better than that of Paper I, and has improved the detection rate of thermal lines towards the class I CH₃OH masers. Paper I had detectable CS emission towards 95 per cent of class I CH₃OH masers, whereas these data have detectable CS towards every maser. Thermal SiO emission detection statistics are greatly improved; these data have detectable SiO towards 83 per cent of regions (64/77), which is a significant increase over Paper I (30 per cent). The thermal 1_0-0_0 A⁺ line of CH₃OH was not characterised in Paper I, but auto-correlations have also been produced for this chapter. The MALT-45 data cube of thermal CH₃OH had a similar detection rate compared to thermal SiO, but here it is detected towards almost all regions (75/77; 97 per cent). Additionally, we list detections of H53 α and C³⁴S with the targeted

maser regions, along with median RMS noise levels in Table 4.1, but do not list their properties for conciseness. The thermal lines are used for various comparisons in §4.4.

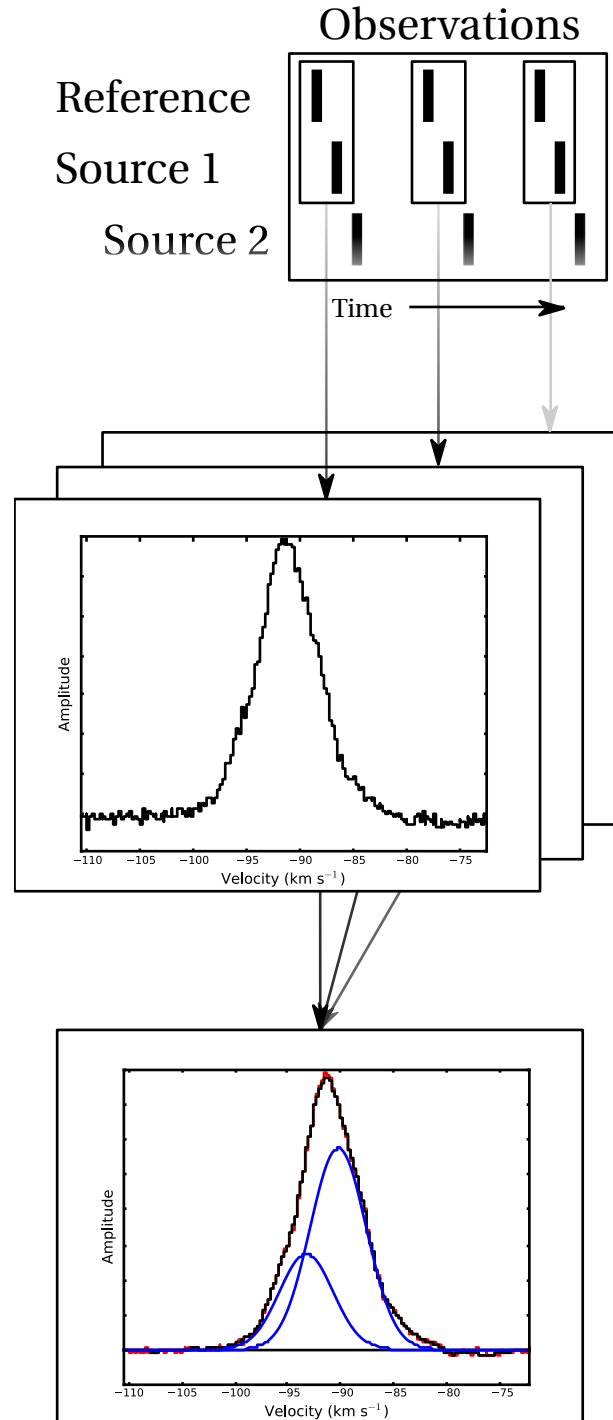


Figure 4.1: A graphical representation of the reduction procedure for auto-correlation data used in this chapter. The data from each source cut is combined with the nearest reference cut in time to produce a baselined cut. All baselined cuts are then averaged to produce an auto-correlation product. This procedure is performed for each antenna of the ATCA, and all products are then averaged together for a final product. The final panel contains the raw spectrum (red) and the Hanning-smoothed (black). This example uses two Gaussians (blue) to characterise the data.

Table 4.2: Targeted class I CH₃OH masers, as well as their parameters. Column 1 lists the region name taken from Paper I. Column 2 lists the refined region name, based on the average position of maser spots found within that region. The refined region names are used throughout this chapter instead of the Paper I names. A refined name is not supplied if no maser emission was detected in interferometry. Columns 3 and 4 list the targeted position for these observations. Column 5 gives the date on which the region was observed (7 or 8 September 2013). Column 6 lists the median RMS noise value for the self-calibrated cube. Column 7 lists the smallest radius of a circle to encompass all emission of the region. Column 8 lists the velocity range of emission detected in auto-correlation data. All maser regions were observed with an approximate local standard of rest velocity coverage between -353 and 195 km s^{-1} . Note that regions with a radius of <1 arcsec contain either only one maser spot, or spots very close together. Regions without a radius were not detected in interferometry. Regions without a velocity range were not detected in interferometry or auto-correlation (likely false-positives; see §4.3). Regions labelled with an asterisk (*) were not listed by Paper I, but have class I CH₃OH maser emission detected by these observations. Regions labelled with a dagger (†) are designated as ‘young’; see §4.4.3.

Paper I region name	Refined region name	Pointing centre		Obs. date	Median RMS noise level	Radius (arcsec)	Velocity range
		α_{2000} (h:m:s)	δ_{2000} (°:′:″)	(Sep. 2013)	(mJy)		(km s^{-1})
G330.30-0.39	G330.294-0.393	16:07:37.0	-52:30:59	8	46	4	-82 to -76
G330.67-0.40	G330.678-0.402	16:09:30.6	-52:16:08	8	42	< 1	-69 to -60
G330.78+0.24†	G330.779+0.249	16:07:12.2	-51:43:07	8	42	< 1	-46 to -41
G330.83+0.18		16:07:40.6	-51:43:54	8	44		
G330.87-0.36	G330.876-0.362	16:10:16.6	-52:05:50	8	45	22	-66 to -57
G330.88-0.38	G330.871-0.383	16:10:21.1	-52:06:42	8	44	< 1	-67 to -57
G330.92-0.41†	G330.927-0.408	16:10:44.2	-52:05:56	8	45	3	-44 to -40
G330.93-0.26†	G330.931-0.260	16:10:06.6	-51:59:23	8	43	1	-91 to -87
G330.95-0.18	G330.955-0.182	16:09:52.0	-51:54:59	8	46	< 1	-98 to -84
G331.13-0.48†	G331.131-0.470	16:11:59.8	-52:00:32	8	44	< 1	-70 to -65
G331.13-0.25	G331.132-0.244	16:10:59.7	-51:50:25	8	46	10	-93 to -78
G331.13-0.50	G331.134-0.488	16:12:05.9	-52:01:33	8	37	< 1	-68 to -68
G331.13+0.15	G331.134+0.156	16:09:14.8	-51:32:47	8	46	4	-79 to -73
G331.21+0.10		16:09:50.8	-51:32:39	8	44		
G331.29-0.20	G331.279-0.189	16:11:27.0	-51:41:54	8	45	21	-95 to -84
G331.34-0.35	G331.341-0.347	16:12:25.6	-51:46:16	8	46	< 1	-67 to -64
G331.37-0.40†	G331.370-0.399	16:12:48.2	-51:47:26	8	44	< 1	-66 to -64
G331.37-0.13†	G331.371-0.145	16:11:40.3	-51:35:52	8	47	< 1	-89 to -86
G331.39+0.15†	G331.380+0.149	16:10:26.2	-51:22:52	8	46	< 1	-47 to -43
G331.41-0.17†	G331.409-0.164	16:11:59.2	-51:35:33	8	45	< 1	-85 to -85
G331.44-0.14*†		16:11:57.9	-51:33:08	8	45		-87 to -84
G331.44-0.19	G331.440-0.187	16:12:11.5	-51:35:02	8	44	5	-92 to -85
G331.44-0.16*†	G331.442-0.158	16:12:05.0	-51:33:45	8	40	< 1	-87 to -85
G331.50-0.08	G331.492-0.082	16:11:59.6	-51:28:14	8	46	22	-93 to -84
G331.50-0.10	G331.503-0.109	16:12:10.5	-51:29:23	8	44	17	-101 to -86
G331.52-0.08	G331.519-0.082	16:12:07.5	-51:27:25	8	44	8	-93 to -85
G331.54-0.10	G331.530-0.099	16:12:14.5	-51:27:34	8	45	19	-95 to -85
G331.55-0.07	G331.544-0.067	16:12:11.3	-51:25:29	8	45	7	-92 to -85
G331.56-0.12	G331.555-0.122	16:12:26.7	-51:27:41	8	44	3	-104 to -97
G331.72-0.20†		16:13:34.4	-51:24:25	8	46		-49 to -45
G331.86-0.13†	G331.853-0.129	16:13:52.3	-51:15:42	8	46	< 1	-52 to -48
G331.88+0.06†	G331.887+0.063	16:13:10.5	-51:06:09	8	44	12	-91 to -84
G331.92-0.08†	G331.921-0.083	16:13:58.0	-51:10:56	8	46	< 1	-53 to -51
G332.09-0.42	G332.092-0.420	16:16:15.6	-51:18:31	8	46	7	-59 to -54
G332.24-0.05†	G332.240-0.044	16:15:17.6	-50:55:59	8	47	8	-51 to -46
G332.30-0.09	G332.295-0.094	16:15:46.0	-50:55:54	8	46	8	-55 to -45
G332.32+0.18†	G332.318+0.179	16:14:40.0	-50:43:11	8	45	10	-50 to -44
G332.36-0.11	G332.355-0.114	16:16:07.3	-50:54:16	8	45	< 1	-51 to -49
G332.59+0.15	G332.583+0.147	16:15:58.5	-50:33:22	8	45	< 1	-45 to -42
G332.60-0.17	G332.604-0.167	16:17:28.1	-50:46:20	8	46	2	-48 to -44
G332.72-0.05†	G332.716-0.048	16:17:28.6	-50:36:34	8	45	2	-41 to -38
G333.00-0.43	G333.002-0.437	16:20:27.7	-50:41:06	8	45	< 1	-57 to -55
G333.01-0.46*	G333.014-0.466	16:20:37.1	-50:41:31	7	41	< 1	-55 to -52
G333.02-0.06	G333.029-0.063	16:18:55.9	-50:24:03	8	43	1	-43 to -39
G333.03-0.02	G333.029-0.024	16:18:45.9	-50:22:21	7	41	< 1	-43 to -41
G333.07-0.44	G333.068-0.446	16:20:49.6	-50:38:51	7	46	< 1	-55 to -51
G333.07-0.40	G333.071-0.399	16:20:37.0	-50:36:33	7	42	6	-54 to -51
G333.10-0.51	G333.103-0.502	16:21:13.4	-50:39:56	7	41	11	-60 to -53
G333.12-0.43*	G333.121-0.433	16:20:58.5	-50:35:41	7	54	3	-57 to -44
G333.13-0.44	G333.126-0.439	16:21:02.3	-50:35:53	7	55	12	-57 to -42
G333.14-0.42	G333.137-0.427	16:21:03.0	-50:34:59	7	49	17	-59 to -43
G333.16-0.10	G333.162-0.101	16:19:41.4	-50:19:55	7	35	4	-93 to -90
G333.18-0.09	G333.184-0.090	16:19:45.2	-50:18:45	7	37	10	-89 to -84
G333.22-0.40	G333.220-0.402	16:21:16.9	-50:30:17	7	42	4	-57 to -49
G333.23-0.06	G333.233-0.061	16:19:49.4	-50:15:17	7	42	14	-96 to -81
G333.24+0.02†		16:19:26.0	-50:11:29	7	42		-71 to -66
G333.29-0.38	G333.284-0.373	16:21:28.1	-50:26:35	7	43	< 1	-55 to -49
G333.30-0.35	G333.301-0.352	16:21:24.5	-50:24:47	7	40	< 1	-54 to -48
G333.31+0.10	G333.313+0.106	16:19:27.6	-50:04:45	7	55	8	-51 to -43
G333.33-0.36	G333.335-0.363	16:21:36.4	-50:23:53	7	44	18	-55 to -46
G333.37-0.20†	G333.376-0.202	16:21:05.2	-50:15:18	7	44	5	-63 to -56
G333.39+0.02	G333.387+0.031	16:20:08.2	-50:04:49	7	39	3	-73 to -68
G333.47-0.16	G333.467-0.163	16:21:19.5	-50:09:42	7	40	12	-49 to -38

Table 4.2: *continued*

MALT-45 region name	Refined region name	Pointing centre		Obs. date (Sep. 2013)	Median RMS noise level (mJy)	Radius (arcsec)	Velocity range (km s ⁻¹)
		α_{2000} (h:m:s)	δ_{2000} ($^{\circ}$: $'$: $''$)				
G333.50+0.15 [†]	G333.497+0.143	16:20:06.5	-49:55:25	7	42	2	-115 to -111
G333.52-0.27	G333.523-0.275	16:22:03.4	-50:12:08	7	42	< 1	-52 to -49
G333.56-0.30	G333.558-0.293	16:22:19.2	-50:11:28	7	42	27	-47 to -44
G333.56-0.02	G333.562-0.025	16:21:07.9	-49:59:49	7	44	< 1	-43 to -37
G333.57+0.03 [†]	G333.569+0.028	16:20:55.4	-49:57:25	7	42	< 1	-86 to -81
G333.59-0.21	G333.595-0.211	16:22:06.2	-50:06:30	7	45	4	-52 to -44
G333.70-0.20	G333.694-0.197	16:22:27.7	-50:01:22	7	41	9	-52 to -49
G333.71-0.12 [†]	G333.711-0.115	16:22:10.8	-49:57:21	7	41	5	-32 to -30
G333.77-0.01 [†]	G333.772-0.010	16:21:59.6	-49:50:20	7	42	< 1	-91 to -88
G333.77-0.25 [†]	G333.773-0.258	16:23:02.8	-50:00:31	7	40	< 1	-50 to -47
G333.82-0.30 [†]	G333.818-0.303	16:23:29.5	-50:00:40	7	41	1	-50 to -46
G333.90-0.10	G333.900-0.098	16:22:56.3	-49:48:43	7	41	4	-66 to -61
G333.94-0.14	G333.930-0.133	16:23:14.1	-49:48:40	7	44	5	-43 to -39
G333.98+0.07 [†]	G333.974+0.074	16:22:31.0	-49:38:08	7	40	< 1	-62 to -57
G334.03-0.04 [†]	G334.027-0.047	16:23:16.7	-49:40:57	7	41	< 1	-85 to -83
G334.74+0.51 [†]	G334.746+0.506	16:23:57.9	-48:46:40	7	38	4	-66 to -59

Table 4.3: Associations with each of the targeted class I CH₃OH masers. Note that the presence of CS (1-0) is not listed, because it is detected towards every source. Column 1 lists the average position of all maser emission in Galactic coordinates. Columns 2 and 3 list the same average position in right ascension and declination. Column 4 lists the kinematic distance. Uncertainties are listed in units of the least significant figure. Column 5 lists the presence of other masers and ATLASGAL sources within 1 arcmin of the centre position. If there is more than one of a type of association, the number is listed as a subscript. Column 6 lists whether thermal SiO (1-0) emission is detected (‘Y’) or not (‘N’). Regions labelled with a dagger (†) are designated as ‘young’; see §4.4.3.

Region name	Centre of maser emission		Kinematic distance	Associations within 1 arcmin ¹	Presence of SiO (1-0) $v = 0?$	Presence of CH ₃ OH $1_0-0_0 A^+?$	Presence of H53 α ?	Presence of C ³⁴ S (1-0)?
	α_{2000} (h:m:s)	δ_{2000} ($^{\circ}$: $'$: $''$)	(kpc)					
G330.294-0.393	16:07:37.9	-52:30:58.29	4.9 (2)	WA	N	Y	Y	Y
G330.678-0.402	16:09:31.7	-52:15:50.68	4.1 (2)	A	Y	Y	Y	Y
G330.779+0.249 [†]	16:07:09.8	-51:42:53.76	3.1 (2)	A	Y	Y	N	Y
G330.871-0.383	16:10:22.1	-52:07:08.28	4.1 (2)	MA	Y	Y	Y	Y
G330.876-0.362	16:10:17.9	-52:05:59.37	4.0 (2)	MWSCGA ₂	Y	Y	Y	Y
G330.927-0.408 [†]	16:10:44.7	-52:05:57.33	3.1 (2)	A	Y	Y	N	Y
G330.931-0.260 [†]	16:10:06.7	-51:59:18.13	5.3 (2)	A	N	Y	N	Y
G330.955-0.182	16:09:53.0	-51:54:52.84	5.5 (2)	MWCA	Y	Y	Y	Y
G331.131-0.470 [†]	16:11:59.4	-52:00:19.88	4.3 (2)	GA	Y	Y	N	Y
G331.132-0.244	16:10:59.8	-51:50:21.78	5.4 (2)	WCGA	Y	Y	N	Y
G331.134-0.488	16:12:05.1	-52:01:01.37	4.3 (2)	A	Y	Y	Y	Y
G331.134+0.156	16:09:15.1	-51:32:39.79	4.6 (2)	MWA	Y	Y	N	Y
G331.279-0.189	16:11:27.2	-51:41:57.04	5.3 (2)	MWCA	Y	Y	Y	Y
G331.341-0.347	16:12:26.4	-51:46:20.50	4.2 (2)	MWCGA	Y	Y	Y	Y
G331.370-0.399 [†]	16:12:48.5	-51:47:24.39	4.2 (2)	GA	N	Y	N	Y
G331.371-0.145 [†]	16:11:41.2	-51:36:15.36	5.2 (2)	A	N	Y	N	Y
G331.380+0.149 [†]	16:10:26.8	-51:22:58.46	3.2 (2)	A	Y	Y	N	Y
G331.409-0.164 [†]	16:11:57.4	-51:35:32.03	5.1 (2)	A ₃	Y	Y	N	Y
G331.44-0.14 [†]	16:11:57.9	-51:33:07.81	5.1 (2)	A	Y	Y	N	N
G331.440-0.187	16:12:11.9	-51:35:15.76	5.2 (2)	MWCA	Y	Y	N	Y
G331.442-0.158 [†]	16:12:04.8	-51:33:55.74	5.1 (2)	A	Y	Y	N	Y
G331.492-0.082	16:11:59.0	-51:28:34.01	5.3 (2)	A ₂	Y	Y	Y	Y
G331.503-0.109	16:12:09.3	-51:29:14.95	5.2 (2)	WSCA ₃	Y	Y	Y	Y
G331.519-0.082	16:12:06.6	-51:27:25.69	5.3 (2)	A	Y	Y	Y	Y
G331.530-0.099	16:12:14.3	-51:27:44.11	5.4 (2)	A	Y	Y	Y	Y
G331.544-0.067	16:12:09.7	-51:25:44.35	5.2 (2)	MCA	Y	Y	Y	Y
G331.555-0.122	16:12:27.1	-51:27:42.69	5.8 (2)	MW ₂ CA ₂	Y	Y	N	Y
G331.72-0.20 [†]	16:13:34.4	-51:24:24.91	3.3 (2)	A	Y	Y	N	Y
G331.853-0.129 [†]	16:13:52.5	-51:15:46.63	3.4 (2)	A	Y	Y	N	Y
G331.887+0.063 [†]	16:13:11.2	-51:05:58.39	5.2 (2)	A	Y	Y	N	Y
G331.921-0.083 [†]	16:13:59.2	-51:10:56.00	3.5 (2)	A	Y	Y	N	Y
G332.092-0.420	16:16:15.7	-51:18:27.64	3.7 (2)	MWA	Y	Y	N	Y
G332.240-0.044 [†]	16:15:17.2	-50:56:01.32	3.4 (2)	A	Y	Y	N	Y
G332.295-0.094	16:15:45.3	-50:55:54.87	3.5 (2)	MWGA	Y	Y	Y	Y
G332.318+0.179 [†]	16:14:40.1	-50:43:07.07	3.4 (2)	WA	Y	Y	N	Y
G332.355-0.114	16:16:07.2	-50:54:19.92	3.5 (2)	MWCGA	N	Y	N	Y
G332.583+0.147	16:16:01.0	-50:33:30.96	3.1 (2)	MGA	N	N	N	Y
G332.604-0.167	16:17:29.3	-50:46:12.92	3.3 (2)	MWGA	Y	Y	N	Y
G332.716-0.048 [†]	16:17:28.5	-50:36:23.32	3.0 (2)	A	N	Y	N	Y

¹M - 6.7 GHz CH₃OH maser from Caswell et al. (2011); W - 22 GHz H₂O maser from any of Breen et al. (2010a); Walsh et al. (2014); S - 1612 MHz OH maser from Sevenster et al. (1997); C - 1665 or 1667 MHz OH maser from Caswell (1998); G - EGO from Cyganowski et al. (2008); A - ATLASGAL point source from Contreras et al. (2013).

Table 4.3: *continued*

Region name	Centre of maser emission α_{2000} (h:m:s)	δ_{2000} ($^{\circ}$: $'$: $''$)	Kinematic distance (kpc)	Associations within 1 arcmin ¹	Presence of SiO (1-0) $v = 0$?	Presence of CH ₃ OH $1_0-0_0 A^+$?	Presence of H53 α ?	Presence of C ³⁴ S (1-0)?
G333.002-0.437	16:20:28.7	-50:41:00.91	3.8 (2)	WA ₃	Y	Y	Y	Y
G333.014-0.466	16:20:39.5	-50:41:47.45	3.6 (2)	A	Y	Y	Y	Y
G333.029-0.063	16:18:56.7	-50:23:54.64	3.0 (2)	MWA	N	Y	N	Y
G333.029-0.024	16:18:46.6	-50:22:14.57	3.1 (2)	MA ₂	Y	Y	N	Y
G333.068-0.446	16:20:48.7	-50:38:38.68	3.7 (2)	MWA	Y	Y	Y	Y
G333.071-0.399	16:20:37.2	-50:36:30.13	3.6 (2)	A	Y	Y	Y	Y
G333.103-0.502	16:21:13.1	-50:39:31.37	3.8 (2)	MA	Y	Y	Y	Y
G333.121-0.433	16:20:59.5	-50:35:51.03	3.4 (2)	M ₄ W ₆ C ₂ A ₂	Y	Y	Y	Y
G333.126-0.439	16:21:02.6	-50:35:52.44	3.5 (2)	M ₄ W ₆ C ₂ A ₂	Y	Y	Y	Y
G333.137-0.427	16:21:02.2	-50:34:56.03	3.5 (2)	MWC ₂ A	Y	Y	N	Y
G333.162-0.101	16:19:42.5	-50:19:56.29	5.3 (2)	MA ₂	N	Y	Y	Y
G333.184-0.090	16:19:45.5	-50:18:34.59	5.1 (1)	MGA	Y	Y	Y	Y
G333.220-0.402	16:21:17.9	-50:30:19.97	3.6 (2)	A	Y	Y	Y	Y
G333.24+0.02 [†]	16:19:26.0	-50:11:29.26	4.4 (1)	A	Y	Y	N	Y
G333.233-0.061	16:19:50.8	-50:15:15.94	5.1 (1)	M ₂ W ₃ SCA	Y	Y	N	Y
G333.284-0.373	16:21:27.3	-50:26:22.48	3.6 (2)	A	Y	Y	Y	Y
G333.301-0.352	16:21:25.9	-50:24:46.26	3.5 (2)	A ₂	Y	Y	Y	Y
G333.313+0.106	16:19:28.5	-50:04:45.61	3.2 (2)	MWGA	Y	Y	Y	Y
G333.335-0.363	16:21:38.0	-50:23:46.78	3.6 (2)	A	Y	Y	Y	Y
G333.376-0.202 [†]	16:21:06.2	-50:15:13.21	4.0 (2)	WA	Y	Y	N	Y
G333.387+0.031	16:20:07.5	-50:04:49.51	4.4 (1)	MWCA	Y	Y	N	Y
G333.467-0.163	16:21:20.2	-50:09:41.70	3.1 (2)	MWCGA	Y	Y	Y	Y
G333.497+0.143 [†]	16:20:07.6	-49:55:26.21	6.3 (2)	A ₂	Y	Y	N	Y
G333.523-0.275	16:22:04.5	-50:12:05.32	3.5 (2)	A	Y	Y	Y	Y
G333.558-0.293	16:22:18.7	-50:11:23.38	3.1 (2)	A ₂	Y	Y	Y	Y
G333.562-0.025	16:21:08.7	-49:59:48.85	3.0 (2)	MA	Y	Y	N	Y
G333.569+0.028 [†]	16:20:56.6	-49:57:15.91	5.0 (1)	A	Y	Y	N	Y
G333.595-0.211	16:22:06.7	-50:06:21.28	3.5 (2)	WSCA	Y	Y	Y	Y
G333.694-0.197	16:22:29.1	-50:01:31.84	3.5 (2)	A ₂	Y	Y	Y	Y
G333.711-0.115 [†]	16:22:12.1	-49:57:20.77	2.5 (2)	A	N	N	N	Y
G333.772-0.010 [†]	16:22:00.3	-49:50:15.79	5.2 (1)	A	N	Y	N	Y
G333.773-0.258 [†]	16:23:06.2	-50:00:43.31	3.5 (2)	A	Y	Y	N	Y
G333.818-0.303 [†]	16:23:30.0	-50:00:41.97	3.4 (2)	A	N	Y	N	Y
G333.900-0.098	16:22:57.3	-49:48:35.60	4.2 (2)	MSA	Y	Y	N	Y
G333.930-0.133	16:23:14.5	-49:48:45.94	3.1 (2)	MWA	Y	Y	N	Y
G333.974+0.074 [†]	16:22:31.4	-49:38:08.31	3.9 (2)	A	N	Y	N	Y
G334.027-0.047 [†]	16:23:16.7	-49:41:00.19	5.0 (1)	A ₂	N	Y	N	Y
G334.746+0.506 [†]	16:23:58.0	-48:46:59.12	4.2 (1)	A	Y	Y	N	Y

4.4 Discussion

4.4.1 Properties of detected class I CH₃OH masers

Using the information gathered from these observations, we conduct analyses of the basic properties of class I CH₃OH masers. Fig. 4.2 shows the luminosities, projected linear sizes and velocity spreads of these masers. The linear size is calculated using the angular size of maser emission across a region, as well as the kinematic distance. Evolved sources are categorised based on the presence of class II CH₃OH masers, OH masers or H53 α emission; further detail is given in §4.4.3.

The distribution of luminosities approximates a Gaussian with a peak around $10^{-6.25} L_{\odot}$. Non-evolved sources appear to be limited to luminosities less than $10^{-5.25} L_{\odot}$, with only two exceptions. Further discussion on evolved/non-evolved sources is continued in §4.4.3.

The majority of sources have small linear sizes (<0.5 pc) and small velocity spreads (<5 km s⁻¹). Panel 2 of Fig. 4.2 features a comparison similar to Fig. 5 of Voronkov et al. (2014), velocity spread against linear size, although they use the presence of OH masers instead of the evolved criterion used here. Despite this difference, the distributions appear similar. The non-evolved class I CH₃OH masers in our distribution are mostly bound within 5 km s⁻¹, but Voronkov et al. (2014) masers without OH maser associations seem to have an average velocity spread of 5 km s⁻¹. This is likely to be due to the Voronkov et al. (2014) sample being typically biased toward class II CH₃OH masers, which are more evolved than our non-evolved population.

Many masers can be seen with a linear size near 0 pc; these correspond to regions with only one or two maser spots. An expanded discussion of the non-evolved nature of regions with few maser spots is given in §4.4.3.

Small spatial distributions of class I CH₃OH masers have been discussed in literature. However, unlike other investigations, the distribution shown in Fig. 4.2 is without a reference point; Kurtz et al. (2004) measure the distance between class I CH₃OH masers and an H II region, and Voronkov et al. (2014) use class II CH₃OH masers as references. A more appropriate comparison with literature is presented in §4.4.2.1.

Six maser regions can be seen with a linear size greater than 0.8 pc; these regions are G330.876–0.362, G331.279–0.189, G331.492–0.082, G331.503–0.109, G331.530–0.099 and G333.558–0.293. Upon inspection of the distribution of these masers with infrared maps, it is likely that not all the class I CH₃OH masers are related to a single high-mass object; see Appendix B.3. G330.876–0.362 has only two spots, very distant from each other; one is closely associated with class II CH₃OH, H₂O and OH masers, the other with an infrared dark cloud (IRDC). G331.279–0.189 has a single maser spot very distant from the rest of the relatively clustered spots, but this spot may not be powered by the same obvious infrared source. G331.492–0.082 has two groups of spots; both are very compact, but widely separated from each other and have different infrared colours. G333.558–0.293 has the largest offset within these observations, from two individual spots; the infrared map shows what appears to be a different IRDC associated with each. G331.503–0.109 and G331.530–0.099 may be exceptions; both may be powered by the same source located at G331.512–0.100, which also features a H₂O and OH maser.

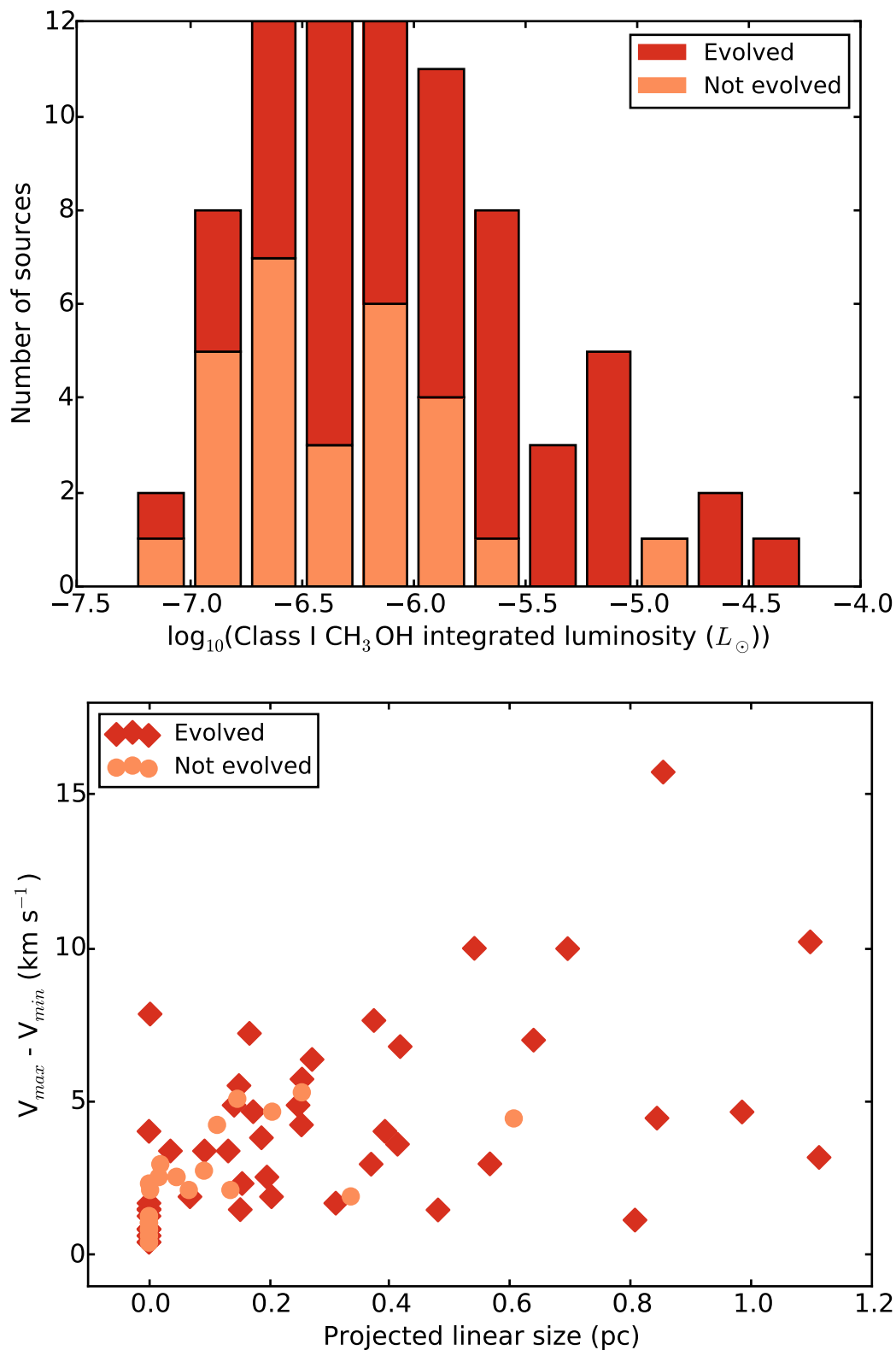


Figure 4.2: Luminosities, projected linear sizes and velocity spreads of class I CH_3OH maser regions. The distribution of luminosities approximates a Gaussian, with a peak around $10^{-6.25} L_{\odot}$. The majority of maser regions have small spatial sizes and velocity spreads. Regions that are not evolved tend to have lower luminosities, projected linear sizes and velocity spreads.

While it is difficult to disentangle the origin of each maser spot, it seems that the large offsets between spots are not necessarily common, and may be artificially generated by calculating a radius for each observed maser region. This in turn strengthens the argument that class I CH₃OH maser regions tend to have small spatial sizes and velocity spreads. While these masers are collisionally-excited, they are perhaps tracing weak shocks rather than powerful ones. We expect stronger shocks to at least have broad velocity coverage. An indication of regions where more powerful shocks are present may be gleaned by the presence of thermal SiO, or even more evolved maser species such as class II CH₃OH or OH.

4.4.2 Comparing class I CH₃OH masers with other masers and thermal lines

Paper I investigated maser associations of class I CH₃OH masers with class II CH₃OH, H₂O and OH masers. As Paper I used class I CH₃OH maser positions from auto-correlated data, the positional uncertainty is much higher than these data. Maser associations within 60 arcsec between each of the four species can be seen as a Venn diagram in Fig. 3.20 of Paper I. The same analysis was carried out with these data, but with a more stringent 45 arcsec; the resulting populations within each intersection of the same Venn diagram changes only very slightly (1 or 2 differences in some intersections). Consequently, MALT-45 observations accurately reveal the maser associations toward class I CH₃OH masers without the need for high-resolution follow-up observations. However, we are able to use the high-resolution data for various other comparisons with maser species, as well as thermal lines from MALT-45, owing to the improved sensitivity of these observations.

4.4.2.1 Separation from star-forming maser species

Using the positions of every class I CH₃OH maser spot detected, distances to class II CH₃OH, OH and H₂O masers are calculated and presented in Fig. 4.3. The other star-forming maser positions were gathered from Caswell et al. (2011); Sevenster et al. (1997); Caswell (1998); Breen et al. (2010a); Walsh et al. (2014). Masers were only considered up to 60 arcsec away. If more than one of the same type of maser are within range of a class I CH₃OH maser spot, only the closest was used comparison.

Most distances are contained within 0.5 pc. Kurtz et al. (2004) find that the distance between class I CH₃OH masers and H II regions tend to be within 0.5 pc, agreeing with our results. Voronkov et al. (2014) were able to model an exponential decay to the number of class I CH₃OH masers with distance from class II CH₃OH masers; with their larger sample size, they see many masers at distances beyond 0.5 pc. However, the vast majority are within 0.5 pc, also agreeing with our results. Given that our maser spots are derived from an unbiased sample, it seems that most regions of HMSF influence class I CH₃OH maser activity within a radius of 0.5 pc.

There is a small, isolated population at distances around 0.8 pc, particularly with OH masers. The class I CH₃OH maser regions comprising distances between 0.65 and 0.95 pc to OH masers are: G330.876–0.362, G331.279–0.189, G331.503–0.109, G333.121–0.433, G333.126–0.439, G333.595–0.211 and G333.900–0.099. Of these regions, G330.876–0.362

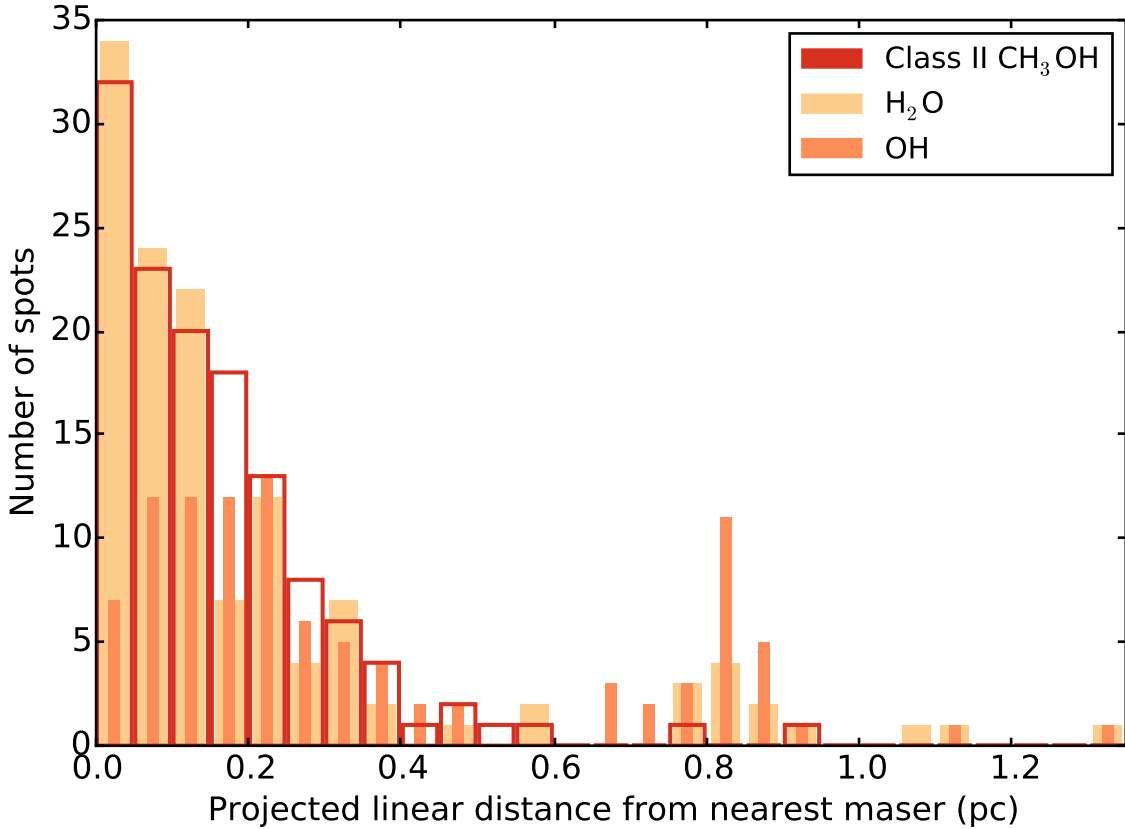


Figure 4.3: Histogram of the projected linear distance between every class I CH₃OH maser spot position and any other species of maser. This histogram uses a maximum angular offset of 60 arcsec. The majority of distances to masers are contained within 0.5 pc, and a second population appears around 0.8 pc.

and G331.279–0.189 have been discussed in §4.4.1 as examples of maser regions without a single, common high-mass object. Therefore, these regions may not be affected by the OH maser at a distance of ~ 0.8 pc. The remaining regions are discussed in the following text. Figures contained within Appendix B.3 aid to clarify the spatial association of the masers in question.

G331.503–0.109 includes four class I CH₃OH maser spots, with one very distant from the others. The three spots clustered spots are at a distance of ~ 0.85 pc to the OH maser, while the fourth spot is at a distance of 1.4 pc (the largest of all offsets within 60 arcsec). Infrared GLIMPSE images show that all masers appear to be associated with the same cloud. If the class I CH₃OH masers are related to the location featuring both OH and H₂O masers, the region of influence is great indeed. This would may also explain the class I CH₃OH maser emission seen at G331.530–0.099; the maser spot from this region nearest to the OH maser is at a distance of 1.1 pc. The other spots are further than 60 arcsec from the OH maser, and have a curious linear distribution.

G333.121–0.433 and G333.126–0.439 are both at distances ~ 0.8 pc from the same OH 1665/1667 MHz maser region located at G333.135–0.432. Each of these class I CH₃OH maser regions appear to be closely associated with their own distinct class II CH₃OH masers. As the OH maser in question is cospatial with another class II CH₃OH maser, and features its

own nearby class I CH₃OH masers, it seems likely that this is an independent HMSF region from the other class I CH₃OH maser regions. While it is possible that the presence of the OH maser could influence class I CH₃OH masers at these large distances, the whole region (located within the G333 giant molecular cloud) is obviously a complex, evolved region of HMSF, making interpretation of cause-and-effect difficult.

The class I CH₃OH masers located at G333.595–0.211 appear near to a very bright H II region. This region features 1612, 1665 and 1667 MHz OH masers, as well as H₂O masers, although all at projected distances ~ 0.8 pc from the class I CH₃OH masers. Interestingly, CS (1–0) emission from MALT-45 peaks at the location where class I CH₃OH masers are detected.

Unlike the other maser regions discussed, G333.900–0.099 has few class I CH₃OH maser spots. Only two spots are detected on either side of a class II CH₃OH maser. The OH maser is at a distance ~ 0.8 pc from these masers, and appears cospatial with an infrared star in GLIMPSE. Given the small count of spots and the presence of a star with the OH maser, we do not believe a connection exists between the OH maser and class I CH₃OH masers here.

In general, maser associations are well characterised within distances of 0.5 pc. Genuine associations with distances exceeding 0.5 pc seem to be rare, and perhaps limited to powerful, evolved regions of HMSF.

4.4.2.2 Velocities

The peak velocities of auto-correlated class I CH₃OH masers are compared with class II CH₃OH masers, thermal CS, SiO and CH₃OH in Fig. 4.4. We discuss the resulting distributions in the following text.

Voronkov et al. (2014) used a large sample of class I and class II CH₃OH masers to investigate their relative velocities. They find a peak at -0.57 ± 0.07 km s⁻¹ with a standard deviation of 3.32 ± 0.07 km s⁻¹ and a slight blueshifted asymmetry. The cause of the blueshift could not be attributed to either the class I or class II CH₃OH masers. The relatively wide spread of class II CH₃OH maser velocities is characterised by the proximity to a YSO; a greater dispersion is expected for molecules found near to the powering source.

The relevant distribution in Fig. 4.4 has the statistics $\mu = -1.17 \pm 0.87$ km s⁻¹, $\tilde{x} = -1.90$ km s⁻¹ and $\sigma = 4.75 \pm 0.61$ km s⁻¹ (μ is the mean, \tilde{x} the median and σ the standard deviation). The parameters of this comparison are consistent with that of Voronkov et al. (2014). The median and mean are blueshifted, but the relatively large standard deviation diminishes their significance; the blueshift assertion requires a larger population to establish its validity. As the sample of Voronkov et al. (2014) is much larger than the one presented here, proving a systematic blueshift would be difficult to achieve, and may never escape low-number statistics.

Paper I presented a histogram of the velocity difference between peak velocities in class I CH₃OH masers and CS (1–0). The resulting mean was 0.0 ± 0.2 km s⁻¹ with a standard deviation of 1.5 ± 0.1 km s⁻¹; given that CS traces very dense gas ($n_c > 10^5$ cm⁻³), the peak CS velocity is likely closely related to the systemic velocity of a molecular cloud. Hence, the statistics suggest that class I CH₃OH masers are also good tracers of systemic velocities, and may be better than using the middle of the velocity range seen by class II CH₃OH masers.

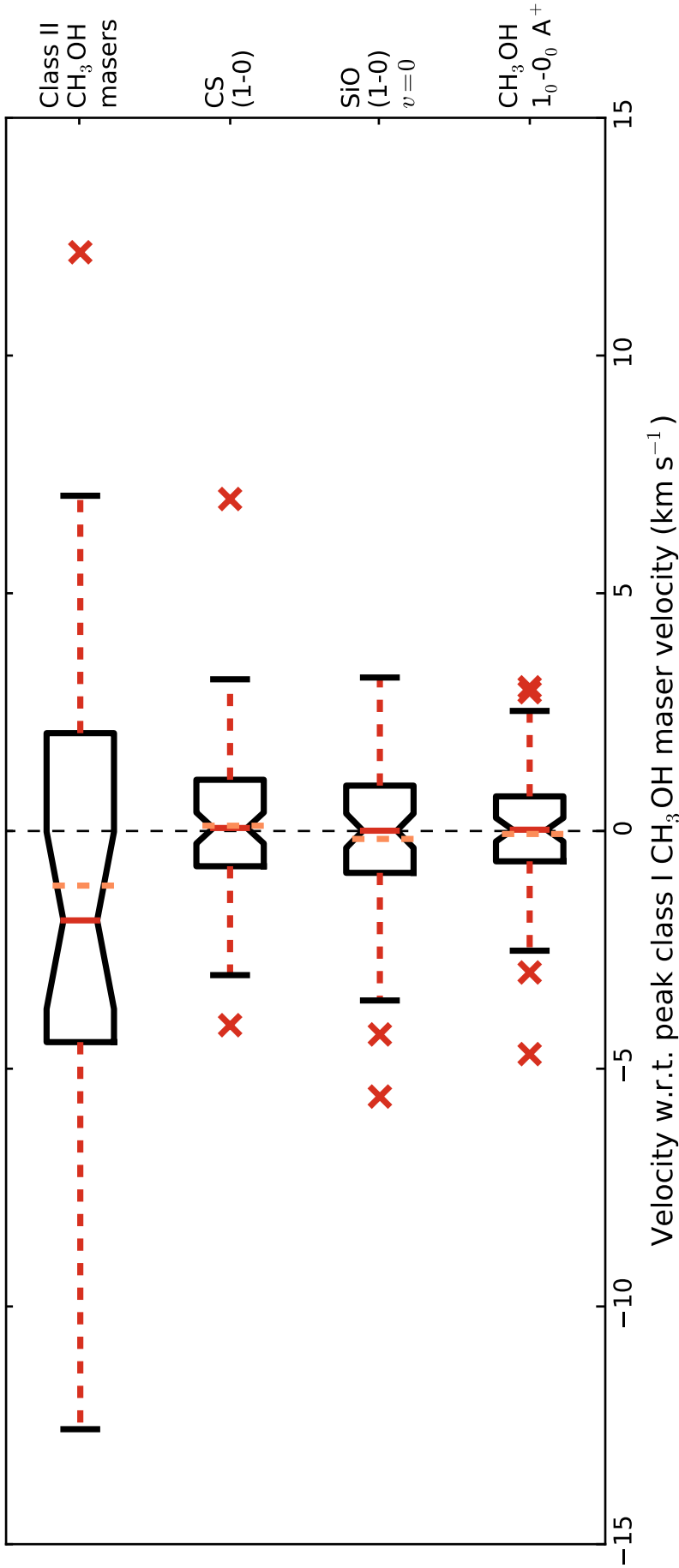


Figure 4.4: Notched box-and-whisker plot of peak velocity differences between class I CH₃OH masers and various star-forming species. The red solid vertical line within the boxes indicates the median, the lighter dashed lines the mean. The notched region about the median indicates the 95 per cent confidence interval on the median, and the box covers the interquartile region (IQR; middle 50 per cent of data). Whiskers extend past the IQR by up to 1.5×IQR. Red crosses indicate outlying data. The dashed black line indicates zero peak velocity difference. The class II CH₃OH maser box plot has a wide spread of velocity differences, while each of the other lines does not. CS, SiO and thermal CH₃OH velocities are all closely associated with the maser velocity.

The results of the CS comparison in these data confirm that of Paper I: $\mu = 0.09 \pm 0.18 \text{ km s}^{-1}$, $\tilde{x} = 0.04 \text{ km s}^{-1}$ and $\sigma = 1.56 \pm 0.17 \text{ km s}^{-1}$. If we assume that CS peak velocities accurately trace the systemic velocities of molecular clouds, then class I CH₃OH masers are also very good probes for these velocities. However, we have discussed class II CH₃OH masers tracing systemic velocities, although the mean and median of CS are quite different to class II CH₃OH masers. As we are probing very dense, star-forming regions, the CS emission may be optically thick, which may cause the peak CS velocity to not reflect the systemic velocity. To help confirm CS as a reliable tracer of systemic velocities, we analysed the peak velocity of C³⁴S emission. With only one exception, C³⁴S was detected toward each observed class I CH₃OH region, and the peak velocity of C³⁴S agrees with the peak CS velocity to within 0.5 km s^{-1} . This rules out the possibility of optically thick CS regions having non-systemic peak velocities, and therefore peak CS velocities should be considered as more accurate systemic velocity tracers than class II CH₃OH masers.

The sensitivity of the MALT-45 survey provided a small detection rate of thermal SiO emission with class I CH₃OH maser regions. With the additional sensitivity provided by these observations, we are able to reliably compare these two shock-tracing species. The velocity distribution presented is similar to that of CS: $\mu = 0.17 \pm 0.20 \text{ km s}^{-1}$, $\tilde{x} = 0.01 \text{ km s}^{-1}$ and $\sigma = 1.64 \pm 0.14 \text{ km s}^{-1}$. The distribution is slightly wider than that of CS, but uncertainties are too great to draw any conclusions. Overall, the peak velocities of class I CH₃OH masers and SiO emission closely agree.

The thermal 1_0-0_0 A⁺ line of CH₃OH has an even tighter association with class I CH₃OH maser velocities than CS: $\mu = -0.08 \pm 0.15 \text{ km s}^{-1}$, $\tilde{x} = 0.01 \text{ km s}^{-1}$ and $\sigma = 1.33 \pm 0.11 \text{ km s}^{-1}$. As a sufficient abundance of CH₃OH gas is needed for maser emission, it is perhaps not surprising that the thermal velocity is closely matched to the maser velocity. Given the distribution relative to CS, it seems that thermal CH₃OH is also a good tracer of systemic velocities.

The velocity differences for the thermal CS, SiO and CH₃OH spectral lines all appear similarly, with uncertainties of only a few km s^{-1} . The class II CH₃OH maser distribution, however, is broad and has a relatively distinct mean and median blueshift. This hints that class II CH₃OH masers indeed have a systematic blueshift bias, although the statistics presented above can not conclude this observation. The blueshift is consistent with class II CH₃OH masers being detected in the foreground of star-forming regions rather than in the background; as these 6.7 GHz masers are the lowest frequency of all species considered here, they may be affected by optically thick emission close a high-mass star. This would especially be true for younger sources, which would be more optically thick.

4.4.2.3 Brightness

In this subsection, we use the auto-correlated integrated flux densities of class I CH₃OH maser emission to compare with the brightness of other star-forming species. Similar to Paper I, the luminosity of class I CH₃OH and class II CH₃OH masers was compared, but no correlation was observed. The only difference in this comparison is the sensitivity to class I CH₃OH maser emission, so this result was not unexpected. Thermal CS, SiO and CH₃OH integrated intensities were also compared with class I CH₃OH integrated flux densities; the results can

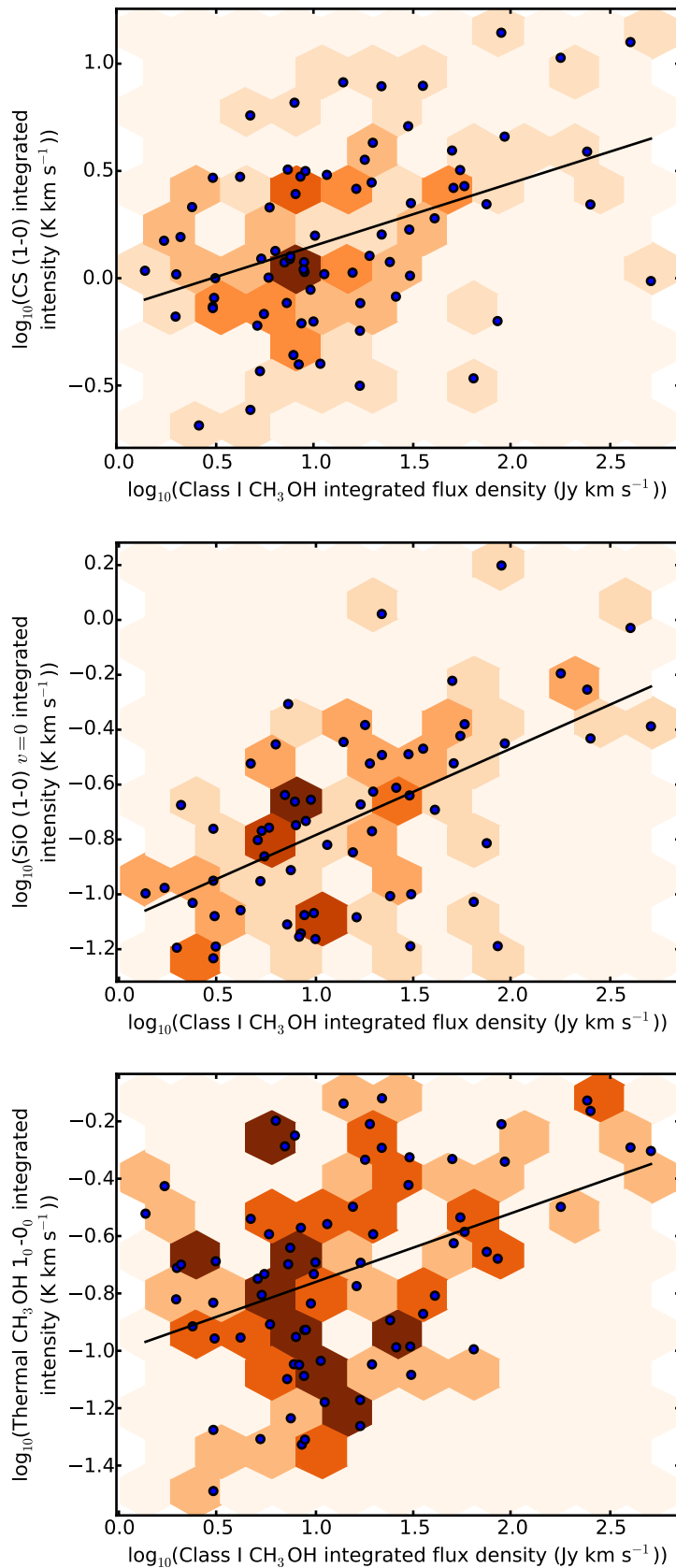


Figure 4.5: Scatter plots of class I CH₃OH maser integrated flux density against CS, SiO and thermal CH₃OH integrated flux densities. Hexagon tile colours represent the density of data, similar to a two-dimensional histogram. All three comparisons show a trend, although the degree of scatter is large. In addition, CS and SiO appear to cluster, indicating some values to be more typical than others.

be seen in Fig. 4.5.

The brightness of CS, SiO and thermal CH₃OH all show a positive correlation with the brightness of class I CH₃OH maser emission, although the degree scatter in each plot is large. The correlation coefficient (*r*-value) for the CS comparison is 0.41. Curiously, the data in the scatter plot featuring CS seem to be clustered about the median integrated flux density (IFD) of both species; this is more apparent on Fig. 4.5 with the use of a two-dimensional density histogram. The CS vs. class I CH₃OH maser plot in Paper I (Fig. 3.12) does not appear to have a concentrated cluster, although that plot made use of luminosities. The median CS integrated intensity is 1.3 K km s⁻¹, with a median class I CH₃OH maser IFD of 9.9 Jy km s⁻¹.

As discussed earlier, a brightness comparison with SiO was not possible in Paper I, due to their low intensities. Consequently, Paper I speculates on the nature of the class I CH₃OH maser regions, given that the SiO detection rate was quite low (30 per cent). As the majority or regions now have confirmed SiO detections, it seems that a large portion of class I CH₃OH masers are triggered by weak shocks, given that associated bright SiO emission is rare. The *r*-value for this comparison is 0.57. SiO has a median integrated intensity of 0.18 K km s⁻¹, and the median class I CH₃OH maser IFD is 12.8 Jy km s⁻¹. As with the CS, these median values are close to the most clustered bin in panel 2 of Fig. 4.5.

Similar to SiO, comparisons with thermal CH₃OH was not possible in Paper I. The correlation here is the poorest, with a *r*-value of 0.40. Unlike the other thermal species, the degree of scatter in these data is so large that no cluster is apparent either. The median thermal CH₃OH integrated intensity is 0.20 K km s⁻¹, with a median class I CH₃OH maser IFD of 10.1 Jy km s⁻¹.

4.4.3 Class I CH₃OH masers on a HMSF evolutionary timeline

In this subsection, we attempt to divide class I CH₃OH masers into ‘young’ or ‘evolved’ categories. Paper I briefly discusses masers with associated class II CH₃OH or OH masers, noting that more masers have no associations and therefore seem to be better associated with earlier stages of HMSF. With the additional sensitivity provided by these observations, we can use radio recombination line (RRL) data to help discriminate evolved regions. RRLs are associated with H II regions, which in turn tend to signpost more evolved stages of HMSF than class II CH₃OH masers (Walsh et al. 1998). Class I CH₃OH maser regions with detected H53α emission are listed in Table 4.3. We use the presence of class II CH₃OH masers, OH masers and H53α emission to deem a region as evolved or not.

Fig. 4.6 shows the populations of class I masers with and without these tracers of evolved stages of star formation. Due to the additional discrimination provided by the presence of H53α, we find that class I CH₃OH masers tend to appear in more evolved regions, unlike Paper I. It is surprising that 17 regions featuring H53α emission are all without class II CH₃OH and OH masers. Are there new masers at these locations? The population of OH masers within the MALT-45 survey region are primarily from the catalogue of Caswell (1998); while the number of detections are low, this survey is somewhat complete to ~0.16 Jy, limited by the number of channels in each maser detection. Additional masers from the SPLASH survey may reveal new associations (Dawson et al. 2014). Across the MALT-45 survey region,

Class II and/or OH masers

		with	w/o
H53 α	with	15	17
	w/o	17	28

Figure 4.6: A diagram depicting the relative populations of evolved species associated with class I CH₃OH masers. The majority of sources are evolved (49/77, 64 per cent).

class II CH₃OH masers from the Methanol MultiBeam survey are complete to 0.17 Jy (Caswell et al. 2011). Given the good sensitivity of these surveys, it seems unlikely that undiscovered class II CH₃OH and OH masers are associated with these class I CH₃OH masers, but follow-up observations at these transitions may prove effective for finding new detections.

The population of class I CH₃OH maser regions without any evolved tracer is about a third of all regions in these data; clearly, class I CH₃OH masers are still strongly associated with younger star-forming regions. In order to help identify younger regions of star formation, we discuss the properties of this sub-population.

In the following text, we qualitatively discuss infrared associations with young class I CH₃OH masers. Images in Appendix B.3 show the infrared environment of the detected masers. It can be seen that many masers are cospatial with dark infrared regions, presumably IRDCs, which are dense regions of gas projected in front of a bright background. IRDCs are known sites of star formation, even HMSF, thus it is not surprising to find a large population of class I CH₃OH masers towards these locations. However, some slight differences appear between young and evolved regions. The young population appears to better associated with dark infrared features, but have less bright infrared counterparts, and generally only one maser spot. A good example of the difference in the typical infrared properties of younger and more evolved sources can be seen on the same page in Appendix B.3 between G331.279–0.189 (evolved) and G331.370–0.399, G331.371–0.145, G331.380+0.149 and G331.409–0.164 (young). G331.279–0.189 appears to have dark infrared lanes coalescing into a region with excess extended green emission, coincident with class II CH₃OH, H₂O and OH masers, surrounded by class I CH₃OH masers. In contrast, the four young regions are all associated with dark infrared regions, although there is little else in the infrared to pin-point or identify these as masing regions.

One extreme exception is G330.931–0.260; two maser spots are detected towards the end of what appears to be an extended and diffuse photon-dominated region. No other masers are detected, and no dark infrared regions apparent, but an infrared feature at G330.938–0.255

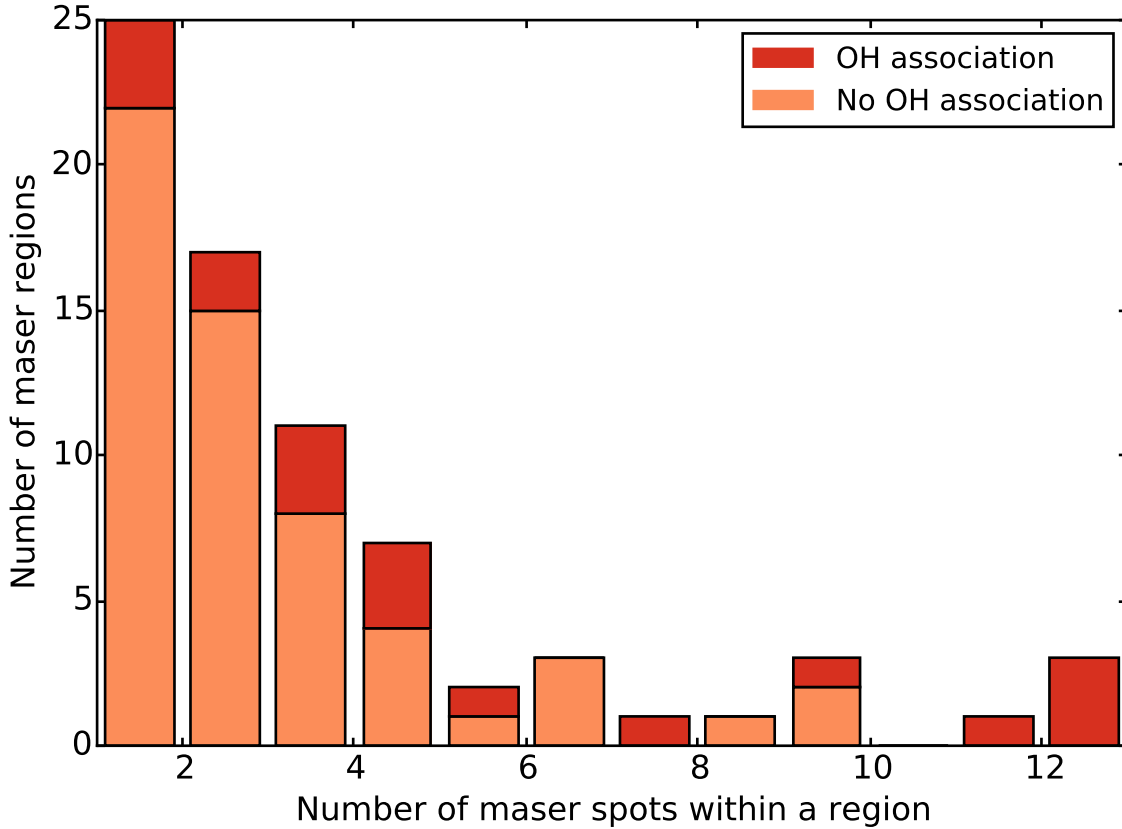


Figure 4.7: A histogram of class I CH_3OH maser spot counts within each maser region, highlighting those associated with an OH maser. There are few OH maser associations with all class I CH_3OH maser regions, but regions with only one or two spots are particularly without OH maser association.

might be the powering source.

The histogram in Fig. 4.2 presents luminosities of evolved and non-evolved class I CH_3OH maser regions. Luminosities less than $10^{-5.75} L_\odot$ have a total of 57 maser regions, of which 26 are classified young (46 per cent). The remainder of the histogram (luminosities $>10^{-5.75} L_\odot$) has only 2 non-evolved maser regions out of 20 (10 per cent). Thus, class I CH_3OH masers in non-evolved regions tend to have lower luminosities.

G332.240–0.044 is the outlying, large-valued datum; unlike other young regions, there are many maser spots associated with this region, concentrated about a bright infrared feature embedded in an IRDC. This may be an example of a region about to produce class II CH_3OH maser emission, given the infrared appears similar to other regions with class II CH_3OH masers.

The three regions with 44 GHz CH_3OH emission detected in auto- but not cross-correlation are also within the young population. G331.72–0.20 and G333.24+0.02 appear to be typically associated with dark infrared regions, but G331.44–0.14 lacks any obvious infrared feature; it may be an example of a non-star-forming maser region.

Fig. 4.7 reveals that the number of class I CH_3OH maser spots detected hint at the presence of an OH maser association. Maser regions with one or two spots are particularly without an OH association, while those with eleven or twelve spots all have an association.

Unfortunately, not many OH masers are available for comparison. However, this finding helps to explain why evolved class I CH₃OH maser regions have larger projected linear sizes and velocity spreads in Fig. 4.2; more spots indicate more maser activity, presumably caused by a further evolved region of HMSF. The presence of a class II CH₃OH maser is less apparent with class I CH₃OH maser spot counts, but regions with only one or two spots are mostly without association (11/42; 26 per cent).

MALT-45 observations provided the initial detections of the class I CH₃OH masers detailed in this paper. With only a few possible exceptions, each of the class I CH₃OH masers identified by MALT-45 appear to be associated with HMSF. Further observations will isolate more young-type star-forming regions, and purely through masers, identify HMSF in its early stages. In addition, without other maser data, the number of spots detected can hint at the evolutionary stage of the region.

4.4.4 Comparing class I CH₃OH masers with ATLASGAL

The ATLASGAL survey maps 870 μ m emission across a large part of the Galactic plane, including the MALT-45 region. This sub-millimetre emission is optically thin, tracing a colder, pre-YSO stage of HMSF, and provides information on column density and clump mass.

Using the catalogue provided by Contreras et al. (2013), we are able to investigate the various properties of our class I CH₃OH masers. Associations between class I CH₃OH masers and ATLASGAL sources are listed in Table 4.3.

A histogram of the offsets between class I CH₃OH maser spots and ATLASGAL sources is seen in Fig. 4.8. The vast majority of maser spots are within 0.4 pc of an ATLASGAL source. This is similar to the distances between class I CH₃OH maser spots and other star-forming masers found in Fig. 4.3. Unlike the distances between masers, there appears to be no trend when distinguishing evolved and non-evolved maser regions. Relatively few maser spots are within 0.05 pc of an ATLASGAL source, with many more having distances within 0.15 pc.

Note that Fig. 4.8 uses any ATLASGAL source within 60 arcsec from a maser spot. Maser regions without ATLASGAL associations are discussed in §4.4.4.1.

Chen et al. (2012) and Urquhart et al. (2013) estimate clump mass with the integrated intensity of millimetre-wavelength continuum emission, assuming the emission is optically thin. In the same manner, we use ATLASGAL data to estimate clump masses via:

$$M_{gas} = \frac{S_{\nu} D^2 R_d}{\kappa_d B_{\nu}(T_{dust})} \quad (1)$$

where M_{gas} is the mass of the gas, S_{ν} is the integrated flux density of ATLASGAL 870 μ m emission, D is kinematic distance to the maser, R_d is the ratio of gas and dust masses, κ_d is the mass-absorption coefficient per unit mass of dust, and $B_{\nu}(T_{dust})$ is the Planck function at temperature T_{dust} . Urquhart et al. (2013) justify the choice of $T_{dust} = 20$ K and $\kappa_d = 1.85 \text{ cm}^2 \text{ g}^{-1}$, which we also use here. We also assume $R_d = 100$. The histogram of determined masses can be seen in Fig. 4.9.

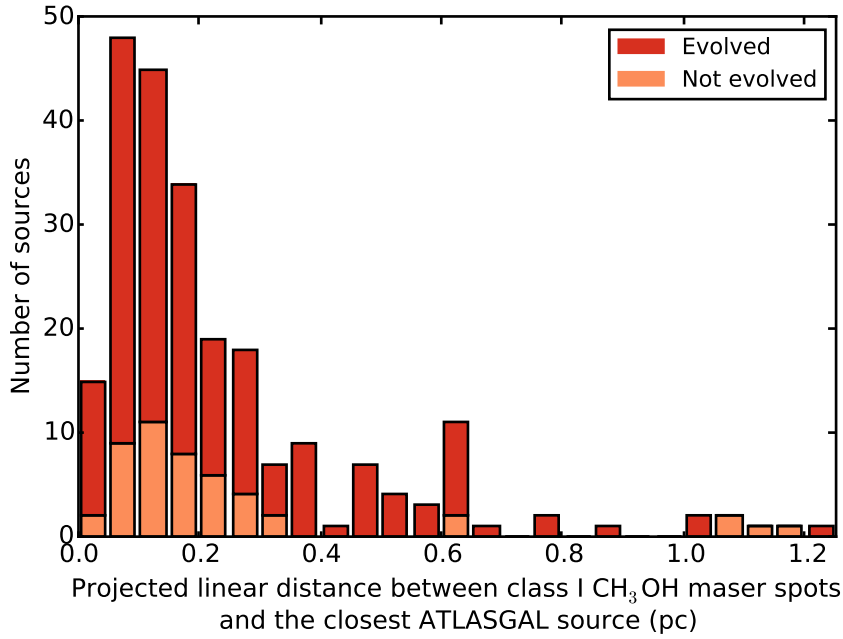


Figure 4.8: A histogram of offsets between ATLASGAL sources and flux-weighted average positions of class I CH_3OH masers. The majority of sources are within 10 arcsec, and almost all are within 20 arcsec. This indicates a strong relation between the region containing the ATLASGAL source and class I CH_3OH maser emission. A small population also exists around 30 to 55 arcsec. Note that for each class I CH_3OH maser, if multiple ATLASGAL sources are present within 60 arcsec, only the closest was used.

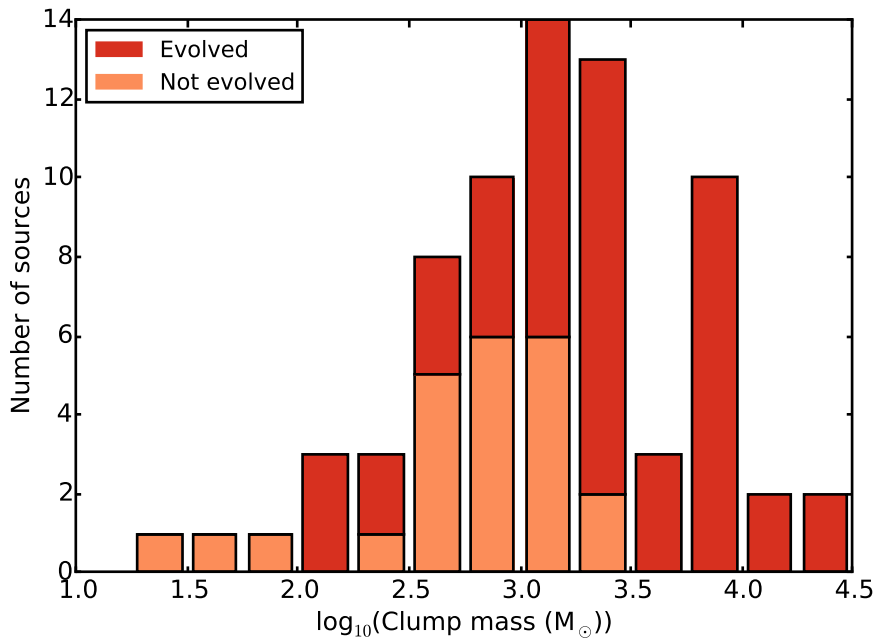


Figure 4.9: A stacked histogram of clump masses associated with class I CH_3OH masers, determined by ATLASGAL properties. The distribution peaks between 10^3 and $10^{3.5} M_{\odot}$, but has a wide spread of low- and high-mass clump associations. The highest mass values are restricted to evolved masers regions, while the lower masses tend to have non-evolved maser regions.

According to these data, class I CH₃OH masers appear to be associated with a wide range of clump masses. This is not unexpected; we knew of associations with low-mass star formation as well as non-star-forming phenomena. Unfortunately, this analysis fails to help isolate or predict where class I CH₃OH maser emission can occur. Non-evolved class I CH₃OH maser regions have masses up to $10^{3.5} M_{\odot}$, but tend to have lower mass values, and evolved maser regions dominate masses larger than $10^{3.25} M_{\odot}$.

Clump masses were compared with the brightness of class I CH₃OH masers, but no significant correlation was found. Chen et al. (2012) performed a similar comparison, using 95 GHz class I CH₃OH masers towards Bolocam Galactic Plane Survey (BGPS) 1.1 mm thermal dust emission (Fig. 6). They find a strong correlation between the maser luminosity and clump mass, with a p -value of 8.1×10^{-13} and r -value 0.84. Using auto-correlation, our line of best fit has the coefficients $r = 0.43$, $p = 1.6 \times 10^{-4}$. The Chen et al. (2012) sample may have a significant correlation due to the selection bias of targeting BGPS sources.

Fig. 4.10 shows a comparison between the IFD of ATLASGAL sources and class I CH₃OH masers, but any correlation is unlikely. Further analyses were conducted with offsets and integrated intensities, but no correlation is found in any comparison. While class I CH₃OH masers are often found towards ATLASGAL sources, their properties are seemingly independent of the sub-millimetre dust emission. However, CS (1–0) demonstrates a close relation with the gas; Fig. 4.11 compares their IFDs and finds a correlation coefficient $r = 0.84$. As the correlation between the brightness of CS and class I CH₃OH maser emission is also weak, the brightness of class I CH₃OH masers seems difficult to predict with respect to other star formation tracers.

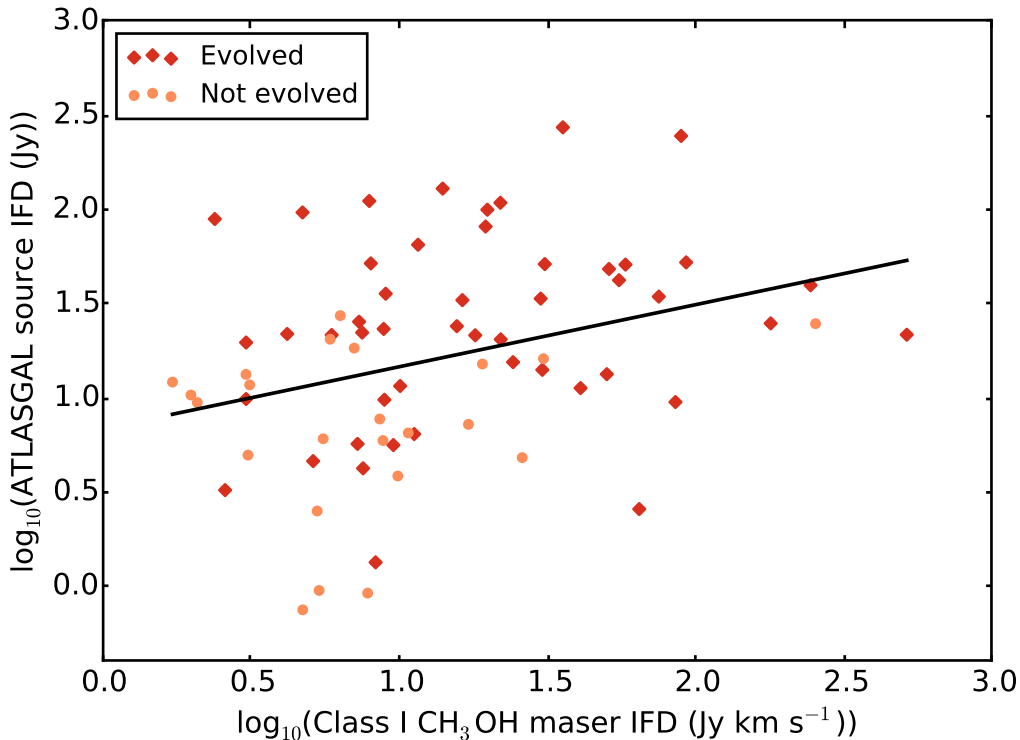


Figure 4.10: Scatter plot of integrated flux densities from ATLASGAL and class I CH₃OH maser regions. The correlation is very poor with a r -value of 0.33.

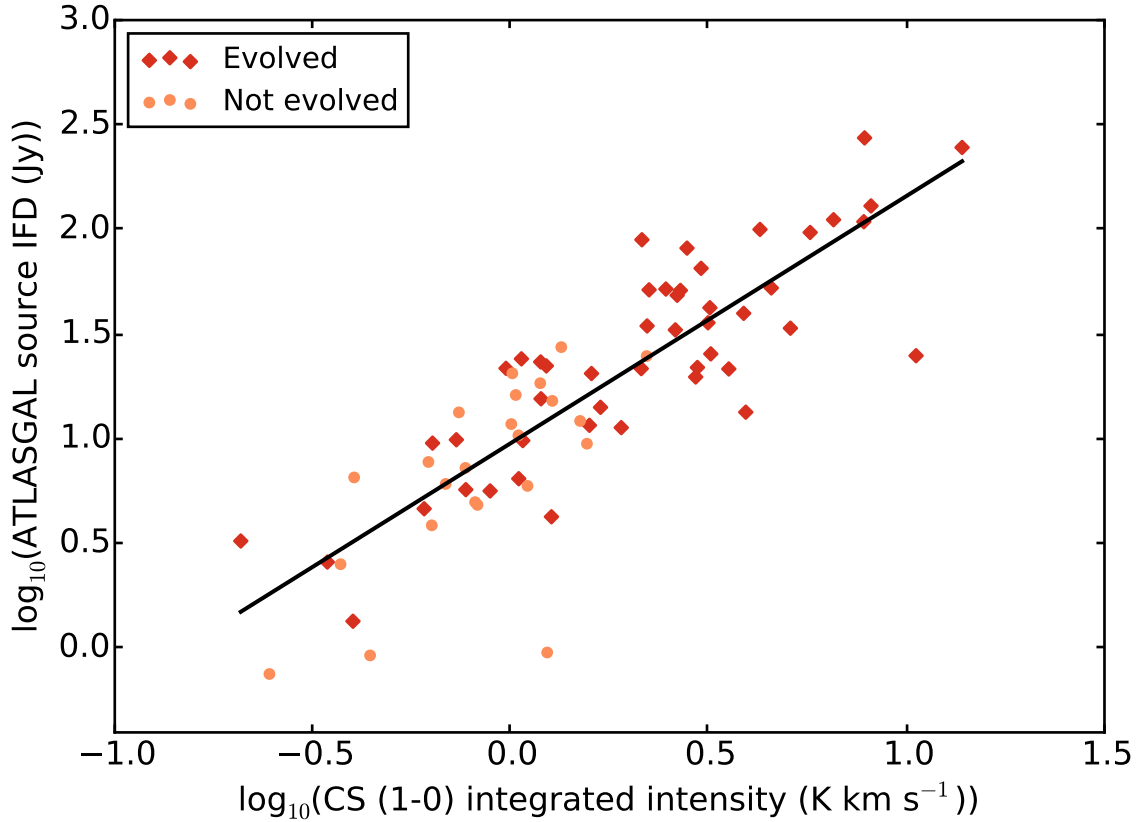


Figure 4.11: Scatter plot of integrated flux densities from ATLASGAL and CS emission from class I CH_3OH maser regions. A strong correlation is apparent with a r -value of 0.84. As the integrated intensity of the dust emission is directly proportional to clump mass, CS appears to be a good indicator of mass.

4.4.4.1 Class I CH_3OH masers without an ATLASGAL source

Only four class I CH_3OH maser regions are without an ATLASGAL point source classified by Contreras et al. (2013): G331.371–0.145, G331.442–0.158, G333.772–0.010 and G333.818–0.303. Using the data provided by the ATLASGAL team, we are able to investigate the $870\ \mu\text{m}$ emission in each of these regions. Within two ATLASGAL pixels (~ 12 arcsec), G331.371–0.145, G331.442–0.158 and G333.818–0.303 each have peak pixel ATLASGAL flux densities of 0.41 , 0.63 and $0.23\ \text{Jy beam}^{-1}$, respectively. Contreras et al. (2013) presents RMS values for ATLASGAL over the MALT-45 area, which is approximately $60\ \text{mJy beam}^{-1}$. These pixel values are at least 3σ , and were probably not classified as point sources by Contreras et al. (2013) to be on the conservative side. However, we do consider the $870\ \mu\text{m}$ emission towards these masers to be genuine. To calculate the corresponding clump masses, the pixel values are needed to convert to an integrated intensity. Peak pixel values were inflated by a factor of 4 to provide an integrated intensity, which is then used in Equation 4.1. These values correspond to clump masses of 245 , 353 and $59\ M_\odot$, respectively. These masses are relatively small compared to those found in §4.4.4, but even smaller values were calculated using official ATLASGAL sources.

G333.772–0.010 has a single ATLASGAL pixel with a peak flux density of $0.25\ \text{Jy beam}^{-1}$

at a distance of ~ 27 arcsec. However, unlike the other ATLASGAL regions, nearby pixels are relatively dim ($< 0.14 \text{ Jy beam}^{-1}$, $< \sim 2\sigma$), indicating this pixel is likely a random noise spike. Compared to other ATLASGAL sources at a similar distance (~ 5.2 kpc), we expect to see a similar distribution of $870 \mu\text{m}$ emission, but this is not the case. The peak pixel is near to but not cospatial with an IRDC, whereas the class I CH_3OH maser emission is closely associated with compact infrared emission. Interestingly, the maser emission is strong (peak of 17.7 Jy , IFD of $11.7 \text{ Jy km s}^{-1}$). The lack of dust emission toward this maser region does not necessarily indicate non-star-forming mechanisms, as class II CH_3OH masers have also been detected without $870 \mu\text{m}$ emission (Urquhart et al. 2015).

4.4.5 Comparing class I CH_3OH masers in cross- and auto-correlation

Minier et al. (2002) and Bartkiewicz et al. (2014) discuss class II CH_3OH maser emission in very-long-baseline interferometry and single-dish/auto-correlation. These comparisons between cross- and auto-correlation data reveals a wide range of flux being resolved out; Bartkiewicz et al. (2014) report between 24 and 86 per cent. The authors also note that the ‘missing flux’ is not dependant on distance, and that lower-resolution cross-correlation data have similar compact structures. This suggests that missing emission is quite diffuse, and is seemingly independent of the properties of compact maser emission. Minier et al. (2002) also attribute missing flux as being due to diffuse emission.

While these investigations were exclusively focused on class II CH_3OH masers, the observations detailed in this chapter are able to undertake a similar investigation for class I CH_3OH masers. It is worth noting that the observations of Minier et al. (2002) and Bartkiewicz et al. (2014) have a spatial accuracy approximately two orders of magnitude smaller than ours, which may result in differences. Auto-correlation spectra for the CH_3OH masers were extracted using the method discussed in §4.2.1.2. Cross-correlation spectra were then plotted with their corresponding auto-correlation spectrum; three example regions are shown in Fig. 4.12. With the 1.5A array configuration for the ATCA, the smallest baselines for these observations have distances of 153 and 321 m, corresponding to synthesised beams of approximately 9.2 and 4.4 arcsec, respectively.

Fig. 4.13 shows a histogram of the ratio of cross-correlation IFD and auto-correlation IFD. As demonstrated in Fig. 4.12, a large variation in missing flux-density is apparent across several regions. No trends are apparent for evolved, non-evolved or total populations. Class I CH_3OH emission can be strongly maser dominated (cross-correlation \approx auto-correlation), quasi-thermal dominated (auto-correlation \gg cross-correlation), or a mixture. This helps to explain why three target regions were not detected in cross-correlation (G331.44–0.14, G331.72–0.20 and G333.24+0.02); their 44 GHz emission is likely too extended and lacks any bright, compact maser components.

The relative strength of compact maser emission to diffuse emission of a class I CH_3OH maser region was assessed by computing the ratio of cross-correlation IFD to auto-correlation IFD, i.e., if the cross-correlation IFD closely matches the auto-correlation IFD, the maser strength is high. To test if maser- or quasi-thermal-dominated regions can be separated, populations were investigated with and without various maser associations. These associations included class II CH_3OH , H_2O and OH masers, but no dependence was found for maser

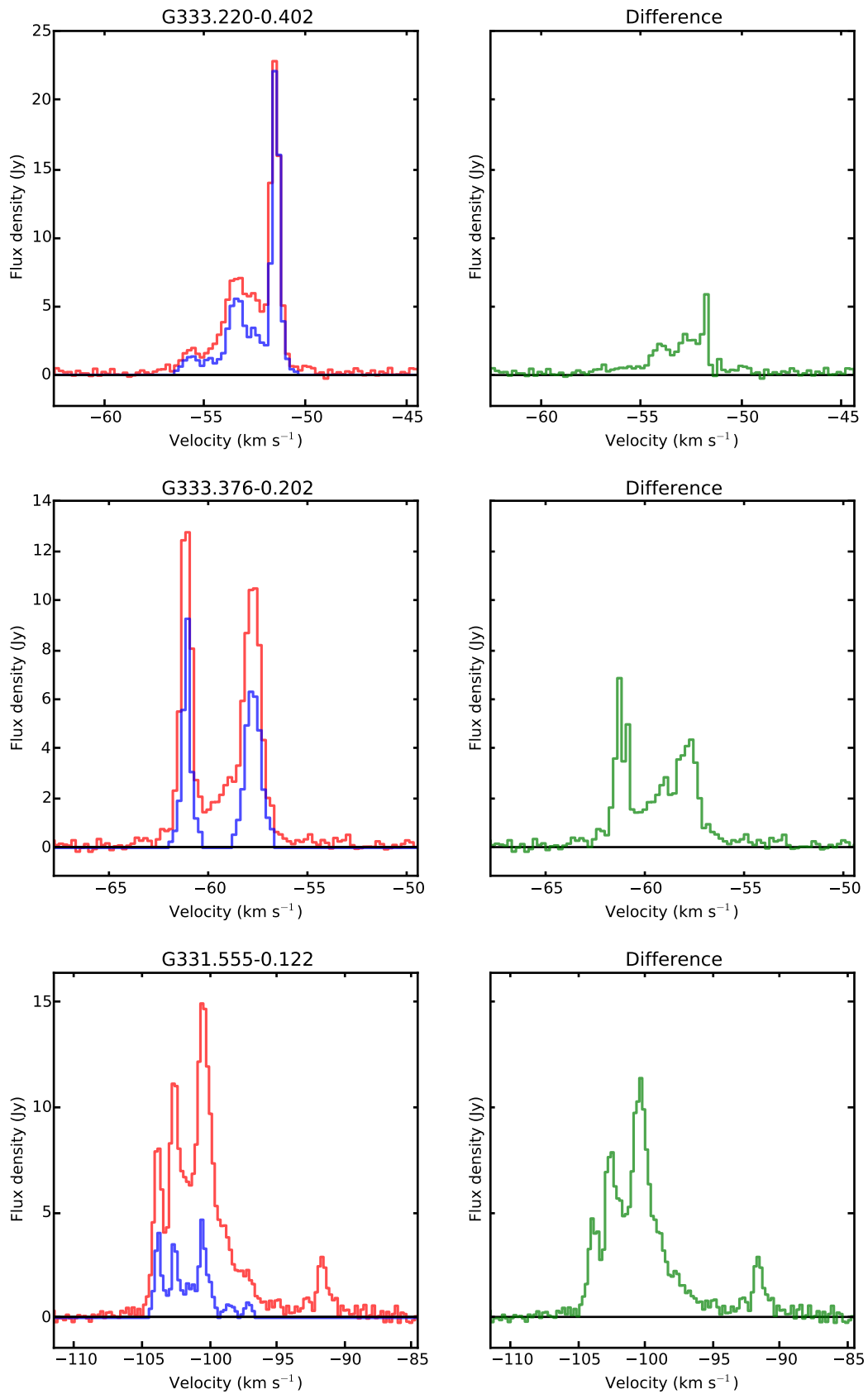


Figure 4.12: Cross- and auto-correlation spectra of three class I CH_3OH maser regions, with strong, moderate and weak maser strengths. Auto-correlation spectra are plotted red, cross-correlation spectra blue and the difference green. These comparisons allow maser strength determination for each region.

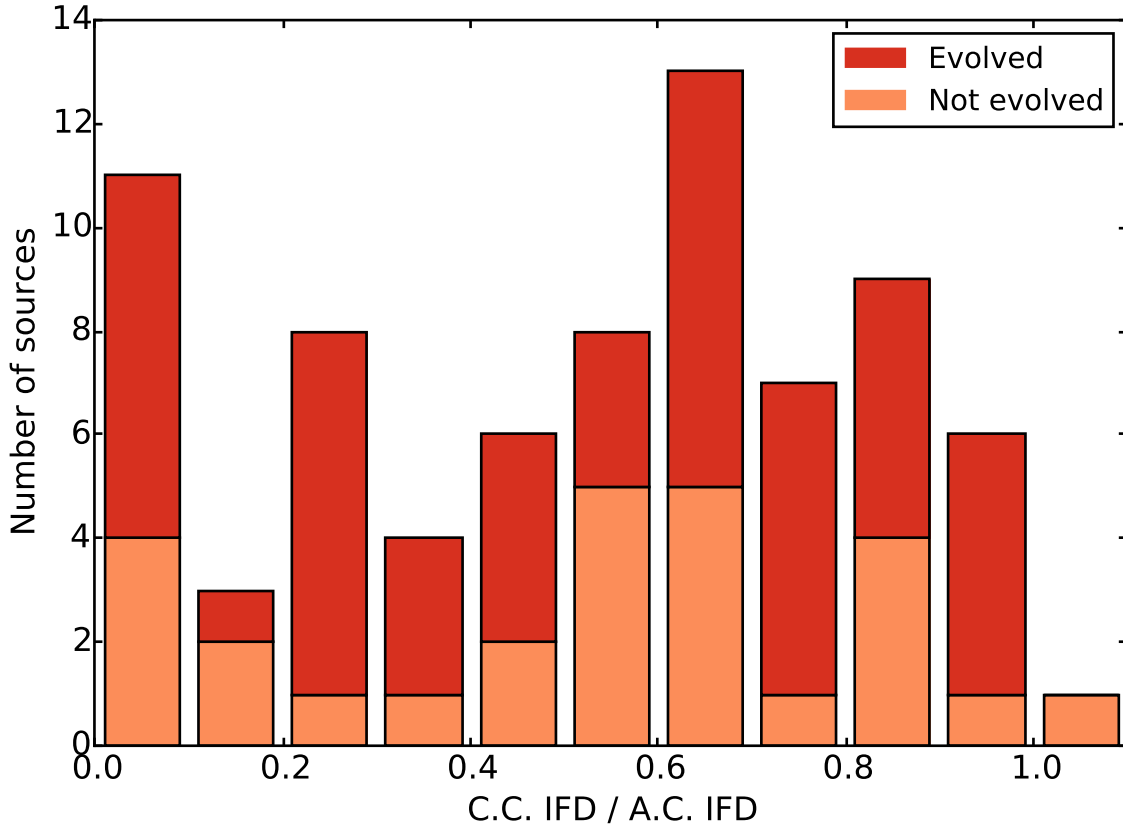


Figure 4.13: Histogram of the ratio of IFD in cross-correlation (C.C.) and auto-correlation (A.C.), for each class I CH_3OH maser region. No trend is apparent in the overall population, nor in evolved and non-evolved categories. The single datum with a ratio greater than one is due to an over-contribution of cross-correlation emission, due to spectral blending in nearby maser spots.

strength with and without these associations. Maser strength was also compared with thermal line integrated intensities in CS (1–0), SiO (1–0) $v = 0$ and CH_3OH 1_0-0_0 ; see Fig. 4.14. There is a large scatter in the data, but a similar trend can be seen in each comparison. The maser strength of class I CH_3OH regions decreases with the integrated intensity of each thermal line, which may be explained by the additional gas in these regions, which would also include additional CH_3OH . The additional CH_3OH in turn provides more opportunity for quasi-thermal emission.

The predictability of class I CH_3OH emission being maser-dominated or otherwise remains a mystery. Another star-forming tracer may reveal a correlation with the property of maser strength discussed here. Further observations of class I CH_3OH maser regions with better sensitivity and uv -coverage will also help to identify weaker, more diffuse cross-correlation emission.

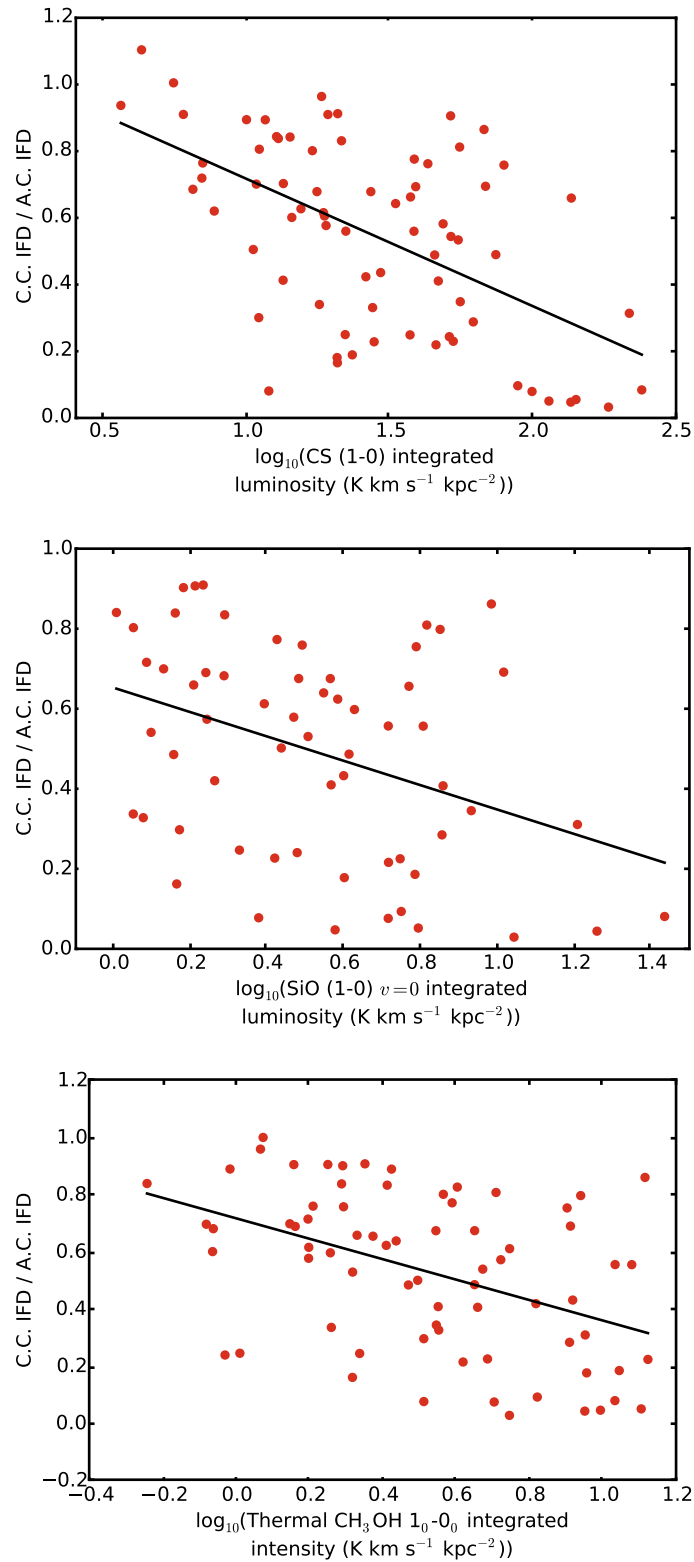


Figure 4.14: Scatter plots of the ratio of cross-correlation IFD to auto-correlation IFD (maser strength) against the thermal integrated intensity of CS, SiO and CH_3OH . The solid line represents the least squares fit. A similar, weak trend appears for all lines, but the large scatter hampers correlation (r -values of -0.55 , -0.38 and -0.45 , respectively). The single datum with a maser strength above 1 has an over-contribution of cross-correlation emission, due to spectral blending in nearby maser spots.

4.5 Summary and Conclusions

We have extracted high-resolution positions, flux-densities and velocities for class I methanol masers detected in the MALT-45 survey, and presented various properties for each observed region. The unbiased population from MALT-45 provides the first opportunity to assess class I methanol masers free from other selection biases, such as class II methanol masers or extended green objects. In addition, the thermal lines mapped by MALT-45 were refined for each maser region, providing better information about the regions containing the class I methanol masers. The science cases presented in this chapter have determined:

- (i) Class I methanol masers found towards younger sources have lower luminosities.
- (ii) Class I methanol masers typically possess small projected linear sizes and are confined to small velocity differences, particularly for non-evolved regions;
- (iii) Class I methanol masers are generally located within 0.5 pc of a class II CH₃OH or OH maser, but can be up to 0.8 pc away;
- (iv) Class I methanol masers are reliable tracers of systemic velocities;
- (v) The brightness of class I methanol masers correlate poorly with that of the thermal CS (1–0), SiO (1–0) $v = 0$ and CH₃OH 1₀–0₀ lines, but some clustering is apparent in a two-dimensional histogram;
- (vi) Class I methanol masers have high association rates with 870 μ m dust sources classified by ATLASGAL, with typical offsets not exceeding 0.4 pc;
- (vii) Class I methanol masers are found towards a large range of clump masses ($10^{1.25}$ to $10^{4.5} M_{\odot}$), but peak between $10^{3.0}$ and $10^{3.5} M_{\odot}$. Additionally, masers associated with clump masses between $10^{3.25}$ and $10^{4.5} M_{\odot}$ are almost all evolved;
- (viii) The amount of quasi-thermal emission in the 44 GHz class I methanol transition is poorly understood, but appears to increase as the brightness of thermal lines increase.

Chapter 5

Additional analyses with CS (1–0)

This chapter provides additional investigations with CS (1–0) mapped by MALT-45. Temperatures calculated using HOPS NH₃ (1,1) and (2,2) data are compared with the distribution of CS emission. The projected distances from CS peaks to class I CH₃OH masers and ATLASGAL sources are also detailed.

5.1 Temperature

Fig. 4.11 of Chapter 4 reveals the close association between CS (1–0) intensity and clump mass. Furthermore, differences in the CS (1–0) and NH₃ (1,1) distributions were discussed in Chapter 3. Another useful physical parameter in studying the star-forming process is the kinetic temperature of the gas within dense molecular gas. Using HOPS NH₃ (1,1) and (2,2) data, the temperatures across the MALT-45 survey region can be calculated and compared with the CS data.

5.1.1 Methodology

Temperatures were derived using a similar procedure to that of Lu et al. (2014). The pipeline steps include:

- (i) HOPS NH₃ (1,1) and (2,2) cubes were smoothed with a 60 arcsec FWHM kernel;
- (ii) The optical depth of the NH₃ (1,1) line was derived using:

$$\frac{T_B(1, 1, m)}{T_B(1, 1, s)} = \frac{1 - \exp(-\tau(1, 1, m))}{1 - \exp(-a\tau(1, 1, m))} \quad (5.1)$$

where T_B is the brightness temperature, (J, K, m) designates the main line, (J, K, s) designates the inner satellite line, a is the relative intensity between the main and inner satellite lines under optically thin conditions and τ is the optical depth. Note that this is the same as Equation 1.3, and assumes equal beam-filling factors and excitation temperatures for hyperfine lines, local thermodynamic equilibrium and that the cosmic microwave background temperature of 2.7 K can be ignored. The a value is taken from (Purcell 2006) ($^{0.139}/_{0.502} \approx 0.277$);

- (iii) The optical depth of the NH₃ (2,2) line was derived using the NH₃ (1,1) optical depth:

$$\frac{T_B(1, 1, m)}{T_B(2, 2, m)} = \frac{1 - \exp(-\tau(1, 1, m))}{1 - \exp(-\tau(2, 2, m))} \quad (5.2)$$

This equation assumes the excitation temperature for both transitions is the same;

(iv) The rotational temperature is derived using:

$$T_R = \frac{-41.5 \text{ K}}{\ln \left(\frac{0.282 \tau_{(2,2,m)}}{\tau_{(1,1,m)}} \right)} \quad (5.3)$$

(v) Kinetic temperature is derived from the rotational temperature via:

$$T_R = \frac{T_K}{1 + \frac{T_K}{41.5} \ln \left(1 + 0.6 \exp \left(\frac{-15.7}{T_K} \right) \right)} \quad (5.4)$$

Equations 5.1, 5.2, 5.3 and 5.4 were taken from Lu et al. (2014). Temperatures were calculated on a pixel-by-pixel basis from the HOPS data. Unfortunately, a number of issues were encountered when building this pipeline. Primarily, the sensitivity of HOPS NH₃ (1,1) and (2,2) is poor, resulting in reliable temperatures being derived for only a few clumps. The restrictions put into place were:

(i) The HOPS team provides integrated intensity (moment 0) maps of NH₃ data. These maps are blanked where no emission is detected, and are smoothed over regions of emission. Calculations of optical depth (and consequently temperature) are not performed on pixels that have been blanked;

(ii) Using the spatially smoothed maps described above, the spectral data of NH₃ (1,1) and (2,2) was smoothed with a Hanning window of width 5. This results in a velocity resolution of $\sim 0.38 \text{ km s}^{-1}$. Gaussian fits were then attempted for the main and inner satellite components, in order to derive values necessary for Equation 5.1. As the sensitivity is poor, detection of satellite lines is unreliable, and thus cannot properly derive values for τ . This problem was resolved by comparing the Gaussians fitted to the main line of NH₃ (1,1) emission and their corresponding moment 0 values: any pixels with a moment 0 value less than 1 K km s^{-1} were considered optically thin (assigned $\tau = 0.001$), otherwise, the integrated intensity of the Gaussian was subtracted from the moment 0 value. If the remainder of this subtraction was less than 0, it was assumed that there were no detected satellite lines, as the Gaussian characterised all the emission present, and thus the pixel is optically thin. If the remainder was positive, the remaining emission was characterised based on the relative intensities of satellite lines to the main line. Furthermore, the presence of satellite lines was modulated by the moment 0 value. This is expressed algebraically as:

$$I(1, 1, s) = \frac{\text{remainder}}{2} \left(1 - \frac{b}{a+b} \left(1 - \exp \left(\frac{-\text{mom0}}{5} \right) \right) \right) \quad (5.5)$$

where $I(1, 1, s)$ is the integrated intensity of the inner satellite line, ‘remainder’ is the emission left after performing the subtraction described above, a is the relative intensity between the main and inner satellite lines (b is for the outer satellite lines, $^{0.111}/_{0.502} \approx 0.221$) and ‘mom0’ is the moment 0 value. The division by two is necessary to calculate the integrated intensity of only one of the inner satellite lines. The moment 0 value is divided by 5 such that only pixels with significant integrated intensities contribute with $b/a+b$. The $b/a+b$ factor isolates the inner satellite from the outer. Note that Equation 5.1 uses brightness temperatures instead of integrated intensities; by also using the integrated intensity

of the main line, i.e. $I(1,1,m)$, we assume that the ratio of $I(1,1,m)/I(1,1,s)$ approximates $T_B(1,1,m)/T_B(1,1,s)$;

(iii) Gaussian widths were restricted. Given the general form of a Gaussian:

$$f(x) = a \exp\left(\frac{-(x-b)^2}{2c^2}\right) \quad (5.6)$$

the standard deviation c was restricted to be no greater than 2.3, which is equivalent to a FWHM of 5.4 km s^{-1} . This permits the widest main lines of NH_3 (1,1) to be fitted accurately, without automated fitting routines contaminating the main line with satellite lines;

(iv) If $I(1,1,s)/I(1,1,m) > 0.8$, $I(1,1,s)/I(1,1,m)$ was set to 0.8. The calculated $I(1,1,s)$ can sometimes be much larger than $I(1,1,m)$, due to the moment 0 value provided being much larger than the intensity of the Gaussian fitted to the main line of NH_3 (1,1). This cap effectively sets the corresponding pixel to be optically thick. Consequently, this restricts the minimum possible kinetic temperature to be around 10 K. This effect was noticed primarily in the centres of cold clumps, such as those seen over the G333 giant molecular cloud;

(v) If the peak spectral value of a pixel was less than 0.4 K for NH_3 (2,2), it was rejected as insignificant. Without this requirement, noise peaks were often fitted as they were brighter than real emission;

(vi) If a negative τ was produced, it was due to insufficient satellite line contribution, and the pixel was considered optically thin;

(vii) Finally, if $\tau_{(1,1)} < 0.5$, instead of using Equation 5.3 the rotational temperature was calculated directly with:

$$T_R = \frac{-41.5 \text{ K}}{\ln\left(0.282 \frac{T_B(2,2,m)}{T_B(1,1,m)}\right)} \quad (5.7)$$

This pipeline was developed in the PYTHON programming language, using the ASTROPY library for FITS file reading and saving, and the SCIPY library for Gaussian fitting and equation solving. The resulting kinetic temperature map (T_K) is shown in Fig. 5.1.

There are a few gas clumps with temperatures less than 15 K. Typically, these regions are surrounded by gas with temperatures up to 30 K. There are three distinct clumps containing only high-temperature gas (pixels of at least 30 K); two of these (G330.95–0.19 and G333.60–0.20) are particularly active regions, and were discussed in Chapter 3.

5.1.2 Relation with CS (1–0)

In an attempt to investigate if there is a relationship between temperature and CS (1–0) emission, values have been compiled in Table 5.1. Typically, the available temperature information coincides with a peak of CS emission. Hence, the temperature recorded is the average value around the peak of CS emission. One exception is G333.33–0.36, which does not have a distinct peak of CS emission, but has many class I CH_3OH masers, and a different temperature to nearby CS peaks. Detailed descriptions of each region are given in §5.1.3.

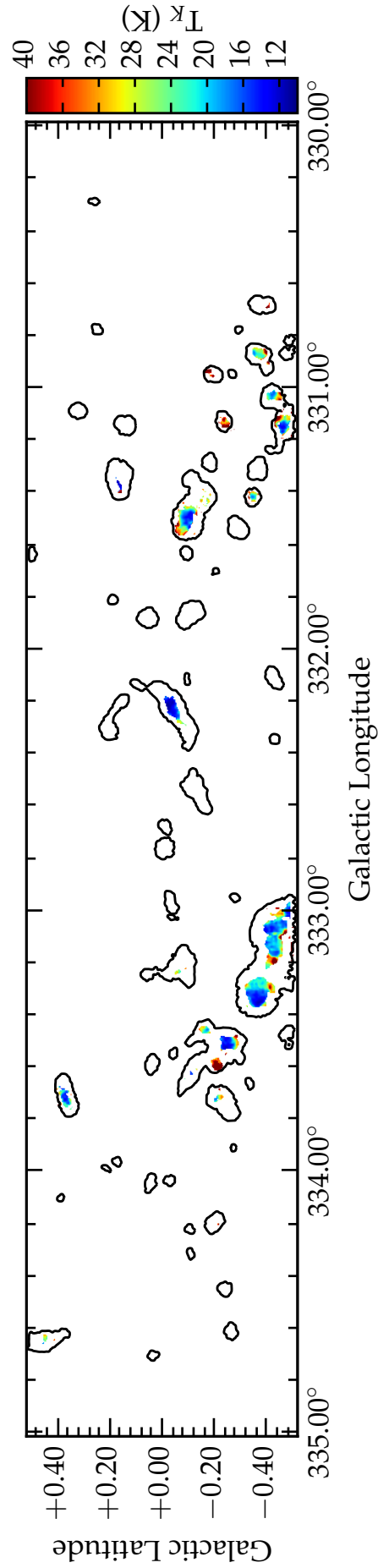


Figure 5.1: Gas temperatures calculated via NH_3 (1,1) and (2,2). Contours indicate regions with detected NH_3 (1,1). Temperature information exists in few regions across the map, primarily limited by NH_3 (2,2) detections. Many regions have temperatures less than 20 K, surrounded by warmer gas. Only three regions have consistently high temperatures (>30 K; G330.95–0.19, G331.14–0.24 and G333.60–0.20).

Many of the clumps with available temperature information are also detailed by Lowe et al. (2014). Using the 70 m Tidbinbilla radio telescope, Lowe et al. (2014) conducted observations of NH_3 (1,1) and (2,2) over the G333 giant molecular cloud, and used these data to calculate kinetic temperatures. There are differences between their derived temperatures and those calculated by this work. With only two outliers, these differences are well characterised by the following relation:

$$T_L = 1.98T_H - 9.39 \quad (5.8)$$

where T_L is the kinetic temperature derived by Lowe et al. (2014) and T_H is the temperature derived from HOPS data (this work). Including the two outliers, the correlation coefficient (r -value) is 0.87, which indicates a predictable systematic differences between these datasets. These differences can be explained by two factors. Tidbinbilla is much larger than Mopra (70 m compared to 22 m), resulting in a significantly smaller primary beam for the observations of NH_3 (1,1) and (2,2) (~ 119 arcsec compared to ~ 37 arcsec). Consequently, the cores of NH_3 used are less affected by spatial smearing, resulting in a more representative spectrum of emission within gas clumps, which leads to more accurate temperatures. Another significant difference from HOPS is the additional sensitivity, providing more accurate satellite lines of NH_3 (1,1) and detections of NH_3 (2,2). For these reasons, the published temperatures of Lowe et al. (2014) should be trusted over the ones derived here. Despite this, the HOPS temperatures remain useful for discussion.

The two exceptions to the relation given in Equation 5.8 are G333.01–0.48 and G333.72–0.21. Only a few pixels of temperature were derived from the HOPS data for G333.01–0.48, but the additional sensitivity by the observations of Lowe et al. (2014) are able to provide an accurate temperature. G333.72–0.21 also has few temperature pixels from HOPS data, although this kinetic temperature closely agrees with that of Lowe et al. (2014). HOPS sensitivity is likely exacerbating the issue here, but there is not enough information to conclude this point.

A scatter plot of temperature against CS intensity can be seen in Fig. 5.2. There is a reasonable correlation after removing two outliers (r^2 -value of 0.46); this indicates that observations of CS may be used to help indicate the temperature of gas. However, this result should be taken with caution, as it suffers from low-number statistics. Additionally, the temperature is derived from the optical depth of NH_3 , which may also correlate with the amount of CS present. The presence of other star-forming tracers was noted for each region, but no trends associated with their presence or absence is apparent.

CS (1–0) is a good tracer of all dense gas in a clump, not just that near to a YSO or in an outflow. Higher transitions of CS are less susceptible to the bulk of the gas as they require higher temperatures to be excited, and thus may be better at discriminating high-mass, hot regions. If the luminosity of CS does correlate with temperature, then higher CS transitions, when compared with CS (1–0), should also help to identify cold regions of gas, given that it is less likely to appear there.

5.1.3 Individual source descriptions

The following text briefly discusses CS (1–0) emission with select regions, given the availability of temperature information. Fig. 5.3 shows the temperature of each of these regions along

Table 5.1: Regions with temperature information. Each region is focused around a peak of CS emission (except for G333.33–0.36); temperature values here reflect an average around this peak of emission. Column 1 lists the coordinates of the CS peak in Galactic coordinates. Column 2 lists the calculated kinetic temperature derived from NH_3 (1,1) and (2,2) data. Column 3 lists the main-beam temperature of the CS peak. Column 4 lists the assumed distance, which is taken from the kinematic distances in Chapter 4. If a region was without a kinematic distance, a value was taken from another nearby gas clump with a similar peak CS velocity. Columns 5 through 9 list the presence of various star formation tracers. These are indicated if known ('Y') or not ('N'). If the presence is uncertain, it is designated with a question mark ('?'); these only apply to the H53 α radio recombination lines. Column 10 lists the kinetic temperature from Lowe et al. (2014), where available. The single dashed value corresponding to G333.60–0.20 represents the inability of Lowe et al. (2014) to supply a kinetic temperature for this region.

Region of interest	Kinetic temp. (K)	Peak CS (1-0) (K)	Assumed distance (kpc)	Presence of:				Kinetic temp. from Lowe et al. (2014) (K)	
				Class I CH ₃ OH maser?	Class II CH ₃ OH maser?	OH maser?	H ₂ O maser?		H53 α RRL?
G330.88–0.37	22	1.9	4.0	Y	Y	Y	Y	Y	
G330.95–0.18	33	1.5	5.5	Y	Y	Y	Y	Y	
G331.03–0.43	18	0.97	4.3	N	N	N	N	?	
G331.13–0.24	30	0.85	5.4	Y	Y	Y	Y	N	
G331.13–0.48	20	1.10	4.3	Y	N	N	N	?	
G331.42–0.35	20	0.61	4.2	N	N	N	N	?	
G331.52–0.10	17	1.4	5.2	Y	N	Y	Y	Y	
G332.24–0.04	13	0.67	3.4	Y	N	N	N	N	
G333.00–0.44	35	0.88	3.8	Y	N	N	Y	Y	63.6
G333.01–0.48	15	0.82	3.6	Y	N	N	N	Y	35.6
G333.07–0.40	15	0.8	3.6	Y	Y	N	Y	Y	19.8
G333.07–0.44	18	1.4	3.7	Y	Y	N	Y	Y	25.7
G333.13–0.43	20	2.6	3.5	Y	Y	Y	Y	Y	31.9
G333.28–0.38	20	1.9	3.6	Y	N	N	N	Y	29.2
G333.30–0.35	20	1.8	3.5	Y	N	N	N	Y	25.5
G333.33–0.36	14	1.1	3.6	Y	N	N	N	Y	
G333.46–0.16	20	0.61	3.1	Y	Y	Y	Y	Y	24.4
G333.52–0.27	15	0.85	3.5	Y	N	N	N	Y	20.3
G333.60–0.20	50	2.0	3.5	Y	N	Y	Y	Y	-
G333.72–0.21	18	0.67	3.5	Y	N	N	N	Y	17.8
G333.72+0.37	15	0.47	3.5	N	N	N	N	?	

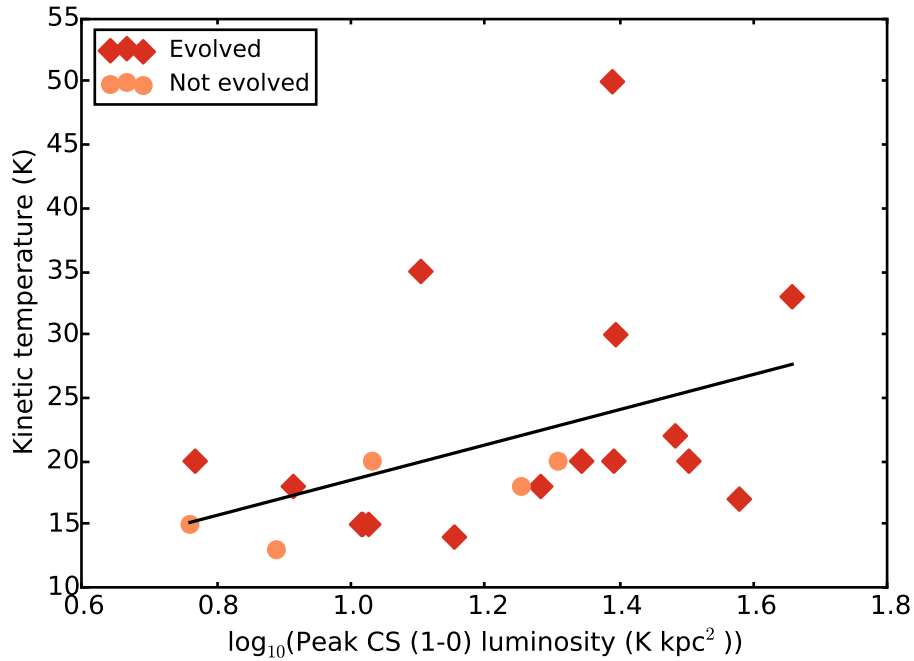


Figure 5.2: Scatter plot of temperature vs. peak CS (1–0) luminosity in clumps with temperature information. The line of best fit for all data has an r^2 -value of 0.17. When removing the two outlying data points (temperature >35 K), the r^2 increases to 0.36. The outliers are G333.00–0.44 and G333.60–0.20. Clumps are classified as evolved if the CS peak has an associated class II CH₃OH maser, OH maser or H53 α radio recombination line; not enough data is present to identify trends with or without evolved species.

with CS contours. The peak velocity of CS emission is used to infer the distance of objects; if velocities are similar between nearby clumps, they are assumed to be at similar distances. Unless otherwise stated, when referring to all types star-forming masers, the presence of class I CH₃OH, class II CH₃OH, H₂O and OH masers is indicated.

5.1.3.1 Regions near G331.03–0.32

The three southern-most clumps seen in Fig. 5.3 all have similar temperatures (~ 20 to 25 K), but have some other differences. The G330.87–0.37 clump has a very high peak of CS (~ 1.5 K), as well as all types of star-forming masers, but has similar temperatures to the other two clumps, despite their lack of other star-forming masers. Both other clumps have an approximate peak of 1 K in CS, but G331.13–0.48 has two class I CH₃OH masers while G331.03–0.43 has none. Given the strong presence of NH₃ (required to calculate temperature) and CS (well correlated with mass), perhaps these clumps are young star-forming regions that may eventually appear similar to G330.87–0.37.

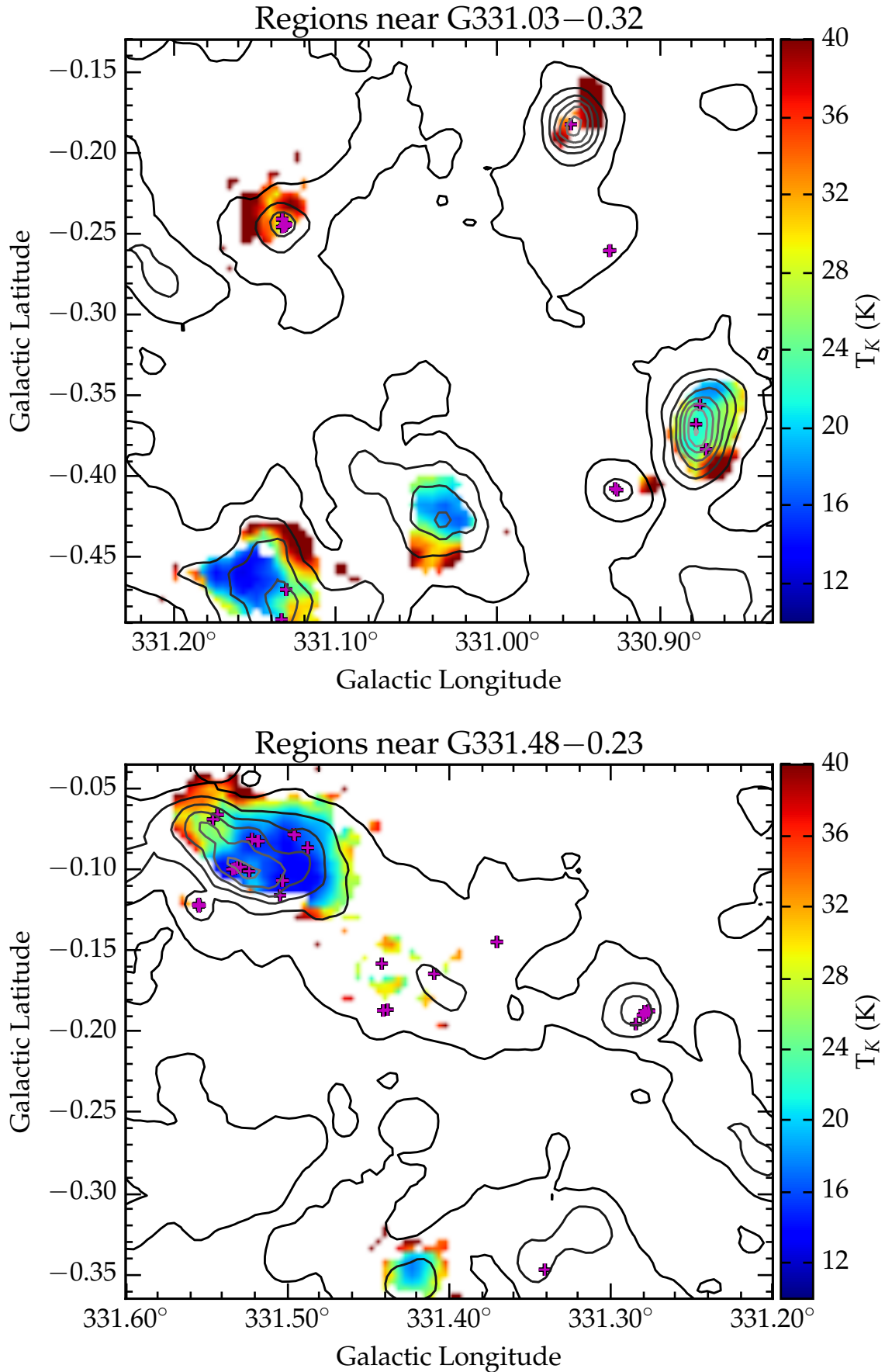
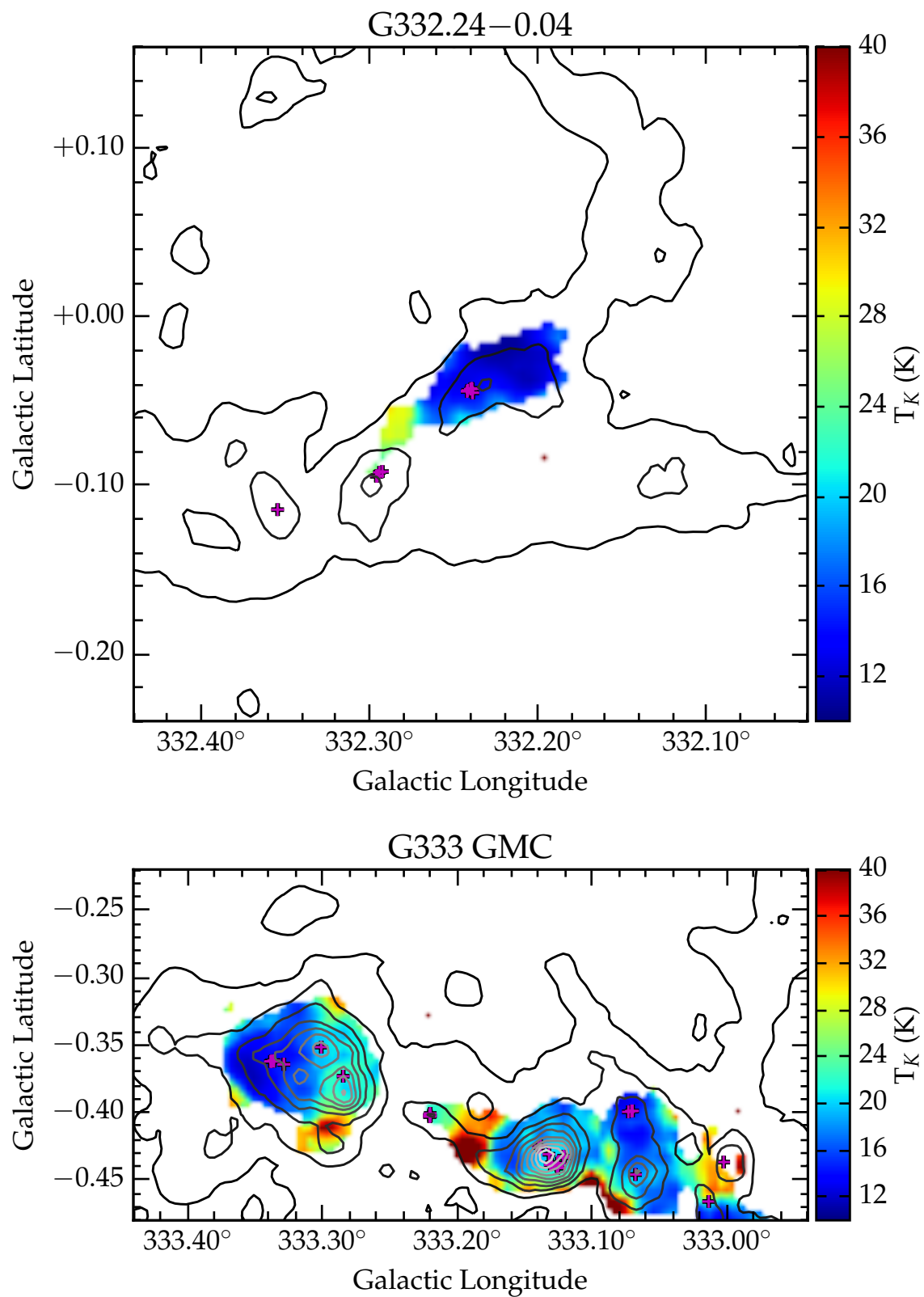
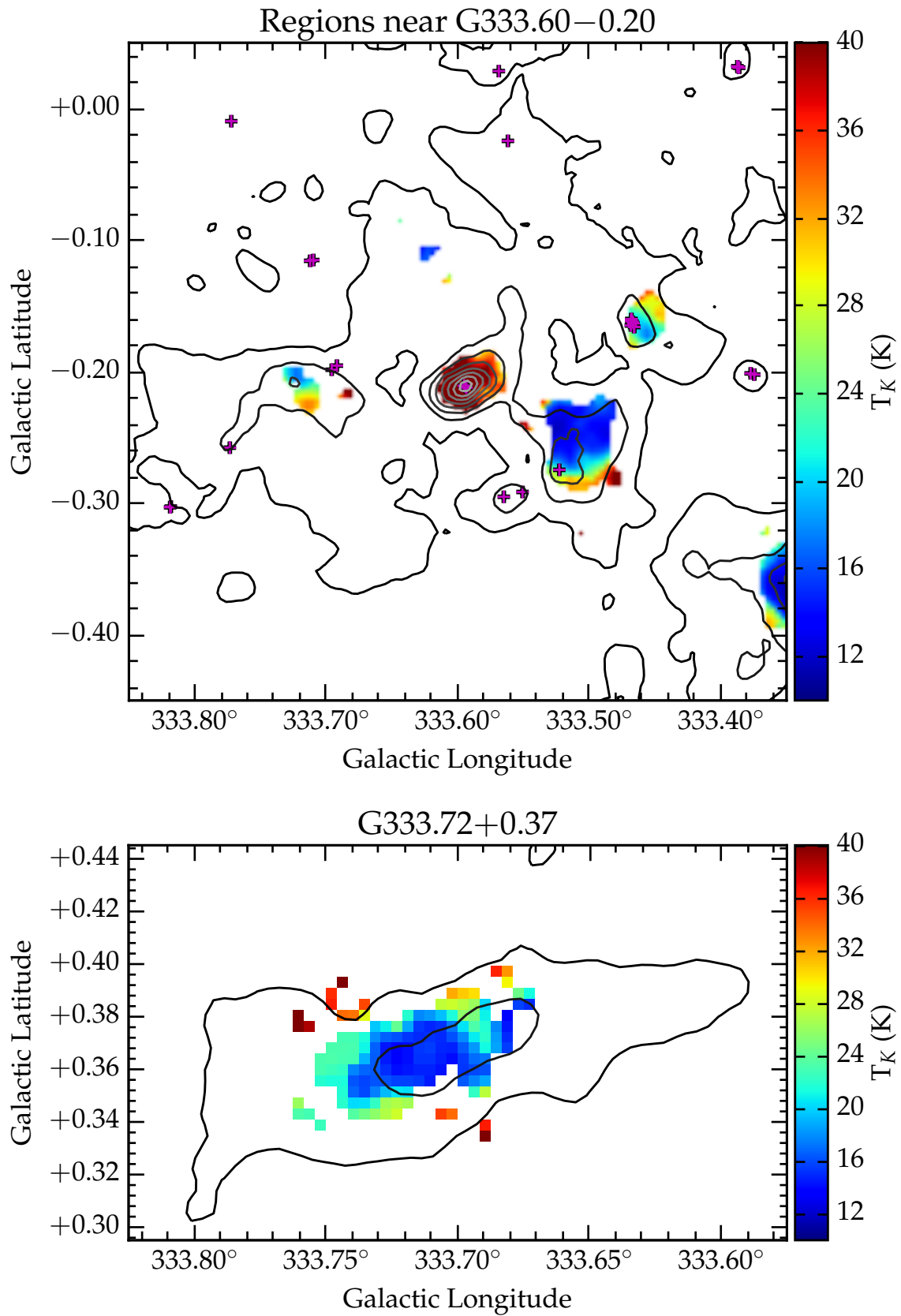


Figure 5.3: Specific regions with kinetic temperature information. Contours are CS (1-0) emission from MALT-45, and magenta plus symbols designate high-resolution class I CH_3OH maser positions. Contour levels are 0.15, 0.40, ..., 2.9 K.

Figure 5.3: *continued*

Figure 5.3: *continued*

Both of the northern-most clumps (G330.95–0.19 and G331.13–0.24) have high temperatures (at least 30 K), are associated with all types of star-forming masers and are approximately at the same distance. However, they exhibit very different strengths in CS; 1.5 K for G330.95–0.19 and 0.8 K for G331.13–0.24.

5.1.3.2 Regions near G331.48–0.23

The large region centred on G331.52–0.09 is a giant H II region with many class I CH₃OH masers, but one distinct CS peak. This peak is cool (~ 16 K) but is slightly offset from the coldest gas to the west (~ 14 K).

G331.42–0.35 appears similar to G331.03–0.43 and G331.13–0.48; the temperature is approximately 20 K with a CS peak of 0.6 K, but no star-forming masers are present. Like the others, the presence of CS and NH₃ hints that this clump is in the early stages of star formation.

5.1.3.3 G332.24–0.04

The arc structure traced by CS here closely follows infrared absorption, highlighting dense IRDCs. The temperature data is roughly cospatial with the class I CH₃OH masers detected; in Chapter 4 I show that when class I CH₃OH masers appear in large numbers and spatial extent, the associated star-forming region is more evolved in an evolutionary timeline. This source is the exception, classified as ‘young’ due to its lack of class II CH₃OH or OH masers, as well as H51 α or H53 α emission. This classification is reinforced by the low temperature found here (~ 13 K). The peak of CS (0.7 K) is slightly offset from the maser emission (~ 36 arcsec).

5.1.3.4 G333

The CS peak at G333.01–0.48 has a temperature ~ 15 K. This may be contaminated by hot gas originating to the north, with a temperature around 30 K. Another nearby CS peak at G333.00–0.44 has an even higher temperature (between 35 and 40 K), and is seemingly active; G333.00–0.44 and the region between G333.00–0.44 and G333.01–0.48 both have a H₂O maser detection, highlighting outflow activity. This is also presumably the cause of these higher temperatures. If the hotter gas is not associated with G333.01–0.48, then G333.01–0.48 may be another example of a cold, dense core with some class I CH₃OH maser activity. The RMS survey classifies both of these clumps as diffuse H II regions (Urquhart et al. 2014a).

The CS structure of the peak at G333.07–0.44 is interesting. This peak has a temperature of 18 K and CS brightness 1.4 K. There is a class II CH₃OH maser cospatial with the CS peak, while approximately 50 arcsec to the north-west of the peak lies a H₂O maser detection. Far to the north at G333.07–0.40, the temperature drops to 13 K and there are multiple class I CH₃OH masers. There appears to be an infrared source cospatial with these masers, such that this region is probably distinct from G333.07–0.44, but the significantly offset H₂O maser may indicate the presence of a powerful outflow that influences the CS presence in G333.07–0.40. Both maser sources have RRL detections in Chapter 4; the emission may

originate from both regions, or one is contaminating the other. Given the low temperature and weak star-forming maser association of G333.07–0.40, the latter seems more likely.

G333.13–0.43 is the brightest CS peak in the entire MALT-45 survey (2.6 K), and has a kinetic temperature of ~ 20 K. This region features many star-forming maser species, with four class II CH₃OH maser detections from the MMB. Only the most north-eastern class I CH₃OH masers are without an RRL detection. Perhaps there is such a large mass of molecular gas that despite the evolved nature of this source, the temperature still appears low as it better reflects the bulk of the gas present.

Another CS peak at G333.22–0.40 has temperature information. The temperature of this small region is between 20 and 25 K, but this may be contaminated by the hot bridge between G333.22–0.40 and G333.13–0.43. Like G333.07–0.40, Chapter 4 lists the presence of RRL emission, although given the temperature and lack of star-forming masers, this may be originating elsewhere.

The G333.33–0.36 clump appears to have three distinct regions, highlighted by the presence class I CH₃OH masers. G333.28–0.38 and G333.30–0.35 have CS peaks of 1.9 and 1.8 K, respectively, but both have temperatures ~ 20 K. Another CS peak at G333.31–0.38 has a strength of 1.5 K, but is not as closely associated with class I CH₃OH masers. This temperature is a little lower at ~ 16 K. The remaining class I CH₃OH masers appear toward the coldest part of the clump (~ 13 K). As RRL emission was detected toward each of these masers in Chapter 4, this clump appears to feature a giant H II region; indeed, Urquhart et al. (2014a) classify both G333.28–0.38 and G333.31–0.38 as H II regions.

5.1.3.5 Regions near G333.60–0.20

G333.60–0.20 is noted for being the brightest H II region in the MALT-45 survey. It has been discussed in Chapter 3 as being quite an evolved stage of HMSF, and is thought to contain about 10 O-type stars. The weak NH₃ emission gives questionable temperature information; the temperature varies from 30 to 55 K across the clump. The strong CS peak (2.0 K) coincides with class I CH₃OH maser positions, which is offset from H₂O and OH masers (~ 36 arcsec). Lowe et al. (2014) do not supply a temperature for this clump, due to the weak NH₃ emission; the fact that we were able to calculate a temperature with the HOPS NH₃ data suggests that the NH₃ emission is smeared from outside the clump. This in turn helps to explain variable temperature seen over the clump.

G333.46–0.16 features all star-forming masers with a temperature of 20 K. However, unlike other regions which also feature multiple masers, this one has a relatively dim peak CS (0.61 K), despite having the smallest distance of those analysed (3.1 kpc).

Temperature information is available throughout a large fraction of the G333.52–0.27 clump, indicating the widespread presence of NH₃ (1,1) and (2,2). Across the CS peak shown, the temperature gradient increases to the south, and the CS peak ends near the detection of a class I CH₃OH maser. Using 1.2 mm dust emission, Lowe et al. (2014) detail three dust clumps over the single clump discussed here (G333.521–0.239, G333.524–0.272 and G333.539–0.245). In their interpretation, the authors note that each of the three clumps is associated with 160 μ m emission from *Herschel* Hi-GAL data.

G333.72–0.21 has a small CS peak, unusually offset from masers. Two class I CH₃OH

masers have a large offset from the CS peak, and a class II CH₃OH maser is approximately the same distance away from the CS peak to the south-east. Lowe et al. (2014) note a compact 160 μm object toward the peak of their 1.2 μm dust emission, and speculate that this clump is likely to be in the earliest stages of star formation.

5.1.3.6 G333.72+0.37

The CS contours trace an IRDC, with temperature information lying within. The lowest temperature pixel (13.4 K) lies to the east of the cloud, and is cospatial with infrared emission in this IRDC, but the average temperature value was taken to be 15 K. There are no maser detections associated with this IRDC, despite this spatial overlap. This IRDC may be pre-star-forming, and thus a good example to study the initial conditions of star formation.

5.1.3.7 Summary

Fig. 5.2 shows a slight correlation between CS (1–0) luminosity and temperature, although this relation suffers from small number statistics. Qualitative investigations of these regions shows that both cold and hot regions of gas can have very different CS brightnesses; without high-resolution observations, it is difficult to disentangle the bulk of the gas from cores containing YSOs. For example, the CS brightnesses of ‘hot’ clumps are 0.8, 1.5 and 2.0 K. These are not unusual values when compared to the ‘cold’ clumps (G333.13–0.43 is brightest at 2.6 K with a temperature of 20 K).

The discussion above is primarily limited by the quality of NH₃ (1,1) and (2,2) data used to determine the temperatures. Higher resolution and higher sensitivity observations of NH₃ (1,1), (2,2) and CS (1–0), as well as higher energy transitions of CS, would be effective at highlighting the gas temperature distribution across clumps. This is relatively easy to do, as all of these spectral lines are bright and the ATCA is capable of producing high-quality data in a short amount of time. All of the regions discussed have a CS (1–0) peak of at least 0.6 K. A preliminary target list could include CS (1–0) peaks from MALT-45 with a brightness of at least 0.3 K ($\sim 10\sigma$). Chapter 3 mentions a few class I CH₃OH maser regions with dim CS association (<0.11 K); these, and other class I CH₃OH maser regions, would also make for interesting targets for follow-up observations of thermal gas with the ATCA.

5.2 Offsets between CS (1–0) peaks and class I CH₃OH masers

At a few points in this thesis, CS (1–0) has been compared with class I CH₃OH masers. Chapter 4 shows that their intensities appear to be un-correlated, although their velocities match very closely; see Fig. 4.4. As seen in §5.1, peaks of CS emission also tend to feature class I masers. Chapter 4 also discusses the offsets between class I CH₃OH maser positions and other maser species, finding that offsets tend to be within <0.5 pc. What is the distribution of offsets between these two star-forming species? An investigation is detailed below.

5.2.1 Methodology

Similar to §5.1.1, results were calculated using PYTHON with ASTROPY for FITS file reading. The peak intensity map (moment -2) of CS (1–0) was taken from the MALT-45 survey detailed in Chapter 3, and high-resolution class I CH₃OH positions were taken from Chapter 4. To smooth the data, CS channels were binned into groups of 10. This CS (1–0) data was read into a matrix of pixels in Galactic longitude and latitude. From the position of each class I CH₃OH spot, all CS pixels within 4 pixels (~ 60 arcsec) were identified from the spot. Rather than simply accepting the brightest CS pixel within 4 pixels as the CS peak, CS intensities were modulated with distance according to the following formula:

$$T_m = T_d \cos\left(\frac{\text{dist}}{\frac{3}{2}\pi}\right) \quad (5.9)$$

where T_m is the modulated main-beam temperature, T_d is main-beam temperature of the CS pixel, and ‘dist’ is distance in pixels. The $\cos(\text{dist}/\frac{3}{2}\pi)$ factor tapers the CS values at large distances from the class I CH₃OH maser spots, such that local peaks are preferred. At a distance of 4 pixels, a CS brightness is tapered by a factor of ~ 0.66 . Finally, offsets are converted to projected distances using the kinematic distances prescribed to each maser in Chapter 4.

In an effort to obtain more precise CS peak positions, rather than just using pixel values, two-dimensional Gaussian fits were attempted with both PYTHON libraries and the MIRIAD software suite. However, these proved unreliable even in simple cases, and so pixel positions were used instead. This results in the uncertainty of each CS peak position being approximately 15 arcsec.

5.2.2 Results and discussion

Fig. 5.4 shows the resulting histogram of projected linear distances between class I CH₃OH masers and the associated CS peak. As with the distance between class I CH₃OH masers and other star-forming masers, almost all class I CH₃OH maser spots appear within 0.5 pc of a CS peak. This result further highlights the close association between CS and class I CH₃OH masers. The lack of sources in the smallest bin may be erroneous, given the crude spatial resolution of the CS data. With high-resolution data, more associations within 0.05 pc may be observed.

There are two population peaks in Fig. 5.4; the approximate centres of simultaneously fitted Gaussians are 0.10 and 0.33 pc. It is difficult to tell if these distinct offsets are real or otherwise; again, the relatively poor spatial resolution of the CS data hinders detailed interpretation of this histogram. The evolved criterion of Chapter 4 is also used in this plot, although no trend is apparent for evolved or non-evolved populations. The linear distance was also compared with the integrated intensity of both CS and class I CH₃OH masers, but no correlation was found.

Without high-resolution CS data, robust interpretation is difficult. However, the observation of this 0.5 pc boundary similar to that discussed in Chapter 4 affirms that class I CH₃OH masers typically have a maximum separation from other star-forming species.

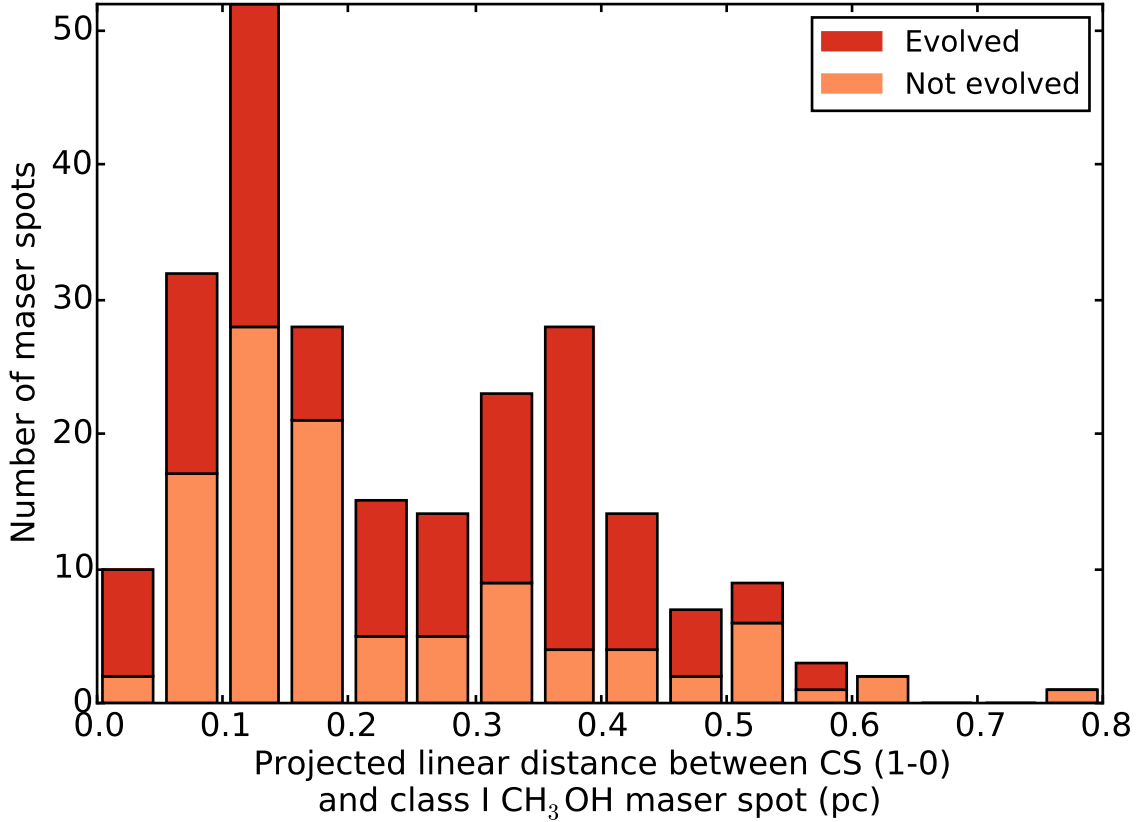


Figure 5.4: Projected distances between CS (1–0) and class I CH₃OH masers. Most maser spots are within 0.5 pc to a CS peak. Two peaks are apparent, centred on approximately 0.10 and 0.33 pc. The presence of a class II CH₃OH maser, OH maser or the H53 α radio recombination line classifies a maser spot as evolved. No trend with or without evolved star-forming tracers is apparent.

5.3 CS (1–0) and ATLASGAL 870 μ m dust emission

Within the region mapped by the MALT-45 survey, 664 ATLASGAL point sources have been classified by Urquhart et al. (2014b). Using the same method to determine offsets in §5.2, the vast majority of ATLASGAL sources are near to a CS (1–0) peak with a brightness of at least 0.1 K (624/664, 94 per cent). The distribution of these sources with CS (1–0) emission can be seen in Fig. 5.5.

Fig. 5.6 shows the projected angular distances between ATLASGAL sources and peaks of CS. Few associations are within 2.5 arcsec, but this is probably due to the relatively poor spatial resolution of the CS. Otherwise, a steady decrease in the associations is observed with increasing offset. Determining kinematic distances for each of the ATLASGAL point sources is likely to be erroneous, as some portion of this large sample will be at a the far distance. However, the majority are expected to be at the near distance, which gives some direct indication between projected angular offsets and projected linear distances. At this longitude range, a typical distance of 4 kpc with an angular offset of 25 arcsec corresponds to a linear distance of 0.48 pc. Therefore, most ATLASGAL sources and CS peaks are within 0.5 pc of each other, similar to star-forming masers.

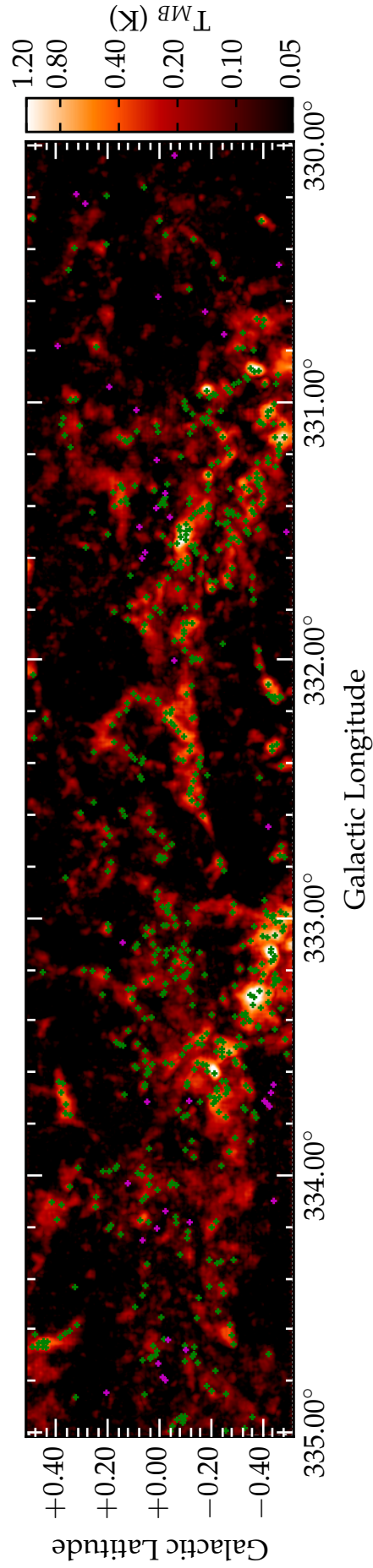


Figure 5.5: MALT-45 CS (1-0) emission with ATLASGAL point sources. Plus symbols represent ATLASGAL point sources; green symbols are associated with a CS peak of at least 0.1 K, whereas magenta symbols have peaks of CS less than 0.1 K. A main-beam temperature of 0.1 K represents a 3σ peak of emission.

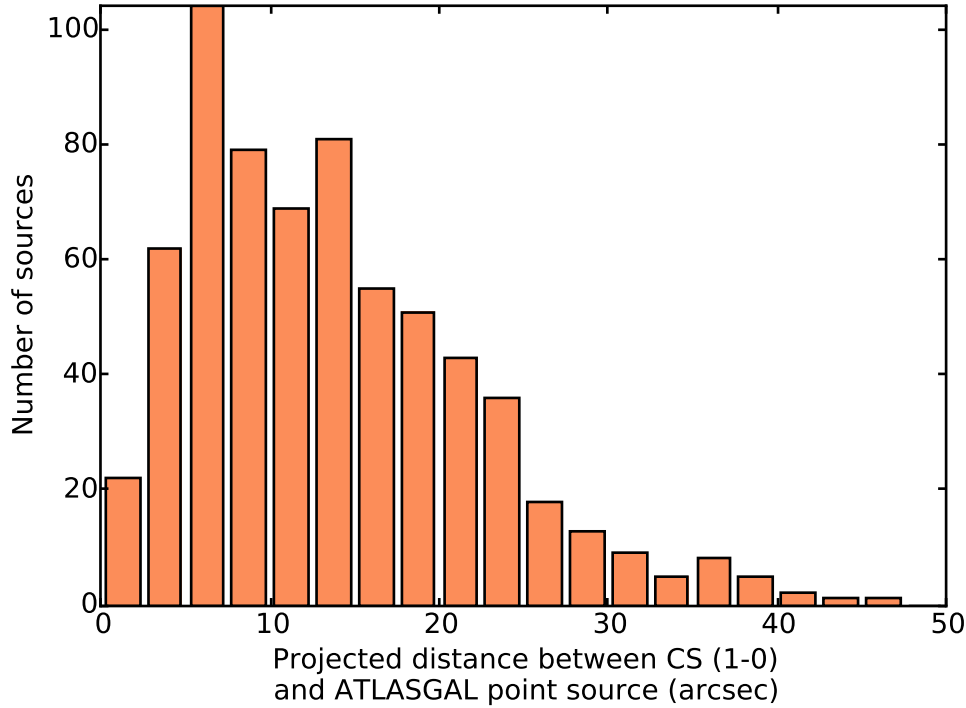


Figure 5.6: Projected distances between ATLASGAL sources and associated CS peaks. Few ATLASGAL sources are within 2.5 arcsec to a CS peak, likely due to the poor spatial resolution of the CS data. Most projected offsets are approximately 8 arcsec, and the association steadily decreases with offset. The majority of the sample is within 25 arcsec.

Fig. 5.7 compares the brightness of ATLASGAL point sources against associated CS peaks. The trend is similar to Fig. 4.11 of Chapter 4, but the correlation is not as good. Fig. 4.11 uses an integrated intensity of CS, whereas Fig. 5.7 uses only peak intensity; in this case, the difference in correlation is insignificant. It is possible that the comparison shown in Chapter 4 does not have a large enough sample of CS data reproduce the relatively poor correlation observed here. On the other hand, perhaps CS correlates more closely with 870 μ m dust emission when associated with class I CH₃OH masers.

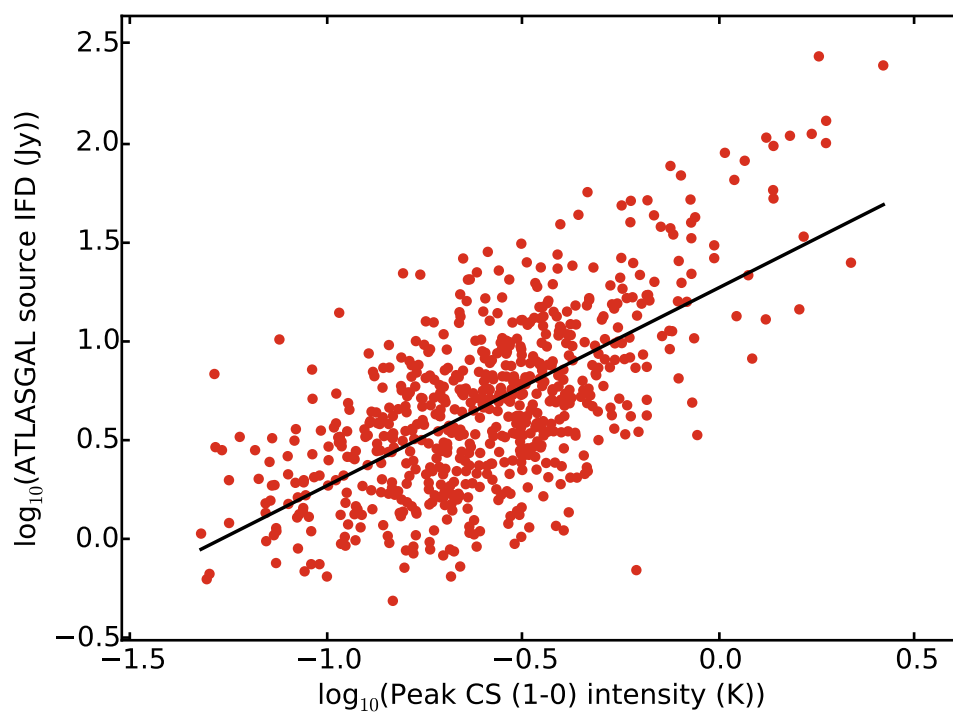


Figure 5.7: Scatter plot of ATLASGAL point source intensities with associated CS peak intensities. The positive trend in this comparison is obvious, but correlation is hampered by the scatter. The line of best fit is shown in black, and has r -value is 0.65.

Chapter 6

Summary and conclusion

This thesis has investigated the 7 mm environment of HMSF through the MALT-45 survey, primarily by searching for CS (1–0) and class I CH₃OH masers. The following text briefly discusses the major results of the previous chapters, as well as future project investigations which may build upon these results.

The MALT-45 pilot survey (Chapter 2) demonstrated the feasibility of auto-correlation with an interferometer, to achieve a sensitivity that would otherwise be too demanding on national facility telescope time. By doing so, this work paved the way for a 5 square-degree survey with MALT-45. This technique is not limited to the 7 mm waveband, and could easily be used for other star-formation surveys.

The MALT-45 survey (Chapter 3) observed the $330^\circ \leq l \leq 335^\circ$, $b = \pm 0.5^\circ$ region of the Galactic Plane, using a technique refined from the pilot observations. This technique was successful in detecting many new class I CH₃OH masers and SiO masers, as well as detecting extended CS (1–0) over the entire region.

The number of known class I CH₃OH masers in the MALT-45 region was increased from 19 to 77, and all SiO masers were new detections. With an unbiased sample of class I CH₃OH masers, as well as CS information toward each maser, class I CH₃OH masers were found to have small velocity offsets from systemic velocities. Additionally, class I masers were found with and without any other star-forming maser counterpart, indicating their association with a wide range of HMSF evolutionary stages. For class I masers associated with other star-forming masers, no correlation in intensity or luminosity was observed between maser species.

Using the high-density gas tracer NH₃ (1,1) from HOPS, a comparison with CS (1–0) from MALT-45 revealed dense clumps of hot and cold gas. The cold regions typically feature self-absorption of CS and a relatively high amount of NH₃, while the hotter regions contain trace amounts of NH₃. It seems that NH₃ is destroyed in these hotter regions as they are more evolved regions of star formation, while the CS is enhanced. Comparisons with CS and C³⁴S also reveal a close infrared alignment for regions containing an over-abundance of C³⁴S.

All SiO masers detected by MALT-45 appear to be associated with infrared evolved stars. The brightness these SiO masers usually decreases with vibrational mode ($v = 1, 2, 3$), but 11 regions have stronger $v = 2$ line emission than $v = 1$. Another 2 regions contain only $v = 2$ maser lines. Additionally, 3 rare $v = 3$ maser lines were detected.

High-resolution, follow-up observations of the class I CH₃OH masers detected by MALT-

45 further detail the properties of these masers (Chapter 4). These masers are typically near to other maser species (<0.5 pc), but are more spread out when associated with OH masers, indicating the more evolved nature of the source.

Almost all class I masers are associated with an $870\ \mu\text{m}$ dust emission point source from the ATLASGAL survey. ATLASGAL data was used to calculate clump masses, but no relation was found with the masers. However, the clump mass correlated well with CS (1–0) emission in these maser regions. Additionally, the majority of projected linear distances between class I CH_3OH masers and ATLASGAL sources was less than 0.5 pc.

Class I CH_3OH maser emission was compared in both cross- and auto-correlation. In some cases, cross-correlation identified most of the emission contained in auto-correlated data, but most masers had some degree of emission being resolved out. No relation of cross- to auto-correlation with some other factor could be established.

In an effort to identify the evolutionary state of class I maser regions, the presence of class II CH_3OH masers, OH masers and the $\text{H}53\alpha$ radio recombination line were used. Regions without these evolved tracers were found to have lower luminosities than those with an evolved tracers. Almost all non-evolved regions appear toward an IRDC. In addition, class I CH_3OH maser regions without an associated OH maser tend to have only a few maser spots.

A temperature map of the MALT-45 region was calculated using HOPS NH_3 (1,1) and (2,2) data; a slight correlation between peak CS (1–0) luminosity and the temperature was found, although this suffers from low-number statistics. The temperature of the molecular gas appears to be independent of the presence or absence of class I CH_3OH masers.

Spatial peaks of CS (1–0) emission appear to be closely related to both class I CH_3OH masers and ATLASGAL point sources. Peak velocities of CS are also closely related to class I CH_3OH masers, although their luminosities do not appear to be correlated. On the other hand, ATLASGAL luminosities are well correlated with CS (1–0).

6.1 Future work

The amount of information gleaned from MALT-45 observations is vast. With additional observations, MALT-45 can reveal more Galactic structure and dense clumps of gas through CS, simultaneously identifying new class I CH_3OH and SiO masers. Finding more class I CH_3OH masers would be particularly interesting, as they may designate un-studied, young regions of HMSF. High-resolution observations of new class I masers adds data to the statistically-complete population, aiding our understanding of these masers.

6.1.1 Short-term projects

Chapter 5 was able to use noisy NH_3 (1,1) and (2,2) to analyse temperatures across the MALT-45 region; ATCA observations of these lines towards other CS (1–0) peaks and class I CH_3OH masers would provide a large dataset for temperature comparisons. Are CS peaks usually cold? Do peaks of NH_3 (1,1) and (2,2) coincide better with masers than that of CS? Are the temperatures of regions featuring class I CH_3OH masers dictated by evolutionary stage? Such observations could help to answer these questions relatively quickly. Additionally,

any observations for NH_3 (1,1) and (2,2) could easily include the other HOPS spectral lines. In particular, the 22 GHz H_2O maser line may have a greater association rate with class I CH_3OH masers than is currently observed.

Continuum comparisons are notably absent from the work presented in this thesis. It may yet be possible to extract data from the MALT-45 survey, although this is potentially a significant investment in time. These data potentially hold great value; the 7 mm waveband represents an important component of the spectral energy distribution for star formation regions, as this is where the dominant emission mechanism changes from cool dust to ionised gas. Therefore, not only does MALT-45 continuum data potentially reveal new regions of star formation, it could also help to identify the evolutionary stage by determining the frequency at which the spectrum transitions from being dominated by ionised emission to cool dust. In addition, comparison with other dust continuum surveys, such as ATLASGAL and BGPS, may reveal interesting properties.

Bibliography

- Aguirre, J. E., Ginsburg, A. G., Dunham, M. K., et al. 2011, *ApJS*, 192, 4
- Assaf, K. A., Diamond, P. J., Richards, A. M. S., & Gray, M. D. 2011, *MNRAS*, 415, 1083
- Bains, I., Wong, T., Cunningham, M., et al. 2006, *MNRAS*, 367, 1609
- Bania, T. M., Anderson, L. D., Balser, D. S., & Rood, R. T. 2010, *ApJ*, 718, L106
- Barnes, P. J., Muller, E., Indermuehle, B., et al. 2015, *ArXiv e-prints*, arXiv:1507.05095
- Barrett, A. H., Schwartz, P. R., & Waters, J. W. 1971, *ApJ*, 168, L101
- Bartkiewicz, A., Szymczak, M., & van Langevelde, H. J. 2005, *A&A*, 442, L61
- . 2014, *A&A*, 564, A110
- Bartkiewicz, A., Szymczak, M., van Langevelde, H. J., Richards, A. M. S., & Pihlström, Y. M. 2009, *A&A*, 502, 155
- Batrla, W., Matthews, H. E., Menten, K. M., & Walmsley, C. M. 1987, *Nature*, 326, 49
- Battersby, C., Bally, J., Ginsburg, A., et al. 2011, *A&A*, 535, A128
- Bayet, E., Yates, J., & Viti, S. 2011, *ApJ*, 728, 114
- Benjamin, R. A., Churchwell, E., Babler, B. L., et al. 2003, *PASP*, 115, 953
- Bergin, E. A., Ciardi, D. R., Lada, C. J., Alves, J., & Lada, E. A. 2001, *ApJ*, 557, 209
- Beuther, H., Churchwell, E. B., McKee, C. F., & Tan, J. C. 2007, *Protostars and Planets V*, 165
- Beuther, H., Schilke, P., Sridharan, T. K., et al. 2002, *A&A*, 383, 892
- Bolatto, A. D., Wolfire, M., & Leroy, A. K. 2013, *ARA&A*, 51, 207
- Bonnell, I. A., Bate, M. R., & Zinnecker, H. 1998, *MNRAS*, 298, 93
- Braiding, C., Burton, M. G., Blackwell, R., et al. 2015, *PASA*, 32, 20
- Breen, S. L., Caswell, J. L., Ellingsen, S. P., & Phillips, C. J. 2010a, *MNRAS*, 406, 1487
- Breen, S. L., Ellingsen, S. P., Caswell, J. L., et al. 2011, *ApJ*, 733, 80

- Breen, S. L., Ellingsen, S. P., Caswell, J. L., & Lewis, B. E. 2010b, *MNRAS*, 401, 2219
- Breen, S. L., Ellingsen, S. P., Contreras, Y., et al. 2013, *MNRAS*, 435, 524
- Brogan, C. L., Goss, W. M., Hunter, T. R., et al. 2013, *ApJ*, 771, 91
- Bronfman, L., Nyman, L.-A., & May, J. 1996, *A&AS*, 115, 81
- Burton, M. G., Braiding, C., Glueck, C., et al. 2013, *PASA*, 30, 44
- Carey, S. J., Clark, F. O., Egan, M. P., et al. 1998, *ApJ*, 508, 721
- Carruthers, G. R. 1970, *ApJ*, 161, L81
- Caselli, P., & Myers, P. C. 1995, *ApJ*, 446, 665
- Caswell, J. L. 1997, *MNRAS*, 289, 203
- . 1998, *MNRAS*, 297, 215
- Caswell, J. L., Fuller, G. A., Green, J. A., et al. 2011, *MNRAS*, 417, 1964
- Cesaroni, R., Beltrán, M. T., Zhang, Q., Beuther, H., & Fallscheer, C. 2011, *A&A*, 533, A73
- Chen, X., Ellingsen, S. P., Baan, W. A., et al. 2015, *ApJ*, 800, L2
- Chen, X., Ellingsen, S. P., Shen, Z.-Q., Titmarsh, A., & Gan, C.-G. 2011, *ApJS*, 196, 9
- Chen, X., Ellingsen, S. P., He, J.-H., et al. 2012, *ApJS*, 200, 5
- Cheung, A. C., Rank, D. M., Townes, C. H., Thornton, D. D., & Welch, W. J. 1968, *Physical Review Letters*, 21, 1701
- Chin, Y.-N., Henkel, C., Whiteoak, J. B., Langer, N., & Churchwell, E. B. 1996, *A&A*, 305, 960
- Cho, S.-H., Kim, H.-G., Park, Y.-S., Choi, C.-H., & Ukita, N. 2005, *ApJ*, 622, 390
- Churchwell, E. 2002, *ARA&A*, 40, 27
- Claussen, M. J., Goss, W. M., Frail, D. A., & Seta, M. 1999, *AJ*, 117, 1387
- Contreras, Y., Schuller, F., Urquhart, J. S., et al. 2013, *A&A*, 549, A45
- Cooper, H. D. B., Lumsden, S. L., Oudmajer, R. D., et al. 2013, *MNRAS*, 430, 1125
- Cragg, D. M., Johns, K. P., Godfrey, P. D., & Brown, R. D. 1992, *MNRAS*, 259, 203
- Csengeri, T., Urquhart, J. S., Schuller, F., et al. 2014, *A&A*, 565, A75
- Cyganowski, C. J., Brogan, C. L., Hunter, T. R., & Churchwell, E. 2009, *ApJ*, 702, 1615
- Cyganowski, C. J., Whitney, B. A., Holden, E., et al. 2008, *AJ*, 136, 2391
- Dame, T. M., Hartmann, D., & Thaddeus, P. 2001, *ApJ*, 547, 792

- Dame, T. M., & Thaddeus, P. 2008, *ApJ*, 683, L143
- Dawson, J. R., Walsh, A. J., Jones, P. A., et al. 2014, *MNRAS*, 439, 1596
- De Buizer, J. M. 2003, *MNRAS*, 341, 277
- De Buizer, J. M., Bartkiewicz, A., & Szymczak, M. 2012, *ApJ*, 754, 149
- De Buizer, J. M., Redman, R. O., Longmore, S. N., Caswell, J., & Feldman, P. A. 2009, *A&A*, 493, 127
- De Buizer, J. M., & Vacca, W. D. 2010, *AJ*, 140, 196
- de Villiers, H. M., Chrysostomou, A., Thompson, M. A., et al. 2015, *MNRAS*, 449, 119
- di Francesco, J., Evans, II, N. J., Caselli, P., et al. 2007, *Protostars and Planets V*, 17
- Draine, B. T. 2003, *ARA&A*, 41, 241
- Egan, M. P., Shipman, R. F., Price, S. D., et al. 1998, *ApJ*, 494, L199
- Eldridge, J. J., & Relaño, M. 2011, *MNRAS*, 411, 235
- Elitzur, M. 1992, *ARA&A*, 30, 75
- Ellingsen, S. P. 2005, *MNRAS*, 359, 1498
- . 2006, *ApJ*, 638, 241
- Ellingsen, S. P., Breen, S. L., Sobolev, A. M., et al. 2011, *ApJ*, 742, 109
- Ellingsen, S. P., Breen, S. L., Voronkov, M. A., & Dawson, J. R. 2013, *MNRAS*, 429, 3501
- Ellingsen, S. P., Chen, X., Qiao, H.-H., et al. 2014, *ApJ*, 790, L28
- Ellingsen, S. P., von Bibra, M. L., McCulloch, P. M., et al. 1996, *MNRAS*, 280, 378
- Evans, II, N. J. 1999, *ARA&A*, 37, 311
- Felli, M., Palagi, F., & Tofani, G. 1992, *A&A*, 255, 293
- Foster, J. B., Jackson, J. M., Barnes, P. J., et al. 2011, *ApJS*, 197, 25
- Fujiyoshi, T., Smith, C. H., Caswell, J. L., et al. 2006, *MNRAS*, 368, 1843
- Fuller, G. A., & Myers, P. C. 1993, *ApJ*, 418, 273
- Gan, C.-G., Chen, X., Shen, Z.-Q., Xu, Y., & Ju, B.-G. 2013, *ApJ*, 763, 2
- Garay, G., Mardones, D., Bronfman, L., et al. 2010, *ApJ*, 710, 567
- Garay, G., Mardones, D., Rodríguez, L. F., Caselli, P., & Bourke, T. L. 2002, *ApJ*, 567, 980
- Garay, G., Mardones, D., Bronfman, L., et al. 2007, *A&A*, 463, 217
- Gibb, A. G., Hoare, M. G., Little, L. T., & Wright, M. C. H. 2003, *MNRAS*, 339, 1011

- Goddi, C., Greenhill, L. J., Chandler, C. J., et al. 2009, *ApJ*, 698, 1165
- Goddi, C., & Moscadelli, L. 2006, *A&A*, 447, 577
- Goddi, C., Moscadelli, L., Alef, W., et al. 2005, *A&A*, 432, 161
- Gómez, Y. 2007, in *IAU Symposium*, Vol. 242, *IAU Symposium*, ed. J. M. Chapman & W. A. Baan, 292–298
- Gonidakis, I., Chapman, J. M., Deacon, R. M., & Green, A. J. 2014, *MNRAS*, 443, 3819
- Gonidakis, I., Diamond, P. J., & Kembball, A. J. 2013, *MNRAS*, 433, 3133
- Gray, M. D., Wittkowski, M., Scholz, M., et al. 2009, *MNRAS*, 394, 51
- Green, A. J., Frail, D. A., Goss, W. M., & Otrupcek, R. 1997, *AJ*, 114, 2058
- Green, J. A., & McClure-Griffiths, N. M. 2011, *MNRAS*, 417, 2500
- Green, J. A., Caswell, J. L., Fuller, G. A., et al. 2009, *MNRAS*, 392, 783
- . 2012, *MNRAS*, 420, 3108
- Guibert, J., Rieu, N. Q., & Elitzur, M. 1978, *A&A*, 66, 395
- Habart, E., Walmsley, M., Verstraete, L., et al. 2005, *Space Sci. Rev.*, 119, 71
- Hirota, T., Kim, M. K., Kurono, Y., & Honma, M. 2014, *ApJ*, 782, L28
- Ho, P. T. P., & Townes, C. H. 1983, *ARA&A*, 21, 239
- Hoare, M. G., Kurtz, S. E., Lizano, S., Keto, E., & Hofner, P. 2007, *Protostars and Planets V*, 181
- Hoare, M. G., Purcell, C. R., Churchwell, E. B., et al. 2012, *PASP*, 124, 939
- Ilee, J. D., Wheelwright, H. E., Oudmaijer, R. D., et al. 2013, *MNRAS*, 429, 2960
- Jackson, J. M., Finn, S. C., Chambers, E. T., Rathborne, J. M., & Simon, R. 2010, *ApJ*, 719, L185
- Jackson, J. M., Rathborne, J. M., Shah, R. Y., et al. 2006, *ApJS*, 163, 145
- Jeans, J. H. 1902, *Royal Society of London Philosophical Transactions Series A*, 199, 1
- Jordan, C. H., Walsh, A. J., Lowe, V., et al. 2013, *MNRAS*, 429, 469
- . 2015, *MNRAS*, 448, 2344
- Kahn, F. D. 1974, *A&A*, 37, 149
- Kalenskii, S. V., Johansson, L. E. B., Bergman, P., et al. 2010, *MNRAS*, 405, 613
- Kalenskii, S. V., & Sobolev, A. M. 1994, *Astronomy Letters*, 20, 91

- Kauffmann, J., & Pillai, T. 2010, *ApJ*, 723, L7
- Kaufmann, P., Gammon, R. H., Ibanez, A. L., et al. 1976, *Nature*, 260, 306
- Kim, K.-T., & Koo, B.-C. 2001, *ApJ*, 549, 979
- Kim, M. K., Hirota, T., Honma, M., et al. 2008, *PASJ*, 60, 991
- Kurtz, S., Hofner, P., & Álvarez, C. V. 2004, *ApJS*, 155, 149
- Lada, C. J., & Lada, E. A. 2003, *ARA&A*, 41, 57
- Lee, K., Looney, L. W., Schnee, S., & Li, Z.-Y. 2013, *ApJ*, 772, 100
- Leurini, S., Codella, C., López-Sepulcre, A., et al. 2014, *A&A*, 570, A49
- Lilley, A. E., & Palmer, P. 1968, *ApJS*, 16, 143
- Lizano, S. 2008, in *Astronomical Society of the Pacific Conference Series*, Vol. 387, *Massive Star Formation: Observations Confront Theory*, ed. H. Beuther, H. Linz, & T. Henning, 232
- Lo, N., Redman, M. P., Jones, P. A., et al. 2011, *MNRAS*, 415, 525
- Lo, N., Cunningham, M. R., Jones, P. A., et al. 2009, *MNRAS*, 395, 1021
- Lockman, F. J. 1979, *ApJ*, 232, 761
- Longmore, S. N., Rathborne, J., Bastian, N., et al. 2012, *ApJ*, 746, 117
- Lopez, R., Morata, O., Sepulveda, I., et al. 1994, *Ap&SS*, 216, 151
- López-Sepulcre, A., Codella, C., Cesaroni, R., Marcelino, N., & Walmsley, C. M. 2009, *A&A*, 499, 811
- Lowe, V., Cunningham, M. R., Urquhart, J. S., et al. 2014, *MNRAS*, 441, 256
- Lu, X., Zhang, Q., Liu, H. B., Wang, J., & Gu, Q. 2014, *ApJ*, 790, 84
- Lumsden, S. L., Hoare, M. G., Urquhart, J. S., et al. 2013, *ApJS*, 208, 11
- Martin-Pintado, J., Bachiller, R., & Fuente, A. 1992, *A&A*, 254, 315
- McClure-Griffiths, N. M., Dickey, J. M., Gaensler, B. M., et al. 2005, *ApJS*, 158, 178
- McEwen, B. C., Pihlström, Y. M., & Sjouwerman, L. O. 2014, *ApJ*, 793, 133
- Menten, K. M. 1991, *ApJ*, 380, L75
- Minier, V., Booth, R. S., & Conway, J. E. 2002, *A&A*, 383, 614
- Minier, V., Ellingsen, S. P., Norris, R. P., & Booth, R. S. 2003, *A&A*, 403, 1095
- Moeckel, N., & Clarke, C. J. 2011, *MNRAS*, 410, 2799

- Moscadelli, L., Cesaroni, R., & Rioja, M. J. 2005, *A&A*, 438, 889
- Moscadelli, L., & Goddi, C. 2014, *A&A*, 566, A150
- Moscadelli, L., Testi, L., Furuya, R. S., et al. 2006, *A&A*, 446, 985
- Müller, H. S. P., Schlöder, F., Stutzki, J., & Winnewisser, G. 2005, *Journal of Molecular Structure*, 742, 215
- Müller, H. S. P., Spezzano, S., Bizzocchi, L., et al. 2013, *Journal of Physical Chemistry A*, 117, 13843
- Navarete, F., Daminieli, A., Barbosa, C. L., & Blum, R. D. 2015, *MNRAS*, 450, 4364
- Nguyen-Lu'o'ng, Q., Motte, F., Carlhoff, P., et al. 2013, *ApJ*, 775, 88
- Niederhofer, F., Humphreys, E. M. L., & Goddi, C. 2012, *A&A*, 548, A69
- Norris, R. P., Caswell, J. L., Gardner, F. F., & Wellington, K. J. 1987, *ApJ*, 321, L159
- Olguin, F. A., Hoare, M. G., Wheelwright, H. E., et al. 2015, *MNRAS*, 449, 2784
- Ott, J., Weiß, A., Staveley-Smith, L., Henkel, C., & Meier, D. S. 2014, *ApJ*, 785, 55
- Peretto, N., & Fuller, G. A. 2009, *A&A*, 505, 405
- Peretto, N., Fuller, G. A., Duarte-Cabral, A., et al. 2013, *A&A*, 555, A112
- Pihlström, Y. M., Sjouwerman, L. O., Frail, D. A., et al. 2014, *AJ*, 147, 73
- Pratap, P., Dickens, J. E., Snell, R. L., et al. 1997, *ApJ*, 486, 862
- Purcell, C. R. 2006, PhD thesis, The University of New South Wales, Australia
- Purcell, C. R., & Hoare, M. G. 2010, *Highlights of Astronomy*, 15, 781
- Purcell, C. R., Balasubramanyam, R., Burton, M. G., et al. 2006, *MNRAS*, 367, 553
- Purcell, C. R., Minier, V., Longmore, S. N., et al. 2009, *A&A*, 504, 139
- Purcell, C. R., Longmore, S. N., Walsh, A. J., et al. 2012, *MNRAS*, 426, 1972
- Purcell, C. R., Hoare, M. G., Cotton, W. D., et al. 2013, *ApJS*, 205, 1
- Rathborne, J. M., Jackson, J. M., & Simon, R. 2006, *ApJ*, 641, 389
- Rathborne, J. M., Longmore, S. N., Jackson, J. M., et al. 2015, *ApJ*, 802, 125
- Reid, M. J., Menten, K. M., Zheng, X. W., et al. 2009, *ApJ*, 700, 137
- Robitaille, T. P., Meade, M. R., Babler, B. L., et al. 2008, *AJ*, 136, 2413
- Rodgers, A. W., Campbell, C. T., & Whiteoak, J. B. 1960, *MNRAS*, 121, 103
- Schilke, P., Walmsley, C. M., Pineau des Forets, G., & Flower, D. R. 1997, *A&A*, 321, 293

- Sevenster, M. N., Chapman, J. M., Habing, H. J., Killeen, N. E. B., & Lindqvist, M. 1997, *A&AS*, 124, 509
- Shu, F. H. 1977, *ApJ*, 214, 488
- Simon, R., Jackson, J. M., Rathborne, J. M., & Chambers, E. T. 2006, *ApJ*, 639, 227
- Sjouwerman, L. O., Pihlström, Y. M., & Fish, V. L. 2010, *ApJ*, 710, L111
- Slysh, V. I., Kalenskii, S. V., Val'tts, I. E., & Otrupcek, R. 1994, *MNRAS*, 268, 464
- Stahler, S. W., & Palla, F. 2005, *The Formation of Stars*
- Tafalla, M., Myers, P. C., Caselli, P., & Walmsley, C. M. 2004, *A&A*, 416, 191
- Tafalla, M., Myers, P. C., Caselli, P., Walmsley, C. M., & Comito, C. 2002, *ApJ*, 569, 815
- Taylor, S. D., Morata, O., & Williams, D. A. 1998, *A&A*, 336, 309
- Tielens, A. G. G. M. 2008, *ARA&A*, 46, 289
- Titmarsh, A. M., Ellingsen, S. P., Breen, S. L., Caswell, J. L., & Voronkov, M. A. 2013, *ApJ*, 775, L12
- . 2014, *MNRAS*, 443, 2923
- Townes, C. H., & Schawlow, A. L. 1955, *Microwave Spectroscopy*
- Urquhart, J. S., Figura, C. C., Moore, T. J. T., et al. 2014a, *MNRAS*, 437, 1791
- Urquhart, J. S., Hoare, M. G., Lumsden, S. L., et al. 2009, *A&A*, 507, 795
- Urquhart, J. S., Hoare, M. G., Purcell, C. R., et al. 2010, *PASA*, 27, 321
- Urquhart, J. S., Moore, T. J. T., Schuller, F., et al. 2013, *MNRAS*, 431, 1752
- Urquhart, J. S., Csengeri, T., Wyrowski, F., et al. 2014b, *A&A*, 568, A41
- Urquhart, J. S., Moore, T. J. T., Menten, K. M., et al. 2015, *MNRAS*, 446, 3461
- Val'tts, I. E., Ellingsen, S. P., Slysh, V. I., et al. 2000, *MNRAS*, 317, 315
- van Dishoeck, E. F., & Blake, G. A. 1998, *ARA&A*, 36, 317
- Voronkov, M. A., Caswell, J. L., Britton, T. R., et al. 2010a, *MNRAS*, 408, 133
- Voronkov, M. A., Caswell, J. L., Ellingsen, S. P., et al. 2012, in *IAU Symposium*, Vol. 287, *IAU Symposium*, ed. R. S. Booth, W. H. T. Vlemmings, & E. M. L. Humphreys, 433–440
- Voronkov, M. A., Caswell, J. L., Ellingsen, S. P., Green, J. A., & Breen, S. L. 2014, *MNRAS*, 439, 2584
- Voronkov, M. A., Caswell, J. L., Ellingsen, S. P., & Sobolev, A. M. 2010b, *MNRAS*, 405, 2471

- Walsh, A. J., Burton, M. G., Hyland, A. R., & Robinson, G. 1998, *MNRAS*, 301, 640
- Walsh, A. J., Lo, N., Burton, M. G., et al. 2008, *PASA*, 25, 105
- Walsh, A. J., Purcell, C. R., Longmore, S. N., et al. 2014, *MNRAS*, 442, 2240
- Walsh, A. J., Breen, S. L., Britton, T., et al. 2011, *MNRAS*, 416, 1764
- Wang, K., Testi, L., Ginsburg, A., et al. 2015, *MNRAS*, 450, 4043
- Ward-Thompson, D., & Whitworth, A. P. 2011, *An Introduction to Star Formation*
- Weaver, H., Williams, D. R. W., Dieter, N. H., & Lum, W. T. 1965, *Nature*, 208, 29
- Weinreb, S., Barrett, A. H., Meeks, M. L., & Henry, J. C. 1963, *Nature*, 200, 829
- Whelan, E. T., Ray, T. P., Comeron, F., Bacciotti, F., & Kavanagh, P. J. 2012, *ApJ*, 761, 120
- Wilson, T. L., Walmsley, C. M., Jewell, P. R., & Snyder, L. E. 1984, *A&A*, 134, L7
- Wilson, W. E., Ferris, R. H., Axtens, P., et al. 2011, *MNRAS*, 416, 832
- Wong, T., Ladd, E. F., Brisbin, D., et al. 2008, *MNRAS*, 386, 1069
- Wu, J., Evans, II, N. J., Shirley, Y. L., & Knez, C. 2010, *ApJS*, 188, 313
- Yu, N., & Wang, J.-J. 2014, *MNRAS*, 440, 1213
- Yusef-Zadeh, F., Cotton, W., Viti, S., Wardle, M., & Royster, M. 2013, *ApJ*, 764, L19
- Zapata, L. A., Menten, K., Reid, M., & Beuther, H. 2009, *ApJ*, 691, 332
- Zinnecker, H., & Yorke, H. W. 2007, *ARA&A*, 45, 481

Appendices

Appendix A

Supplementary material from the MALT-45 survey

This appendix contains reference material for the publication outlined in Chapter 3. For each of the spectral lines discussed, a noise map can be seen §A.1. Detected class I CH₃OH maser spectra are contained in §A.2. Auto-correlated images not contained in the main body of the publication are shown in §A.3. Finally, SiO $v = 1, 2, 3$ maser spectra are contained in §A.4.

A.1 RMS noise maps

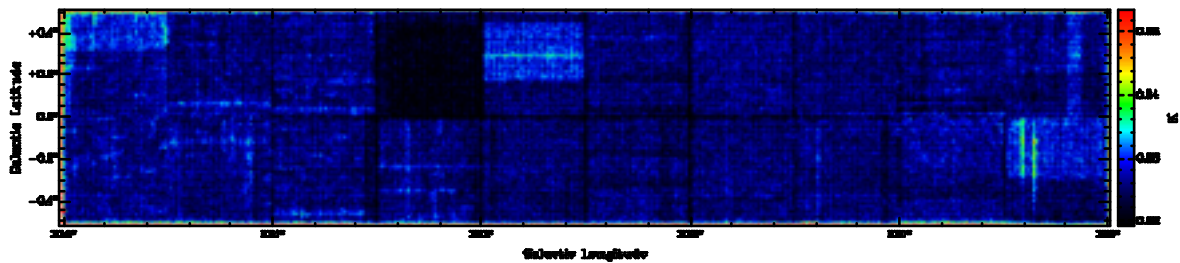


Figure A.1: RMS noise map for the SiO (1-0) $v = 0$ zoom window.

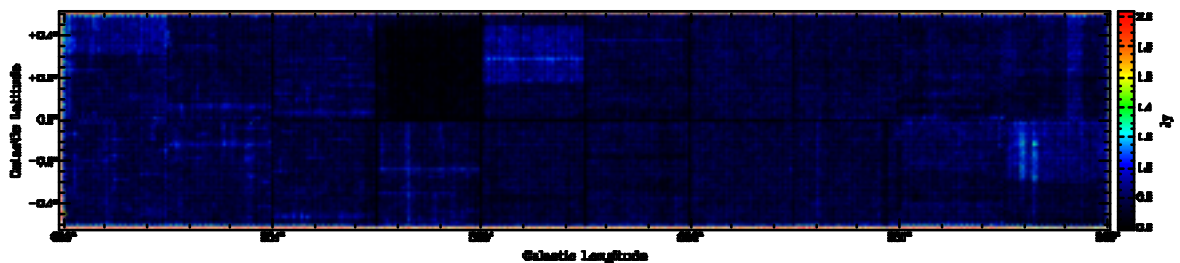


Figure A.2: RMS noise map for the SiO (1-0) $v = 1$ zoom window.

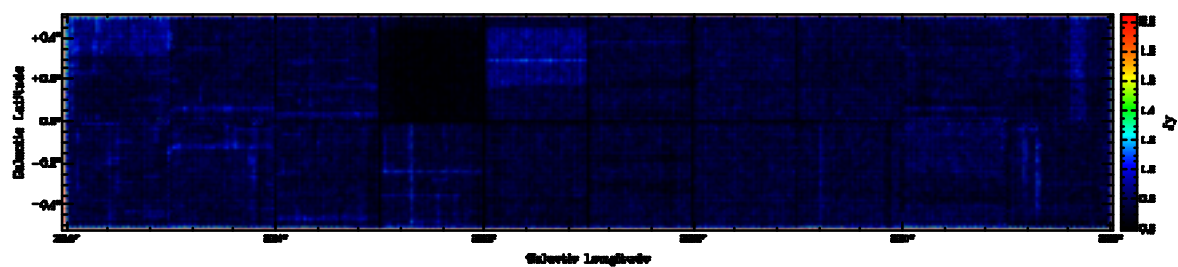


Figure A.3: RMS noise map for the SiO (1-0) $v = 2$ zoom window.

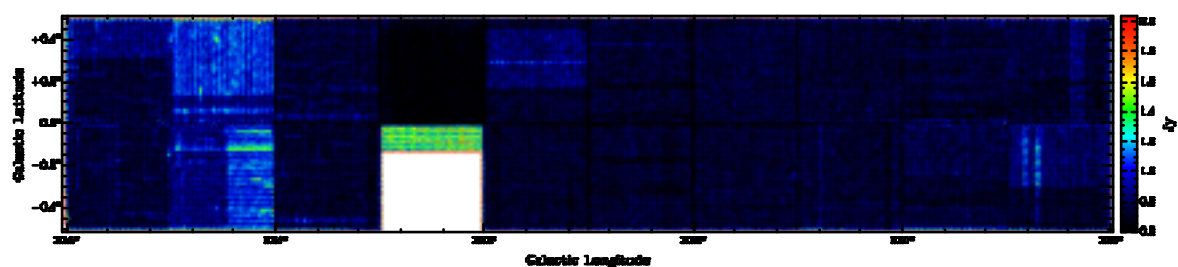


Figure A.4: RMS noise map for the SiO (1-0) $v = 3$ zoom window.

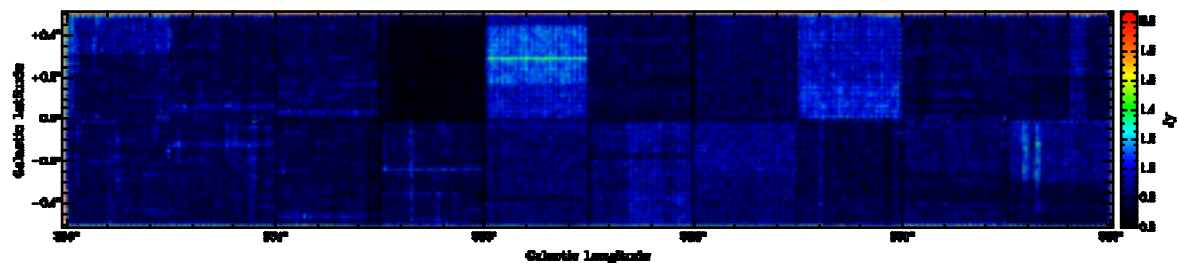


Figure A.5: RMS noise map for the class I CH₃OH zoom window.

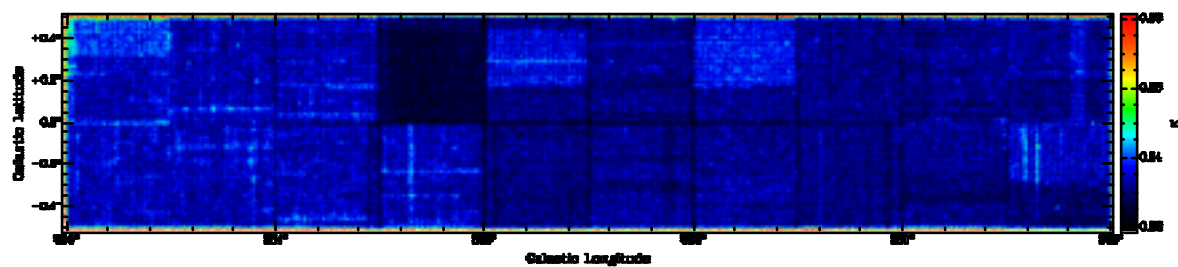
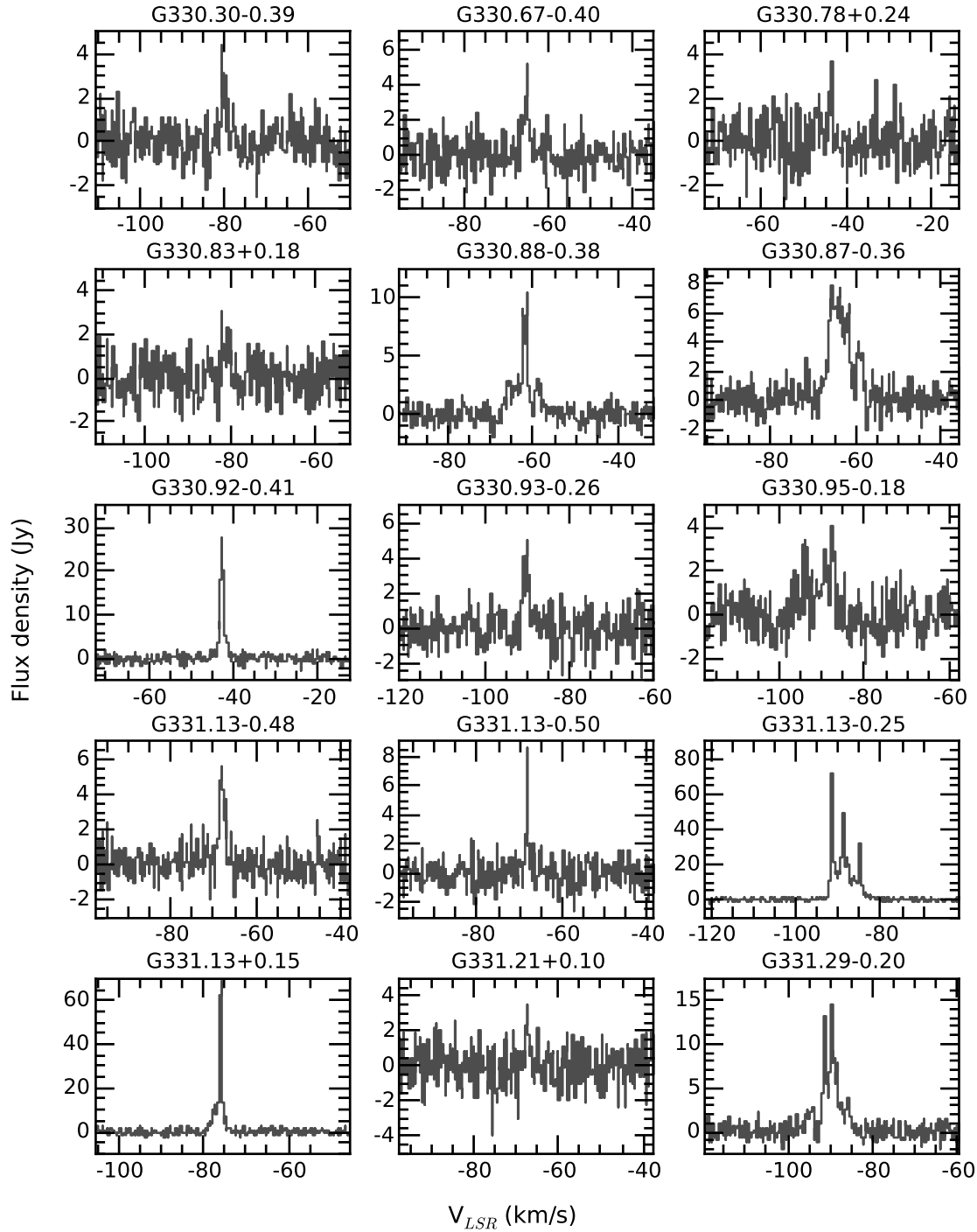


Figure A.6: RMS noise map for the CS (1-0) zoom window.

A.2 Class I CH₃OH maser spectraFigure A.7: Spectra of each detected class I CH₃OH maser.

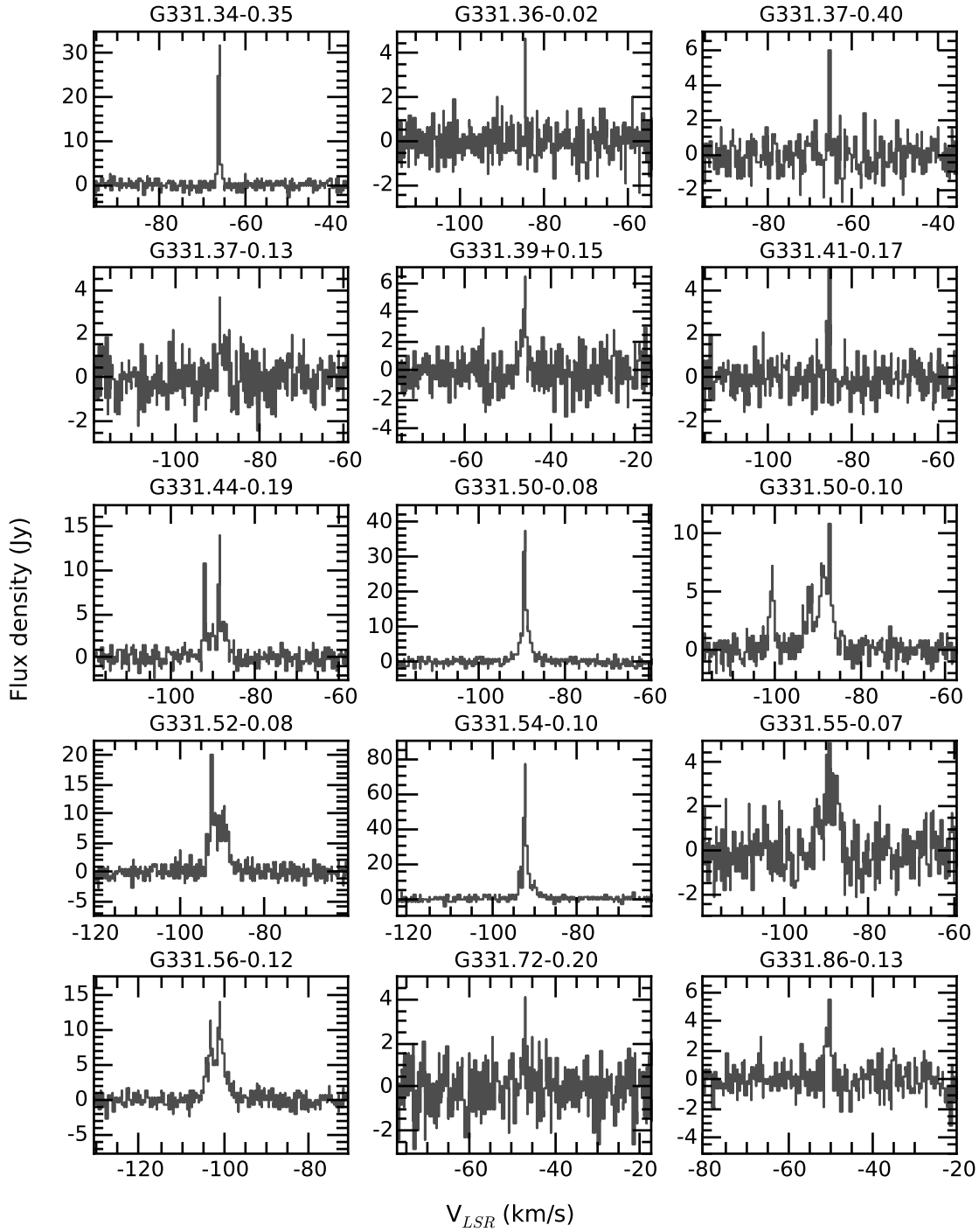
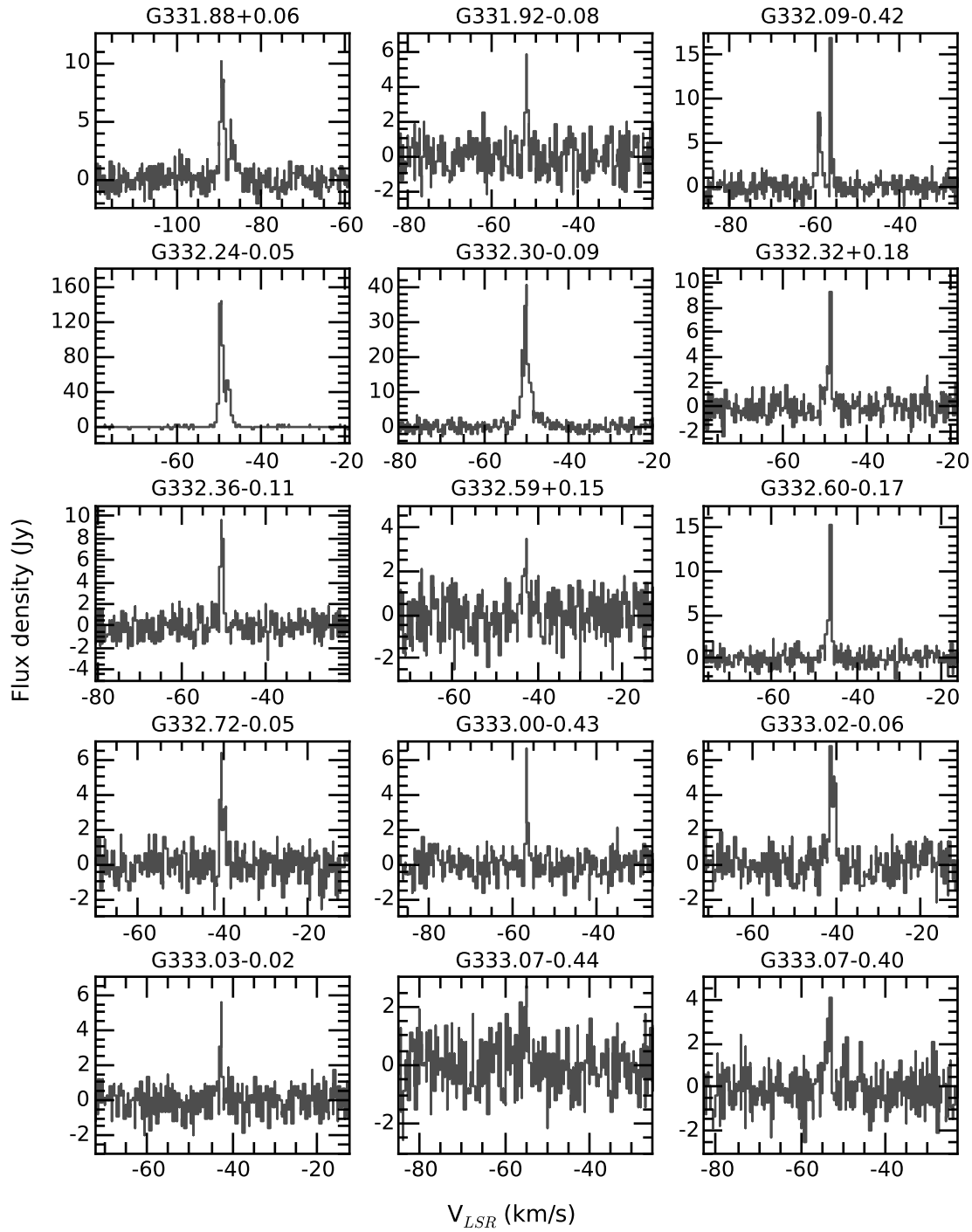


Figure A.7: *continued*

Figure A.7: *continued*

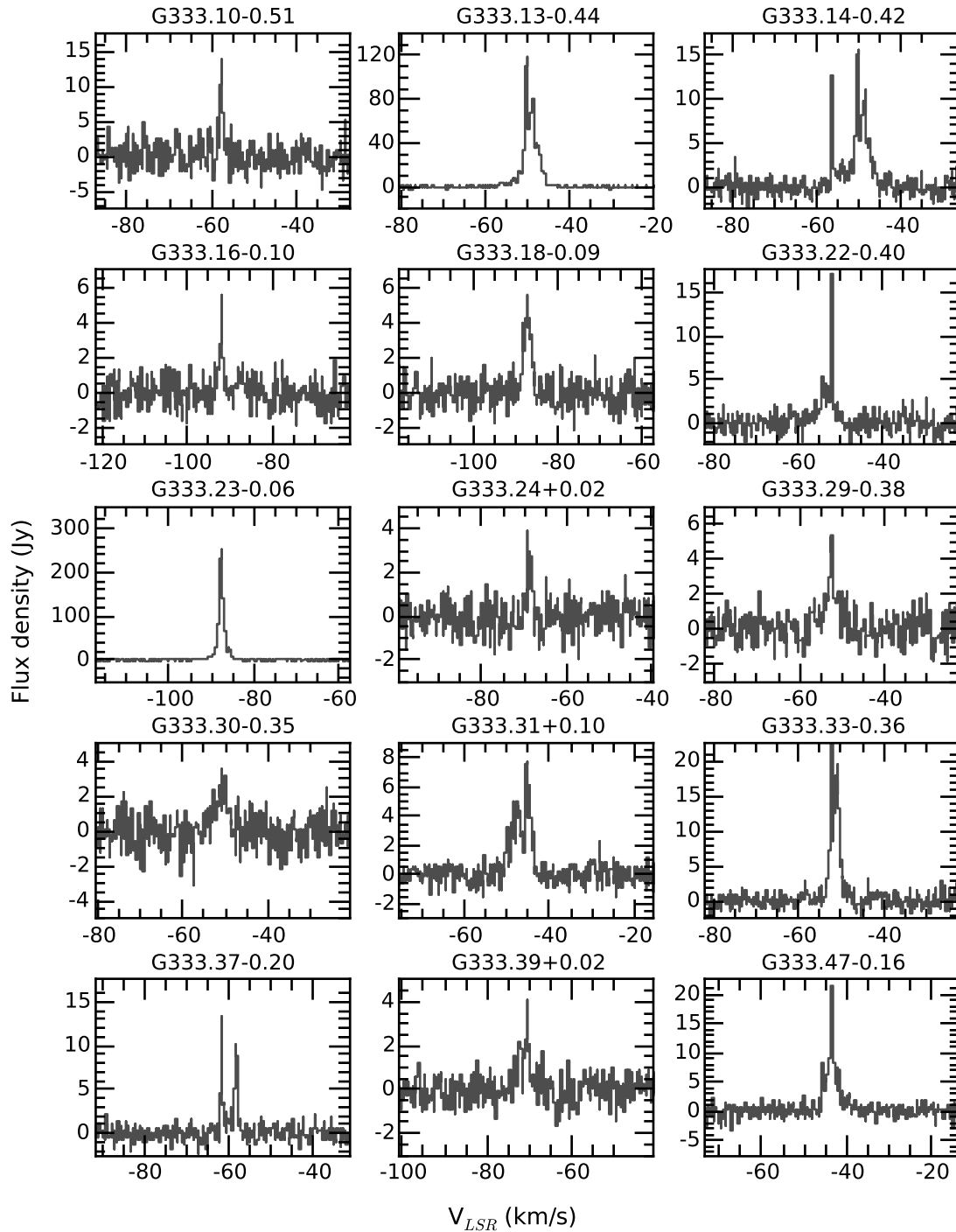
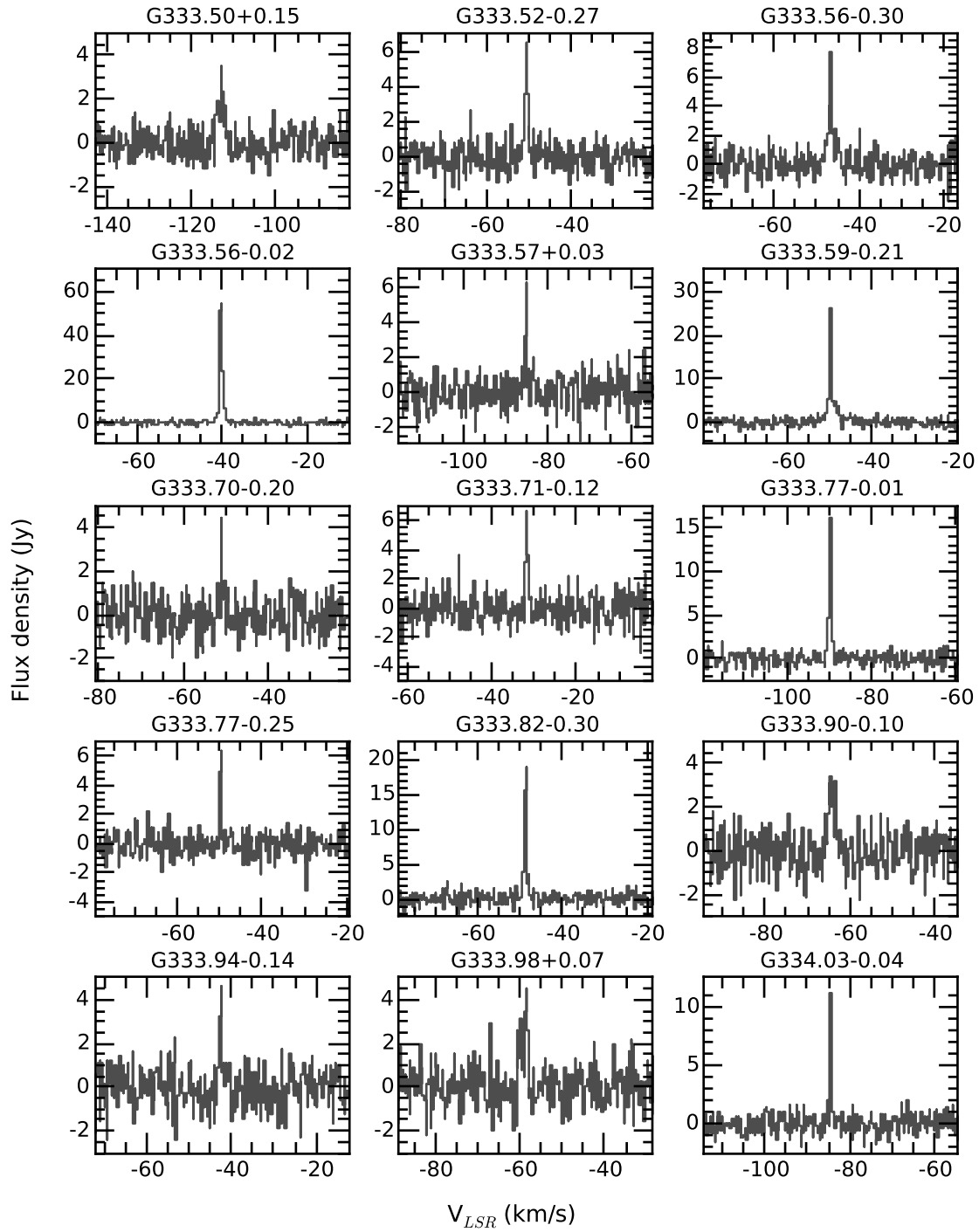


Figure A.7: *continued*

Figure A.7: *continued*

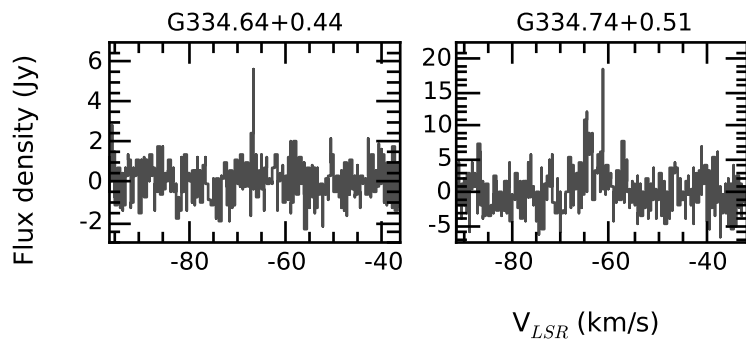


Figure A.7: *continued*

A.3 Auto-correlated maps

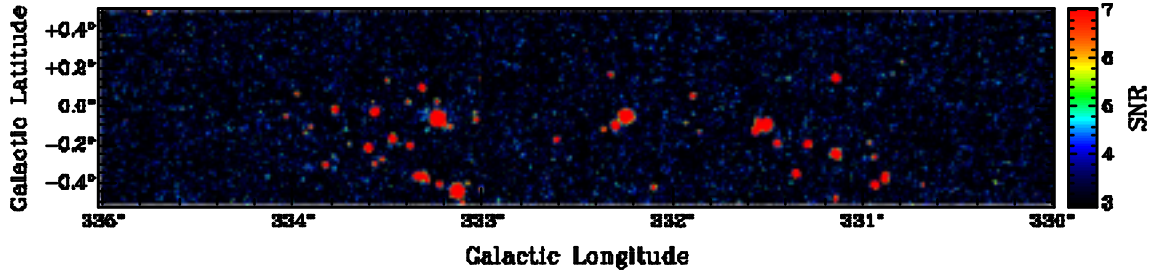


Figure A.8: Auto-correlated class I CH_3OH maser emission, in a peak signal-to-noise map. 77 masers are found within these data.

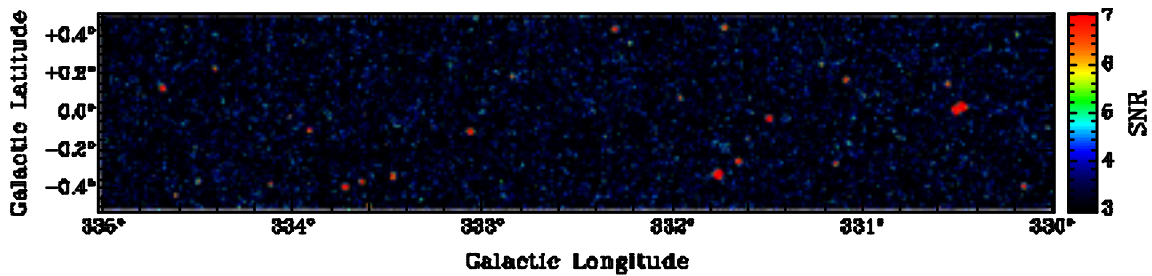


Figure A.9: Auto-correlated SiO (1-0) $v = 1$ maser emission, in a peak signal-to-noise map. 45 masers are found within these data.

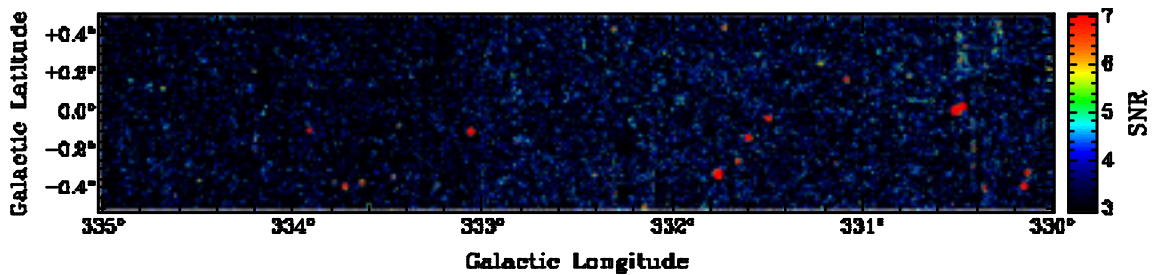


Figure A.10: Auto-correlated SiO (1-0) $v = 2$ maser emission, in a peak signal-to-noise map. 37 masers are found within these data.

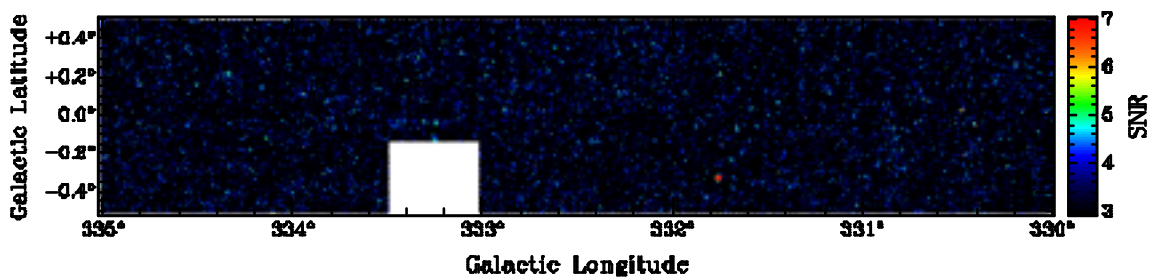


Figure A.11: Auto-correlated SiO (1-0) $v = 3$ maser emission, in a peak signal-to-noise map. The gap in the G333.0-0.5 tile is due to a correlator fault for that day of observing. 3 masers are found within these data.

A.4 SiO maser spectra

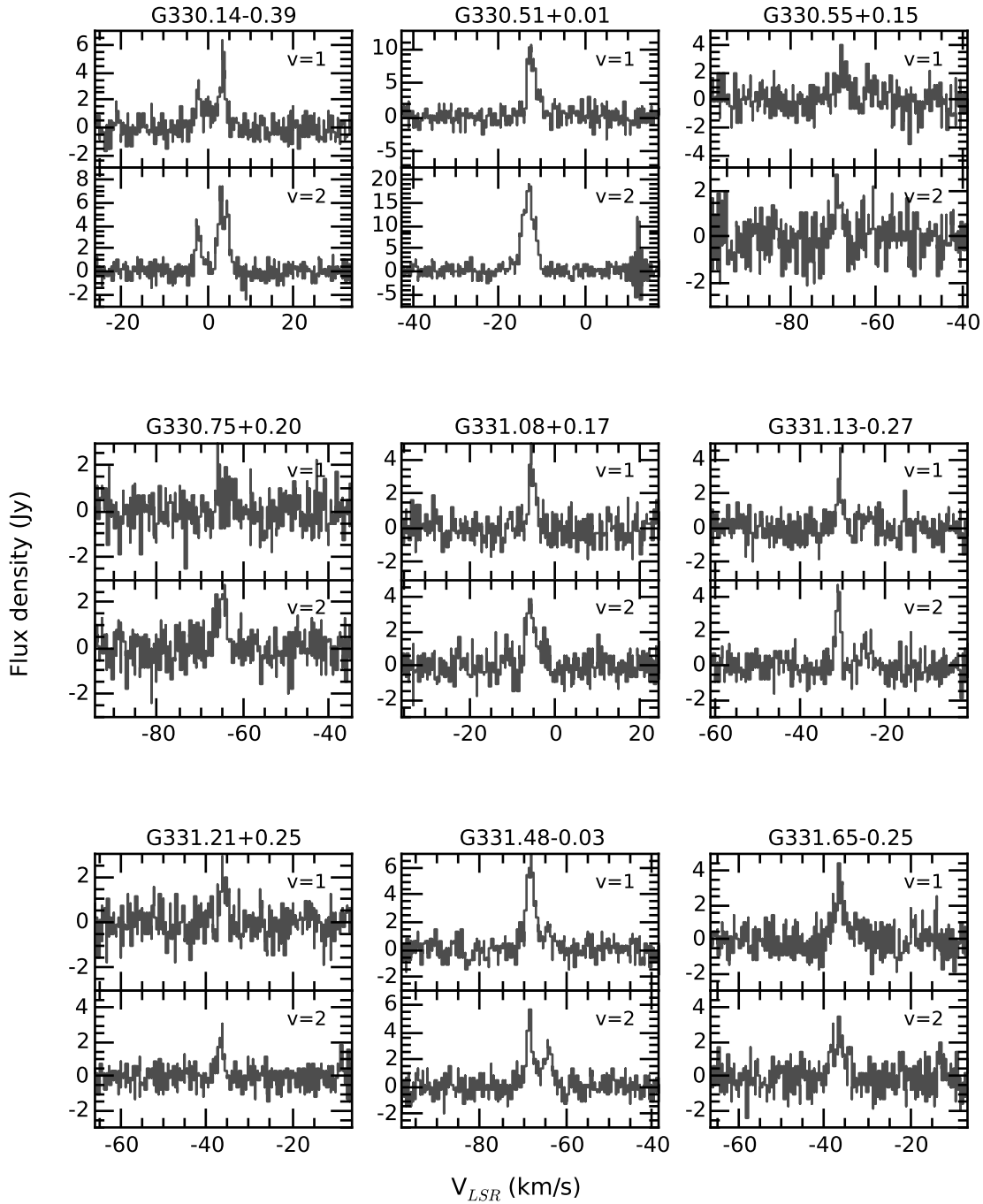
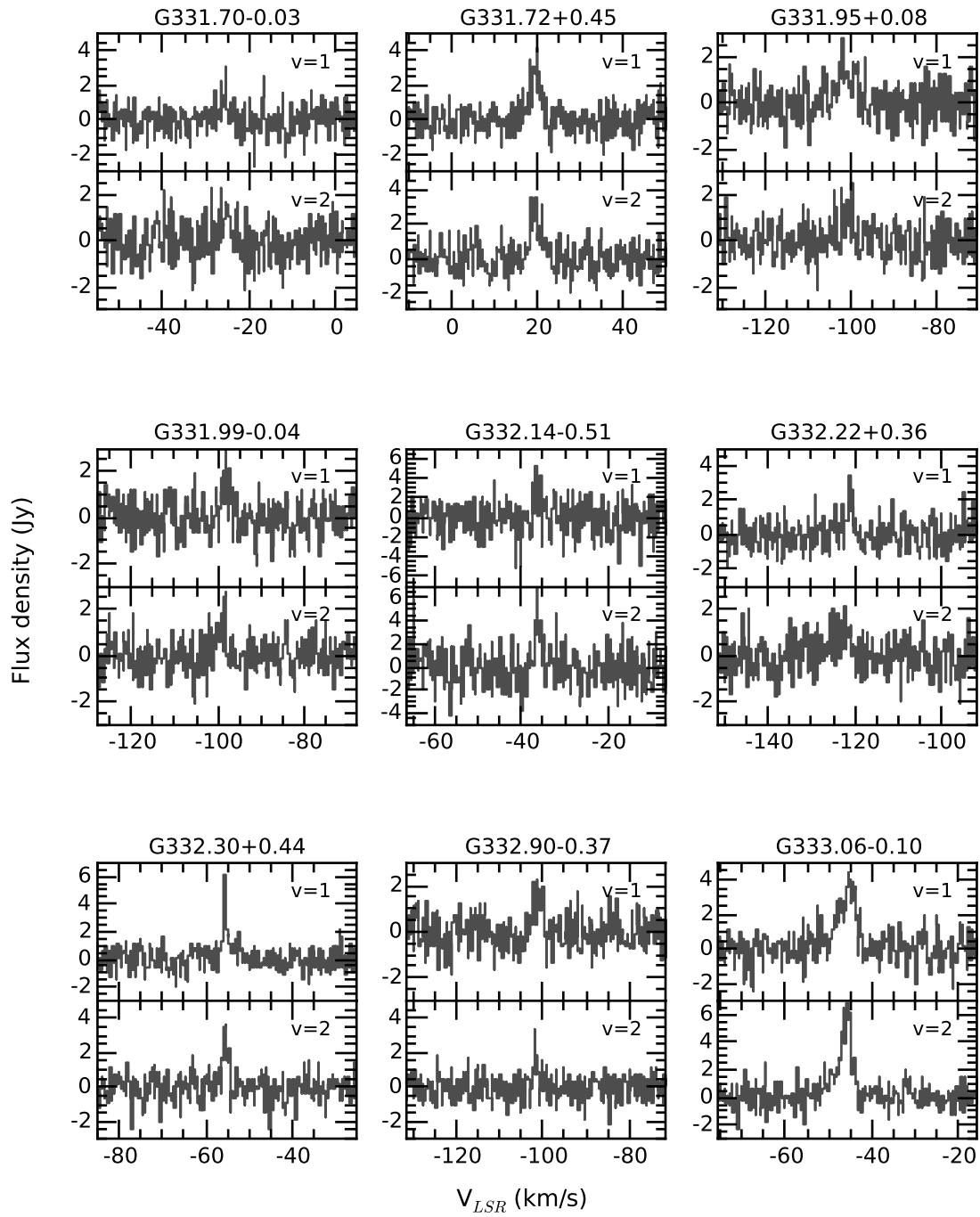


Figure A.12: Spectra of regions containing SiO $v = 1$ and $v = 2$ maser detections. G330.51+0.01 contains a correlator defect within the $v = 2$ spectrum at around $v = 10 \text{ km s}^{-1}$.

Figure A.12: *continued*

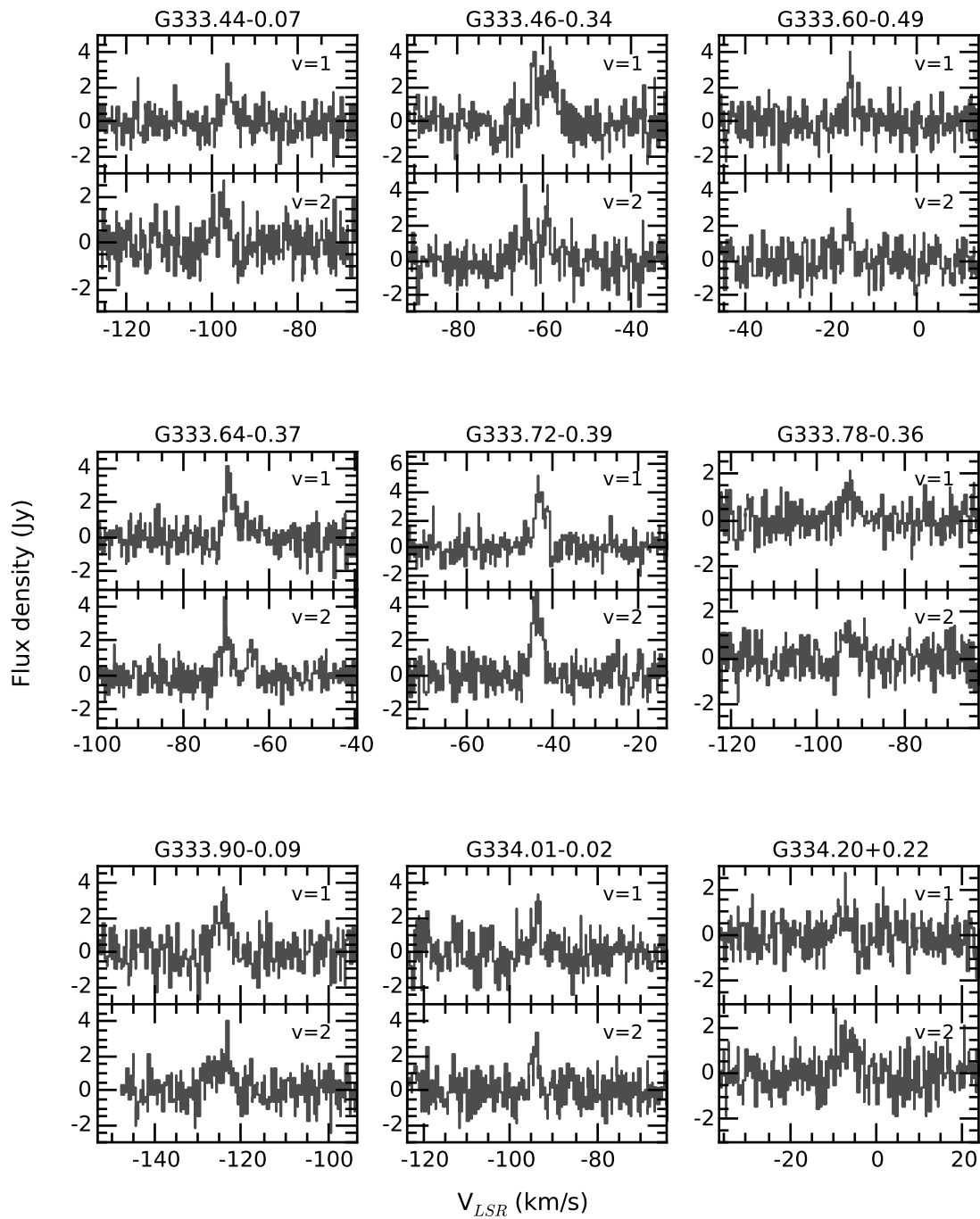


Figure A.12: *continued*

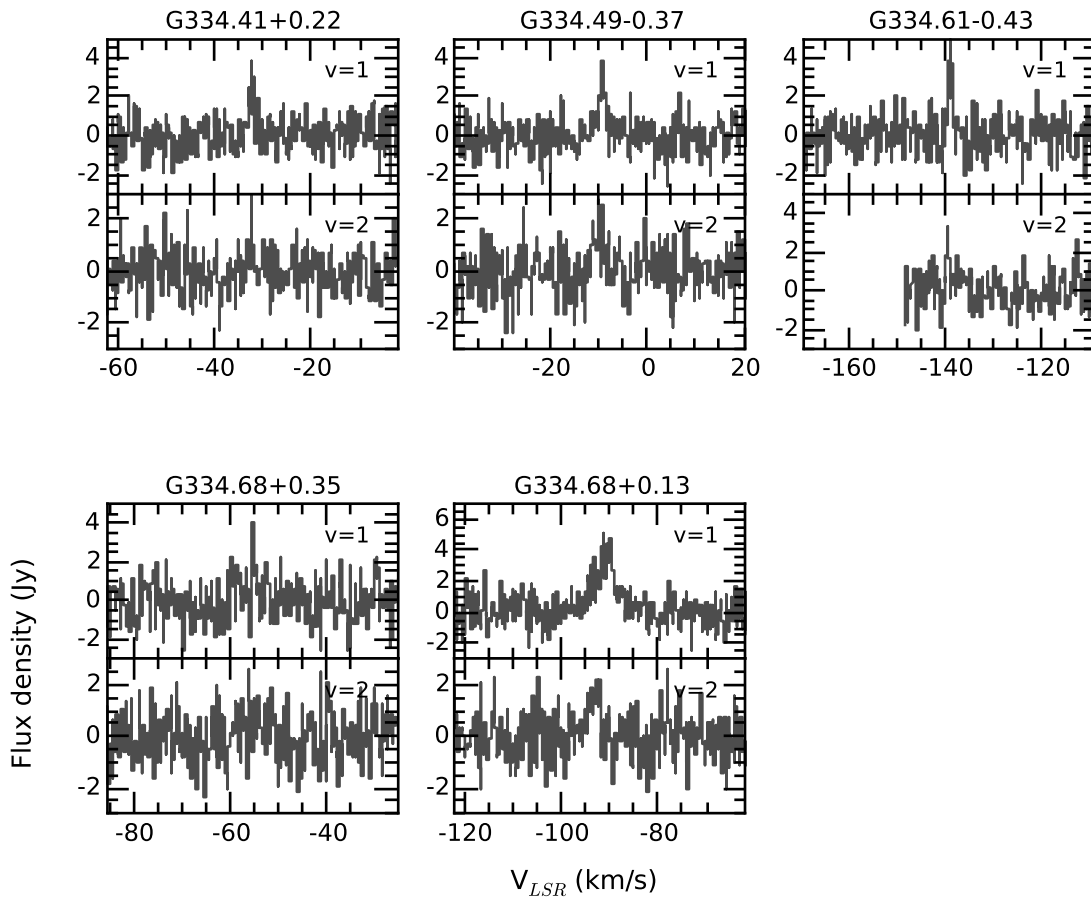


Figure A.12: *continued*

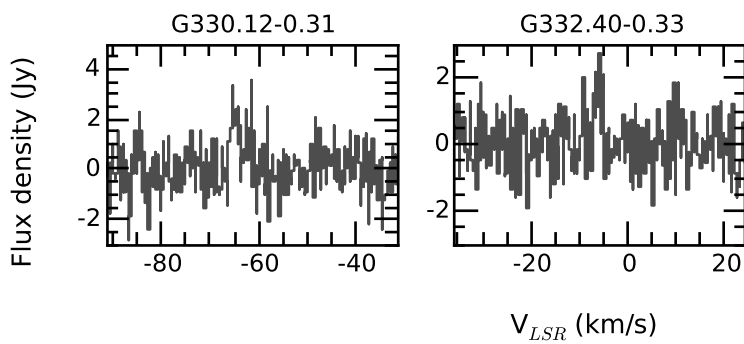


Figure A.13: Spectra of regions containing only SiO $v = 2$ maser detections.

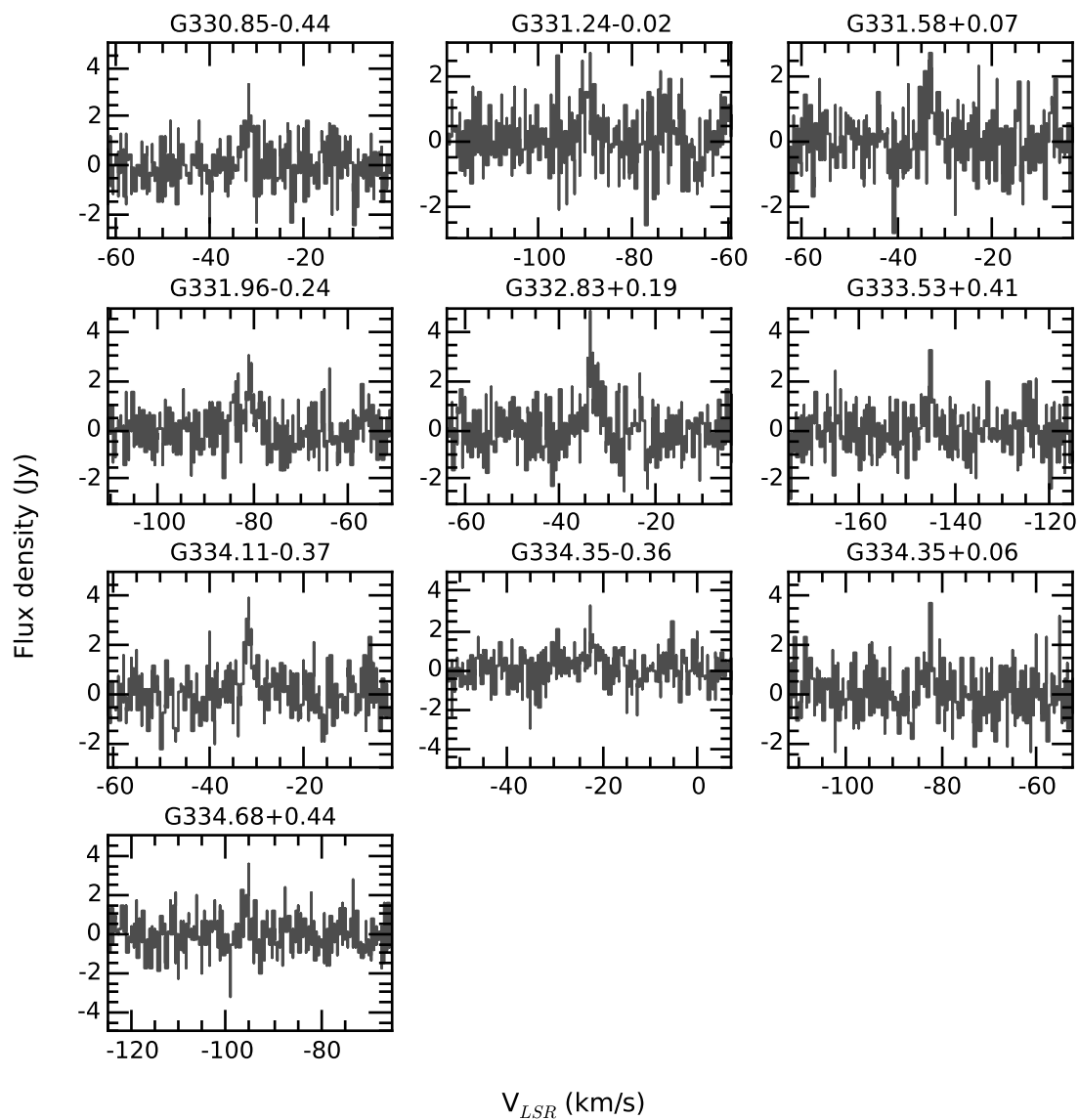


Figure A.14: Spectra of regions containing only SiO $v = 1$ maser detections.

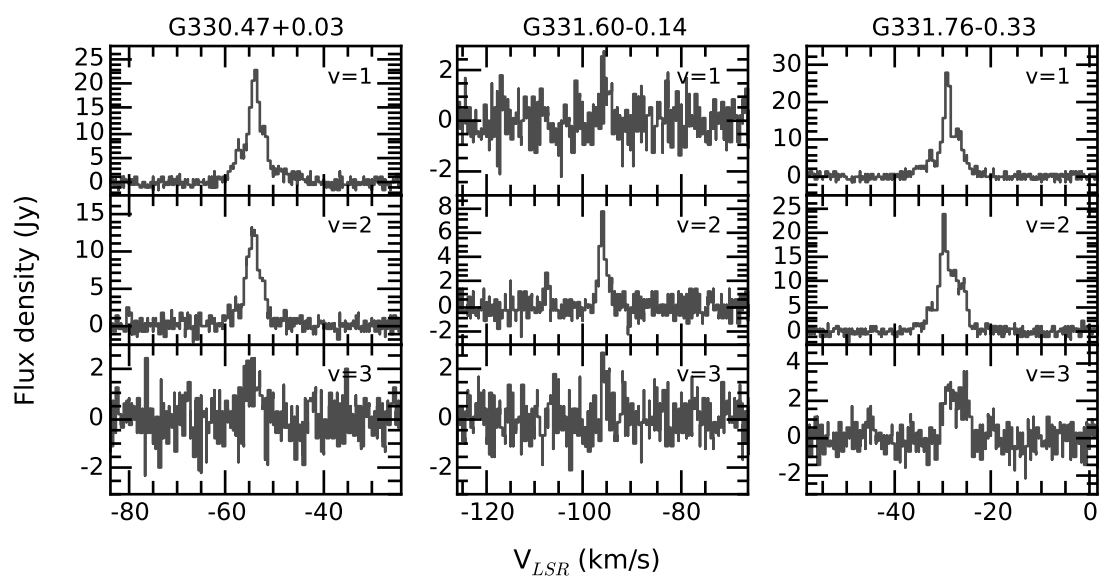


Figure A.15: Spectra of regions containing SiO $v = 1$, $v = 2$ and $v = 3$ masers.

Appendix B

Supplementary material from the MALT-45 class I CH₃OH maser follow-up survey

This appendix contains reference material for the publication outlined in Chapter 4. Each class I CH₃OH maser spot is characterised by Gaussian fits in §B.1. For each class I CH₃OH maser region, CS, SiO and thermal CH₃OH emission are characterised by Gaussian fits in §B.2. GLIMPSE three-colour images in 3.6, 4.5 and 8.0 μm emission with class I CH₃OH, class II CH₃OH, H₂O and OH masers can be seen in §B.3.

B.1 Gaussian fits to cross-correlation class I CH₃OH maser emission

Table B.1: Gaussian fits for the class I CH₃OH maser spots. Column 1 lists the maser spot name, along with a letter designating the spot. Spots labelled with an asterisk (*) have been manually fitted; see §4.2.1.1. Columns 2 and 3 list the fitted position for the Gaussian. Columns 4 through 6 list the fitted Gaussian parameters. Note that the uncertainty for each parameter is quoted in parentheses, in units of the least significant figure. Column 7 lists the integrated flux density of the Gaussian. Rows without spot names correspond to a second Gaussian fitted to the spot directly above.

Spot name	α_{2000} (h:m:s)	δ_{2000} (°:′:″)	Peak flux density (Jy)	Peak velocity (km s ⁻¹)	FWHM (km s ⁻¹)	Integrated flux density (Jy km s ⁻¹)
G330.2940-0.3921A	16:07:37.51	(5) -52:30:56.1	1.00	(4) -80.13	(2) 0.90	(4) 0.679
G330.2945-0.3943A	16:07:38.24	(4) -52:31:00.5	0.52	(3) -77.55	(2) 0.93	(5) 0.363
G330.6780-0.4023A	16:09:31.70	(5) -52:15:50.7	1.73	(6) -64.78	(1) 0.78	(3) 1.015
G330.7790+0.2488A	16:07:09.75	(3) -51:42:53.76	0.72	(2) -43.227	(6) 0.57	(1) 0.308
G330.8749-0.3557A	16:10:15.99	(6) -52:05:46.6	14.3	(1) -61.284	(2) 0.476	(5) 5.120
G330.8774-0.3676A	16:10:19.8	(1) -52:06:12.1	2.4	(1) -58.06	(2) 0.84	(5) 1.519
G330.8711-0.3830A	16:10:22.13	(8) -52:07:08.23	0.85	(6) -58.10	(4) 1.08	(8) 0.690
G330.8711-0.3830B	16:10:22.1	(1) -52:07:08.3	0.77	(5) -62.86	(3) 0.89	(7) 0.513
G330.9261-0.4083A	16:10:44.6	(2) -52:06:00.37	0.51	(4) -64.50	(8) 2.2	(2) 0.340
G330.9261-0.4083B	16:10:44.6	(2) -52:06:00.37	11.8	(4) -42.36	(1) 0.66	(2) 5.877
G330.9261-0.4083C	16:10:44.6	(2) -52:06:00.37	1.2	(2) -41.37	(5) 0.7	(1) 0.598
G330.9274-0.4072A	16:10:44.723	(9) -52:05:54.29	1.9	(1) -41.41	(2) 0.52	(4) 0.744
G330.9304-0.2602A	16:10:06.61	(4) -51:59:18.5	3.9	(1) -90.00	(1) 0.91	(3) 2.675
G330.9311-0.2605A	16:10:06.87	(6) -51:59:17.78	3.94	(8) -89.014	(5) 0.50	(1) 1.480
G330.9548-0.1823A	16:09:52.99	(5) -51:54:52.8	1.55	(6) -93.66	(1) 0.57	(3) 0.670
G331.1308-0.4696A	16:11:59.38	(9) -52:00:19.5	0.78	(5) -68.94	(2) 0.59	(5) 0.346
G331.1308-0.4698A	16:11:59.4	(1) -52:00:20.24	2.6	(1) -67.45	(3) 1.47	(8) 2.876
G331.1336-0.4882A	16:12:05.14	(2) -52:01:01.37	3.13	(6) -67.911	(4) 0.459	(9) 1.082
G331.1308-0.2441A	16:10:59.53	(2) -51:50:25.79	13.0	(6) -87.50	(3) 1.45	(7) 14.148
G331.1308-0.2441B	16:10:59.54	(6) -51:50:25.72	21	(4) -90.1	(1) 1.6	(3) 24.901
G331.1308-0.2441C	16:10:59.54	(6) -51:50:25.68	93	(3) -91.11	(1) 0.93	(3) 65.276
G331.1333-0.2458A	16:11:00.7	(5) -51:50:23.97	45	(1) -88.531	(8) 0.70	(2) 23.769
G331.1333-0.2410A	16:10:59.41	(2) -51:50:11.8	23.1	(2) -84.630	(2) 0.610	(5) 10.604
G331.1333-0.2410B	16:10:59.45	(2) -51:50:11.64	2.9	(1) -86.19	(1) 0.53	(3) 1.151
G331.1322-0.2454A	16:11:00.25	(6) -51:50:25.71	6.5	(2) -84.34	(1) 0.81	(3) 3.986
G331.1322-0.2454B	16:11:00.29	(4) -51:50:26.0	6.3	(2) -87.667	(8) 0.47	(2) 2.244
G331.1332-0.2407A	16:10:59.30	(4) -51:50:10.90	2.11	(6) -85.718	(8) 0.59	(2) 0.931
G331.1313-0.2434A	16:10:59.499	(9) -51:50:22.76	4.19	(7) -86.097	(3) 0.412	(7) 1.300
G331.1315-0.2441A	16:10:59.73	(8) -51:50:24.2	0.90	(5) -82.85	(2) 0.57	(4) 0.386
G331.1313-0.2451A	16:10:59.9	(2) -51:50:27.2	0.89	(7) -82.53	(4) 0.91	(8) 0.610
G331.1329+0.1560A	16:09:15.03	(5) -51:32:42.42	1.03	(9) -78.36	(3) 0.66	(7) 0.509
G331.1339+0.1569A	16:09:15.07	(6) -51:32:37.79	1.42	(3) -78.336	(8) 0.72	(2) 0.768
G331.1348+0.1562A	16:09:15.50	(2) -51:32:37.3	10.0	(3) -77.19	(1) 0.77	(3) 5.760
G331.1332+0.1565A	16:09:15.00	(7) -51:32:40.5	76	(1) -75.532	(5) 0.56	(1) 32.195
G331.1332+0.1565B	16:09:15.00	(7) -51:32:40.5	4.0	(6) -76.48	(6) 0.8	(1) 1.694

Table B.1: *continued*

Spot name	α_{2000} (h:m:s)	δ_{2000} ($^{\circ}$: $'$: $''$)	Peak flux density (Jy)	Peak velocity (km s^{-1})	FWHM (km s^{-1})	Integrated flux density (Jy km s^{-1})
G331.1335+0.1562A	16:09:15.16	-51:32:40.63	10.4	-76.139	0.60	4.664
G331.1331+0.1568A	16:09:14.884	-51:32:40.070	4.8	-74.512	0.52	1.889
G331.2846-0.1953A	16:11:30.32	-51:41:59.9	1.08	-94.03	1.44	1.168
G331.2800-0.1899A	16:11:27.57	-51:41:56.89	8.4	-89.31	0.77	4.883
G331.2800-0.1899B	16:11:28	-51:41:57.02	6.3	-89.94	0.9	4.333
G331.2800-0.1899C	16:11:27.58	-51:41:57.03	12.2	-90.77	0.81	7.417
G331.2800-0.1899D	16:11:27.55	-51:41:57.07	6	-91.31	0.2	1.021
G331.2802-0.1898A*	16:11:27.6	-51:41:56.4	1.0	-92.17	1.2	0.170
G331.2803-0.1899A	16:11:27.66	-51:41:56.26	5.4	-89.92	0.8	3.427
G331.2768-0.1870A	16:11:25.91	-51:41:57.21	5.0	-88.49	0.88	3.306
G331.2793-0.1873A	16:11:26.69	-51:41:51.98	3.0	-86.83	0.8	1.861
G331.2764-0.1874A	16:11:25.91	-51:41:59.38	2.7	-85.764	0.44	0.890
G331.2783-0.1884A	16:11:26.71	-51:41:57.3	3.78	-85.259	0.67	1.896
G331.2765-0.1871A	16:11:25.85	-51:41:58.05	1.34	-87.816	0.38	0.382
G331.3409-0.3470A	16:12:26.40	-51:46:20.50	2.0	-87.76	0.50	0.752
G331.3703-0.3990A	16:12:48.54	-51:47:24.39	30.7	-65.69	0.67	15.454
G331.3705-0.1446A	16:11:41.22	-51:36:15.37	5.15	-87.95	0.471	1.826
G331.3705-0.1446B	16:11:41.23	-51:36:15.3	0.90	-89.07	1.09	0.740
G331.3798+0.1490A	16:10:26.81	-51:22:58.5	0.90	-89.07	0.76	0.517
G331.4093-0.1643A	16:11:57.37	-51:35:32.033	1.47	-45.72	0.74	0.816
G331.4407-0.1869A	16:12:12.2	-51:35:14.1	1.27	-85.050	0.54	0.518
G331.4408-0.1869A	16:12:12.25	-51:35:13.88	3.3	-91.66	0.49	1.228
G331.4381-0.1864A	16:12:11.3	-51:35:19.3	0.56	-90.06	1.5	0.208
G331.4417-0.1580A	16:12:04.85	-51:33:55.74	1.10	-87.94	0.65	0.536
G331.4876-0.0863A	16:11:58.9	-51:28:54.33	1.57	-87.756	0.56	0.660
G331.4954-0.0786A	16:11:59.05	-51:28:14.81	0.73	-86.88	0.8	0.294
G331.4962-0.0780A	16:11:59.12	-51:28:11.66	0.73	-85.98	1.05	0.574
G331.4874-0.0865A	16:11:58.87	-51:28:55.23	31.7	-90.19	0.9	0.483
G331.5046-0.1158A	16:12:11.44	-51:29:30.20	1.7	-89.001	0.673	16.069
G331.5033-0.1066A	16:12:08.64	-51:29:09.1	1.41	-88.45	0.84	1.073
G331.5028-0.1068A	16:12:08.55	-51:29:10.76	2.43	-87.906	0.54	0.575
G331.5032-0.1067A	16:12:08.65	-51:29:09.71	0.70	-100.45	1.19	2.171
G331.5219-0.0811A	16:12:07.16	-51:27:16.2	1.39	-88.39	0.73	0.386
G331.5179-0.0823A	16:12:06.36	-51:27:29.28	0.87	-86.18	1.0	0.625
G331.5179-0.0823B	16:12:06.34	-51:27:29.42	0.65	-90.84	0.49	0.237
G331.5185-0.0823A	16:12:06.52	-51:27:27.81	3.7	-88.04	0.97	2.708
G331.5290-0.0982A	16:12:13.665	-51:27:43.92	2.5	-89.36	0.8	1.830
			7.2	-90.08	0.60	3.267
			0.53	-87.063	0.50	0.199
			18.7	-93.017	0.50	7.093

Table B.1: *continued*

Spot name	α_{2000} (h:m:s)	δ_{2000} ($^{\circ}$: $'$: $''$)	Peak flux density (Jy)	Peak velocity (km s^{-1})	FWHM (km s^{-1})	Integrated flux density (Jy km s^{-1})
G331.5327-0.0993A	16:12:15.00	-51:27:37.6	79	(2) -91.827	(9) 0.58	(2) 34.306
G331.5237-0.1009A	16:12:12.87	-51:28:04.02	10	(1) -91.06	(3) 0.45	(6) 4.343
G331.5312-0.0987A	16:12:14.40	-51:27:39.71	4.53	(9) -91.082	(4) 0.422	(9) 1.437
G331.5341-0.0997A	16:12:15.50	-51:27:35.31	1.21	(3) -90.662	(5) 0.42	(1) 0.380
G331.5432-0.0660A	16:12:09.17	-51:25:44.2	3.82	(6) -89.621	(6) 0.75	(1) 2.160
G331.5432-0.0660B	16:12:09.18	-51:25:44.24	1.6	(1) -88.77	(3) 0.74	(8) 0.893
G331.5461-0.0688A	16:12:10.73	-51:25:44.6	0.80	(8) -89.54	(4) 0.9	(1) 0.519
G331.5548-0.1227A	16:12:27.4	-51:27:44.49	0.62	(3) -87.74	(1) 0.59	(3) 0.274
G331.5544-0.1221A	16:12:27.1	-51:27:44.1	0.44	(5) -87.02	(3) 0.52	(7) 0.194
G331.5544-0.1221B	16:12:27.10	-51:27:44.13	3.2	(1) -104.01	(1) 0.59	(3) 1.418
G331.5544-0.1221C	16:12:27.09	-51:27:44.1	3.8	(3) -100.68	(3) 0.95	(8) 2.714
G331.5547-0.1211A	16:12:26.90	-51:27:40.69	1.2	(1) -102.05	(5) 1.0	(1) 0.912
G331.5552-0.1215A	16:12:27.16	-51:27:40.7	0.68	(7) -103.75	(6) 1.2	(1) 0.595
G331.5552-0.1215B	16:12:27.15	-51:27:40.7	4.01	(9) -102.801	(4) 0.40	(1) 1.215
G331.8527-0.1295A	16:13:52.5	-51:15:46.63	0.74	(2) -97.311	(8) 0.62	(2) 0.348
G331.8855+0.0619A	16:13:11.24	-51:06:04.75	0.64	(3) -98.72	(2) 0.87	(5) 0.419
G331.8855+0.0627A	16:13:11.05	-51:06:02.6	1.15	(8) -49.77	(4) 1.05	(9) 0.913
G331.8854+0.0625A*	16:13:11.1	-51:06:03.5	0.99	(2) -89.865	(5) 0.58	(1) 0.433
G331.8847+0.0617A	16:13:11.08	-51:06:07.4	4.3	(3) -88.88	(3) 0.86	(6) 2.774
G331.8854+0.0630A	16:13:10.96	-51:06:02.21	3.7	(2) -88.81	(2) 0.76	(5) 2.112
G331.8892+0.0641A	16:13:11.70	-51:05:49.90	2.06	(4) -88.375	(4) 0.436	(9) 0.675
G331.8864+0.0618A	16:13:11.522	-51:06:02.7	0.82	(2) -87.135	(5) 0.405	(9) 0.250
G331.8898+0.0658A	16:13:11.44	-51:05:43.9	0.85	(3) -86.785	(8) 0.46	(2) 0.294
G331.8880+0.0658A	16:13:10.94	-51:05:48.5	0.56	(3) -86.12	(2) 0.58	(4) 0.194
G331.9209-0.0829A	16:13:59.17	-51:10:56.00	0.73	(3) -86.378	(9) 0.42	(2) 0.230
G332.0933-0.4213A	16:16:16.59	-51:18:27.90	0.80	(3) -85.978	(8) 0.48	(2) 0.286
G332.0911-0.4194A	16:16:15.44	-51:18:28.51	1.51	(1) -86.863	(1) 0.330	(2) 0.375
G332.0908-0.4184A	16:16:15.12	-51:18:26.51	4.7	(2) -51.63	(1) 0.44	(3) 1.549
G332.2420-0.0443A	16:15:17.74	-50:55:58.09	0.7	(2) -52.18	(4) 0.4	(1) 0.231
G332.2420-0.0443B	16:15:17.78	-50:55:58.0	3.6	(2) -58.82	(1) 0.53	(3) 1.442
G332.2417-0.0437A	16:15:17.53	-50:55:57.30	1.7	(2) -58.16	(3) 0.67	(8) 0.681
G332.2393-0.0425A	16:15:16.55	-50:55:60.0	8.1	(2) -55.849	(6) 0.45	(1) 2.742
G332.2401-0.0429A	16:15:16.88	-50:55:59.27	0.68	(3) -58.05	(1) 0.53	(3) 0.270
G332.2390-0.0451A	16:15:17.2	-50:56:07.5	2.4	(2) -47.32	(3) 0.89	(6) 1.599
G332.2387-0.0452A*	16:15:17.1	-50:56:08.7	121	(3) -49.178	(7) 0.63	(2) 57.263
			15	(4) -49.91	(5) 0.36	(9) 7.099
			14.4	(3) -48.527	(4) 0.509	(9) 5.513
			6.8	(5) -48.51	(3) 0.61	(6) 3.146
			6.1	(4) -47.93	(1) 0.40	(3) 1.838
			34	(1) -47.31	(1) 0.86	(3) 21.996
			6.5	(8) -46.78	(3) 0.50	(7) 2.442

Table B.1: *continued*

Spot name	α_{2000} (h:m:s)	δ_{2000} (°:':")	Peak flux density (Jy)	Peak velocity (km s ⁻¹)	FWHM (km s ⁻¹)	Integrated flux density (Jy km s ⁻¹)
G332.2390-0.0428A	16:15:16.55	-50:56:01.78	1.10	-46.247	0.44	0.367
G332.2959-0.0945A	16:15:45.8	-50:55:54.5	20.2	-49.70	0.91	13.820
G332.2959-0.0945B	16:15:45.80	-50:55:54.47	21.4	-50.627	0.59	9.558
			14.9	-49.98	0.13	6.655
G332.2956-0.0945A*	16:15:45.7	-50:55:55.0	15.5	-49.83	0.60	6.951
G332.2953-0.0944A	16:15:45.61	-50:55:55.62	9.0	-48.355	0.58	3.924
G332.2941-0.0924A	16:15:44.771	-50:55:53.23	4.5	-48.915	0.35	1.180
G332.2924-0.0919A	16:15:44.15	-50:55:56.39	2.69	-46.107	0.74	1.492
G332.3191+0.1763A	16:14:41.1	-50:43:12.02	2.9	-48.15	0.82	1.799
G332.3174+0.1817A	16:14:39.18	-50:43:02.11	0.55	-49.28	0.54	0.222
G332.3546-0.1145A	16:16:07.18	-50:54:19.9	6.1	-50.221	0.81	3.698
G332.5832+0.1469A	16:16:00.97	-50:33:30.96	3.01	-42.631	0.76	1.718
G332.6036-0.1679A	16:17:29.34	-50:46:15.0	1.6	-46.15	0.63	0.763
G332.6042-0.1668A	16:17:29.21	-50:46:10.9	10.5	-45.836	0.72	5.714
G332.7163-0.0480A	16:17:28.34	-50:36:22.70	2.8	-40.02	1.11	2.347
G332.7167-0.0488A	16:17:28.65	-50:36:23.9	1.10	-39.71	0.58	0.480
			0.82	-38.66	0.77	0.358
G333.0024-0.4368A	16:20:28.68	-50:41:00.91	5.7	-56.387	0.48	2.041
			1.4	-55.77	0.57	0.501
G333.0289-0.0623A	16:18:56.54	-50:23:53.6	0.755	-42.125	0.513	0.292
			0.768	-43	0.14	0.297
G333.0290-0.0629A	16:18:56.73	-50:23:55.17	6.7	-40.03	0.75	3.800
G333.0290-0.0629B	16:18:56.70	-50:23:55.09	7.4	-40.88	0.63	3.502
G333.0294-0.0243A	16:18:46.64	-50:22:14.57	5.60	-42.224	0.419	1.767
G333.0135-0.4660A	16:20:39.46	-50:41:47.45	1.21	-52.65	0.58	0.528
G333.0678-0.4460A	16:20:48.72	-50:38:38.7	0.49	-54.19	0.71	0.262
G333.0731-0.3996A	16:20:37.76	-50:36:26.66	2.13	-52.639	0.676	1.084
G333.0699-0.3989A	16:20:36.7	-50:36:32.92	0.68	-53.451	0.63	0.321
G333.0708-0.3990A	16:20:37.0	-50:36:30.80	0.68	-53.75	0.81	0.415
G333.1040-0.5027A	16:21:13.55	-50:39:31.22	5.4	-57.356	0.51	2.077
G333.1037-0.5036A	16:21:13.7	-50:39:34.49	1.66	-58.22	0.54	0.677
G333.1045-0.5025A	16:21:13.65	-50:39:29.68	0.89	-56.89	0.55	0.371
G333.1003-0.4985A	16:21:11.43	-50:39:30.1	0.56	-55.15	0.45	0.192
G333.1210-0.4325A	16:20:59.39	-50:35:48.95	4.4	-50.780	0.45	1.505
G333.1205-0.4337A	16:20:59.6	-50:35:53.4	1.30	-53.17	0.56	0.551
G333.1206-0.4330A	16:20:59.42	-50:35:51.3	2.23	-52.661	0.45	0.759
			1.01	-51.86	0.70	0.344
G333.1214-0.4334A	16:20:59.75	-50:35:50.46	0.8	-53.51	0.3	0.181
G333.1254-0.4412A	16:21:02.90	-50:36:00.1	0.62	-53.908	0.372	0.141
G333.1254-0.4412B	16:21:02.87	-50:36:00.1	3.5	-47.16	1.06	2.804
			55	-49.983	0.52	21.447
			13	-49.12	1.4	5.069

Table B.1: *continued*

Spot name	α_{2000} (h:m:s)	δ_{2000} ($^{\circ}$: $'$: $''$)	Peak flux density (Jy)	Peak velocity (km s^{-1})	FWHM (km s^{-1})	Integrated flux density (Jy km s^{-1})
G333.1254-0.4412C	16:21:02.88	-50:36:00.0	6.5	-48.12	0.48	2.339
			3.1	-47.61	0.4	1.115
G333.1300-0.4373A	16:21:03.06	-50:35:38.51	4.35	-51.528	0.358	1.172
G333.1310-0.4389A	16:21:03.75	-50:35:40.05	16.7	-50.238	0.69	8.702
			10	-49.704	0.26	5.211
G333.1256-0.4398A	16:21:02.58	-50:35:56.2	11.8	-49.09	0.56	4.978
G333.1257-0.4378A	16:21:02.0	-50:35:50.7	12	-48.633	0.30	2.680
			3.6	-49.04	0.53	0.804
G333.1256-0.4378A	16:21:02.03	-50:35:50.78	10	-48.69	0.47	3.545
G333.1255-0.4379A	16:21:02.03	-50:35:51.6	16.7	-48.05	0.52	6.571
G333.1260-0.4398A	16:21:02.7	-50:35:55.12	11.6	-47.40	0.56	4.893
G333.1254-0.4387A	16:21:02.20	-50:35:53.79	15.3	-46.730	0.67	7.756
			5.8	-45.81	0.96	2.940
G333.1381-0.4247A	16:21:01.89	-50:34:45.58	10.8	-56.070	0.464	3.771
G333.1319-0.4310A	16:21:01.92	-50:35:17.60	2.33	-55.586	0.40	0.702
G333.1398-0.4260A	16:21:02.69	-50:34:44.92	1.28	-53.770	0.54	0.522
G333.1629-0.1010A	16:19:42.69	-50:19:54.74	5.63	-91.480	0.730	3.093
G333.1631-0.1011A	16:19:42.75	-50:19:54.56	1.4	-90.83	0.7	0.690
G333.1610-0.1009A	16:19:42.15	-50:19:59.57	1.12	-92.337	0.45	0.379
			0.62	-92.83	0.54	0.210
G333.1850-0.0929A	16:19:46.47	-50:18:38.1	0.97	-86.18	0.73	0.536
G333.1839-0.0904A	16:19:45.53	-50:18:34.63	2.0	-86.69	0.90	1.361
G333.1828-0.0880A	16:19:44.59	-50:18:31.04	1.41	-86.83	0.33	0.355
G333.2302-0.0583A	16:19:49.41	-50:15:15.4	280	-87.298	1.07	224.818
			7	-89.2	1.6	5.620
G333.2344-0.0628A	16:19:51.71	-50:15:16.24	1.51	-91.542	0.65	0.733
G333.2323-0.0568A	16:19:49.59	-50:15:06.13	2.4	-90.44	0.70	1.259
G333.2305-0.0582A*	16:19:49.5	-50:15:14.2	35	-87.87	0.59	15.509
			8	-88.3	1.4	3.545
G333.2325-0.0628A	16:19:51.22	-50:15:21.18	3.76	-89.012	0.429	1.213
G333.2332-0.0627A	16:19:51.37	-50:15:19.10	6.3	-88.10	0.44	2.077
G333.2332-0.0627B	16:19:51.38	-50:15:19.0	2.1	-88.5	0.8	1.329
G333.2307-0.0585A	16:19:49.6	-50:15:14.54	5.3	-86.56	0.6	2.583
G333.2307-0.0585B	16:19:49.61	-50:15:14.4	10.2	-88.16	0.47	3.634
G333.2345-0.0640A	16:19:52.10	-50:15:19.02	8.0	-86.098	0.44	2.666
G333.2336-0.0632A	16:19:51.61	-50:15:19.14	2.9	-85.42	1.0	2.107
G333.2337-0.0625A	16:19:51.45	-50:15:17.1	12.1	-85.556	0.377	3.431
			5.2	-84.99	0.7	1.475
G333.2343-0.0610A	16:19:51.24	-50:15:11.92	8.62	-85.492	0.506	3.285
G333.2198-0.4027A	16:21:17.90	-50:30:22.21	21.5	-51.675	0.422	6.821
			1.58	-51.86	1.54	0.501

Table B.1: *continued*

Spot name	α_{2000} (h:m:s)	δ_{2000} ($^{\circ}$: $'$: $''$)	Peak flux density (Jy)	Peak velocity (km s^{-1})	FWHM (km s^{-1})	Integrated flux density (Jy km s^{-1})
G333.2204-0.4030A	16:21:18.13	-50:30:21.58	0.92	-54.65	0.82	0.566
G333.2204-0.4030B	16:21:18.14	-50:30:21.57	1.32	-55.82	1.15	1.146
G333.2200-0.4008A	16:21:17.43	-50:30:16.9	2.9	-53.74	0.90	1.964
G333.2203-0.4018A	16:21:17.8	-50:30:18.6	1.8	-53.61	0.75	1.018
G333.2203-0.4019A	16:21:17.8	-50:30:19.0	2.5	-52.72	0.56	1.050
G333.2845-0.3732A	16:21:27.31	-50:26:22.48	1.6	-53.43	0.8	0.672
G333.3008-0.3516A	16:21:25.92	-50:24:46.3	0.78	-52.09	0.90	0.530
G333.3117+0.1033A	16:19:28.67	-50:04:54.82	0.53	-49.45	0.70	0.279
G333.3137+0.1071A	16:19:28.21	-50:04:39.96	3.34	-45.161	0.480	1.208
G333.3123+0.1063A	16:19:28.05	-50:04:45.64	1.72	-48.22	0.69	0.887
G333.3146+0.1054A	16:19:28.90	-50:04:42.00	1.51	-47.186	0.58	0.658
G333.3358-0.3620A	16:21:38.02	-50:23:43.51	2.5	-44.43	1.0	1.941
G333.3358-0.3620B	16:21:38.05	-50:23:43.35	19.6	-51.927	0.81	11.951
G333.3376-0.3621A	16:21:38.54	-50:23:39.2	12.5	-52.43	0.2	1.883
G333.3376-0.3621B	16:21:38.5	-50:23:39.3	3	-52.87	0.2	0.452
G333.3376-0.3621C	16:21:38.5	-50:23:39.3	2.0	-49.96	0.2	0.369
G333.3284-0.3643A	16:21:36.67	-50:24:08.16	1.0	-49.52	0.25	0.184
G333.3285-0.3645A	16:21:36.73	-50:24:08.35	6.6	-50.29	0.41	2.047
G333.3359-0.3616A	16:21:37.95	-50:23:42.20	0.81	-54.10	0.60	0.365
G333.3384-0.3623A	16:21:38.79	-50:23:37.62	4.9	-50.867	0.68	2.519
G333.3874+0.0322A	16:20:07.52	-50:04:45.95	3.2	-50.22	0.63	1.509
G333.3860+0.0311A	16:20:07.42	-50:04:52.28	4.2	-51.098	0.41	1.303
G333.3862+0.0311A	16:20:07.48	-50:04:51.84	1.92	-50.54	1.01	0.596
G333.3872+0.0316A	16:20:07.62	-50:04:48.0	0.56	-47.60	0.82	0.347
G333.3745-0.2023A	16:21:05.93	-50:15:17.91	3.1	-70.22	0.96	2.231
G333.3773-0.2013A	16:21:06.42	-50:15:08.52	0.97	-72.57	0.65	0.473
G333.4679-0.1601A	16:21:19.62	-50:09:33.1	1.65	-72.03	0.83	1.027
G333.4679-0.1601B	16:21:19.61	-50:09:32.95	1.44	-68.44	0.49	0.528
G333.4669-0.1621A	16:21:19.88	-50:09:40.75	9.1	-61.31	0.44	3.000
G333.4658-0.1660A	16:21:20.62	-50:09:53.44	6.5	-57.979	0.93	4.574
G333.4658-0.1660B	16:21:20.62	-50:09:53.47	17.3	-43.007	0.558	7.267
G333.4664-0.1633A	16:21:20.05	-50:09:45.2	0.6	-43.94	0.9	0.405
G333.4681-0.1613A	16:21:19.97	-50:09:35.64	6.1	-45.275	0.55	2.508
G333.4681-0.1616A	16:21:20.1	-50:09:36.55	0.8	-45.2	1.4	0.329
G333.4684-0.1649A	16:21:21.00	-50:09:44.19	2.1	-44.10	0.52	0.815
G333.4973+0.1431A	16:20:07.59	-49:55:23.7	0.6	-44.79	0.8	0.364
			5.5	-43.467	0.41	1.716
			1.1	-42.11	0.53	0.435
			3.69	-41.518	0.55	1.530
			1.31	-38.91	0.51	0.502
			2.7	-112.39	0.75	1.531
			0.71	-113.60	0.85	0.403

Table B.1: *continued*

Spot name	α_{2000} (h:m:s)	δ_{2000} ($^{\circ}$: $'$: $''$)	Peak flux density (Jy)	Peak velocity (km s^{-1})	FWHM (km s^{-1})	Integrated flux density (Jy km s^{-1})
G333.4967+0.1424A	16:20:07.61	-49:55:26.86	0.70	-113.53	0.64	0.339
G333.4967+0.1421A	16:20:07.69	-49:55:28.0	0.75	-113.060	0.49	0.277
G333.5228-0.2747A	16:22:04.49	-50:12:05.3	7.2	-50.220	0.78	4.211
G333.5507-0.2915A	16:22:16.36	-50:11:36.91	1.96	-46.232	0.44	0.653
G333.5650-0.2952A	16:22:21.11	-50:11:09.8	1.16	-46.65	0.72	0.631
G333.5618-0.0246A	16:21:08.74	-49:59:48.85	60	-39.98	0.85	38.498
G333.5687+0.0284A	16:20:56.61	-49:57:15.91	7.1	-84.796	0.504	2.693
G333.5934-0.2122A	16:22:06.63	-50:06:26.6	27.7	-49.561	0.617	12.863
G333.5950-0.2108A	16:22:06.70	-50:06:19.2	1.2	-48.75	1.1	1.021
G333.5950-0.2108B	16:22:06.7	-50:06:18.8	2.3	-50.25	0.79	1.374
G333.5950-0.2108C	16:22:06.7	-50:06:18.77	0.8	-51.34	0.7	0.407
G333.5941-0.2116A	16:22:06.66	-50:06:23.07	1.26	-48.60	0.81	0.768
G333.6919-0.1955A	16:22:28.19	-50:01:32.9	3.29	-50.610	0.358	0.886
G333.6958-0.1986A	16:22:30.06	-50:01:30.8	0.46	-50.7	1.1	0.124
G333.7123-0.1158A	16:22:12.50	-49:57:18.37	0.94	-51.43	0.76	0.535
G333.7098-0.1152A	16:22:11.69	-49:57:23.17	6.2	-31.495	0.73	3.407
G333.7733-0.2578A	16:23:06.16	-50:00:43.31	0.45	-28.12	0.70	0.236
G333.7722-0.0096A	16:22:00.29	-49:50:15.79	2.55	-49.405	0.51	0.985
G333.8181-0.3026A	16:23:29.83	-50:00:42.0	17.7	-89.33	0.88	11.671
G333.8187-0.3031A	16:23:30.11	-50:00:41.93	20.4	-48.31	0.58	8.895
G333.8993-0.0977A	16:22:56.86	-49:48:35.3	2.3	-47.70	0.70	1.219
G333.9007-0.0993A	16:22:57.65	-49:48:35.9	1.5	-63.65	0.8	0.885
G333.9307-0.1342A	16:23:14.73	-49:48:47.5	1.5	-62.83	0.65	0.885
G333.9305-0.1343A	16:23:14.71	-49:48:48.46	1.36	-64.36	0.84	0.861
G333.9303-0.1316A	16:23:13.95	-49:48:41.8	3.8	-42.10	0.69	1.960
G333.9744+0.0737A	16:22:31.40	-49:38:08.44	3.0	-42.55	0.60	1.356
G333.9746+0.0736A	16:22:31.49	-49:38:08.19	0.89	-41.67	0.52	0.345
G334.0266-0.0465A	16:23:16.67	-49:41:00.19	6.7	-58.30	0.72	3.610
G334.7452+0.5068A	16:23:57.70	-48:46:59.92	3.2	-59.67	0.93	2.246
G334.7459+0.5063A	16:23:57.99	-48:46:59.41	10.4	-84.040	0.721	5.641
G334.7469+0.5058A	16:23:58.40	-48:46:58.0	3.52	-64.554	0.51	1.360
			1.60	-63.49	0.70	0.845
			2.3	-61.15	0.46	0.803
			0.45	-60.22	0.8	0.157

B.2 Gaussian fits to auto-correlated thermal lines

Table B.2: Gaussian fits for the thermal lines detected towards class I CH₃OH maser regions. Column 1 lists the maser region. Columns 2 to 5 contain information for CS, columns 6 to 9 for SiO, columns 10 to 13 for thermal CH₃OH. The columns for each type of emission list the fitted Gaussian parameters, as well as the integrated intensity bounded by these Gaussians. Note that the uncertainty for each parameter is quoted in parentheses, in units of the least significant figure. Rows without region names correspond to a second Gaussian fitted to the region directly above. If no Gaussian information is listed for an emission type, it was not detected.

Region name	CS (1-0) parameters				SiO (1-0) $v = 0$ parameters				CH ₃ OH I ₀₋₀ parameters													
	Peak intensity (K)	Peak velocity (km s ⁻¹)	FWHM (kms ⁻¹)	Integrated intensity (K km s ⁻¹)	Peak intensity (K)	Peak velocity (km s ⁻¹)	FWHM (kms ⁻¹)	Integrated intensity (K km s ⁻¹)	Peak intensity (K)	Peak velocity (km s ⁻¹)	FWHM (kms ⁻¹)	Integrated intensity (K km s ⁻¹)										
G330.294-0.393	0.507	(3)	-80.68	(1)	2.143	(4)	5.62	(4)	0.013	(1)	-64.0	(2)	8.6	(4)	0.084	(4)	-63.53	(3)	9.7	(7)	0.147	(7)
G330.678-0.402	0.298	(4)	-63.87	(3)	1.194	(7)	5.32	(7)	0.027	(1)	-43.81	(9)	6.7	(2)	0.137	(4)	-43.48	(3)	3.4	(2)	0.127	(2)
G330.779+0.249	0.336	(5)	-43.51	(1)	0.687	(3)	2.72	(3)	0.044	(1)	-63.35	(6)	7.1	(1)	0.236	(1)	-62.91	(5)	2.55	(7)	0.192	(7)
G330.876-0.362	1.24	(1)	-62.79	(2)	4.279	(4)	4.58	(4)	0.060	(1)	-63.63	(5)	7.1	(1)	0.322	(1)	-63.25	(5)	4.0	(5)	0.272	(5)
G330.871-0.383	1.39	(1)	-62.94	(2)	5.102	(4)	4.88	(4)	0.016	(1)	-42.5	(1)	5.4	(3)	0.065	(3)	-41.49	(7)	2.8	(4)	0.370	(4)
G330.927-0.408	0.47	(2)	-41.38	(4)	1.040	(1)	2.9	(1)	0.016	(1)	-42.5	(1)	5.4	(3)	0.065	(3)	-41.49	(7)	2.8	(4)	0.106	(4)
G330.931-0.260	0.158	(4)	-90.18	(6)	0.622	(1)	5.2	(1)	0.174	(1)	-90.01	(3)	7.96	(7)	1.043	(7)	-89.1	(2)	3.2	(4)	0.048	(4)
G330.955-0.182	1.483	(8)	-91.16	(1)	7.820	(4)	7.01	(4)	0.023	(1)	-67.2	(1)	4.2	(2)	0.072	(2)	-67.78	(4)	5.5	(1)	0.496	(6)
G331.131-0.470	0.870	(7)	-67.50	(1)	2.979	(3)	4.55	(3)	0.016	(1)	-66.5	(2)	7.7	(4)	0.093	(3)	-66.1	(1)	4.2	(1)	0.286	(1)
G331.134-0.488	0.526	(6)	-66.23	(2)	2.152	(4)	5.43	(5)	0.087	(1)	-86.74	(5)	8.5	(1)	0.554	(4)	-86.33	(3)	5.4	(2)	0.123	(2)
G331.132-0.244	0.897	(5)	-86.94	(1)	3.889	(3)	5.76	(3)	0.017	(1)	-76.2	(1)	5.1	(3)	0.065	(3)	-76.32	(5)	5.35	(8)	0.765	(8)
G331.134+0.156	0.277	(6)	-76.96	(3)	0.637	(1)	3.05	(3)	0.017	(1)	-76.2	(1)	5.1	(3)	0.065	(3)	-76.32	(5)	4.4	(1)	0.198	(1)
G331.279-0.189	0.808	(5)	-88.29	(1)	3.195	(3)	5.25	(3)	0.046	(1)	-87.2	(1)	10.9	(3)	0.376	(3)	-88.06	(3)	3.61	(7)	0.299	(7)
G331.341-0.347	0.519	(8)	-65.90	(2)	1.197	(1)	3.06	(6)	0.019	(1)	-66.5	(1)	6.9	(3)	0.098	(1)	-66.46	(6)	4.2	(1)	0.126	(1)
G331.370-0.399	0.255	(6)	-64.80	(3)	0.695	(8)	3.62	(8)	0.009	(1)	-66.3	(4)	12.3	(8)	0.083	(2)	-66.5	(2)	8.2	(5)	0.124	(5)
G331.371-0.145	0.051	(5)	-69.9	(1)	0.121	(3)	3.1	(3)	0.009	(1)	-66.3	(4)	12.3	(8)	0.083	(2)	-66.5	(2)	8.2	(5)	0.124	(5)
G331.371-0.145	0.167	(3)	-87.06	(4)	0.523	(9)	4.16	(9)	0.069	(1)	-44.63	(6)	6.7	(1)	0.350	(6)	-45.03	(3)	4.32	(7)	0.650	(7)
G331.371-0.145	0.052	(3)	-91.0	(1)	0.145	(3)	3.7	(3)	0.069	(1)	-44.63	(6)	6.7	(1)	0.350	(6)	-45.03	(3)	4.32	(7)	0.650	(7)
G331.380+0.149	0.344	(8)	-45.05	(5)	1.255	(3)	4.8	(3)	0.017	(1)	-85.6	(1)	5.0	(3)	0.105	(3)	-85.99	(4)	4.48	(8)	0.371	(8)
G331.409-0.164	0.348	(4)	-86.36	(4)	1.502	(3)	5.73	(3)	0.028	(1)	-85.05	(9)	5.0	(2)	0.105	(3)	-85.99	(4)	4.48	(8)	0.371	(8)
G331.44-0.14	0.169	(5)	-86.6	(1)	1.049	(8)	8.2	(8)	0.017	(1)	-85.6	(1)	5.0	(3)	0.064	(3)	-85.89	(8)	5.7	(2)	0.213	(2)
G331.440-0.187	0.240	(7)	-88.0	(1)	1.605	(3)	8.9	(3)	0.060	(1)	-87.97	(6)	7.1	(1)	0.320	(4)	-88.36	(3)	5.51	(7)	0.746	(7)
G331.442-0.158	0.203	(3)	-87.10	(6)	1.090	(1)	7.1	(1)	0.021	(1)	-87.0	(1)	6.4	(3)	0.101	(4)	-86.75	(5)	4.5	(1)	0.306	(1)
G331.492-0.082	0.586	(7)	-88.14	(2)	1.908	(6)	4.33	(6)	0.035	(1)	-88.8	(1)	7.4	(2)	0.202	(2)	-88.72	(7)	3.3	(2)	0.149	(2)
G331.503-0.109	0.63	(2)	-88.14	(7)	2.511	(2)	5.3	(2)	0.037	(1)	-88.0	(1)	7.4	(3)	0.206	(5)	-88.72	(7)	3.3	(2)	0.149	(2)
G331.503-0.109	0.269	(6)	-101.38	(6)	1.055	(1)	5.2	(1)	0.032	(1)	-100.8	(2)	8.5	(4)	0.169	(4)	-101.30	(6)	4.0	(1)	0.238	(1)
G331.519-0.082	0.785	(4)	-89.35	(1)	2.797	(3)	4.73	(3)	0.027	(1)	-89.3	(2)	8.3	(4)	0.206	(4)	-89.3	(1)	3.3	(3)	0.100	(3)
G331.530-0.099	1.196	(6)	-88.58	(1)	4.566	(3)	5.07	(3)	0.063	(1)	-88.63	(6)	7.4	(1)	0.353	(1)	-89.16	(4)	4.21	(9)	0.443	(9)
G331.544-0.067	0.842	(9)	-88.27	(2)	3.036	(6)	4.79	(6)	0.038	(1)	-88.50	(7)	5.3	(2)	0.151	(5)	-88.66	(5)	3.8	(1)	0.287	(1)
G331.555-0.122	0.558	(7)	-100.37	(3)	1.894	(6)	4.51	(6)	0.024	(1)	-98.2	(2)	16.5	(6)	0.299	(5)	-100.56	(5)	3.6	(1)	0.247	(1)
G331.555-0.122	0.113	(5)	-88.8	(2)	0.747	(4)	8.8	(4)	0.020	(1)	-46.5	(1)	4.3	(2)	0.064	(4)	-46.7	(1)	6.0	(3)	0.225	(3)
G331.72-0.20	0.464	(6)	-47.44	(2)	1.007	(4)	2.88	(4)	0.056	(1)	-50.69	(5)	5.4	(1)	0.229	(6)	-50.84	(7)	5.4	(2)	0.531	(2)
G331.853-0.129	0.452	(4)	-50.57	(2)	1.191	(4)	3.50	(4)	0.081	(1)	-50.9	(3)	4.89	(7)	0.298	(4)	-50.84	(7)	5.4	(2)	0.531	(2)
G331.887+0.063	0.343	(3)	-87.57	(2)	1.278	(5)	4.95	(5)	0.015	(1)	-50.9	(3)	4.89	(7)	0.298	(4)	-50.84	(7)	5.4	(2)	0.531	(2)
G331.921-0.083	0.297	(8)	-51.59	(4)	0.742	(1)	3.3	(1)	0.015	(1)	-50.9	(3)	4.89	(7)	0.298	(4)	-50.84	(7)	5.4	(2)	0.531	(2)
G332.092-0.420	0.776	(6)	-56.73	(2)	2.613	(4)	4.47	(4)	0.018	(1)	-57.0	(2)	6.1	(4)	0.082	(4)	-56.97	(4)	4.1	(2)	0.185	(2)
G332.240-0.044	0.462	(5)	-47.97	(2)	1.365	(5)	3.93	(4)	0.053	(1)	-48.67	(8)	9.2	(2)	0.368	(6)	-48.18	(4)	4.8	(1)	0.693	(1)
G332.240-0.044	0.080	(3)	-48.6	(2)	0.847	(5)	14.1	(5)	0.053	(1)	-48.67	(8)	9.2	(2)	0.368	(6)	-48.18	(4)	4.8	(1)	0.693	(1)
G332.295-0.094	0.564	(7)	-48.86	(2)	1.561	(5)	3.68	(5)	0.022	(1)	-50.3	(1)	9.2	(3)	0.153	(3)	-49.38	(8)	5.3	(2)	0.239	(2)
G332.295-0.094	0.095	(4)	-49.3	(2)	0.656	(5)	9.2	(5)	0.022	(1)	-50.3	(1)	9.2	(3)	0.153	(3)	-49.38	(8)	5.3	(2)	0.239	(2)
G332.318+0.179	0.197	(5)	-48.30	(3)	0.370	(7)	2.50	(7)	0.022	(1)	-47.9	(1)	5.2	(3)	0.085	(4)	-48.23	(6)	4.1	(1)	0.183	(1)
G332.318+0.179	0.059	(3)	-48.2	(2)	0.264	(4)	5.9	(4)	0.022	(1)	-47.9	(1)	5.2	(3)	0.085	(4)	-48.23	(6)	4.1	(1)	0.183	(1)
G332.355-0.114	0.523	(5)	-49.97	(1)	2.076	(3)	2.73	(3)	0.03	(3)	-50.20	(5)	2.1	(2)	0.048	(2)	-50.20	(5)	2.1	(2)	0.048	(2)
G332.583+0.147	0.124	(9)	-45.03	(8)	0.209	(2)	2.2	(2)	0.025	(1)	-46.5	(1)	7.5	(3)	0.142	(4)	-46.51	(9)	6.1	(2)	0.320	(2)
G332.604-0.167	0.40	(1)	-46.66	(5)	1.068	(1)	3.5	(1)	0.025	(1)	-46.5	(1)	7.5	(3)	0.142	(4)	-46.51	(9)	6.1	(2)	0.320	(2)

Table B.2: *continued*

Region name	CS (1-0) parameters			SiO (1-0) $v = 0$ parameters			CH ₃ OH 1 ₀ -0 ₀ parameters			Integrated intensity (K km s ⁻¹)
	Peak intensity (K)	Peak velocity (km s ⁻¹)	FWHM (km s ⁻¹)	Peak intensity (K)	Peak velocity (km s ⁻¹)	FWHM (km s ⁻¹)	Peak intensity (K)	Peak velocity (km s ⁻¹)	FWHM (km s ⁻¹)	
G332.716-0.048	0.140	-39.54	4.2	0.443	-54.5	6.1	0.03	-39.8	3.5	0.080
G333.002-0.437	0.860	-55.62	3.31	2.140			0.02	-54.6	6.5	0.097
G333.029-0.063	0.358	-51.63	3.08	0.831			0.03	-41.3	3.4	0.077
G333.029-0.024	0.49	-41.24	2.87	1.058			0.02	-41.77	2.1	0.031
G333.014-0.466	0.818	-54.33	2.16	2.707	-41.3	4.9	0.058	-54.9	5.9	0.045
G333.068-0.446	1.43	-60.6	3.2	0.239	-53.8	8.5	0.173	-53.73	4.1	0.306
G333.071-0.399	0.190	-53.48	4.68	5.039	-53.27	6.2	0.298	-53.08	4.6	0.209
G333.103-0.502	0.842	-59.9	4.7	0.671	-52.5	6.0	0.213	-53.67	3.5	0.106
G333.121-0.433	2.24	-51.50	5.65	3.212	-58.4	18	0.278	-56.37	5.7	0.302
G333.126-0.439	0.207	-60.8	6.8	1.063	-55.4	9.1	0.184	-51.23	6.0	0.455
G333.137-0.427	2.54	-50.98	5.74	10.976	-51.54	8.8	0.634	-52.82	6.4	0.625
G333.162-0.101	0.30	-59.5	6.7	1.521	-50.99	8.9	0.927	-88.8	16	0.242
G333.184-0.090	2.84	-52.32	6.48	13.843	-52.80	6.8	0.876	-86.23	3.6	0.216
G333.233-0.061	0.151	-92.06	2.47	0.651	-86.4	5.1	0.069	-87.93	4.52	0.510
G333.220-0.402	0.522	-87.0	5.1	0.580	-87.85	5.9	0.407	-52.24	2.7	0.081
G333.24+0.2	0.134	-90.4	3.7	0.370	-52.3	4.9	0.100	-69.1	6.8	0.153
G333.284-0.373	0.842	-88.7	8.3	0.976	-68.4	11.9	0.170	-51.90	4.44	0.668
G333.301-0.352	1.623	-52.00	3.19	2.024	-51.52	4.4	0.357	-50.48	4.06	0.551
G333.313+0.106	0.191	-47.1	2.9	0.220	-50.42	4.4	0.217	-46.25	5.5	0.459
G333.335-0.363	1.112	-69.87	4.7	1.240	-46.8	7.8	0.228	-50.29	3.80	0.457
G333.387+0.031	0.324	-51.947	5.46	8.154	-49.93	6.0	0.302	-69.88	3.6	0.136
G333.376-0.202	0.357	-50.27	4.80	5.868	-49.3	6.0	0.293	-59.0	4.9	0.111
G333.467-0.163	0.284	-58.7	4.8	0.690	-59.3	21	0.220	-43.49	4.6	0.244
G333.497+0.143	0.18	-43.81	3.0	0.802	-69.3	11.7	0.220	-113.28	2.4	0.053
G333.523-0.275	0.936	-44.52	8.8	1.890	-55.5	15.4	0.244	-49.64	2.9	0.110
G333.558-0.293	0.589	-113.3	2.8	0.379	-44.1	9.6	0.298	-45.95	2.4	0.055
G333.562-0.025	0.145	-49.68	3.51	2.474	-58.2	14	0.117	-39.5	4.2	0.096
G333.569+0.028	0.256	-45.83	2.87	1.272	-49.3	6.4	0.178	-84.64	4.2	0.254
G333.595-0.211	1.96	-46.7	3.2	0.345	-47.8	12.5	0.122	-47.9	3.8	0.000
G333.694-0.197	0.289	-84.67	5.3	7.858	-38.9	7.8	0.094	-50.47	2.98	0.180
G333.711-0.115	0.071	-47.56	5.33	0.606	-47.93	6.5	0.157	-48.66	4.9	0.220
G333.773-0.258	0.377	-50.53	4.6	0.247	-49.9	8.0	0.08	-86.8	7.5	0.057
G333.772-0.010	0.121	-29.0	2.8	1.563	-48.64	5.8	0.211	-86.8	4.9	0.057
G333.818-0.303	0.141	-47.69	5.5	0.319	-86.0	11	0.01	-46.6	9	0.069
G333.900-0.098	0.134	-86.0	3.5	0.574	-65.1	6.6	0.070	-64.9	4.6	0.104
G333.930-0.133	0.198	-65.1	5.4	0.401	-39.4	5.2	0.078	-39.9	5.1	0.077
G333.974+0.074	0.22	-40.01	9.0	0.773	-39.4	1	0.001	-58.0	10	0.072
G334.027-0.047	0.366	-59.93	7.4	0.406	-84.93	4	0.03	-84.72	3.3	0.075
G334.746+0.506	0.06	-89.0	2.0	1.011	-62.0	12.2	0.212	-62.36	4.4	0.201
	0.255	-62.45	4.0	0.771			0.06			

B.3 GLIMPSE images

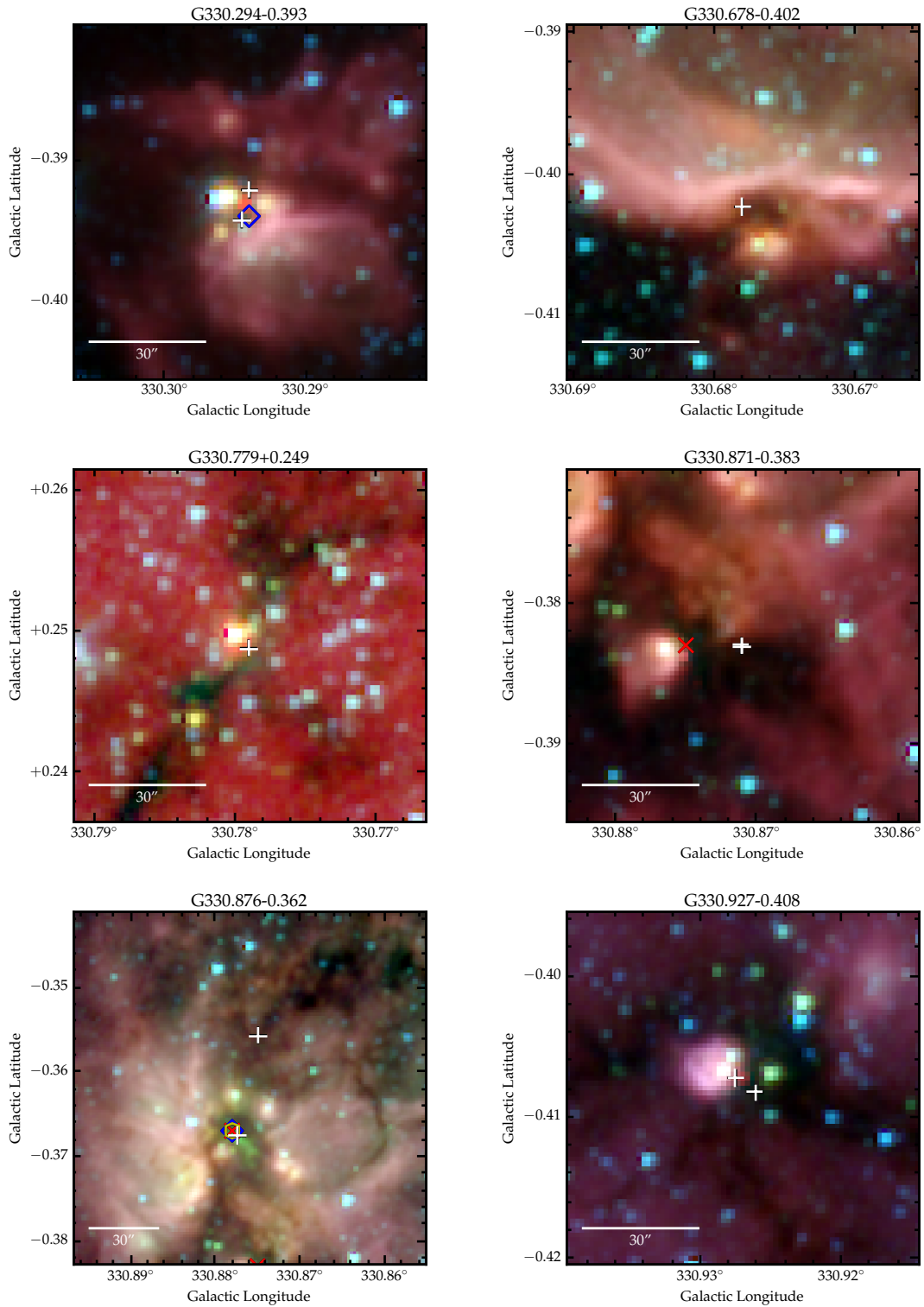


Figure B.1: *Spitzer* GLIMPSE three-colour images (RGB = 3.6, 4.5 and 8.0 μm) overlaid with the positions of class I CH₃OH masers (white plus symbols). The size of these symbols reflects the maximum positional uncertainty for maser spot. The published positions of class II CH₃OH, H₂O and OH masers are overlaid (red crosses, blue diamonds and yellow hexagon symbols, respectively; Caswell et al. 2011; Breen et al. 2010a; Walsh et al. 2011, 2014; Sevenster et al. 1997; Caswell 1998).

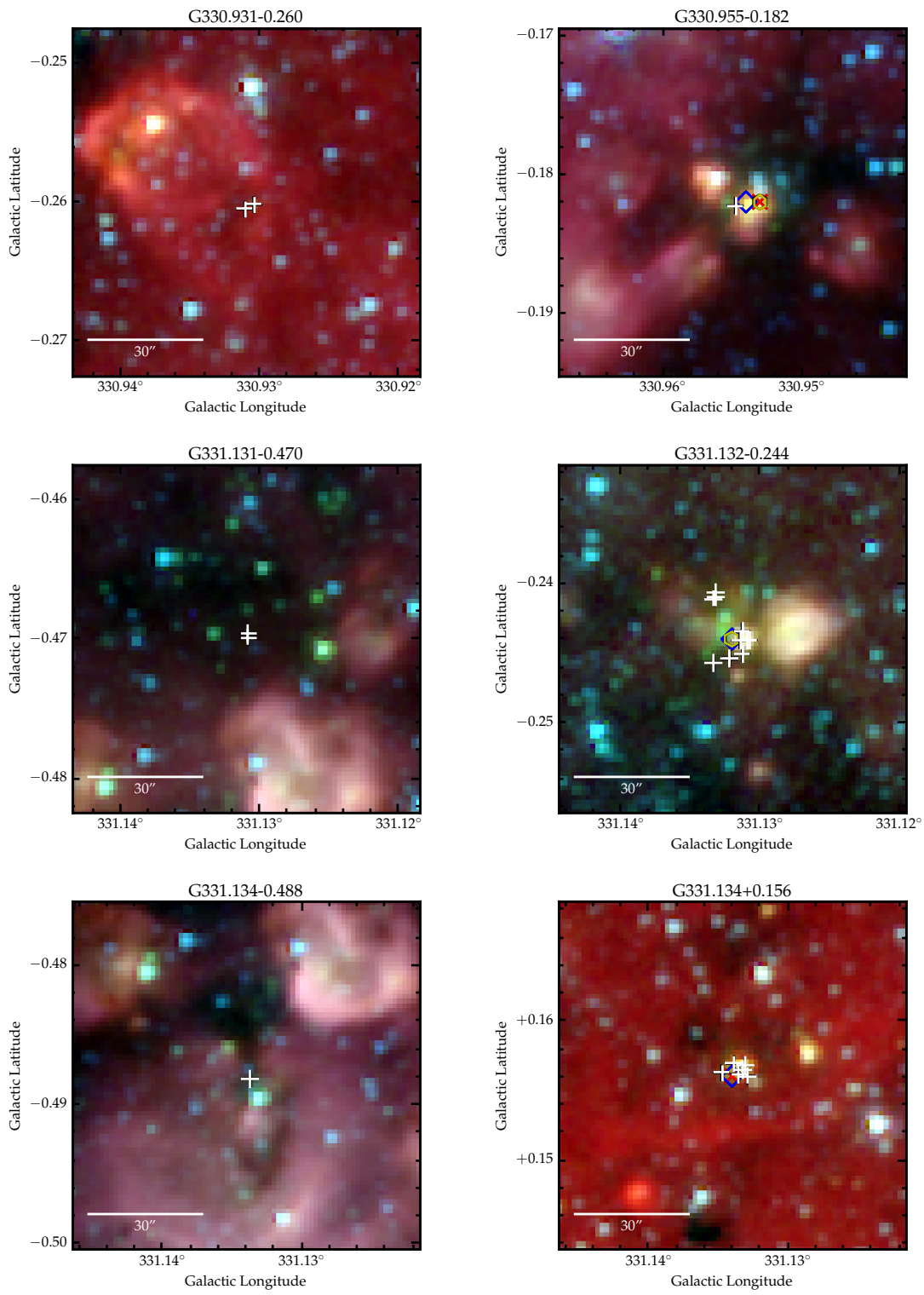
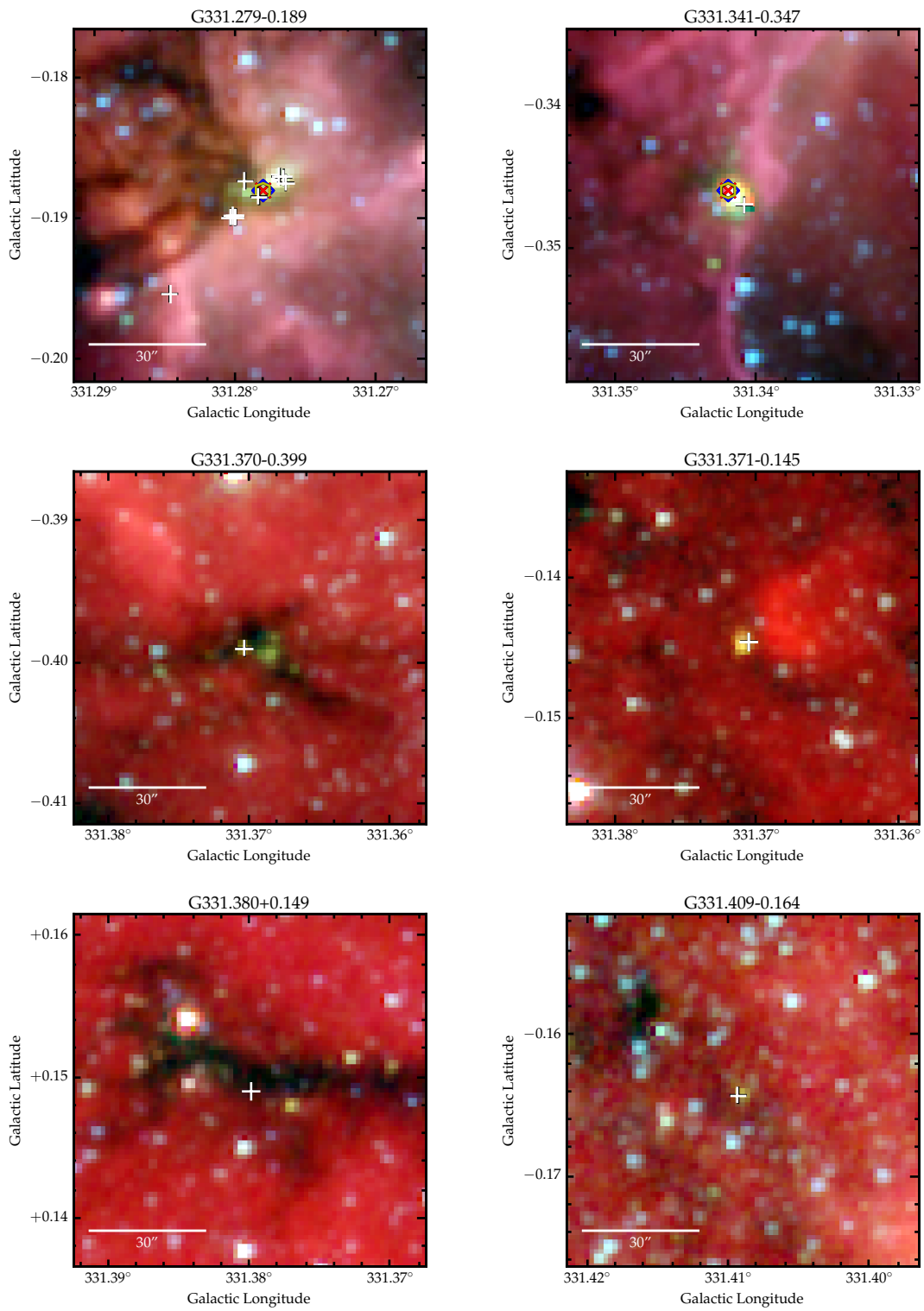


Figure B.1: *continued*

Figure B.1: *continued*

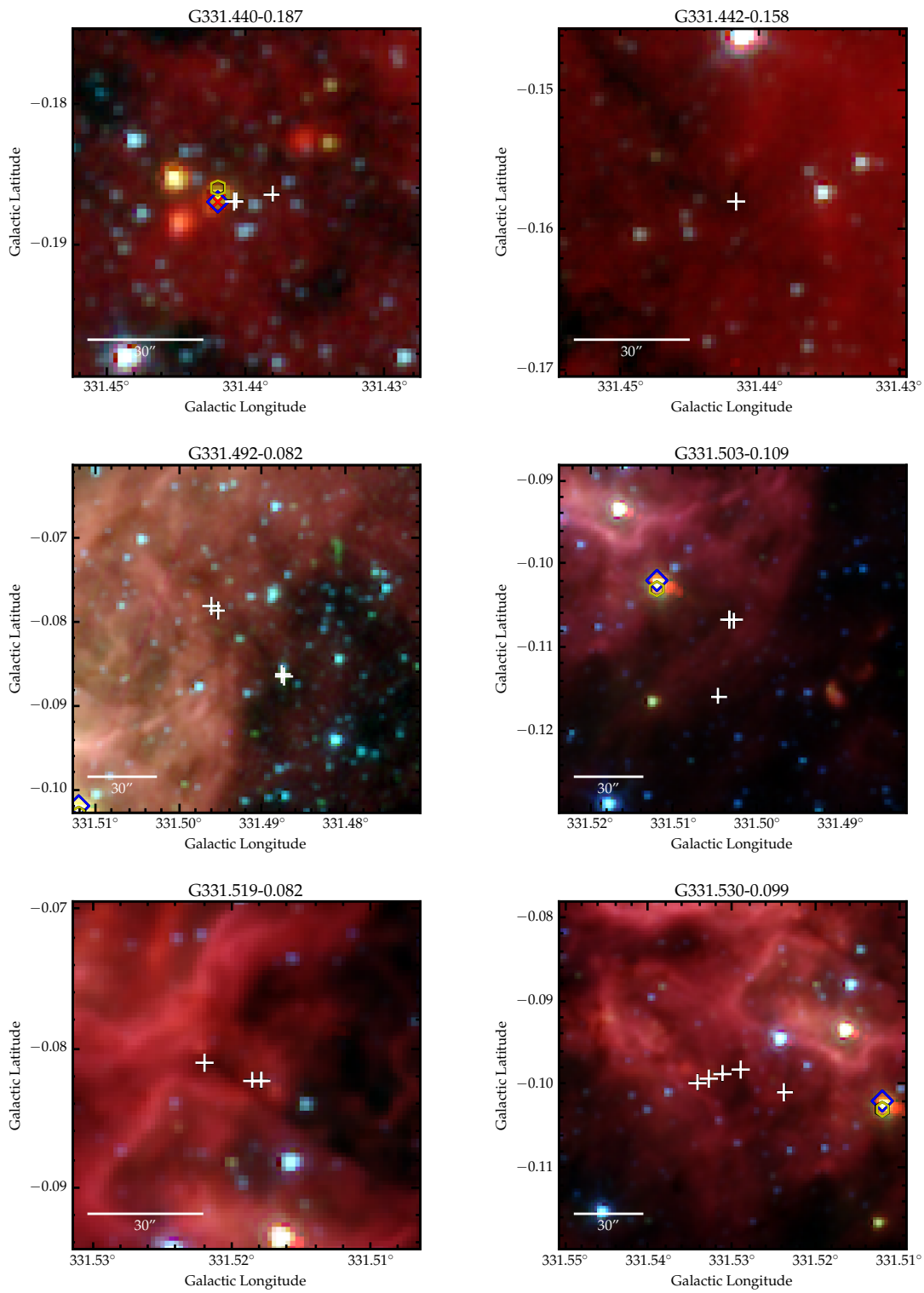
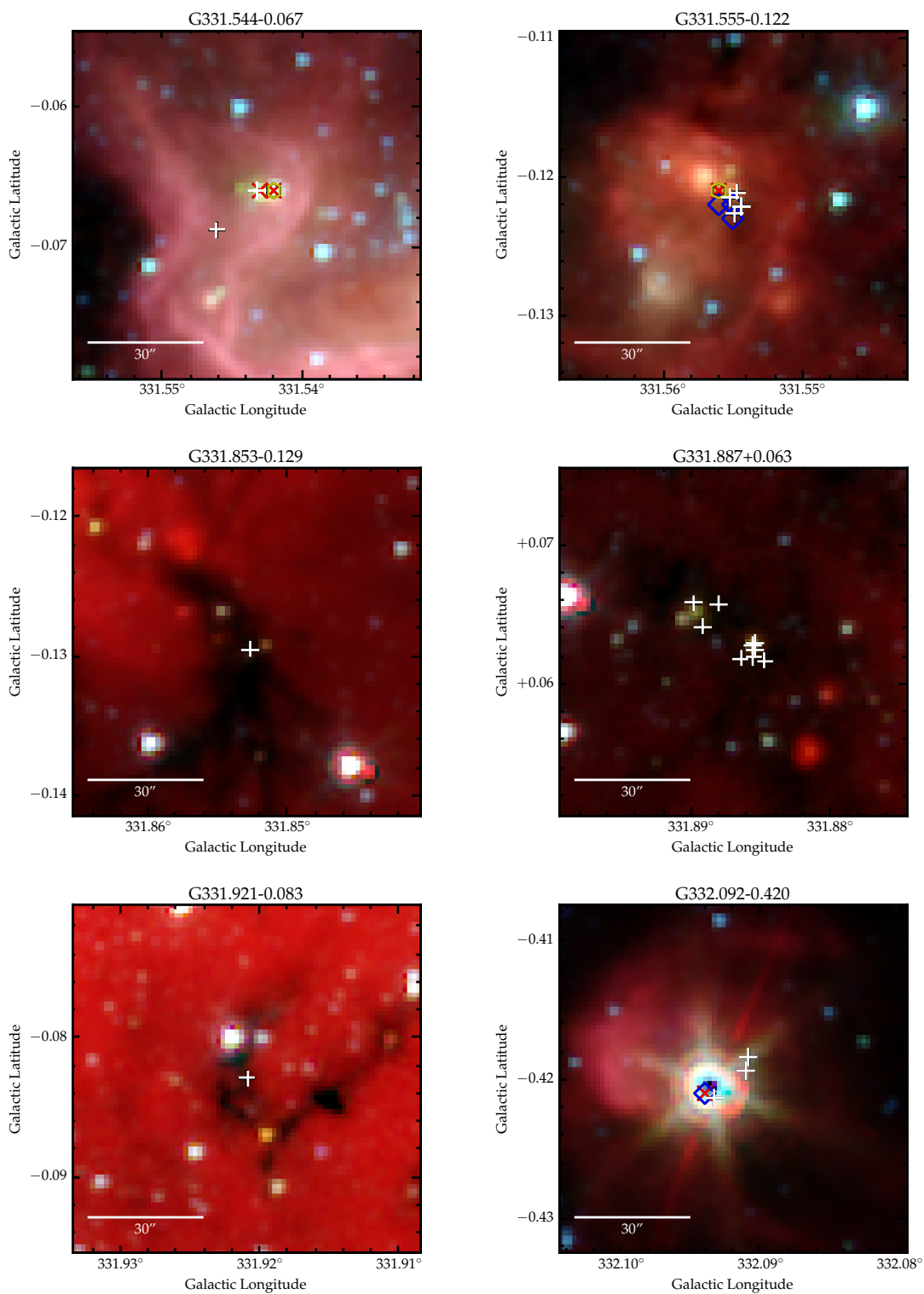


Figure B.1: *continued*

Figure B.1: *continued*

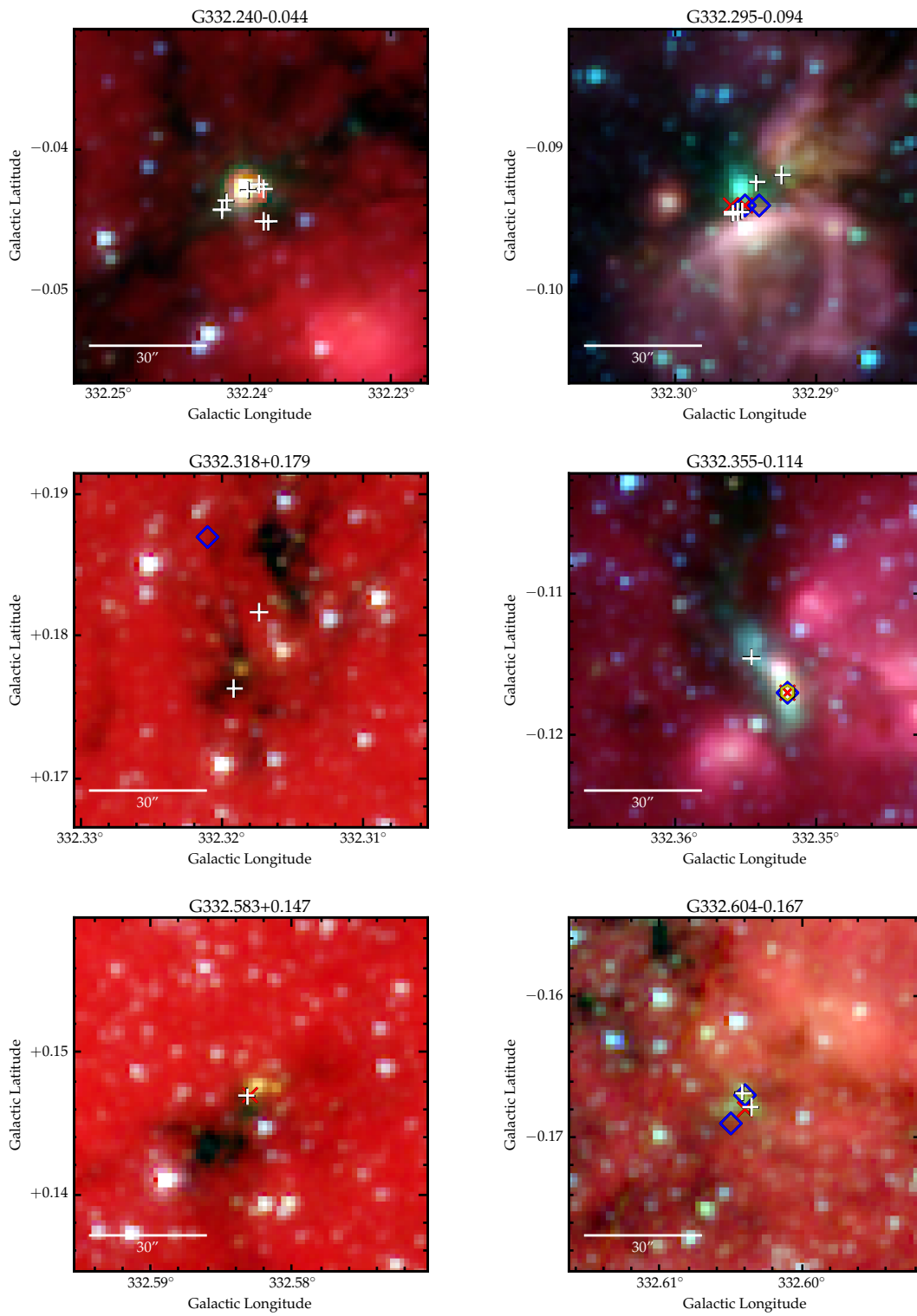
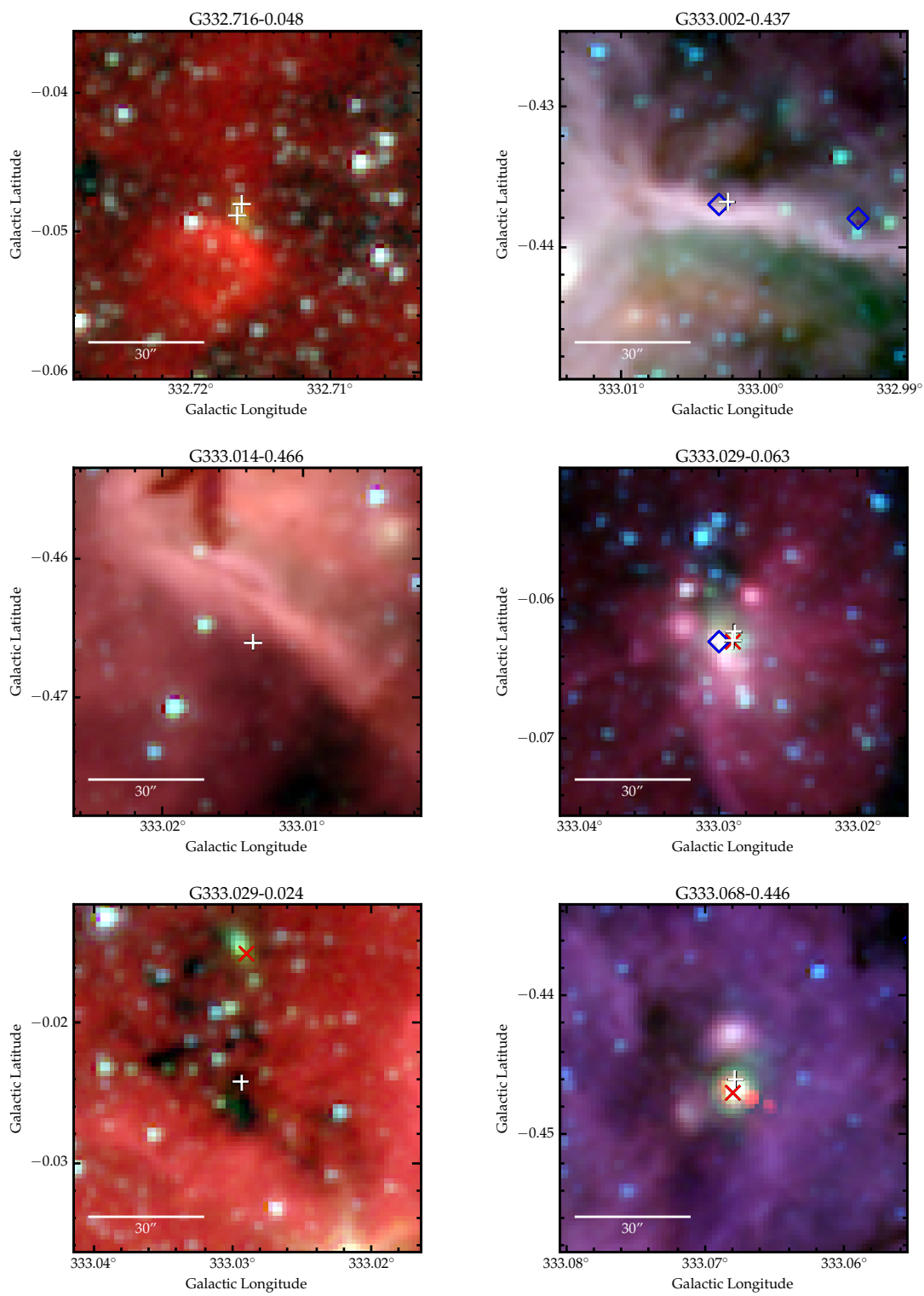


Figure B.1: *continued*

Figure B.1: *continued*

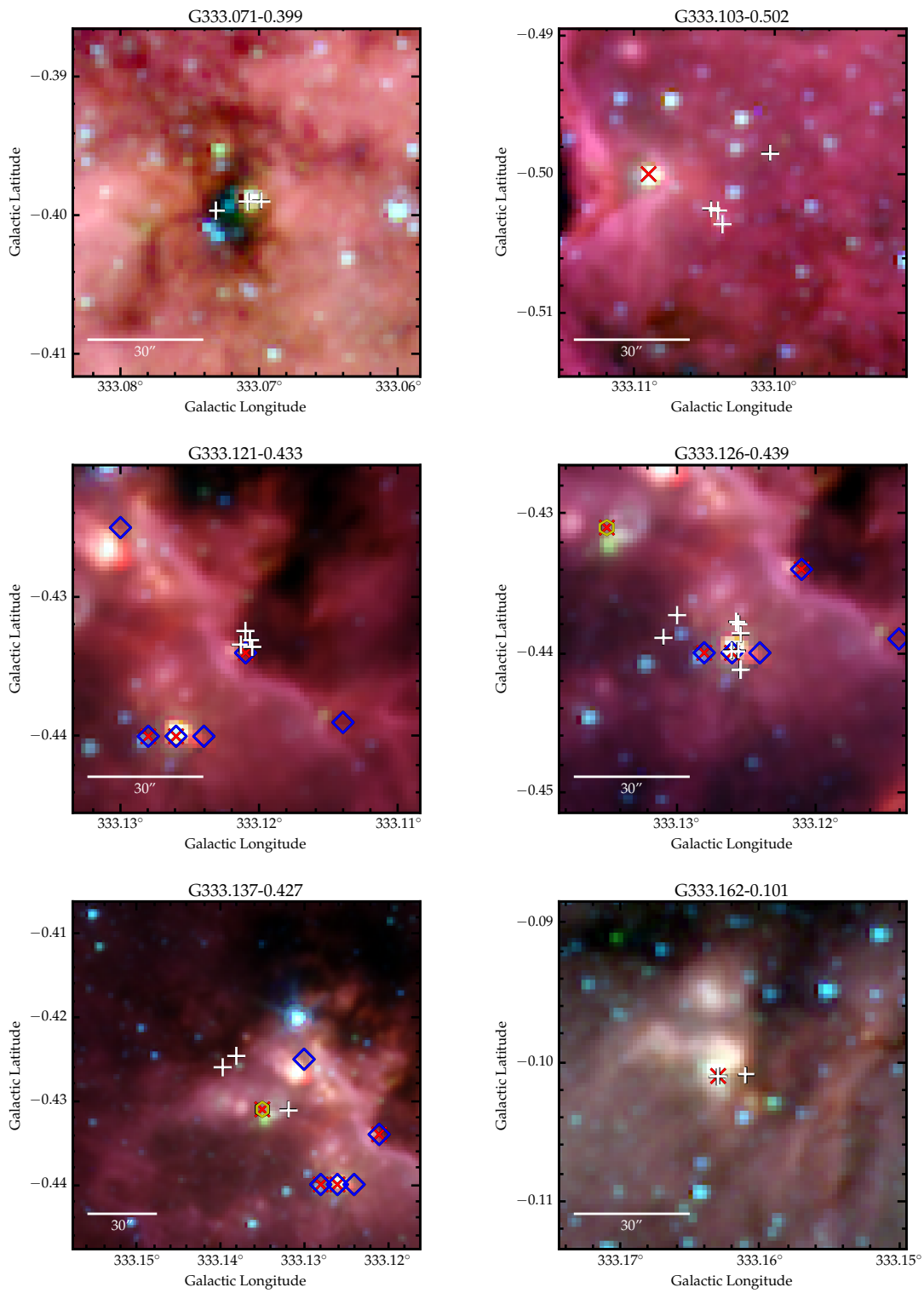
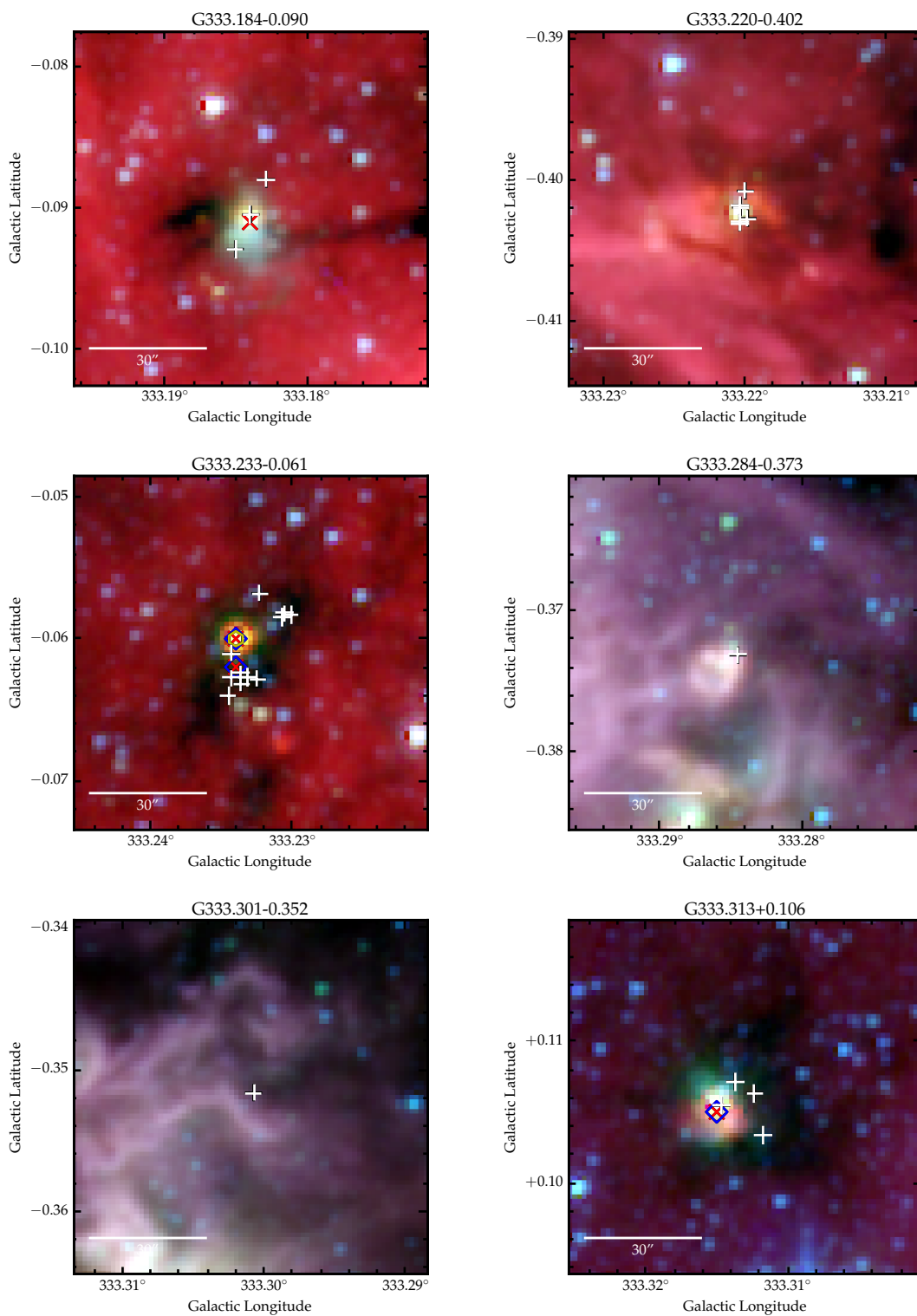


Figure B.1: *continued*

Figure B.1: *continued*

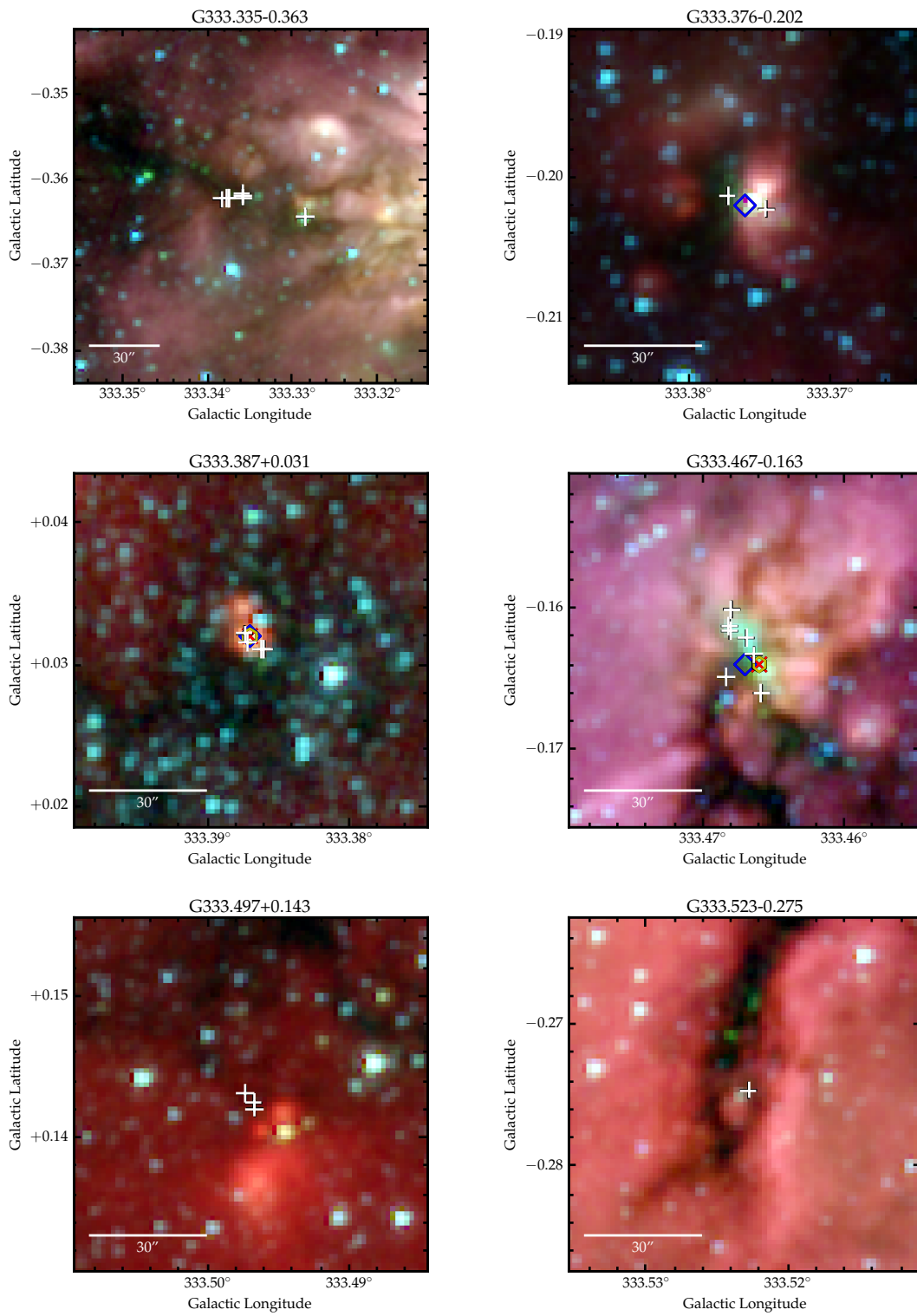
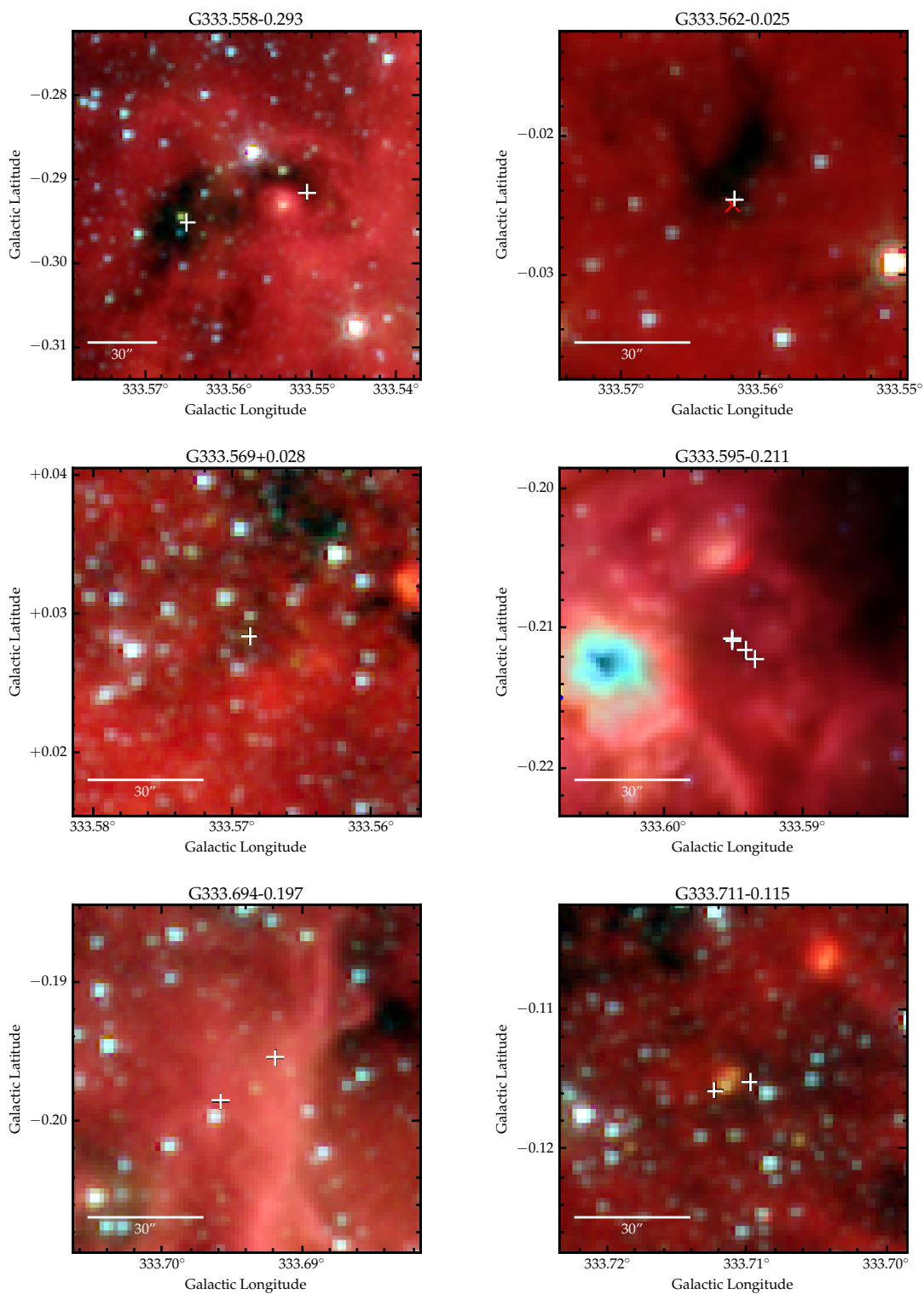


Figure B.1: *continued*

Figure B.1: *continued*

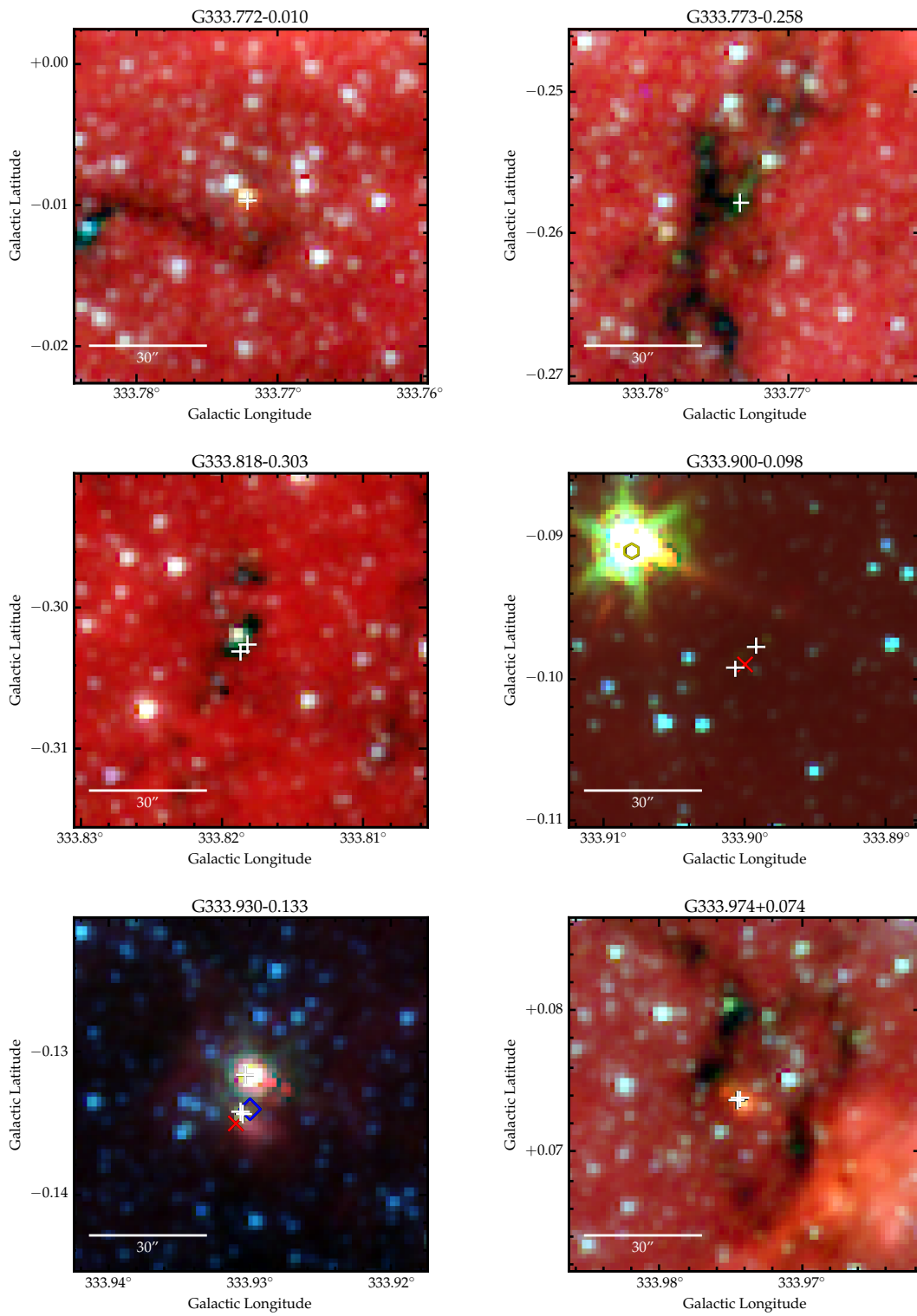
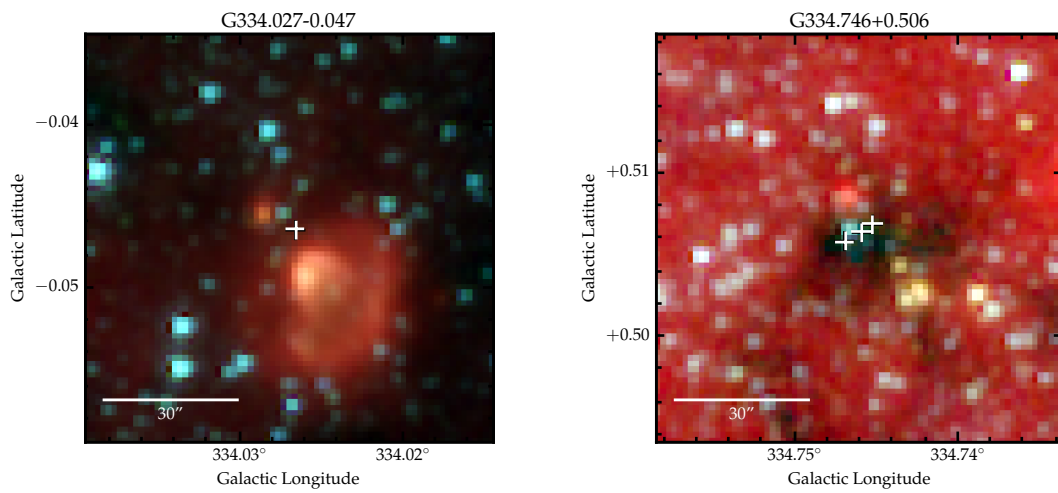


Figure B.1: *continued*

Figure B.1: *continued*